# Investigation of Sulfur Poisoning of Ni-based Anodes in Solid Oxide Fuel Cells

**Von der Fakultät Energie-, Verfahrens- und Biotechnik der Universität Stuttgart zur Erlangung der Würde eines Doktors der Ingenieurwissenschaften (Dr.-Ing.) genehmigte Abhandlung**

**Vorgelegt von**

**Matthias Riegraf**

**aus Ludwigsburg**

| | |
|---|---|
| **Hauptberichter:** | **Prof. Dr. K. Andreas Friedrich** |
| **Mitberichter:** | **Prof. Dr. Anke Hagen** |
| **Tag der mündlichen Prüfung:** | **19.02.2019** |

**Institut für Gebäudeenergetik, Thermotechnik und Energiespeicherung der Universität Stuttgart**

**2019**

## Abstract

The solid oxide fuel cell (SOFC) is an energy conversion technology that promises high electrical efficiencies, low emissions and fuel flexibility. However, its commercial application is still hindered by its high manufacturing costs and limited lifetime. One of the degradation processes that decrease SOFC lifetime is sulfur poisoning of the state-of-the-art Ni-based electrodes due to impurities in the fuel. The objective of the present thesis is to advance the fundamental understanding of sulfur poisoning phenomena in SOFC with Ni-based anodes to allow their optimized operation and design.

An elementary kinetic model was developed to predict the influence of sulfur poisoning on the behavior of Ni/Yttria-stabilized zirconia (YSZ) anodes. A detailed multi-step reaction mechanism of sulfur formation and oxidation at Ni/YSZ anodes coupled with channel gas-flow, porous-media transport and elementary charge transfer chemistry was established for SOFC operating with trace amounts of $H_2S$. A thermodynamic and kinetic data set of sulfur formation and oxidation was derived based upon various literature sources and includes a coverage-dependent description of the enthalpy of surface-adsorbed sulfur. The validity of the model is demonstrated on SOFC at different operating conditions operating both on $H_2/H_2O/H_2S$ and $CH_4/H_2/H_2O/H_2S$ fuel mixtures using various electrochemical literature experiments. The results reveal that sulfur surface coverage on nickel increases with current density demonstrating a low sulfur oxidation rate.

Furthermore, the sulfur poisoning behavior of various commercial, high-performance electrolytes-supported cells with Ni/Gadolinium-doped ceria (CGO) anodes was experimentally investigated. Different SOFC with Ni/CGO-based anodes were characterized by means of impedance spectroscopy and current-voltage characteristics at different temperatures and in $H_2/H_2O$ and reformate fuels. The short-time sulfur poisoning behavior was systematically investigated for varying temperatures of 800 – 950 °C and for current densities of 0 – 0.75 $A \cdot cm^{-2}$ with $H_2S$ concentrations of 1 – 20 ppm. A sulfur poisoning mitigation effect was observed at high current loads and temperatures. The poisoning behavior was shown to be reversible for short exposure times. It was observed that the sulfur-affected processes exhibited significant different relaxation times depending on the Gd content in the CGO phase. Moreover, it was demonstrated that the capacitance of Ni/CGO10 anodes is strongly dependent on temperature and gas phase composition reflecting a changing $Ce^{3+}/Ce^{4+}$ ratio.

The sulfur poisoning behavior of Ni/CGO10 anodes in reformate fuels was compared with Ni/YSZ anodes. Various methane and carbon monoxide containing fuels were used in order to

elucidate the underlying reaction mechanism. The analysis of the cell resistance increase in $H_2/H_2O/CO/CO_2$ fuel gas mixtures revealed that the poisoning behavior is mainly governed by an inhibited hydrogen oxidation reaction at low current densities. At higher current densities, the resistance increase becomes increasingly large, indicating a particularly severe poisoning effect on the carbon monoxide conversion reactions. However, the ability of Ni/CGO anodes to convert carbon monoxide even at $H_2S$ concentrations up to 20 ppm was demonstrated, while this was not possible for Ni/YSZ. From methane steam reforming experiments, it is deduced that the Ni surface is blocked and thus, the water gas shift reaction is fully deactivated as well. However, electrochemical CO oxidation on the CGO surface was shown to be still active.

Moreover, this work presents an in-depth analysis of long-term degradation due to sulfur poisoning of Ni/CGO anodes. A parameter study of sulfur-induced irreversible long-term degradation was carried out at 900 °C for different $H_2S$ concentrations, varying $H_2/N_2/H_2O$ fuel gas atmospheres, current densities and different Ni/CGO anodes. The sulfur poisoning periods of the different cells varied from 200 to 1500 h. The possibility of stable long-term Ni/CGO anode operation under sulfur exposure is established and the critical operating regime is outlined. Degradation was observed to be triggered by a combination of a small anodic (Galvani) potential step and high sulfur coverage on Ni and is accompanied by an increase in anode charge transfer and ohmic resistance. The microstructural evolution of altered Ni/CGO anodes was examined post-mortem by means of scanning electron microscopy (SEM) and focused ion beam (FIB)-SEM, and is correlated to the anode performance degradation, establishing Ni depletion in the anode functional layer. It is shown that short-term sulfur poisoning behavior can be used to assess long-term stability.

The present results clearly demonstrate that the superior sulfur tolerance of Ni/CGO not only is limited to $H_2/H_2O$ fuel systems, but also extends to CO-containing gases. In addition, their stable long-term operation under sulfur exposure was established. These results offer guidelines for stable SOFC operation strategies and encourage the continued optimization of Ni/CGO anode performance and sulfur tolerance.

## Zusammenfassung

Die Festoxidbrennstoffzelle (SOFC) ist eine Technologie zur Energiewandlung, die hohe elektrische Wirkungsgrade, niedrige Emissionen und Brennstoffflexibilität verspricht. Die kommerzielle Anwendung der SOFC wird momentan jedoch noch durch ihre hohen Herstellungskosten und ihre geringe Lebensdauer erschwert. Einer der Degradationsprozesse, die die SOFC-Lebensdauer einschränken, ist die Schwefelvergiftung von Ni-basierten Elektroden durch Verunreinigungen im Brenngas. Das Ziel der vorliegenden Arbeit ist das grundlegende Verständnis von Schwefelvergiftungsvorgängen in SOFC mit Ni-basierten Anoden voranzubringen, um die Voraussetzungen für eine optimierte Zellentwicklung und Betriebsweise zu schaffen.

Ein elementarkinetisches Model wurde entwickelt, um den Einfluss von Schwefelvergiftung auf das Verhalten von Nickel/Yttrium-stabilisierten Zirkonoxid (YSZ)-Elektroden vorherzusagen. Ein detaillierter Mehrschritt-Reaktionsmechanismus für Schwefelbildung und Schwefeloxidation auf Ni/YSZ wurde hergeleitet und mit Stofftransportprozessen im Gaskanal und in der porösen Elektrode, und elementarkinetischem Ladungstransfer gekoppelt. Ein thermodynamischer und kinetischer Datensatz für Schwefelbildung und -oxidation, inklusive einer oberflächenbedeckungsabhängigen Beschreibung der Enthalpie von adsorbiertem Schwefel, wurde auf Basis verschiedener Literaturquellen entwickelt. Das Model wurde für $H_2/H_2O/H_2S$ und $CH_4/H_2/H_2O/H_2S$-Brenngase unter verschiedenen Betriebsbedingungen anhand von verschiedenen elektrochemischen Literaturexperimenten validiert. Die Simulationen zeigen, dass der Schwefelbedeckungsgrad auf Nickel mit zunehmender Stromdichte ansteigt, was eine niedrige Schwefeloxidationsgeschwindigkeit bedeutet.

Weiterhin wurde das Schwefelvergiftungsverhalten von verschiedenen leistungsstarken kommerziellen elektrolytgestützten Zellen mit Ni/Gadolinium-dotierten Ceroxid (CGO)-Anoden experimentell untersucht. Verschiedene SOFC mit Ni/CGO-basierten Anoden wurden mithilfe von elektrochemischer Impedanzspektroskopie und Strom-Spannungs-Kennlinien bei verschiedenen Temperaturen und im $H_2/H_2O$ und Reformat-Betrieb untersucht. Das Kurzzeitvergiftungsverhalten wurde mit $H_2S$-Konzentrationen von 1 – 20 ppm bei verschiedenen Temperaturen zwischen 800 – 950 °C und Stromdichten zwischen 0 – 0.75 $A \cdot cm^{-2}$ systematisch untersucht. Ein mindernder Einfluss von hoher Stromdichte und Temperatur wurde festgestellt. Das Vergiftungsverhalten bei kurzen Vergiftungszeiten war vollständig reversibel. Es wurde nachgewiesen, dass der schwefelbeeinflusste Prozess abhängig vom Gd-Gehalt in der CGO-Phase unterschiedliche Relaxationszeiten aufweist. Zudem

wurde aufgezeigt, dass die Kapazität des Ladungstransferprozesses der Ni/CGO10-Anode stark von Temperatur und $pO_2$-Gehalt abhängt, was das veränderliche Verhältnis zwischen $Ce^{3+}$ und $Ce^{4+}$ widerspiegelt.

Das Schwefelvergiftungsverhalten von Ni/CGO10-Anoden im Reformatbetrieb wurde mit Ni/YSZ-Anoden verglichen. Dabei wurden unterschiedliche Methan und Kohlenstoffmonoxid-basierte Brenngase benutzt um den zugrundeliegenden Reaktionsmechanismus aufzuklären. Die Analyse des Widerstandsanstiegs in $H_2/H_2O/CO/CO_2$-Brenngasen zeigte, dass das Vergiftungsverhalten bei niedrigen Stromdichten hauptsächlich durch eine gehemmte Wasserstoffoxidation bestimmt ist. Bei höheren Stromdichten nimmt der Widerstandsanstieg durch Schwefelvergiftung zu, was einen besonders ausgeprägten Vergiftungseinfluss auf die Kohlenstoffmonoxid-Oxidationsreaktionen andeutet. Allerdings wurde nachgewiesen, dass Ni/CGO selbst bei hohen Schwefelwasserstoffkonzentrationen von 20 ppm in der Lage ist, Kohlenstoffmonoxid zu oxidieren, was auf Ni/YSZ nicht möglich ist. Von Untersuchungen der Methandampfreformierung wurde abgeleitet, dass die Nickeloberfläche für diese Reaktion und auch für die Wasser-Gas-Shift-Reaktion komplett deaktiviert ist. Allerdings ist die elektrochemische Kohlenstoffmonoxid-Oxidation auf der CGO-Oberfläche bei gleichen Schwefelwasserstoffkonzentrationen immer noch aktiv.

Weiterhin präsentiert die vorliegende Arbeit eine Analyse der Langzeitstabilität von Ni/CGO unter Schwefelvergiftung. Eine Parameterstudie von schwefelinduzierter, irreversibler Langzeitdegradation wurde bei 900 °C und für verschiedene $H_2S$-Konzentrationen durchgeführt. Weiterhin wurden auch der Einfluss von Brenngaszusammensetzung, Stromdichte und Ni/CGO-Zusammensetzung untersucht. Die Schwefelvergiftungszeiträume der verschiedenen Zellen betrugen zwischen 200 und 1500 Stunden. Die Möglichkeit eines stabilen Langzeitbetriebs von Ni/CGO unter Schwefelbeauschlagung wurde aufgezeigt und das kritische Betriebsfenster skizziert. Es wurde festgestellt, dass die irreversible Schwefeldegradation durch eine Kombination von hohem Schwefelbedeckungsgrad auf Ni und niedrigem Anodenpotentialschritt ausgelöst wird, was zu einem Anstieg des Ohmschen und des Anoden-Ladungstransfer-Widerstands führt. Die mikrostrukturelle Veränderung der gealterten Ni/CGO-Anoden wurde mithilfe von REM und FIB-SEM-Methoden post-mortem untersucht und mit der Leistungsabnahme korreliert. Dabei wurde eine Ni-Verarmung in der Anoden-Funktionsschicht festgestellt. Weiterhin wurde gezeigt, dass das Kurzzeitschwefelvergiftungsverhalten zur Vorhersage der Langzeitstabilität genutzt werden kann.

## Content

## List of abbreviations

| | |
|---|---|
| APU | Auxiliary power unit |
| ASC | Anode-supported cell |
| ASR | Area-specific resistance |
| BSE | Backscattered electrons |
| CGO | Gadolinium-doped ceria |
| CGO10 | $(Gd_2O_3)_{0.1}(CeO_2)_{0.9}$ |
| CGO40 | $(Gd_2O_3)_{0.4}(CeO_2)_{0.6}$ |
| CHP | Combined heat and power |
| CNLS | Complex nonlinear square |
| CPE | Constant phase elements |
| CPOX | Catalytic partial oxidation |
| CTE | Coefficient of thermal expansion |
| DFT | Density functional theory |
| DPB | Double phase boundary |
| DR | Dry reforming |
| DRT | Distribution of relaxation times |
| ECM | Equivalent circuit model |
| EDX | Energy dispersive X-ray spectroscopy |
| EIS | Electrochemical impedance spectroscopy |
| ESC | Electrolyte-supported cell |
| fcc | Face centered cubic |
| FEG | Field emission gun |
| FIB-SEM | Focused ion beam scanning electron microscopy |
| GDC | Gadolinium-doped ceria |
| hcp | Hexagonal closed packed |
| IAM-WET | Institute for Applied Materials - Materials for Electrical and Electronic Engineering |
| IKTS | Fraunhofer Institute for Ceramic Technologies and Systems |
| KIT | Karlsruhe Institute of Technology |
| LF | Low frequency |
| LSCF | Lanthanum strontium cobalt ferrite |
| LSM | Lanthanum strontium manganite |

| | |
|---|---|
| LST | Lanthanum-doped strontium titanate |
| MEA | Membrane electrode assembly |
| MIEC | Mixed ionic-electronic conductor |
| MF | Middle frequency |
| ML | Monolayer |
| MSC | Metal-supported cell |
| MSR | Methane steam reforming |
| OCV | Open circuit voltage |
| PEMFC | Polymer electrolyte membrane fuel cell |
| PSD | Particle size distribution |
| r-WGS | Reverse water gas shift |
| RVE | Representative volume element |
| S/C | Steam-to-carbon |
| ScSZ | Scandia-stabilized zirconia |
| 10Sc1CeSz | $(Sc_2O_3)_{0.1}(CeO_2)_{0.01}(ZrO_2)_{0.89}$ |
| 6ScSz | $(Sc_2O_3)_{0.06}(ZrO_2)_{0.94}$ |
| SE | Secondary electrons |
| SEM | Scanning electron microscopy |
| SOEC | Solid oxide electrolysis cell |
| SOFC | Solid oxide fuel cell |
| TC | Thermocouple |
| TEM | Transmission electron microscopy |
| TLM | Transmission line model |
| TPB | Triple phase boundary |
| TPD | Temperature-programmed desorption |
| TOF-SIMS | Time-of-flight secondary-ion mass spectrometry |
| WGS | Water gas shift |
| YSZ | Yttria-stabilized zirconia |
| 3YSZ | $(Y_2O_3)_{0.03}(ZrO_2)_{0.97}$ |
| 8YSZ | $(Y_2O_3)_{0.08}(ZrO_2)_{0.92}$ |
| XPS | X-ray photoelectron spectroscopy |
| XRD | X-ray diffraction |
| XRF | X-ray fluorescence |

## List of symbols

| Symbol | Unit | Description |
|---|---|---|
| $a$ | – | Steric coefficient |
| $a$ | – | Reaction order of $H_2$ |
| $a_j$ | – | Activity of species j |
| $A$ | $m^2$ | Area |
| $A_j^V$ | $m^2 \cdot m^{-3}$ | Volume-specific surface area of species j |
| $ASR$ | $\Omega \cdot m^2$ | Area-specific resistance |
| $b$ | – | Reaction order of $H_2O$ |
| $B$ | $m^2$ | Permeability |
| $B$ | $\Omega \cdot m^2$ | Pre-exponential factor global approach |
| $C$ | F | Ideal capacitance |
| $CPE$ | F | Non-ideal capacitance |
| $d$ | m | Distance |
| $d_j$ | m | Thickness of material j |
| $d_P$ | m | Pore size |
| $D_j$ | $m^2 \cdot s^{-1}$ | Diffusion coefficient of species j |
| $D_j^{eff}$ | $m^2 \cdot s^{-1}$ | Effective diffusion coefficient of species j |
| $D_j^K$ | $m^2 \cdot s^{-1}$ | Knudsen diffusion coefficient of species j |
| $E^0$ | V | Reversible cell voltage at the standard state |
| $E^{th}$ | V | Equilibrium Nernst potential |
| $E_{act}$ | $J \cdot mol^{-1}$ | Activation energy barrier |
| $E$ | V | Potential |
| $f$ | $s^{-1}$ | Frequency |
| $F$ | 96 485 C | Faraday constant |
| $FU$ | – | Fuel utilization |
| $FU_{H2}$ | – | Hydrogen utilization |
| $g(f)$ | $\Omega \cdot s$ | Distribution function of relaxation times |
| $h_{j_i}$ | $J \cdot mol^{-1}$ | Molar enthalpy of species j |
| $i$ | $\sqrt{-1}$ | Imaginary unit |
| $i$ | $A \cdot cm^{-2}$ | Current density |

| | | |
|---|---|---|
| $I$ | A | Current |
| $i_0$ | $A \cdot cm^{-2}$ | Amplitude of current density in EIS measurement |
| $i_0$ | $A \cdot cm^{-2}$ | Exchange current density |
| $I_F$ | A | Faradaic current |
| $J_j^D$ | $mol \cdot m^{-2} \cdot s^{-1}$ | Diffusive flux of species j |
| $k$ | $A \cdot cm^{-2}$ | Pre-factor of exchange current density |
| $k_0$ | $cm^2 \cdot mol^{-1} \cdot s^{-1}$ | Pre-exponential factor elementary kinetic approach |
| $k_f$ | $mol^{1-n} \cdot m^{3(n-1)} \cdot s^{-1}$ | Forward reaction rate constant for n-th order reaction |
| $k_r$ | $mol^{1-n} \cdot m^{3(n-1)} \cdot s^{-1}$ | Reverse reaction rate constant for n-th order reaction |
| $l$ | m | Length |
| $l_{Ni/YSZ}^{V}$ | $m \cdot m^{-3}$ | Volumetric TPB length between Ni and YSZ |
| $M_j$ | $kg \cdot mol^{-1}$ | Molar mass of species j |
| $n$ | – | Exponent in non-ideal capacitor element $Q$ |
| $p$ | Pa/atm | Pressure |
| $p_j$ | Pa/atm | Partial pressure of species j |
| $P_{el}$ | $W \cdot m^{-3}$ | Power density |
| $Q$ | $m^3 \cdot s^{-1}$ | Discharge rate through a porous medium |
| $Q$ | C | Charge |
| $Q$ | F | Non-ideal capacitance |
| $r_p$ | m | Mean pore radius |
| $R$ | $8.314\ J \cdot mol^{-1} \cdot K^{-1}$ | Universal gas constant |
| $R^2$ | – | Coefficient of determination |
| $R_{ohm}$ | $m^2$ | Ohmic resistance |
| $R_{pol}$ | $\Omega \cdot m^2$ | Polarization resistance |
| $\dot{s}$ | $mol \cdot s^{-1}$ | Net change of charged species |
| $s_j$ | $J \cdot K^{-1} \cdot mol^{-1}$ | Molar entropy of species j |
| $s_j^0$ | – | Sticking coefficient of species j |
| $t$ | s | Time |
| $\tau$ | – | Power coefficient |
| $T$ | K | Temperature |
| $z$ | – | Number of electrons |
| $\underline{Z}$ | $\Omega$ | Complex impedance |

| | | |
|---|---|---|
| $Z'$ | Ω | Real part of the complex impedance |
| $Z''$ | Ω | Imaginary part of the complex impedance |
| □ | – | Free active surface site |
| $\Delta G^0$ | J | Standard Gibbs free reaction enthalpy |
| $\Delta h^0$ | $J \cdot mol^{-1}$ | Standard molar reaction enthalpy |
| $\Delta s^0$ | $J \cdot K^{-1} \cdot mol^{-1}$ | Standard molar reaction entropy |
| $\Delta \phi_j$ | V | Electrostatic (Galvani) potential step at location (interface) j |
| $\Delta \chi$ | V | Surface potential step at surface/gas phase double layer |
| $\nabla cj$ | $mol \cdot m^{-4}$ | Concentration gradient of species j |
| $\alpha$ | – | Apparent charge transfer coefficient |
| $\beta$ | – | Temperature exponent |
| $\varepsilon$ | – | Porosity |
| $\Theta$ | ° | Angle |
| $\Theta_j$ | ML | Surface coverage of species j |
| $\Theta_{max}$ | ML | Saturation coverage |
| $\lambda$ | m | wavelength |
| $\mu$ | Pa·s | Gas viscosity |
| $\nu_j$ | – | Stoichiometric coefficient of species j |
| $\eta$ | V | Overpotential |
| $\eta_\Omega$ | V | Ohmic overpotential |
| $\eta_D$ | V | Kinetic activation overpotential |
| $\eta_M$ | V | Mass transport overpotential |
| $\rho_j$ | $kg \cdot m^{-3}$ | Bulk density of species j |
| $\sigma_j$ | $S \cdot m^{-1}$ | Ionic conductivity of species j |
| $\tau$ | – | Tortuosity |
| $\Gamma_j$ | $mol \cdot m^{-2}$ | Surface site density on material j |
| $\varphi$ | – | Phase shift between voltage and current |
| $\omega$ | $s^{-1}$ | Angular frequency |

# 1 Introduction

At the 2015 United Nations Climate Change Conference in Paris, the participating 194 countries agreed to a global pact to reduce their carbon output to hold the increase in the global average temperature to below 2 °C above pre-industrial levels and to pursue efforts to limit the temperature increase to 1.5 °C above pre-industrial levels.[1] Furthermore, some experts predict that the world oil production will peak before 2020, indicating declining oil supplies.[2]

In Germany, the government subsidizes the purchase of electric cars in an effort to put 1 million electric cars on the road by 2020 and help fulfill its zero-emission mobility vision. Moreover, it was decided to withdraw from the use of nuclear energy until 2022.[3]

These examples illustrate increasing global awareness towards the influence of humans on the environment and the question how sustainable development can be achieved while the world population still continuously increases. Hence, there is great interest in the development of highly efficient energy conversion devices that can reduce the consumption of fossil fuels or ideally even allow the use of renewable fuels such as hydrogen, syngas or biogas.

One of such a device is the fuel cell that is able to convert the chemical energy of a redox reaction directly into electricity. In contrast to conventional combustion engines in fuel cells the chemical energy of a redox reaction is not first converted into thermal and mechanical energy before being transformed into electricity. Therefore, fuel cells are not limited by the Carnot efficiency and thus, can reach high electrical efficiencies of up to 60 %. As the primary fuel of fuel cells is hydrogen, the product of its electrochemical conversion is mainly water making the fuel cell a low-emission technology. Moreover, fuel cells can be used in decentralized power plants, opening up the possibility of co-generation of electricity and heat. These smaller systems allow an efficient distribution and utilization of the produced heat, which further increases the systems' energy efficiency.

In this context, due to their high operating temperatures that give rise to fast reaction kinetics, solid oxide fuel cells (SOFC) are a promising technology since they are capable to readily convert hydrocarbons, carbon monoxide and biofuels without the necessity of employing noble metals as catalysts.[4] Hence, SOFC are not dependent on the expansion of the hydrogen infrastructure. Accordingly, SOFC are a well-suited electrical power source in a variety of applications, ranging from small-scale stationary combined heat and power (CHP) systems for residential use to auxiliary power unit (APU) in mobile applications such as trucks to large-

scale power generation in hybrid power plants.[5,6]

Major challenges hindering the market readiness of SOFC are limited durability and high costs. In this context, a lifetime over 40,000 hours is targeted in order to make commercialization of SOFC viable.[7,8] Although continuous progress is being achieved with respect to lifetime and performance improvements, SOFC continue to struggle with commercialization. One option to decrease the cost of SOFC systems would be to simplify the balance of plant by reducing the number of upstream fuel processing components, such as the desulfurization unit. However, a variety of degradation phenomena lead to a large deterioration of SOFC performance over time. One important degradation process is the sulfur poisoning of Ni-based anodes due to sulfur-containing impurities in the prospective fuels such as natural gas, diesel or biogas. These impurities lead to significant performance losses, thus making the use of desulfurization units before the SOFC indispensable. As a result, there is significant incentive to understand the mechanisms of SOFC degradation since their knowledge possibly provides the foundation for the development of more sulfur-tolerant novel designs and process optimization.[9]

Therefore, the aim of the present thesis is the measurement and understanding of sulfur poisoning processes on Ni-based anodes. In particular, the promising sulfur tolerance of Ni/Gadolinium-doped ceria (CGO) anodes in comparison to Ni/Yttria-stabilized (YSZ) anodes is explored throughout the work.

In chapter 2 the scientific and technological background of the present thesis is described. Chapter 3 presents the employed methodology. The elementary kinetic modeling of sulfur poisoning of Ni/YSZ anode-based cells is described in chapter 4 for both $H_2/H_2O$ and $CH_4$-containing fuels. Subsequently, in chapter 5 the superior short-term sulfur tolerance of Ni/CGO anode-based cells is established in $H_2/H_2O$ fuels and the effect is investigated for a wide range of operating conditions. Moreover, sulfur poisoning of Ni/CGO anodes operated on a variety of reformate fuels is systematically investigated in chapter 6. In chapter 7, an extensive long-term degradation study of Ni/CGO-based cells is presented and the parameters responsible for the onset of sulfur-induced degradation are outlined. Eventually, conclusions and future perspectives are presented.

# 2 Background

## *2.1 Solid oxide fuel cells*

The operating principle of a fuel cell is to convert chemical energy into electrical energy based on redox reactions. Therefore, the oxidation reaction and the reduction reaction are spatially separated by an ionic conductor (the electrolyte). Thus, the electron transfer necessary for the bonding reconfiguration from high-energy reactants to low-energy products occurs over an extended length scale, which allows harnessing the electrons as an electrical current.

Accordingly, in an SOFC a simple hydrogen combustion reaction is split into two electrochemical reactions, the hydrogen oxidation and the oxygen reduction reaction:

$$H_2 + O^{2-} \rightleftharpoons H_2O + 2\ e^- \quad (1)$$

$$0.5\ O_2 + 2\ e^- \rightleftharpoons O^{2-}. \quad (2)$$

The term solid oxide fuel cell originates from the use of solid oxide materials as electrolyte.[10] The basic operating principle of an SOFC in $H_2/O_2$ operation is illustrated in Figure 2.1. The basic structure of a SOFC consists of three main components: the fuel electrode (anode), the air electrode (cathode) and a gas-tight electrolyte with high ionic and low electronic conductivity in between. In SOFC, oxygen ions ($O^{2-}$) ions are transported from the cathode to the anode, with the driving force being a difference in oxygen partial pressure between the two gas compartments.

At the cathode, oxygen molecules are electrochemically reduced to $O^{2-}$ ions, which migrate through the electrolyte to the anode where they electrochemically oxidize the fuel (mainly hydrogen), and the products (mainly water) are formed. During the oxidation reactions, electrons are set free which cannot flow through the electrolyte and thus, create a current while flowing through the external circuit back to the cathode to reduce oxygen. The reactants are gaseous and are supplied to the cell via flow channels.

In commercial applications, single cells are connected in series to form SOFC stacks. The gas chambers of the individual cells are separated by interconnects which also provide the electrical connection between the cells.

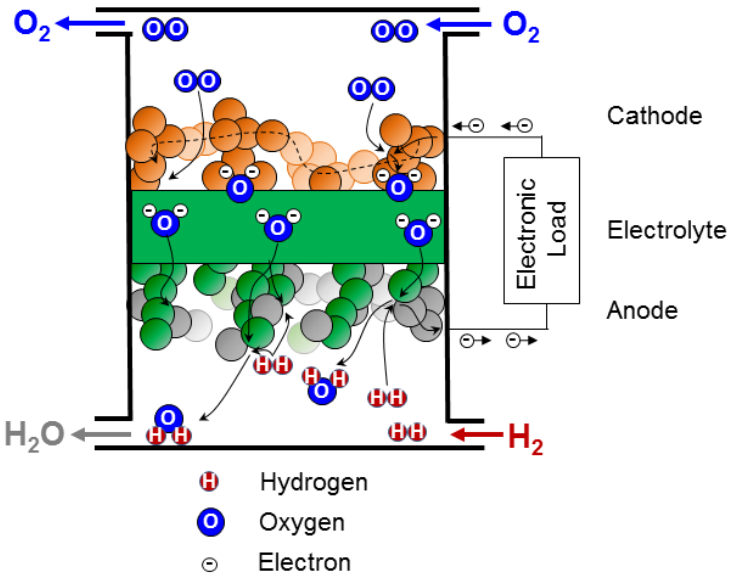


Figure 2.1: Schematic illustration of an SOFC. On the fuel gas side, the oxidation of hydrogen on a composite anode (such as Ni/YSZ) is depicted. On the air side, reduction of oxygen on a mixed ionic electronic conductor (such as LSCF) illustrated.

## *2.2 The composition of SOFC*

SOFC exist in multiple geometries such as the tubular or the planar design. The tubular design is used due to its mechanical robustness and good sealing.[11,12] However, the utilization of tubes gives rise to low volumetric power densities. Therefore, in many applications the planar design is favored, owing to its higher power densities and easy and inexpensive manufacturing.

Depending on which layer provides the mechanical stability of the planar SOFC, they are further divided into electrolyte-supported (ESC), anode-supported (ASC) and metal-supported cells (MSC). Schematic illustrations of the different planar designs are depicted in Figure 2.2. ESC employ thick electrolytes, which provide the high mechanical stability. In the ASC design, thinner electrolytes are used, which gives rise to a better overall performance. However, due to a thick porous anode support layer the ASC design faces other problems, in particular low tolerance towards redox and thermal cycling. In the MSC design, the mechanical support is made from inexpensive and robust metals, which promises increased mechanical and redox stability, and resistivity against rapid thermal cycling.[13] However, their durability is currently still low due to the corrosion of the employed metals.

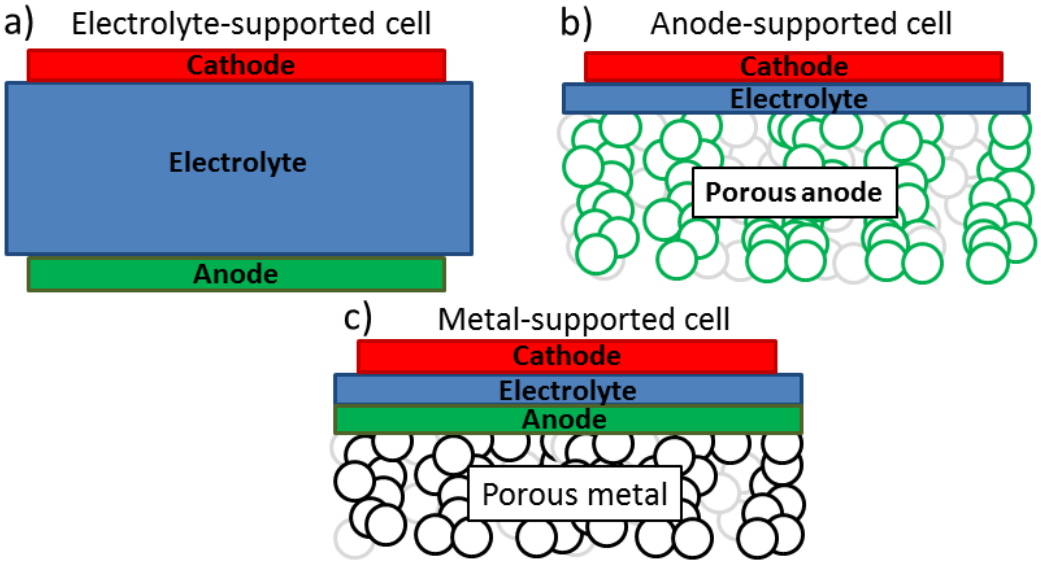


Figure 2.2: Schematic illustration of the different planar SOFC designs: (a) electrolyte-supported cell, (b) anode-supported cell, and (c) metal-supported cell.

However, all of the cells consist of an electrolyte, a cathode and an anode. The requirements and most popular materials for the different components are briefly reviewed in the following subsections.

### *2.2.1 Electrolyte*

In an SOFC, the electrolyte is responsible for ion conduction and thus, must be a good oxygen ion conductor, but a poor electronic conductor. Depending on the design and used materials, SOFC operating temperatures are largely determined by the minimum temperature at which sufficient ionic conductivity can be achieved. A further requirement of the electrolyte is its chemical stability in both a highly reducing anode and oxidizing cathode atmosphere.[14] In ESC, electrolytes are thick (65 – 200 µm) to provide the mechanical stability. However, this leads to significant ohmic losses and thus, operating temperatures of ESC have to be relatively high (800 – 950 °C) to obtain sufficiently high ionic conductivity. In ASC and MSC, the electrolyte thickness is reduced to 5 – 15 µm, allowing operation at significantly lower temperatures (650 – 850 °C). State of the art materials are YSZ and scandia-stabilized zirconia (ScSZ).[15–17] Pure zirconia ($ZrO_2$) has only low ionic conductivity and thus, is not a suitable electrolyte material. Furthermore, zirconia undergoes phase transformations with temperature from monoclinic (room temperature) to tetragonal (at 1170 °C) to cubic (at 2370 °C), which are associated with large volume changes. By doping zirconia with trivalent oxides ($Y_2O_3$, $Sc_2O_3$) the tetragonal or cubic phase can be stabilized from very high temperatures down to

room temperature. Furthermore, doping creates oxygen vacancies in the zirconia lattice to maintain charge neutrality. This significantly increases the ionic conductivity of the doped zirconia depending on the doping level. A doping level of 8 % $Y_2O_3$ (8YSZ) stabilizes the cubic form at room temperature, which displays the highest ionic conductivity among the different phases. A further increase of the doping level is counterproductive as ionic conductivity decreases due to defect ordering, vacancy clustering and electrostatic interactions.[18] The tetragonal phase of zirconia is stabilized for a doping level of 3 % $Y_2O_3$ (3YSZ) and provides an increasing mechanical robustness which makes it a popular choice for electrolyte-supported cells. However, the ionic conductivity of the tetragonal phase is lower than the one of the cubic phase.

Doping of zirconia with $Sc_2O_3$ leads to even higher conductivities than 8YSZ due to a smaller mismatch in size between $Zr^{4+}$ and $Sc^{3+}$.[19] For scandia contents higher than 10 %, transformation from the cubic to the rhombohedral phase occur, which leads to lower conductivity and volume changes. These phase changes can be avoided by co-doping with other oxides, such as ceria or by limiting the scandia content to below 10 %. However, scandia is expensive and the ScSZ exhibits higher degradation rates.[20] Popular scandia doped zirconia compositions are 10Sc1CeSZ ($(Sc_2O_3)_{0.1}(CeO_2)_{0.01}(ZrO_2)_{0.89}$) displaying very high ionic conductivity (cubic phase), but low mechanical robustness, and 6ScSZ ($(Sc_2O_3)_{0.06}(ZrO_2)_{0.94}$) with a lower conductivity (tetragonal phase), but higher mechanical stability.[21]

### *2.2.2 Cathode*

In SOFC, the cathode is responsible for the electrochemical reduction of oxygen (Eq. 2) and should display the following features:[22]

- High electrochemical activity towards the oxygen reduction reaction
- Matching coefficients of thermal expansion (CTE) with the electrolyte material
- No chemical reactivity towards the electrolyte and interconnect materials
- High ionic and electronic conductivity
- High porosity for efficient gas transport
- Long-term stability

Various perovskite materials have been employed as cathode. They are all characterized by the typical $ABO_3$ structure as illustrated in Figure 2.3, in which A and B are cations with total charge of +6. The A cations are generally larger and coordinated to twelve oxygen atoms, while the B cations are coordinated only to six oxygen atoms.[22] It is possible to fully or par-

tially substitute the A or B cations with cations of different valence. When the valence of either the A or the B site adds up to less than six, oxygen vacancies in the lattice or electron-holes are created which leads to enhanced ionic and/or electronic conductivity. Thus, with a reasonable choice of the A and B site cations, perovskites with a high ionic and electronic conductivity can be devised. In most perovskites, the A sites are a mixture of rare and alkaline earths (such as La and Sr, Ca or Ba) and the B sites consists of reducible transition metals (such as Mn, Fe, Co, Ni).

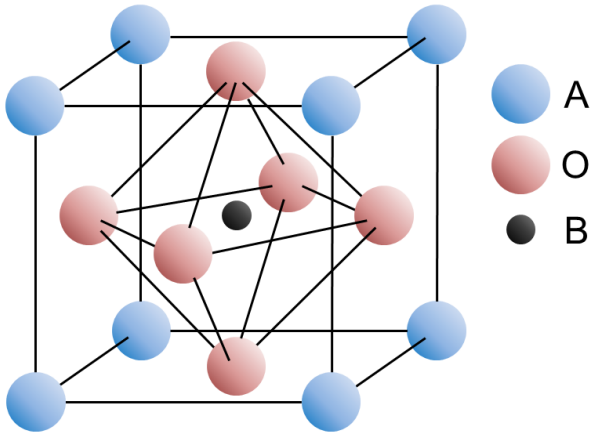


Figure 2.3. Schematic representation of the lattice structure of a perovskite, $ABO_3$.

A very popular choice throughout the last decades has been lanthanum strontium manganite (LSM) with the chemical composition $La_{1-x}Sr_xMnO_{3-\delta}$ where $La^{3+}$ is partially replaced with a lower valence $Sr^{2+}$ cation. As a result, $Mn^{4+}$ is formed to maintain charge neutrality and the $Mn^{3+}/Mn^{4+}$ mix leads to an increased electronic p-type conductivity.[23] The doping also induces ionic conductivity, however, it is comparatively low. Therefore, LSM is usually mixed with YSZ or ScSZ which display similar CTEs.

Another frequently used cathode perovskite material is lanthanum strontium cobalt ferrite (LSCF; $La_{1-x}Sr_xCo_yFe_{1-y}O_{3-\delta}$). It is a mixed ionic/electronic conductor (MIEC) and shows especially superior performance characteristics at intermediate temperatures. In this material, the ionic conductivity is mostly influenced by the A site doping with Sr and the electronic conductivity is mostly influenced by the Co and Fe concentration on the B site.[22]

As LSCF displays high catalytic activity towards the oxygen reduction reaction in addition to both ionic and electronic conductivity, the electrochemical reaction is not confined to the triple phase boundary (TPB) between ionic and electronic conductor and gas phase, but occurs on the whole LSCF surface as illustrated in Figure 2.1. This process is described in detail in subsection 2.3.4. However, these cathodes show higher degradation rates than LSM/YSZ-

based cathodes.[24] Furthermore, LSCF cathodes are not compatible with zirconia-based electrolytes due to the formation of an insulating $SrZrO_3$ interface layer. Thus, a CGO diffusion barrier layer is usually applied between YSZ and LSFC to prevent its formation.

### *2.2.3 Anode*

State-of-the-art materials for the use as SOFC anodes are porous composite electrodes consisting of nickel as catalyst and electronic conductor, and a ceramic ionic conductor.
They fulfill several requirements:

- High catalytic activity towards fuel gas oxidation
- High electronic and ionic conductivity
- Good chemical and mechanical stability
- High thermal expansion compatibility
- Low cost and easy fabrication

The most popular material system is Ni/YSZ. In anode-supported cells, the ceramic structure also provides the mechanical cell stability and robustness. Another advantage of the use of Ni as metal phase is its high activity towards catalytic reforming reactions. Despite their superior performance, Ni-based anodes are susceptible towards multiple degradation phenomena such as redox cycling, Ni agglomeration, carbon deposition and sulfur poisoning. Therefore, a wide range of alternative materials has been examined during recent years. For example, non-metallic perovskites such as lanthanum-doped strontium titanate (LST) are the subject of numerous studies.[25] Perovskite anodes display no performance loss upon sulfur exposure and no formation of coke.[26,27] However, their catalytic activity is comparatively low. Thus, further performance improvements are necessary before they become a viable alternative in commercial applications.
Furthermore, the use of copper as metallic phase in cermet anodes has been investigated and these anodes have shown high tolerance towards both carbon deposition and sulfur poisoning.[28–31] However, copper displays only low catalytic activity and its low melting point (1083 °C) leads to rapid particle agglomeration and evaporation of Cu species and thus, to a rapid performance decrease.
Another approach is the utilization of a cermet anode consisting of Ni and CGO (sometimes also referred to as GDC), which is a MIEC at high temperatures and under reducing atmosphere. While Ni/CGO anodes have been shown to exhibit similar or even higher performance than Ni/YSZ anodes, the CGO phase has a lower mechanical stability.[32] Therefore, Ni/CGO

is currently mainly used as anode material in electrolyte-supported cells, while Ni/YSZ anodes are the state-of-the-art material in anode-supported cells. Besides a higher resistivity of Ni/CGO anodes towards carbon deposition, they also display a high sulfur tolerance.

## *2.3 Electrochemical fundamentals*

The performance of an SOFC can be captured by the relation between its cell voltage (*V*) and the current density (*i*). SOFC can generally be operated under either galvanostatic (constant current density) or potentiostatic (constant cell voltage) mode. The cell performance is mainly defined by (1) thermodynamics, (2) electrochemistry and (3) transport phenomena. In the following subsections, all of these factors are discussed.

### *2.3.1 Thermodynamics*

Thermodynamics can be used to calculate the standard cell voltage, according to:

$$E^0 = -\frac{\Delta G^0}{z\mathrm{F}}, \tag{3}$$

where $E^0$ is the cell voltage at the standard state, $\Delta G^0$ the standard Gibbs free reaction energy of the overall reaction, z the number of transferred electrons and F the Faraday constant. Thus, $E^0$ is directly dependent on tabulated values of the species´ Gibbs energy of formation. However, as standard conditions are typically not met during SOFC operation, Eq. 3 has to be extended and leads to the formulation of the Nernst equation,[10] that describes the theoretical cell voltage under open circuit voltage (OCV) conditions and is here shown for SOFC operated on $H_2/H_2O$ fuels:

$$E^{th} = E^0 - \frac{\mathrm{R}T}{z\mathrm{F}} \ln \frac{\prod a_{products}^{\nu_i}}{\prod a_{reactants}^{\nu_i}} = E^0 - \frac{\mathrm{R}T}{z\mathrm{F}} \ln\left(\frac{p\mathrm{H_2O}}{\sqrt{p\mathrm{O_2}} \cdot p\mathrm{H_2}}\right), \tag{4}$$

with $a_{products}$ and $a_{reactants}$ being the activities of product and reactant species and $\nu_i$ the stoichiometric coefficients of the participating species. The cell voltage represents a measure for the driving force of the electrochemical reaction. During SOFC operation, products are created and thus, according to Eq. 4, the cell voltage decreases, in particular due to an increase of $p\mathrm{H_2O}$ in the fuel electrode compartment.

### *2.3.2 Current-voltage characteristics*

The current-voltage characteristics (also *i-V* curve) is the relationship between cell voltage *V* and electronic current *I* (or current density *i*) and is a straightforward measure for SOFC performance. A typical *i-V* curve is depicted in Figure 2.4 and usually has a characteristic non-

linear S shape due to the loss processes described in the following subsections. The difference between the cell voltage and the voltage at OCV conditions is known as overpotential which can be divided into different contributions. At OCV conditions, no losses occur and the cell voltage can be calculated according to the Nernst equation (Eq. 4). As the current density is increased, the voltage continuously decreases.

The real voltage output of a cell $E_{cell}$ can be written by taking the OCV and subtracting the occurring voltage drops due to different loss mechanisms

$$E_{cell} = \mathrm{OCV} - \eta_{\Omega} - \eta_{D} - \eta_{M}\,, \tag{5}$$

where $\eta_{\Omega}$ denotes the ohmic overpotential, $\eta_{D}$ the kinetic activation overpotential, and $\eta_{M}$ the mass transport overpotential. In Figure 2.4, it is assumed that the partial pressures are constant in the channel. Thus, the OCV, which is governed by the Nernst equation, is not a function of the current density. However, this is only the case for high inlet flows on fuel and air side. If this is not the case, the OCV itself becomes a function of current density. This additional loss process is also known as gas conversion (see subsection 2.3.5).

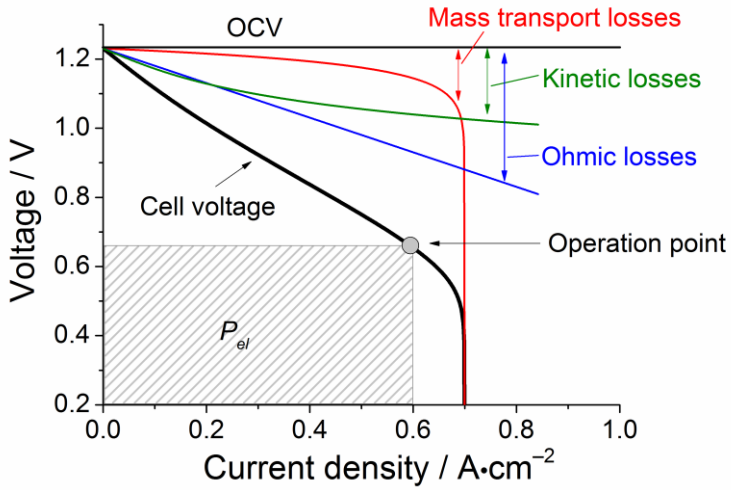


Figure 2.4: Typical *i-V* curve for an SOFC. The overpotentials caused by ohmic losses (blue), kinetic losses on anode and cathode (green), and mass transport (red) are illustrated as well. The power density $P_{el}$ can be calculated as product of cell voltage $V$ and current density $i$ and is indicated at one typical operation point as a grey rectangle.

At low current densities, the cell voltage curve shows an exponential drop. This behavior is mainly due to kinetic losses. Therefore, the low current density region is also often referred to as activation region. After the activation region, the cell is operated in the linear ohmic region where losses are often governed by the ohmic losses. When the fuel utilization (FU) reaches

high values, the *i-V* curve is characterized by a breakdown of the cell voltage in the mass transport limited region due to fuel starvation. The area-specific resistance (*ASR*) of an SOFC denotes its cell resistance. It can be derived from the slope of its *i-V* curve at current density $i_0$ according to:

$$ASR(i_0)=\frac{\mathrm{d}V}{\mathrm{d}i}\Big|_{i=i_0} \tag{6}$$

Alternatively, the ASR can be extracted from electrochemical impedance measurements.

The electrical power density $P_{el}$ at a certain operation point can be derived by calculating the rectangular space beneath the point as depicted in Figure 2.4.

### *2.3.3 Ion transport*

During the electronic and ionic transport through electrolyte and electrode, ohmic losses occur. According to Ohm's law the ohmic losses can be described as

$$\eta_\Omega = I \cdot \sum_{n=1}^{N} R_n = I \cdot R_{ohm}\,, \tag{7}$$

with $R_n$ being the individual ohmic contributions of the different processes and $R_{ohm}$ the overall ohmic resistance. In SOFC, the ohmic resistance is typically governed by the oxygen ion conductivity of the electrolyte. However, the diffusion barrier layer, electrode, and the contacting resistance can also contribute.

### *2.3.4 Electrochemistry*

Since electrons are generated or consumed during electrochemical reactions, the current of an SOFC is a direct measure of the rate of the electrochemical reaction. The Faradaic current $I_F$ of an electrochemical reaction is defined according to Faraday's law

$$I_F = \frac{dQ}{dt} = zF\dot{s}\,, \tag{8}$$

where $Q$ is the charge, $t$ the time, $\dot{s}$ the net molar change of a reactant due to an electrochemical reaction and $z$ the number of transferred electrons.

When no current is drawn, the difference in Gibbs energy between the oxidized (Ox) and reduced state (Re) of a chemical species during a general electrochemical reaction

$$\mathrm{Ox} + \mathrm{e}^- \rightleftharpoons \mathrm{Re} \tag{9}$$

quickly results in a built-up (SOFC anode) or depletion (SOFC cathode) of charge on the electrode, which either increases (relatively negative electrode potential) or decreases (relatively positive electrode potential) the Fermi level of an electrode. This leads to the formation

of an electrostatic (Galvani) potential step $\Delta\phi$ between electrode and electrolyte that counterbalances the difference in chemical Gibbs energy at electrochemical equilibrium. The overall cell voltage is the sum of the potential steps at anode and cathode $\Delta\phi_{an}$ and $\Delta\phi_{cat}$ according to:[33]

$$E(i) = |\Delta\phi_{an}| + |\Delta\phi_{cat}| - iR_{ohm}. \quad (10)$$

Under polarization, the potential loss across the electrolyte also contributes. Under current, the Fermi level of the anode decreases and the one of the cathode increases which leads to decreasing electrostatic potential steps and thus, a lower cell voltage. The slower the electrode reaction kinetics are, the faster the magnitude of the potential steps decreases. The difference between the potential steps at equilibrium and under polarization is defined as activation overpotential $\eta_D$. In SOFC, the charge transfer reaction is frequently the rate-limiting step, however, catalytic surface reactions can also contribute to the electrode resistance. Activation losses can be reduced by increasing temperatures, effective catalyst materials, optimized microstructure, and high pressures.

The physical origin of a potential step is the formation of an electrical double layer at solid/solid interfaces, where excess charge of the electrochemical charge transfer reactions is stored. The type of the observed potential steps differs depending on the electrode material. The two most commonly observed scenarios in SOFC are illustrated in Figure 2.5.

Figure 2.5a shows the charge transfer reaction in a Ni/YSZ cermet anode at the triple phase boundary (TPB) between electrode (Ni), electrolyte (YSZ) and gas phase. In this case, the ceramic phase is purely ionically conducting and the charge transfer reaction between electrode and electrolyte leads to the formation of an interfacial double layer between Ni and YSZ.[34] This scheme can be transferred to other composite electrodes with one mainly ionically and one mainly electronically conducting phase such as a Cu/YSZ anode.

Figure 2.5b depicts the charge transfer in a mixed ionic/electronic conductor (MIEC) electrode in the case of an LSCF cathode.[35] Here, also a double layer with a potential step $\Delta\phi$ forms between electrolyte (in this case CGO) and electrode (LSCF) due to different oxygen potentials.[36] However, the charge transfer reaction occurs at the double phase boundary (DPB) between surface and gas phase. Therefore, an additional surface/gas phase double layer $\Delta\chi$ forms due to charged adsorbates and the formation of a space-charge region close to the surface. In this case, the electric potential between surface and bulk is different, which can lead to the formation of another potential step.[36]

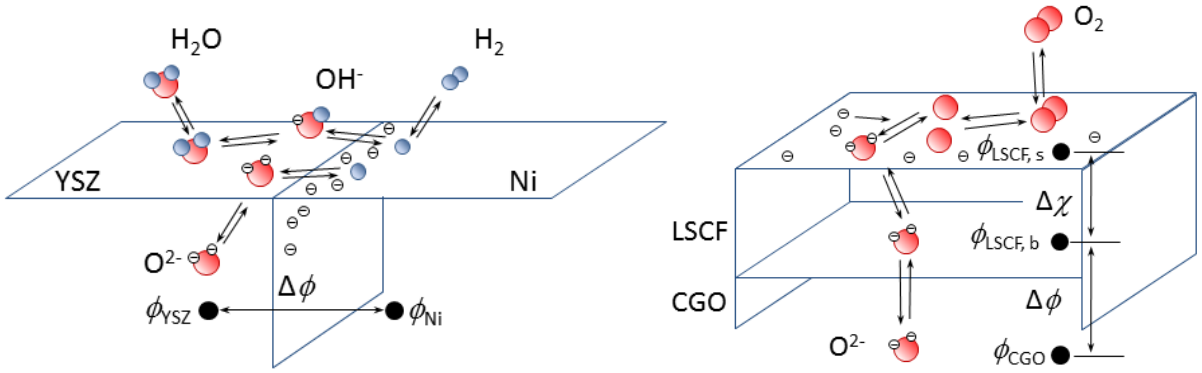


Figure 2.5: Elementary kinetic reaction mechanisms for (a) hydrogen spillover at a Ni/YSZ cermet electrode and (b) oxygen reduction at a mixed ionic electronic conducting LSCF cathode. A potential step $\Delta\phi$ forms in both cases between electrolyte and electrode material. In the case of a MIEC material, also a potential step $\Delta\chi$ between electrode bulk ($\phi_{LSCF,b}$) and electrode surface ($\phi_{LSCF,s}$) is possible.

A frequently used approach to describe the electrochemical kinetics of the global reactions in Eq. 1 and 2 is the Butler-Volmer equation, which was shown to accurately describe the non-linear current-voltage characteristics for a one-step single electron transfer reaction (Figure 2.4).[10] The equation describes the relationship between the current density $i$ and the electrode overpotential $\eta$ by using the exchange current density of the electrode $i_0$:

$$i = i_0 \left[\exp\left(\frac{\alpha z F \eta}{RT}\right) - \exp\left(-\frac{(1-\alpha) z F \eta}{RT}\right)\right], \tag{11}$$

where $\alpha$ is the apparent charge transfer coefficient and $z$ the number of exchanged electrons (in this case $z = 2$). The charge transfer coefficient is an indicator of the symmetry of the activation energy barrier when a positive or negative overpotential is applied. The exponential dependence of the current density on the overpotential contributes to the characteristic shape of the current-voltage characteristics at low overpotentials as displayed in Figure 2.4. The exchange current density is often described as the microscopic flux crossing the electrode/electrolyte interface equally in both directions at equilibrium and is a measure of the electrode kinetics. For $H_2/H_2O$ anode fuels, a global kinetic power law for the partial pressure dependence and an Arrhenius-type temperature dependence is frequently used to calculate the anode exchange current density:

$$i_0 = k\,(pH_2)^a (pH_2O)^b \exp\left(-\frac{E_{act}}{RT}\right) \tag{12}$$

The pre-exponential factor $k$, the exponents $a$ and $b$ and the activation energy barrier $E_{act}$ can

be determined experimentally. For small overpotentials, the Butler-Volmer equation can be approximated by a Taylor series expansion and powers higher than 1 can be neglected which leads to a reduction of Eq. 11 to

$$i = i_0 \frac{2\mathrm{F}\eta}{\mathrm{R}T} \tag{13}$$

This indicates that the evolution of the current density with overpotential at small $\eta$ values is linear. Since

$$\frac{d\eta}{dj}|_{i=0} = R_{el}\ , \tag{14}$$

with $R_{el}$ being the electrode resistance, the following relationship between exchange current density and electrode resistance can be deduced:

$$i_0 = \frac{1}{R_{el}} \frac{RT}{2F}. \tag{15}$$

Thus, $i_0$ values can easily be determined from measurements of the electrode resistance at low overpotentials. As resistance contributions of counter-electrodes and mass transport impede the derivation of $i_0$ directly from the slope of *i-V* curves, electrochemical impedance spectroscopy on symmetrical ESC are frequently employed.

### *2.3.5 Gas transport*

In an SOFC, two main transport mechanisms occur: (1) the gas transport of reactants and products in the porous electrode and (2) gas transport in the gas channels to and away from the electrode.

Gas transport in the porous electrode is predominantly governed by gas diffusion, which is linked to a concentration gradient that develops due to hydrogen consumption and water production at the anode/electrolyte interface. At the cathode, oxygen consumption leads to a reduction of $p\mathrm{O}_2$. If porous gas transport is slow, the changed partial pressures of reactants and product will cause a further drop in cell voltage, according to the Nernst equation (Eq. 4). Free molecular diffusion can generally be described by Fick's first law for binary mixtures under the assumption of steady-state:

$$J_j^D = -D_j \nabla c_j. \tag{16}$$

According to this equation, the diffusion coefficient $D_j$ describes the relation between the diffusive flux $J_j^D$ of species j and its concentration gradient $\nabla c_j$. At high temperatures, the introduction of the effective diffusion coefficient $D_j^{eff}$ accounts for porosity $\varepsilon$ and tortuosity $\tau$ of a porous electrode structure according to

$$D_j^{eff} = \frac{\varepsilon}{\tau} D_j. \tag{17}$$

In SOFC electrodes, the diffusion coefficient $D_j$ must describe both free molecular diffusion and Knudsen diffusion, since Knudsen diffusion in the pores becomes relevant when the pore radii are in the same range as the mean free path. Therefore, effective diffusion coefficients are calculated such as the averaged Bosanquet diffusion coefficients, which take into account both types of diffusion.[33] Free molecular diffusion coefficients in binary mixtures can, for example, be calculated according to the Chapman-Enskog theory.[37] The Knudsen diffusion coefficients of species j can be calculated as:

$$D_j^K = \frac{2}{3} r_p \frac{8RT}{\pi M_j}, \tag{18}$$

where $r_p$ is the mean pore radius, $T$ the temperature and $M_j$ the molar mass of species j. Especially during operation of SOFC in internal reforming mode, pressure differences in the electrode can arise. The corresponding discharge rate $Q$ through a porous medium can be described according to the Darcy law:

$$Q = \frac{B}{\mu} \frac{\partial p}{\partial y}, \tag{19}$$

with $\mu$ being the gas viscosity, $B$ the permeability, $p$ the pressure and $y$ the coordinate perpendicular to the electrolyte.

Gas transport above the electrodes is governed by the interplay of convection and diffusion of the gas phase species in the gas chamber. The geometry of the gas chambers depends on the employed setup. The two main cases are the channel and the button cell geometry. In typical planar cells and stacks transport occurs parallel to the electrode surface. In a button cell geometry, the gases are supplied perpendicularly to the SOFC electrode. Both cases can readily be described by different representations of the transient Navier-Stokes equations.[38]

During typical SOFC operation, $H_2O$ is generated and $H_2$ is consumed which leads to a decrease of the Nernst voltage (Eq. 4). This causes a lowered electrochemical driving force along the gas channel and represents an additional loss process, which is also referred to as gas conversion.[39] In contrast to other electrochemical loss processes, the gas conversion is inherent to SOFC operation and depends mainly on the testing setup and the anode gas flow rate.

In SOFC the characteristic non-linear voltage drop at low current densities depicted in Figure 2.4 is in many cases also partially caused by the gas conversion losses, since at low humidity levels an incremental change in humidity leads to significant changes in the Nernst voltage. In

ESC, the mass transport problem for high current densities is mainly due to a large gas conversion resistance. However, in ASC gas diffusion limitations in the porous anode can also play a critical role.

### *2.4 Fuel flexibility*

Due to high operating temperatures (600 – 900 °C), which give rise to fast electrode reaction kinetics, SOFC are capable of utilizing a variety of renewable fuels without the necessity of employing noble metals as catalysts.[40–42] Possible fuels range from natural gas and syngas, over liquid fuels such as diesel and alcohols, to a variety of bio-derived fuels. As the simplest hydrocarbon, methane is the main component in natural gas and most biogas. While direct $CH_4$ conversion is possible in SOFC, an external steam reforming or partial oxidation process is often used upstream to convert methane into hydrogen and CO before feeding it to the fuel cell.[43] Thus, the most common applications employ pre-reformed gas mixtures mainly consisting of $H_2$, $H_2O$, CO and $CO_2$.[44] While other types of fuel cells with lower operating temperature require complex fuel processing steps such as selective CO oxidation in polymer electrolyte membrane fuel cells (PEMFC) in order to avoid catalyst poisoning, in SOFC direct CO conversion is possible.[45] While it has been shown that state-of-the-art Ni/YSZ-based SOFC can operate on pure CO, its electrochemical oxidation rate on Ni/YSZ is generally accepted to be lower than the one of hydrogen.[46–48] The reason is a low reaction rate of the oxygen spillover from the YSZ to the Ni surface during CO oxidation, in comparison to the rapid hydrogen spillover from Ni to YSZ in the case of hydrogen oxidation. Still, Ni/YSZ-based SOFC operated with $H_2$/CO fuel gas have been shown to display a similar performance as with pure hydrogen due to the rapid kinetics of the water gas shift (WGS) reaction on Ni.[48]

A simple, however, inefficient way to pre-reform the fuel gas is the catalytic partial oxidation (CPOX), where the fuel is partially oxidized by a small amount of oxygen as in

$$CH_4 + 0.5\ O_2 \rightleftharpoons 2H_2 + CO,\ \Delta H^0 = -247\ \text{kJ}\cdot\text{mol}^{-1} \quad (20)$$

The CPOX is, for example, used in APU systems in trucks due to its high flexibility. Frequently, methane steam reforming (MSR) is employed, coupled to the fuel gas outlet via a heat exchanger in order to provide the heat required for the reforming reaction:

$$CH_4 + H_2O \rightleftharpoons 3H_2 + CO,\ \Delta H^0 = +206\ \text{kJ}\cdot\text{mol}^{-1} \quad (21)$$

However, the endothermic reforming process consumes energy and excess steam with a steam-to-carbon (S/C) ratio of 2 or higher is required in order to avoid carbon formation, which leads to reduced fuel efficiency.[49,50] Therefore, an intriguing SOFC operating strategy

is the internal catalytic methane steam reforming directly at the fuel cell electrode. As one of the products is carbon monoxide, the methane steam reforming is inherently coupled to the water gas shift (Eq. 22) and the methane dry reforming reactions (Eq. 23) as schematically illustrated in Figure 2.6.

$$CO + H_2O \rightleftharpoons H_2 + CO_2,\ \Delta H^0 = -41\ kJ\cdot mol^{-1} \quad (22)$$

$$CH_4 + CO_2 \rightleftharpoons 2H_2 + 2CO,\ \Delta H^0 = +247\ kJ\cdot mol^{-1} \quad (23)$$

The methane steam reforming is thermodynamically favorable at high temperatures and is readily catalyzed by Ni-based cermet electrodes. It has the advantage that the heat generated by the electrochemical oxidation can partly be used for the endothermic reforming process. In the direct methane operation mode, the Ni in these electrodes serves as both catalyst for the electrochemical hydrogen oxidation and the methane steam reforming/water gas shift reaction. SOFC with internal reforming can be operated at lower S/C ratios due to $H_2O$ produced by the electrochemical hydrogen oxidation, which in turn can reduce energy requirements for water evaporation.[43] It has been reported that the efficiency of internal reforming can be up to 8 % higher than for external reforming.[51] However, the large temperature gradients induced by the highly endothermic reaction can lead to mechanical stresses within the cells and thus, to accelerated degradation or cell failure. Therefore, internal methane reforming is still an extensively investigated research topic.

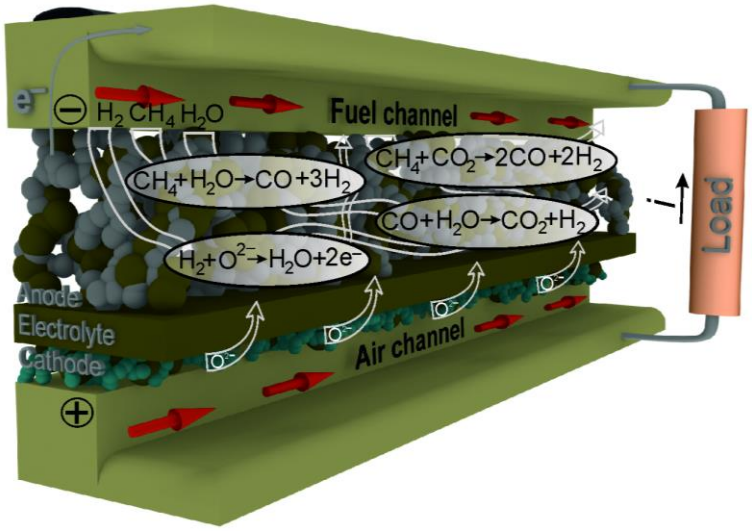


Figure 2.6: Schematic illustration of a Ni/YSZ anode-supported planar SOFC including the general representation of some physico-chemical processes. All structural details and scaling are exaggerated merely for illustration purposes.

### *2.5 SOFC degradation*

The harsh operating conditions of SOFC entail a variety of different degradation processes which represent a challenge in meeting lifetime requirements. Degradation of each cell components can occur as well as degradation originating from their mutual interaction. Generally, degradation is defined as the loss of performance and is often reported as voltage loss per 1000 hours for stacks. For single cells, another measure frequently used is the change of ASR, which can be determined by means of electrochemical impedance spectroscopy. Great research efforts have already been made in order to understand and overcome degradation issues and are discussed in recent reviews.[52,53] In the following, an overview of some of the main degradation processes is given.

The most important degradation mechanisms in doped zirconia electrolytes are related to phase instabilities and chemical incompatibilities with the electrode materials.[53] Processes like grain boundary dopant segregation and kinetic demixing decrease the oxygen vacancy concentrations in the bulk of the electrolyte and the effective ionic conductivity. Moreover, mechanical stress caused by the mismatch of thermal expansion coefficients of different layers or redox cycling can lead to the volume expansion of metals in the anode, which can cause the cracking and ultimately the failure of thin electrolytes in ASC and MSC.

On the cathode side, the most severe extrinsic degradation phenomenon of LSM/YSZ and LSCF cathodes is associated with Cr poisoning. Cr can evaporate from the metallic interconnector when not protected by a coating and deposits on the cathode surface.[54,55] Without the use of chromium-containing metallic interconnectors, degradation rates below 1 % per 1000 h have been observed, demonstrating the minor influence of intrinsic degradation on LSM/YSZ.[56] Although the performance of LSCF cathodes was observed to be significantly higher than the one of LSM/YSZ, their degradation rate was also found to be higher.[24] One main degradation process is the chemical reaction of LSCF with YSZ to form insulating phases like $SrZrO_3$.[52,53] Although CGO barrier layers are frequently used to slow down these reactions, Sr can still diffuse through the interlayer if it is not dense enough, especially during sintering at high temperatures.[57–59] Moreover, Sr surface segregation was reported to be an important degradation process in LSCF.[24,56]

One of the most severe anode degradation phenomena in Ni-based anodes is the coarsening of Ni particles according to the Ostwald ripening mechanism, which describes particle growth as a process that minimizes the free surface energy.[60–63] The nickel particles can be transported via evaporation to $Ni(OH)_x$ and subsequent condensation, and solid state diffusion mecha-

nisms.[52] This leads to a growth in Ni particle size, decrease in TPB length and can also entail a loss of Ni percolation.[64] Moreover, Ni coarsening can have significant effects on the porosity and thus, on the gas transport in the anode. Thermomechanical stress can also arise in the anode caused by temperature gradients or different CTEs and lead to the delamination or cracking of the anode.[65] Thermomechanical stress can become particularly severe under redox- or thermal cycling which can lead to Ni oxidation and a corresponding volume change.[66]

One drawback of the use of biofuels is that they generally contain a number of impurities such as hydrogen sulfide, hydrogen chloride, siloxane and phosphorus.[67,68] Moreover, sulfur-containing mercaptans are often added into natural gas as odorants. These impurities can lead to SOFC degradation. Furthermore, the high activity of Ni towards the C-H bond cracking, can lead to carbon formation on the anode surface when SOFC are operated at low S/C ratios.[69,70]

It is crucial to understand the different degradation phenomena in order to devise countermeasures and to improve SOFC lifetime. The present work focuses on SOFC anode degradation induced by sulfur poisoning. Therefore, this aspect is reviewed in more detail in the following section.

## *2.6 Literature overview: Sulfur poisoning*

### *2.6.1 Catalyst deactivation due to sulfur poisoning*

Poisoning is the loss of catalyst activity caused by strong chemisorption of species on active sites of a catalyst. The adsorbed species on the surface can have several detrimental effects on the catalytic activity. First, the adsorbates block the occupied active sites and possibly other adjacent active sites for other reactants. Second, owing to its strong bond with the metal, the poison electronically alters the neighboring metal atoms. Third, another possible effect is the restructuring of the metal surface since the Gibbs energy of the metal-adsorbate system can be lower for a different metal facet. Fourth, high coverages of a catalyst poison can hamper the surface diffusion, thus blocking access of reactants to each other.[9] In SOFC, another possible effect is the blocking of the TPB of a Ni cermet electrode.

One of the most severe poisoning effects emerging in catalytic systems is the one caused by sulfur on metal catalysts, especially Ni.[71] Sulfur poisoning is a problem in many catalytic processes, such as hydrogenation, methanation, Fischer-Tropsch synthesis and steam reforming of hydrocarbons. There is a variety of different sulfur-containing species known to poison

metal surfaces, including $H_2S$, COS, $CS_2$, $S_2$, thiophene, $SO_2$, and $SO_3$. Their interaction with the metal surfaces depends on their respective oxidation state, that is, the number of free electron pairs and the degree of shielding of the sulfur ion by ligands. Hence, the order of toxicity is $H_2S > SO_2 > SO_4^{2-}$. [9,72] The adsorption of sulfur-containing substances is generally dissociative, leaving a reduced sulfur atom adsorbed on the surface, independent of the starting compound. In the present work, the poisoning of Ni-based anodes with $H_2S$ is investigated since sulfur-containing species are typically converted into $H_2S$ under hydrogen-rich conditions.[71] In Germany, the maximum sulfur limit in diesel fuels for highway vehicles is 10 ppm.[73] Moreover, the sulfur content in the natural gas grid can be up to 30 mg/m³ (~20 ppm $H_2S$).[73] Therefore, anode poisoning with hydrogen sulfide concentrations of up to 20 ppm $H_2S$ is investigated in the present work.

### *2.6.2 Sulfur poisoning of SOFC anodes*

The poisoning of SOFC anodes with sulfur is a well-known and well-documented phenomenon. So far, most studies have focused on the effect of sulfur on Ni/stabilized zirconia anodes (Ni/YSZ or Ni/ScSZ) that display particularly severe degradation.[74–88] However, only few studies have targeted the sulfur poisoning behavior of Ni/CGO anodes, although they are used in several commercial applications and have been shown to possess a significantly higher sulfur tolerance than Ni/YSZ.[85,89–96] So far, the underlying mechanistic reasons for their different behavior are still unclear. An overview of the current state of knowledge about sulfur poisoning of these anodes is given hereafter.

*Sulfur poisoning of Ni/stabilized zirconia anodes* — Sulfur poisoning of Ni/YSZ anodes has been experimentally investigated in numerous studies.[74–88] In these studies, the influence of various parameters (temperature,[74,75,77] current density,[76,79,82] $H_2S$ concentration,[74,76,77,79,80] and operation mode[76]) on the extent of sulfur poisoning was systematically examined. Based upon these results a few general trends can be deduced. Most studies have experimentally investigated the influence of sulfur poisoning on Ni/stabilized zirconia anodes in $H_2/H_2O$ fuel gas and identified the electrochemical hydrogen oxidation process to be severely inhibited under these conditions.[74–80,87] Other studies have also been dedicated to the investigation of sulfur poisoning of Ni/stabilized zirconia anodes operating on hydrocarbon-containing fuels, such as methane,[86,97–99] reformates,[100] syngas[101,102] and biogas.[40] These studies focused on the effect of sulfur poisoning on both the hydrogen oxida-

tion and the reforming reactions and their interplay.Regardless of the employed fuel gas mixture, in all studies a rapid initial power output drop occurs already for concentrations of $H_2S$ as low as 0.05 ppm.[77] Additionally, in many cases a slow second stage degradation is reported that occurs for long-term operation of SOFC in the presence of $H_2S$ and can proceed for thousands of hours.[74,75,79] The initial power output drop is associated with a large increase of anode polarization resistance and is assumed to be the result of the active surface site blockage by adsorbed sulfur. The magnitude of the performance drop has been found to be alleviated by increasing temperatures generally believed to be due to reduced sulfur coverage.[75,77,103,104] Since a higher $H_2S$ concentration also leads to higher sulfur coverage, an increasing power output drop for increasing $H_2S$ concentrations was observed. However, this increase was found to level off at $H_2S$ concentration of about 20 ppm which was concluded to represent saturation coverage of sulfur on Ni.[75,77,80] ScSZ-based anodes have shown a higher sulfur tolerance than YSZ-based anodes, which was explained by their higher ionic conductivity.[74]

However, controversial interpretations of experimental studies exist regarding the influence of current density on the sulfur poisoning of Ni-based anodes. Several authors have reported a lower relative increase of total anode resistance for increasing current densities.[75,76,82] In these studies, the sulfur surface coverage on Ni was suggested to decrease with higher current density due to its electrochemical oxidation and subsequent desorption as $SO_2$. However, recently it was also pointed out that in the Tafel region the relative increase of the total anode resistance due to sulfur poisoning inherently depends inversely on current density.[105] Thus, reduced sulfur surface coverage might not necessarily be the reason for the observed trend. Moreover, Hagen et al. have reported that increasing current density does not alleviate sulfur poisoning of electrochemical reactions during internal methane steam reforming.[103] These contradicting hypotheses illustrate that the mechanistic details underlying sulfur poisoning are still unclear.

In methane-containing fuel gases, the reforming activity was shown to be poisoned to a greater extent than the electrochemical reactions strongly affecting the cell voltage already at OCV.[86,97,99,102,103,106,107] In general, the rate of methane steam reforming reaction on Ni depends on the sulfur coverage to the third power $(1 - \theta_S)^3$ and thus, is more severely affected than the rate of the electrochemical hydrogen oxidation on Ni/YSZ that follows the dependency $(1 - \theta_S)$.[87,88,108] Thus, hydrogen oxidation can still be active at operating conditions where methane steam reforming is fully deactivated. The increased sensitivity of steam re-

forming towards sulfur poisoning has been attributed to the preferred sulfur adsorption on step sites which are particularly active for methane reforming.[86] In a recent study, it was demonstrated that sulfur poisoning has a major influence on both mass and charge transfer in methane-containing fuels.[103] It was shown that upon $H_2S$ exposure at low current densities, the increase of charge transfer resistance dominates, whereas at higher current densities the increase of resistance due to mass transfer and fuel reforming processes is the main deactivation effect. Moreover, the possibility of fuel starvation already at low current densities due to the combined effect of deactivated reforming reactions and high fuel utilization was indicated.[99,103]

Several experimental studies have examined the sulfur poisoning of $CO/CO_2/H_2/H_2O$ gas mixtures in order to extract detailed information about the influence of sulfur on the water gas shift reaction, as a first step towards the elucidation of the poisoning of the methane steam reforming process.[100,102,109,110] The results of these studies show that the water gas shift reaction is also affected more strongly than the electrochemical oxidation of hydrogen, which entails a lack of hydrogen for gas phase mixtures with high CO contents. Water gas shift reaction and methane steam reforming have been shown to display a similar sulfur poisoning behavior on Ni/YSZ with a full deactivation already at 20 ppm $H_2S$.[99,102,106] Kuhn et al. have attributed this similarity to the participation of water in both reactions, which entails a particularly severe poisoning effect.[111]

Eventually, upon removal of $H_2S$ from the feed gas, both complete[74,75,80,84] and partial recovery[79,81,112] of cell performance have been observed. The reasons for incomplete recovery are still unclear. However, they are likely to be related to irreversible, long-term degradation effects leading to microstructural changes. Generally, recovery is observed to progress at a significantly lower rate than the poisoning process.[81]

So far, only few studies have focused on the irreversible, long-term degradation and there is a significant discrepancy regarding the interpretation of their results.[74,75,112] Different mechanisms for the long-term degradation have been proposed. At higher $H_2S$ concentrations bulk nickel sulfide species can be formed, such as $Ni_3S_2$. However, their formation was shown to be unfavorable at $H_2S$ concentrations below 100 ppm and temperatures higher than 600 °C.[74,113,114] Thus, long-term degradation is not solely related to chemical Ni sulfide formation. Furthermore, surface reconstruction of Ni to less active planes and increased Ni diffusion rates, due to the dissolution of sulfur atoms into the Ni bulk phase in the vicinity of TPB were suggested as mechanisms at $H_2S$ concentrations below 100 ppm.[75,114] This could lead to

enhanced Ni particle sintering and in the associated destruction of the Ni percolation network. In a study by Hagen et al., a gradual increase of ohmic resistance was observed over 500 h which was correlated with a loss of Ni percolation at the anode/electrolyte interface.[106] Similarly, Rostrup-Nielsen et al. did not observe sintering in their stack poisoning experiments, but a certain rearrangement of the Ni particles was noted which could cause a partial destruction of the percolation network.[86] Hauch et al. have suggested the overpotential, rather than current density, to be the key parameter determining the onset of irreversible long-term degradation leading to enhanced diffusion of Ni atoms away from the anode/electrolyte interface and thus, a loss of Ni percolation.[112]

Most theoretical analyses of sulfur poisoning of Ni-based anodes have been performed using density functional theory (DFT) calculations. These studies can be structured into two groups: first, the investigation of adsorption of $H_2S$ on Ni surfaces and the subsequent formation of atomic sulfur,[31,105,115–118] and second, the removal of atomic sulfur by oxygen.[119,120] Recently, a unique approach to investigate sulfur poisoning of Ni surface has been performed by Monder et al.[121] They have used DFT calculations to determine the coverage dependency of the thermodynamic properties of nickel-adsorbed sulfur, concluding that the sulfur enthalpy changes depend significantly on its coverage.

Only few modeling attempts in literature were made to investigate the relation between the SOFC performance drop and sulfur coverage on Ni/YSZ anodes.[122–124] Alstrup et al.[122] have proposed a Temkin-like isotherm in order to predict the fractional coverage of sulfur on Ni surfaces

$$\frac{p_{H_2S}}{p_{H_2}} = \exp\left(\Delta h_0^0 (1 - a\theta_S) / RT - \Delta s^0 / R\right), \tag{24}$$

where $\Delta h_0^0$ = 289 kJ·mol$^{-1}$, $\Delta s^0$ = 19 J·mol$^{-1}$·K$^{-1}$ and $a$ = 0.69. This isotherm was also used by Hansen to describe the relation between observed relative power output drops and the calculated sulfur coverage. As a result, a linear relationship between coverage and enthalpy of sulfur was obtained.[87] Prasad et al. published a simple elementary kinetic model developing a rate expression for the sulfur coverage during the poisoning process via formation of surface-adsorbed atomic sulfur which they used to modify the Butler-Volmer equation.[123] In a more recent study, the same research group refined this model by using a much more detailed kinetic model for biogas steam reforming.[125,126] A few studies have employed semi-empirical approaches using correction factors to account for a reduction in TPB length. These models enable the prediction of degradation rates and cell performance losses in Ni/YSZ anodes.[127,128]

However, they do not allow for a mechanistic interpretation of the results and require an initial calibration of physico-chemical parameters. In this thesis, a modeling approach is presented that allows the extraction of more detailed mechanistic information.

*Sulfur poisoning of Ni/CGO anodes* — Several research groups have experimentally investigated the influence of sulfur-containing fuels on Ni/CGO-based SOFC performance.[82,85,89–94] Similar to Ni/stabilized zirconia anodes, a rapid initial power output drop occurs already for low $H_2S$ concentrations. However, the associated resistance increase for Ni/CGO anodes was significantly less severe. Upon poisoning with 2 ppm $H_2S$, Schubert et al. have observed a power output drop of less than 2 % and a full recovery after switching off the $H_2S$ supply.[85] Moreover, Aravind et al. have not witnessed any effect on impedance spectra after sulfur poisoning with 9 ppm $H_2S$.[91] A few studies have directly compared sulfur poisoning of Ni/CGO and Ni/YSZ anodes, and observed the poisoning behavior to be remarkably similar as the saturation of the resistance increase levels off with increasing $H_2S$ concentration in the same manner for both anodes.

Hydrogen oxidation on Ni/CGO was frequently assumed to proceed via the same reaction mechanism as on Ni/YSZ, where hydrogen spillover including electrochemical charge transfer at the TPB between Ni/YSZ/gas phase was shown to be the rate-limiting step. However, recently different mechanisms for fuel oxidation on Ni/CGO have been proposed, which could explain the increased sulfur tolerance.

The hypothetical explanations include the activity of CGO as a hydrogen oxidation catalyst in the Ni/CGO system,[129–134] the oxidation of sulfur to $SO_2$ involving an oxygen spillover from CGO to Ni,[85,92,135] and sulfur diffusion from the surface to the CGO bulk phase.[136,137]

Recent studies of Ni/CGO have suggested that the rate-determining charge transfer reaction is likely to happen at the CGO/gas phase DPB rather than at the TPB between Ni/CGO/gas phase. In these studies, Ni was suggested to act merely as electronic conductor.[132–134] This hypothesis is supported by a number of studies investigating Cu/CGO-based anodes that show high performance, despite the use of catalytically inactive Cu as the metallic phase.[28,29] This behavior can be explained by the high surface activity of CGO towards $H_2$ oxidation and its MIEC at high temperatures and under a reducing atmosphere, which originates from the mixed $Ce^{3+}/Ce^{4+}$ oxidation state of cerium.[129,131,132,138,139] This phenomenon could extend the electrochemical reaction zone in the composite electrodes from the TPB to the DPB.[85,93,129–133,138,139] Thus, the spillover of reaction intermediates at the TPB between ceramic and metal-

lic phase that occurs in Ni/YSZ anodes is likely not the rate-limiting step during hydrogen oxidation on Ni/CGO.[129–133] While the performance drop upon sulfur exposure of SOFC with Ni/YSZ anodes is related to the sulfur surface blockage of Ni, this is unlikely to have an influence on Ni/CGO anodes with Ni acting as a pure electronic conductor, leaving the real impact of sulfur unclear.

Moreover, hydrogen sulfide was shown to dissociate on reduced $CeO_2$(111) surfaces and diffuse into the bulk phase above 800 K.[136] This was recently confirmed by means of time-of-flight secondary-ion mass spectrometry (TOF-SIMS) analysis of CGO microelectrodes under cathodic polarization showing that the incorporation of sulfur into the CGO bulk phase is possible for $H_2S$ concentrations as low as 10 ppm.[137] This could lead to a removal of sulfur from the electrode surface and hence, to an increased sulfur tolerance.

The controversial interpretations illustrate that the mechanistic details of fuel oxidation on Ni/CGO remain unclear. Furthermore, the sulfur poisoning behavior of Ni/CGO anodes operated on reformates and also their long-term degradation behavior is still elusive. The present thesis aims to explore these open questions.

# 3 Methodology

In the past, various *ex situ* and *in situ* measurement techniques have already been applied to investigate the effect of anode sulfur poisoning. However, for *ex situ* surface characterization it is difficult to preserve the sample surface in its state at operating conditions due to a change in temperature and atmosphere. Moreover, sulfur atoms that are usually adsorbed on Ni at typical SOFC operating conditions undergo a reaction to Ni sulfide between 300 – 500 °C when the sample is cooled down.[113,116] For this reason, anodes are generally recovered before cooling down, which limits the relevance of *ex situ* examinations since sulfur is desorbed from the surface and the sulfur-induced microstructural changes can be difficult to detect. *In situ* characterization techniques would be ideal, however, they represent an enormous technical and financial challenge due to the harsh operating environment (high temperature, reducing gas) and thus, have been rarely applied for SOFC.

Therefore, electrochemical measurements have been used for a large part of the present work as they represent a straightforward and efficient method to acquire *in situ* information.

## *3.1 Full cell testing setup*

Figure 3.1 illustrates the experimental full cell testing setup, which enables the characterization of up to four cells simultaneously. This rather unusual configuration provides some important advantages compared to other test rigs. In particular, important parameters for fuel cell characterization, such as current density and hydrogen sulfide concentration in the fuel gas can be varied from cell to cell in the same experiment allowing the establishment of a detailed experimental map of SOFC performance and durability.

The testing cells were placed in the ceramic cell housing illustrated in Figure 3.2, where the anode and the cathode were contacted with nickel and gold meshes, respectively, employing gold as the sealant between the anode and the cathode side. In addition, thermocouples (TC) were positioned just next to the respective electrode in the center of the channel rib.

Humidification was carried out by running the gas through a temperature-controlled water bubbler. $H_2S$ was taken from a pressurized $H_2S/H_2$ bottle containing 150 ppm of $H_2S$. In order to avoid sulfur adsorption on the piping and its dissolution in the water bubbler, the sulfur was injected into the fuel stream only 6 cm away from the cell housing and, furthermore, Teflon-coated tubing was used.

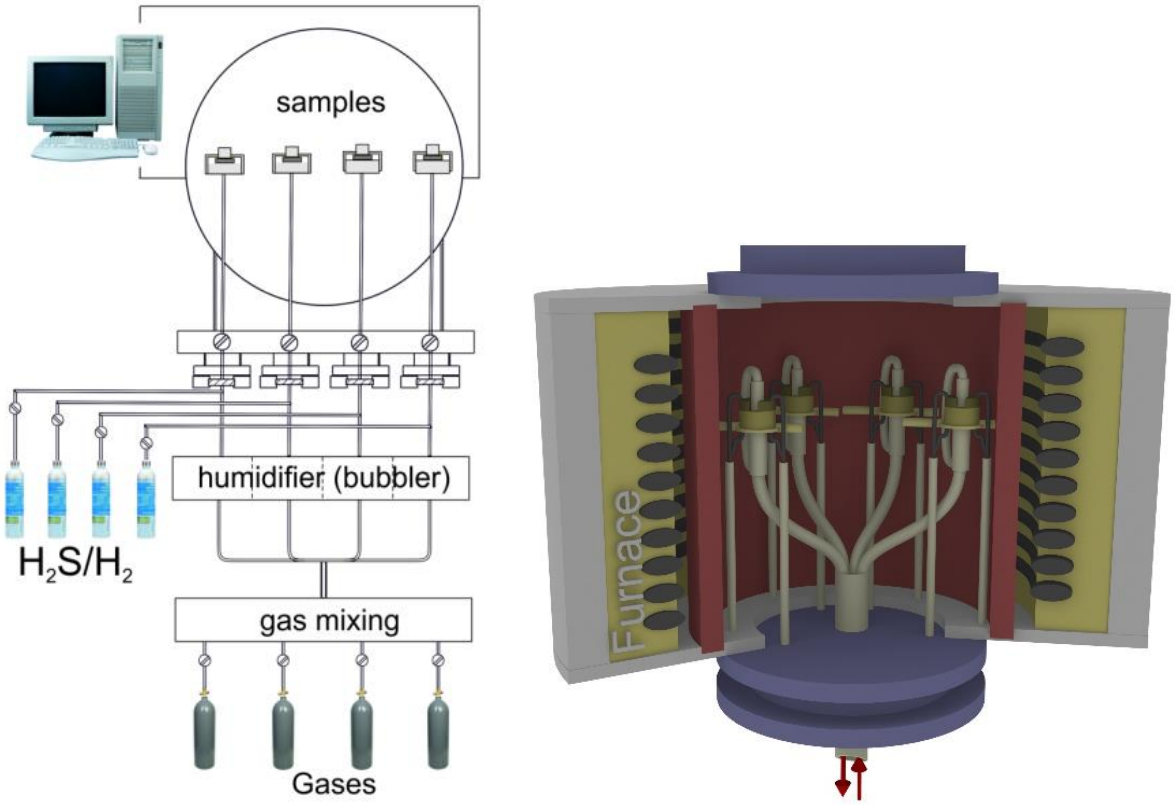


Figure 3.1: Illustrations of the electrochemical experimental device used to obtain impedance spectra, polarization curves and sulfur poisoning tests.

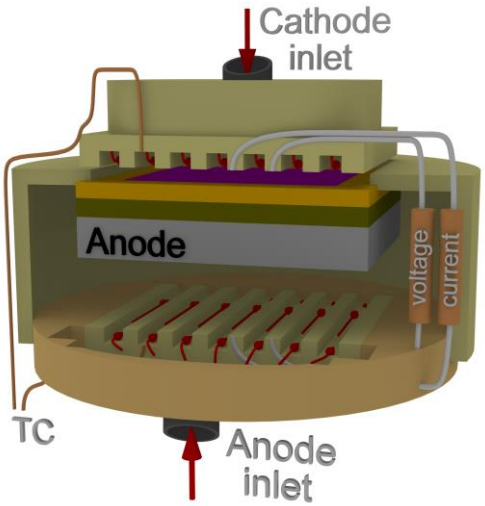


Figure 3.2: Illustration of the ceramic cell housing.

If not indicated otherwise, the cells were operated at a constant total fuel gas flow rate of 1 $L \cdot min^{-1}$ for each cell. The cathode was operated with air at a flow rate of 2 $L \cdot min^{-1}$. The cells were heated (3 $K \cdot min^{-1}$) to 950 °C, where they stayed for 30 min to improve the sealing

and subsequently reduced at 900 °C. Afterwards, the operating temperature was adjusted. The OCV was checked before starting the tests and confirmed to be higher than 1.22 V at 900 °C in pure hydrogen (1 L·min$^{-1}$) and air (1 L·min$^{-1}$) for all investigated cells, assuring proper gas tightness.

### *3.2 Cell preparation and testing*

The SOFC tested in the present work are commercial ESC with dimensions of 50x50 mm$^2$ and an active surface area of 40x40 mm$^2$. The cells were from a number of different suppliers that consist of slightly different geometries and materials. An overview of the different cells is given in Table 3.1. Scanning electron microscopy images of the cross-section of the anodes are depicted in Figure 3.3. Cell D is not shown as it only differs from cell A by a different electrolyte material.

Table 3.1: The properties of the SOFC used in the present study.

| | Supplier | Anode | Electrolyte | Cathode |
|---|---|---|---|---|
| Cell A[140] | Kerafol | Ni/CGO10 (25 µm) | 10Sc1CeSZ (160 µm) | LSM/10Sc1CeSZ (65 µm) |
| Cell B[62,130] | Hexis | NiCu5/CGO40 (25 µm) | 6ScSZ (160 µm) | LSM/8YSZ (70 µm) |
| Cell C[141] | Fraunhofer Institute for Ceramic Technologies and Systems (IKTS) | Ni/CGO10 (20 µm) | 10Sc1CeSZ (160 µm) | LSMM'/10Sc1CeSZ (50 µm) |
| Cell D[140] | Kerafol | Ni/CGO10 (25 µm) | 3YSZ (90 µm) | LSM/3YSZ (65 µm) |
| Cell E[140] | Kerafol | Ni/8YSZ (25 µm) | 10Sc1CeSZ (160 µm) | LSM/10Sc1CeSZ (65 µm) |

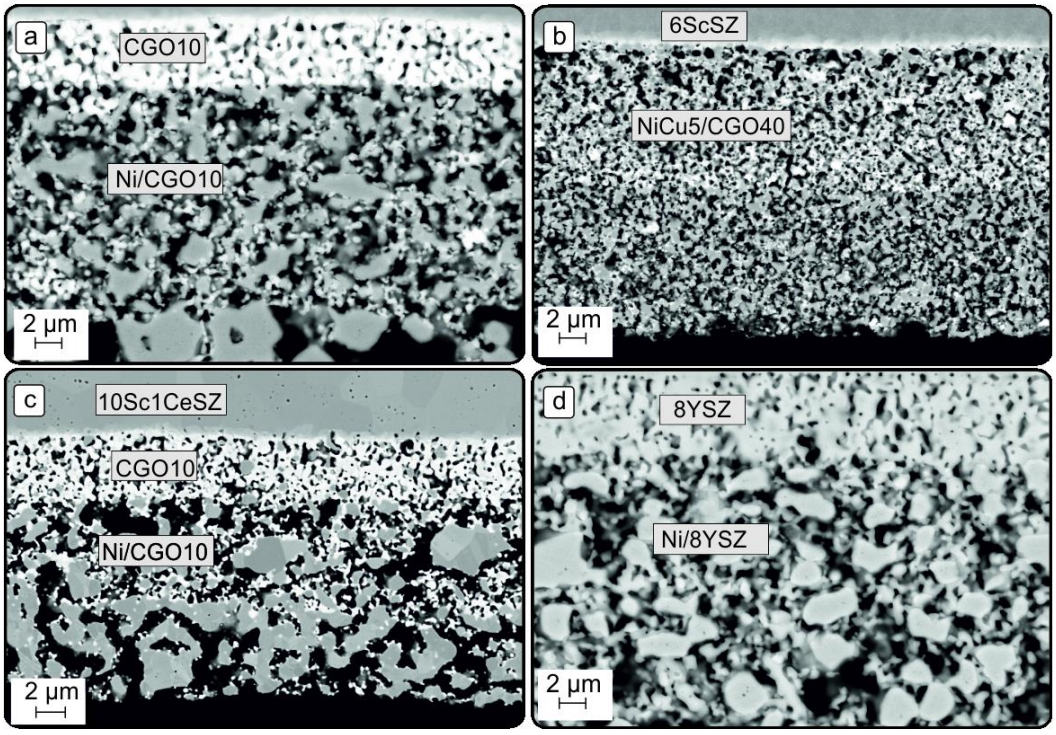


Figure 3.3: Scanning electron microscopy cross section images of the anodes of (a) cell A, (b) cell B, (c) cell C and (d) cell E. SEM image (a) was supplied by the manufacturer. Therefore, (b) and (c) were recorded at the same magnification, with display of the adhesion and functional layer.

The weight ratio between LSM and stabilized zirconia in the composite air electrodes of cells A, B, D, E was 50:50. Cell C employed a LSMM' cathode with another transition metal on the B site. The exact composition of this MIEC cathode is not revealed by the manufacturer.[141] Additionally, all cathodes consisted of a second pure LSM (LSMM') layer that serves as current collector.

The anodes of cells A, C, D and E were composed of three sub layers: an adhesion layer (CGO10 or YSZ, respectively), a functional anode layer and a current collector layer with increased Ni content. Cell B did not contain an adhesion layer, but only a functional and a current collector layer. The intention of the present work was to investigate the influence of sulfur poisoning on different anode materials. The anode structure in cells A and D is exactly the same; however, the electrolyte was varied since the 3YSZ showed higher mechanical stability than 10Sc1CeSZ and prevented these cells from cracking in the test rig. Anodes of the cell C also shows the same nominal composition as anode of cell A/D. However, they were supplied by different manufacturers and exhibit significantly different sulfur poisoning behavior which will be addressed in the following chapters. Cell E contains a Ni/8YSZ anode and

cell B a NiCu5/CGO40 anode with an increased Gd doping content of 40 % in the CGO phase. Moreover, in cell B a NiCu5 alloy is used as metallic phase. The use of copper as anode material is known to entail a higher carbon and sulfur tolerance.[28] It has been reported that in Cu-ceria composite electrodes, the metal phase is simply an electronic conductor and does not play a catalytic role.[29,142] Moreover, copper only accounts for 5 wt% of the metallic phase. Thus, although minor effects on the extent of sulfur poisoning cannot be excluded, the influence of Cu on the general sulfur poisoning behavior of cell B is assumed to be negligible. In any case, also due to different processing conditions and microstructure, this work only presents a qualitative comparison of the cells. Symmetrical cells were of type D, with a Ni/CGO10 anode and a CGO10 adhesion layer on both sides.

### *3.3 Symmetrical cell measurements*

All symmetrical cell measurements in the present work were carried out at the Karlsruhe Institute of Technology (KIT) at the Institute for Applied Materials - Materials for Electrical and Electronic Engineering (IAM-WET). The cell was mounted in a ceramic cell housing as depicted in Figure 3.4 and contacted with Ni meshes on both sides.[143] As a one-atmosphere was employed no sealing between the electrodes was required. The atmosphere in the reactive chamber consisted of $H_2/H_2O/N_2$ gas mixtures and its composition was measured via a lambda sensor close to the sample. Electrochemical impedance spectroscopy measurements were carried out at OCV to determine the cell resistance.

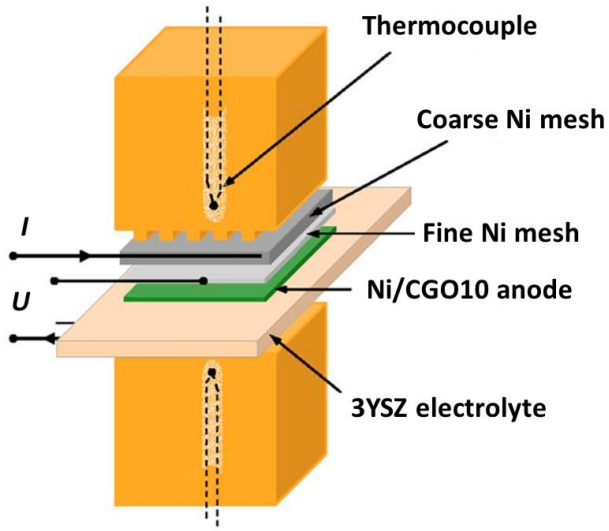


Figure 3.4: Schematic illustration of the sample holder in the symmetrical cell test bench. Adapted from Sonn et al.[143]

## *3.4 Electrochemical characterization*

### *3.4.1 Current-voltage characteristics*

The theoretical fundamentals of the current-voltage characteristics are described in the previous chapter and were measured by stepwise varying the current by 0.024 A every 2 s.

### *3.4.2 Electrochemical impedance spectroscopy*

Electrochemical impedance spectroscopy (EIS) has become a very popular tool for the study of electrochemical cells during the last decades.[144,145] The operation of electrochemical devices such as the SOFC is characterized by the simultaneous occurrence of different loss processes. Upon the system's excitation by a perturbation of voltage or current, these processes relax according to their respective characteristic time constants which are distributed over several orders of magnitude. In an EIS measurement the system is excited by a periodic perturbation with small amplitude of either current (galvanostatic) or voltage (potentiostatic). The stimulus frequency of the signal is varied over several orders of magnitude which should theoretically result in the separate excitation of the different processes at their respective characteristic relaxation frequencies. The response of the system via the other measuring variable (voltage or current) then reveals its dynamics enabling the extraction of more detailed information about the different loss processes.

In the galvanostatic mode which is employed throughout this work, a small sinusoidal current $i(t) = i_0 \cdot \sin(\omega t)$ is superimposed to an applied current, where $t$ is the time, $i_0$ the amplitude that needs to be small and $\omega$ the angular frequency that is related to the frequency $f$ as $\omega = 2\pi f$. From the measured voltage response, the sinusoidal component $u(t) = u_0(\omega)\ \sin[\omega t + \phi(\omega)]$ can be determined. The complex impedance $\underline{Z}$ of the system is the ratio between the voltage and current and can be expressed as:

$$\underline{Z}(\omega) = \frac{\underline{u}(t)}{\underline{i}(t)} = \frac{u_0(\omega)}{i_0} e^{i\varphi(\omega)} = |Z(\omega)| e^{i\varphi(\omega)} = Z' + iZ''. \quad (25)$$

In this equation, $\varphi$ denotes the frequency dependent phase shift between voltage and current. $Z$' and $Z$'' represent the real and the imaginary part of the complex impedance. An impedance measurement is performed for a number of discrete frequency values in a frequency range relevant to the respective analyzed system. The most common way to represent the recorded impedance values of SOFC is the Nyquist plot as illustrated in Figure 3.5a. As the Nyquist plots do not give direct information about the frequency behavior (unless specifically indicated as in Figure 3.5a), it is usually complemented with an imaginary impedance plot (or alter-

natively a Bode plot), as shown in Figure 3.5b. These representations are used throughout the present work. Another way to efficiently analyze EIS data is their illustration as differential imaginary impedance plot. In this plot, an impedance spectra is recorded before and after the change of an operational parameter. Then, the difference in the imaginary part of the two spectra is depicted over the frequency, which allows a clear identification of the affected frequency region.

At very low frequencies, all loss processes are excited and are contributing to the cell resistance. As the perturbation frequency is lower than the relaxation frequency of all processes, the voltage response is in phase with the current perturbation and hence, the imaginary part of the impedance is zero. That means, at the low frequency region of the Nyquist plot the intercept of the curve with the x-axis denotes the total cell resistance at the measured operating point.

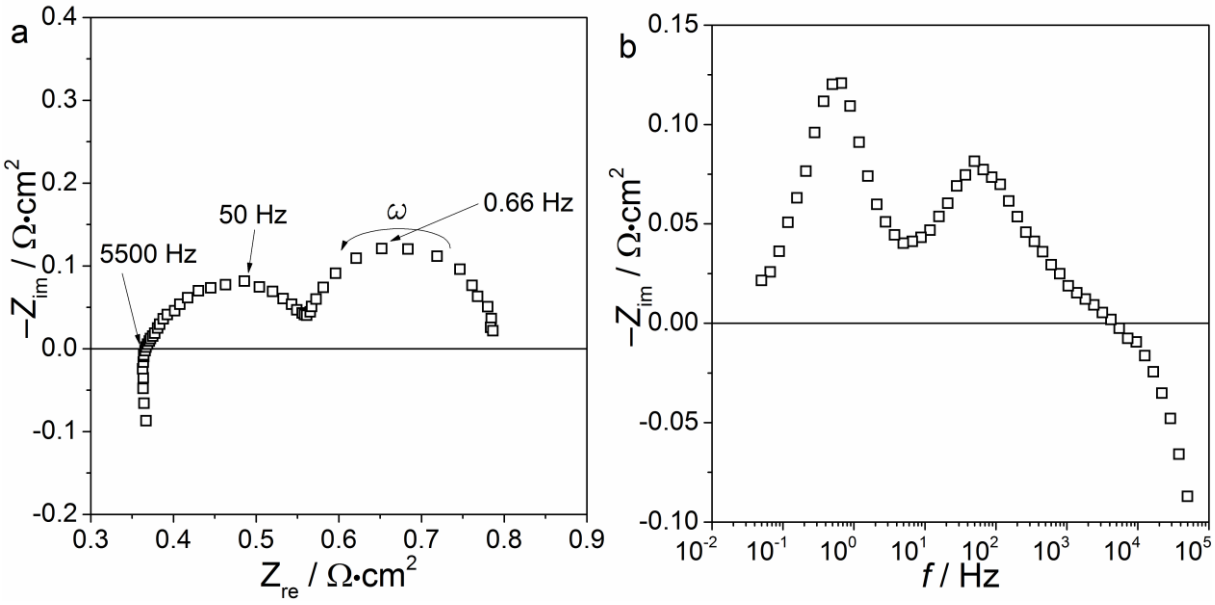


Figure 3.5: Typical (a) Nyquist and (b) imaginary impedance plots of an electrolyte-supported cell.

At higher frequencies, the perturbation frequency becomes faster than the relaxation frequencies of some of the loss processes, that is, their response starts to lag behind and a phase shift and a decreasing amplitude signal are observed. Thus, the real part of the impedance decreases and the imaginary part is unequal zero. As the perturbation frequency increases, an increasing number of processes is not excited anymore, and they do not contribute to the impedance spectra. At high frequencies, no processes are excited at all and again, voltage and current

signal are in phase. The high frequency intercept with the x-axis corresponds to the ohmic resistance $R_{ohm}$, as the relaxation frequency of ionic transport is very large and is convoluted by an inductance contribution. The inductance only has an imaginary component and decreases these values at high frequencies, which ensures the interception with the x-axis. The difference between total cell resistance and ohmic resistance is the so-called polarization resistance $R_{pol}$ which represents the sum of all electrochemical and physical loss processes.
If not mentioned otherwise, the cells were characterized by electrochemical impedance spectroscopy by means of an electrochemical workstation (Zahner PP-240 with Thales software) in a frequency range from 50 mHz to 100 kHz with 8 points per decade. The amplitude of the current stimulus was chosen to be 500 mA and did not result in a voltage response higher than 15 mV.

*Complex nonlinear square fitting* — In order to characterize the single processes contributing to an impedance spectrum, an equivalent circuit model (ECM) and a complex nonlinear square (CNLS) fitting routine are frequently employed.[146,147] An appropriate ECM should provide an accurate description of the occurring physicochemical processes and thus, should represent a good model of the impedance.
As different equivalent circuits can lead to the reproduction of the same impedance, systematic variation of the testing conditions (temperature, gas phase compositions, current density) are often carried out in order to identify the most appropriate one which already represents a tremendous research effort. It is getting increasingly difficult to find the right equivalent circuit as the number of contributing processes is increasing, since more variables are available for fitting. However, with a reasonable ECM, a number of physically meaningful information can be extracted such as activation energy barriers, double layer capacitances and dependencies of physicochemical processes on reactant concentrations.
The ohmic electrolyte resistance is generally modeled by a pure resistor *R*. Electrochemical processes in electrodes are often modeled as a parallel combination of a resistor *R* and a capacitor *C*. Here, *R* is the Faradaic resistance and represents the kinetics of the electrochemical reaction, while *C* is the double layer capacitance.[10] The illustration of such an *RC* element in a Nyquist plot leads to a perfect semicircle. While smooth electrodes behave like an ideal capacitance, the behavior of porous electrodes deviates and shows a non-ideal capacitance which can be accounted for by a factor *n* in a constant phase element (*CPE*, or also *Q* element). The impedance of such an *RQ* element can be described as:

$$\underline{Z} = \frac{1}{\frac{1}{R}+(i\omega)^{n}Q} \tag{26}$$

In a Nyquist plot, this leads to the illustration of a depressed semicircle.

In addition to the description as *RQ* elements, electrochemical processes in MIEC electrodes are also frequently modeled by a Gerischer element.[148,149] Furthermore, the transmission line model (TLM) can be used to describe the spatially distributed electrode reactions in porous electrodes.[143,149,150]

Furthermore, inductor elements are employed in many cases in order to account for the high frequency inductance of the contacting wires.

Also, so-called Warburg elements are used to model porous gas diffusion in ASC.[151]

*The distribution of relaxation times* — Unfortunately, in many applications the contributions of the different processes to the impedance spectrum overlap, making their separation challenging. Thus, a thorough analysis has to be carried out in order to gain an accurate understanding of the different loss processes and the magnitude of their resistances. One way to achieve a higher resolution of impedance spectra and enable a further separation, is the calculation of the distribution of relaxation times (DRT).[152] The DRT method is based on the fact that impedance spectra can be represented by a sufficiently large number of resistor-capacitor (*RC*) elements in series.

With an infinite number of *RC* elements, the impedance $\underline{Z}(\omega)$ can be expressed by using the distribution function $\gamma(\tau)$ as:

$$\underline{Z}(\omega) = R_0 + R_{pol} \int_0^{\infty} \frac{\gamma_n}{1 + i\omega\tau_n} d\tau \tag{27}$$

where $\int_0^{\infty} \gamma(\tau) d\tau = 1$. $\frac{\gamma(\tau)}{1+i\omega\tau} d\tau$ signifies the contribution to the overall polarization resistance at relaxation times between $\tau$ and $\tau + d\tau$. In practice, $\gamma(\tau)$ is approximated by the discrete function $\gamma_N$ for N logarithmically distributed RC-elements in series.

$$\underline{Z}(\omega) = R_0 + R_{pol} \sum_{n=1}^{N} \frac{\gamma_n}{1 + i\omega\tau_n} d\tau \tag{28}$$

Here, $\gamma_N$ weights the contribution of the n-th RC element with the relaxation time $\tau_n$ to the overall polarization resistance. In the present study, the distribution function was calculated from measured impedance data according to references[152,153].

### *3.5 Elementary kinetic modeling*

Elementary kinetic modeling was carried out based upon the previously published modeling framework DENIS[33,35,154] and consists of the following features:

- All chemical processes (thermal and electrochemical) are formulated as elementary reactions. The rate of all processes is described by mass-action kinetics under the mean-field assumption.[155,156]

  According to mass-action kinetics, the net change of species *i* can be calculated as

$$\dot{s}_i = \nu_i (k_f \prod_j a_j^{\nu'_j} - k_r \prod_j a_j^{\nu''_j}), \tag{29}$$

  where $k_f$ and $k_r$ are the forward and reverse reaction rate constants, $\nu_i$ denotes the stoichiometric coefficient of species i, $a_j$ the activities of species *j*, $\nu'_j$ and $\nu''_j$ represent the stoichiometric coefficients for the reactants of the forward and reverse reaction.

  The rate constant is given by a modified Arrhenius expression derived from transition state theory,[33]

$$k = k_0 T^{\beta} \exp(-\frac{E_{act}}{RT}) \exp(-\frac{\alpha z F}{RT} \Delta\phi), \tag{30}$$

  where $k_0$ is the pre-exponential factor, *T* the temperature, $E_{act}$ the activation energy, $\beta$ a temperature exponent, $\Delta\phi$ the electrostatic potential step at the electrode and α the symmetry factor. For non-electrochemical reactions, $z = 0$, the equation reduces to the standard Arrhenius equation.[156]

  Eq. 29 – 30 represent a physically meaningful way to describe the relation between current density *i* and potential *E*, and is also frequently alternatively formulated by means of the Butler-Volmer equation.[157]

- The transport of ions through the electrolyte is included as charge conservation equation assuming a temperature-dependent ionic conductivity with constant ion and vacancy concentrations.
- Composite electrodes are represented in a continuum approach using effective transport coefficients for mass and charge. The gas transport within the porous phase is described by Stefan-Maxwell and Darcy viscous flow. The model is one-dimensional through the thickness of electrodes and electrolyte.
- The gas supply volume in the button cell design is represented by an isothermal finite-gap stagnation point flow model using a one-dimensional representation of Navier-Stokes equations.[39]

- In the planar SOFC design, fuel and air enter the cell through the channels parallel to the electrode surface and their flow is modeled based upon a plug-flow approximation using a 1D representation of the Navier-Stokes equation.

All model equations used in the present modeling and simulation are thoroughly described elsewhere.[33,35] Spatial derivatives are discretized using the finite-volume method and the resulting differential-algebraic equation system is integrated by means of the semi-implicit extrapolation solver LIMEX.[158] In order to characterize SOFC performance during electrochemical operation, both steady-state and transient problems are solved. Electrochemical impedance spectra were simulated using a potential step and current relaxation technique.[159] The impedance is obtained in the frequency domain by a Fourier transformation of the resulting time-domain traces of current and potential. For transient simulations (voltage and current density stability) at each time step, the solution (potential or current density) is determined by solving the transient system, and in the case of polarization curves (steady-state) calculations were carried out by solving the transient system to a steady-state, then the appropriate current density is obtained for a given overpotential.

### *3.6 Scanning electron microscopy / Energy dispersive X-ray spectroscopy*

Scanning electron microscopy (SEM) reveals information about the morphology of material surfaces with a high resolution in the order of 1 nm. To obtain an image, the surface of the sample is swept in a raster pattern with a focused electron beam. Electrons are often generated by heating up a tungsten filament to over 2500 K and are then accelerated with voltages between 100 V and 70 kV. Alternatively, a field emission gun (FEG) can be used where electrons are expelled by using a powerful electric field.

When a sample surface is bombarded with electrons, the electrons interact with the sample material and are scattered. This creates a number of signals including secondary electrons (SE), backscattered electrons (BSE) and characteristic X-rays, which can be measured by the respective detectors. SE are produced by inelastic interactions of the electrons with the valence electrons of the atoms of the sample, which generates electrons with a low kinetic energy (<50 eV).

BSE are produced by elastic interactions of the electron beam with the atom nuclei and are proportional to the atomic number of the sample as larger atoms have a higher probability to produce elastic interactions. Thus, a stronger signal (brighter image) signifies a larger atomic number and low signal (dark image) corresponds to a low atomic number. Therefore, BSE

images are useful to distinguish different phases.

Furthermore, characteristic X-rays are emitted when electrons from the inner shell of the sample atoms are scattered and their position is refilled by electrons of different energy levels. The measurement of characteristic X-rays is possible with an energy-dispersive X-ray spectroscopy (EDX) detector enabling elemental analysis of the sample. SEM images were recorded by using a Zeiss Ultra Plus SEM with a FEG. For EDX analysis, the detector XFlash® 5010 (Bruker) was integrated in the SEM.

### *3.7 Focused ion beam scanning electron microscopy*

Focused ion beam (FIB) underlies the same functional principles as SEM, except for its use of ions (commonly gallium) instead of electrons. The application of an electric field causes the field emission of Ga+-ions from a liquid-metal ion source. The ions are then accelerated to an energy of 1 – 50 keV, and focused onto the sample by electrostatic lenses.

Besides secondary electron emission, the interaction of the heavy ions with the sample results causes neutral atoms or secondary ions to be sputtered away (also referred to as milling). A sample can be precisely milled to desired micro-scaled shapes, which is why FIB is also frequently applied for TEM lamella preparation.

Modern dual FIB-SEM machines are equipped with both an ion (commonly Ga+-ions) and electron beam column. This enables destructive FIB-SEM tomography, or serial sectioning, of a sample by repeated milling with the FIB and imaging of each facet with the SEM detectors.

The resulting stack of images can then be used to reconstruct the 3D microstructure of the sample. Extraction of scientific data from the reconstructed 3D image is a challenging process and requires careful processing of the acquired data. Generally, the grayscale image has to be partitioned into disjoint regions corresponding to different phases in a segmentation procedure. Eventually, quantitative analysis of the microstructural properties such as particle/pore size, TPB length and surface area follows.

A dual focused ion beam scanning electron microscopy (FIB-SEM; Helios NanoLab 600i, FEI, USA) was employed for 3D reconstruction carried out at the University of Oldenburg. The image acquisition, segmentation and processing was recently described in detail.[160] Cells of type B and D were reconstructed within the present work. The reconstructed volume of the anode of cell D was 11.2 x 13.1 x 10.8 $\mu m^3$, for cell B it was 12.2 x 12.73 x 12.75 $\mu m^3$. The respective volumes were reconstructed right next to the anode/adhesion layer interface.

The volumes were ensured to be larger than the representative volume element (RVE) to capture meaningful morphological characteristics of the anodes.

### *3.8 Transmission electron microscopy*

Transmission electron microscopy (TEM) is a powerful tool for imaging and examining materials with high resolution. TEM is based on the transmission of a high energy electron beam (several hundreds of keV) through an ultra-thin (<200 nm) sample. As the attenuation of the beam depends on the density and the thickness of the sample, the transmitted electrons form a 2D projection of the sample that is recorded on a fluorescent screen or a charge-coupled device camera. Since the detected electrons are transmitted with high kinetic energy, the resolution is considerably higher than for SEM. However, the interpretation of TEM images represents a challenging task as 2D images of 3D specimens are acquired. Thus, less information about the sample's morphology can be extracted. Furthermore, the preparation of a sample with a very small thickness is a complex procedure. TEM/EDX measurements in the present work were carried out at the University of Oldenburg on a FEG Jeol JEM 2100 F operated at 200 kV and equipped with an Oxford EDX as well as a high-angle annular dark-field detector.

### *3.9 X-ray fluorescence*

X-ray fluorescence (XRF) uses the interaction of X-rays with a sample to analyze its elemental composition. Fluorescent X-rays are emitted when electrons from the inner orbitals of the sample atoms are scattered and their position is refilled by electrons of a higher energy level. This excess energy is characteristic for all elements, thus, the energy of the emitted fluorescent X-ray can be directly linked to a specific element. The XRF measurements in this work were carried out with a Philips PW 1480 WDS spectrometer using Rhodium excitation and data was analyzed with a UNIQUANT 4.34 program. The measurements were performed on the backside of the electrode and the scanned area was a circle with a 25 mm diameter.[161] The X-ray penetrated the whole anode and most of the electrolyte.

### *3.10 X-Ray diffraction*

X-ray diffraction (XRD) is used to identify crystalline phases in materials by means of structural lattice parameters. X-ray diffraction is based on observing the elastic scattering of an X-ray beam by atoms in a periodic lattice. Scattered monochromatic X-rays that are in phase lead to constructive interference. The angle with which incoming X-rays hit the surface is varied and the signal of outcoming X-rays is measured. The angles of maximum intensity

allow to calculate lattice spacings according to the Bragg relation:

$$n\lambda = 2d\sin\theta; \quad n = 1,2, \ldots \tag{31}$$

where $\lambda$ is the wavelength of the X-rays, $d$ is the distance between two lattice planes, $\theta$ is the angle between the incoming X-rays and the normal to the reflecting lattice plane, $n$ is the order of reflection. X-ray diffractograms were recorded with an X-ray diffractometer, D8 Discover GADDS (Bruker) with a VÅNTEC–2000 areal detector.

# 4 Elementary kinetic modeling of sulfur poisoning of Ni/YSZ anodes

Despite comprehensive experimental investigations, the microscopic details of the elementary chemical reaction mechanism of sulfur poisoning of Ni/YSZ anodes are not fully understood.[123] Yet, the knowledge of elementary kinetics of SOFC electrode degradation is important because the understanding at the fundamental level is a prerequisite for a better predictive capability, which could allow improved design and operation of new SOFC systems.

In this chapter, first an elementary kinetic model is developed to describe Ni/YSZ anode degradation due to sulfur poisoning in systems operating with $H_2/H_2O$ fuel gas mixtures. A consistent thermodynamic and kinetic data set is derived. The developed model is then validated against different experimental data from literature.

As a next step, the model is extended to describe Ni/YSZ anode poisoning of SOFC operating on $CH_4/H_2/H_2O$ gas mixtures. Among many SOFC modeling works the catalytic surface chemistry is neglected or represented as empirical global chemistry, which precludes the establishment of the influence of sulfur formation. In this work, an elementary kinetic description of methane reforming chemistry and electrochemistry is employed to account for the influence of sulfur formation on SOFC performance. The model couples gas transport in the gas channel, porous media transport, and an elementary kinetic description of heterogeneous chemical and electrochemical reactions. All simulations were carried out with the in-house software DENIS presented in the previous chapter. Most of the results shown in this chapter were already published previously.[104,162]

## *4.1 Model parameterization and elementary kinetic reaction mechanism*

Elementary kinetic reaction mechanisms can reveal valuable mechanistic insights, such as information about surface coverages. However, the development of a reaction mechanism and the compilation of the required kinetic and thermodynamic data is a time-consuming process and represents a tremendous research itself. Therefore, in the present work already existing reaction mechanisms for hydrogen oxidation and methane steam reforming on Ni/YSZ are taken and extended with the elementary reactions of sulfur formation and oxidation on Ni.

### *4.1.1 Elementary kinetic reaction mechanism of heterogeneous and charge transfer chemistry*

To describe the hydrogen oxidation process on Ni/YSZ in $H_2/H_2O$ fuel gases, a previously developed and validated reaction mechanism was used.[34,163] The additional thermodynamic

and kinetic parameters of sulfur formation and oxidation derived in the present work are described below in more detail. The thermodynamic data of all species emerging during the formation and oxidation reactions form the basis of thermodynamically consistent kinetic simulations. This data is summarized in Table 4.1. The anode system is assumed to consist of five gas phase species ($H_2O_{gas}$, $H_{2,gas}$, $H_2S_{gas}$, $O_{2,gas}$, $SO_{2,gas}$), ten Ni surface species ($\square_{Ni}$, $O_{Ni}$, $H_{Ni}$, $OH_{Ni}$, $H_2O_{Ni}$, $H_2S_{Ni}$, $HS_{Ni}$, $SO_{2,Ni}$, $SO_{Ni}$, $S_{Ni}$), four YSZ surface species ($\square_{YSZ}$, $O^{2-}_{YSZ}$, $H_2O_{YSZ}$, $OH^{-}_{YSZ}$), and two bulk lattice YSZ species ($O^{x}_{O\,YSZ}$, $V^{\cdot\cdot}_{YSZ}$). Here, $\square_{Ni}$ and $\square_{YSZ}$ represent free surface adsorption sites and are taken as reference species, thus, their enthalpies and entropies are set to zero. Enthalpies and entropies of the gas phase species were calculated using NASA polynomials that account for their temperature dependence.[164] The values of the thermodynamic parameters of $O_{Ni}$, $H_{Ni}$, $OH_{Ni}$ and $H_2O_{Ni}$ were taken from previous modeling studies.[34,163] It was assumed that the presence of additional surface species does not affect the values of these thermodynamic parameters. The enthalpies of $H_2S_{Ni}$ and $HS_{Ni}$ were derived based on a DFT study by Alfonso who carried out calculations on Ni(111) surfaces.[115] Similarly, the enthalpies of $SO_{2,Ni}$ and $SO_{Ni}$ were derived based on DFT calculations by Galea et al. for a Ni(111) oriented plane as well.[120]

Based on the species' binding energies given in these studies, the enthalpies of the adsorbates were calculated as the difference between adsorption energy of the adsorbate species and the sum of the species' gas phase enthalpy and the energy of the bare Ni surface. Since SO und HS are not stable in the gas phase and thus no thermodynamic data is available, their enthalpies were derived based upon the corresponding reaction enthalpy for their formation. As there was no literature data available for these species' entropies, and in order to reduce the number of fitting parameters, their values were set to zero. Regarding the thermodynamic data of nickel-adsorbed sulfur, a coverage-dependent enthalpy, but coverage-independent entropy is assumed, as it was already suggested previously.[116,121,122] For the entropy of sulfur, a value of 52 $J \cdot K^{-1} \cdot mol^{-1}$ was adopted from Monder et al. who used DFT calculations to examine vibrational modes and frequencies of adsorbed species on the Ni surface.[121] This value is also in accordance with the value derived from an experimental study by McCarty et al.[165] The derivation of $h(S_{Ni})$ is explained in the subsequent subsection.

Table 4.1. Thermodynamic data (enthalpies and entropies) for gas phase, surface and bulk species at $T$ = 750 °C. The temperature-dependent data for gas phase species is calculated based upon NASA polynomials, the data for surface and bulk-species is assumed to be temperature-independent.

| Species, $i$ | $h_i$ (kJ·mol$^{-1}$) | $s_i$ (J·K$^{-1}$·mol$^{-1}$) | Ref. |
|---|---|---|---|
| *Gas phase* | | | |
| $H_2S_{gas}$ | 8.6 | 253.5 | [164] |
| $H_{2,gas}$ | 21.4 | 166.9 | [164] |
| $O_{2,gas}$ | 23.5 | 244.4 | [164] |
| $H_2O_{gas}$ | -241.9 | 233.7 | [164] |
| $SO_{2,gas}$ | -261.1 | 306.9 | [164] |
| *Ni surface* | | | |
| $\square_{Ni}$ | 0 | 0 | Reference species |
| $O_{Ni}$ | –221.6 | 38.9 | [34] |
| $H_{Ni}$ | -31.8 | 40.7 | [34] |
| $OH_{Ni}$ | -192.7 | 106.4 | [34] |
| $H_2O_{Ni}$ | -273.2 | 130.7 | [34] |
| $H_2S_{Ni}$ | -43.2 [115] | 0 | |
| $HS_{Ni}$ | -132.0 [115] | 0 | |
| $SO_{2,Ni}$ | -485.9 [166] | 0 | |
| $SO_{Ni}$ | -295.0 [166] | 0 | |
| $S_{Ni}$ | $f(\theta_S)$ | 52.0 [121,165] | See text |
| *YSZ surface* | | | |
| $\square_{YSZ}$ | 0 | 0 | Reference species |
| $O^{2-}_{YSZ}$ | –236.4 | 0 | [34] |
| $H_2O_{YSZ}$ | –273.0 | 97.9 | [34] |
| $OH^{-}_{YSZ}$ | –282.5 | 67.0 | [34] |
| *Bulk species* | | | |
| $O^{x}_{O\ YSZ}$ | –236.4 | 0 | [34] |
| $V^{\cdot\cdot}_{YSZ}$ | 0 | 0 | Reference species |

In this study, all chemical reactions were resolved into elementary steps. The elementary reactions composing the overall electrochemical reaction mechanism are listed in Table 4.2. The rate constants of the forward reactions are calculated via an Arrhenius expression. For the reverse reactions, the rate constants were calculated in a thermodynamically consistent way from the enthalpies and entropies given in Table 4.1.

The (electro-)chemical mechanism used in the present work includes eleven Ni surface reactions (R1 – R11), three YSZ surface reactions (R12 – R14) and one charge transfer reaction (C1). The previously validated electrochemical mechanism for $H_2$ oxidation serves as a basis for the electrochemical mechanism derived in this paper.[34,163] The charge transfer reaction in this mechanism occurs via hydrogen spillover during which a proton is transferred from Ni to a hydroxyl ion on YSZ forming water and delivering one electron to the Ni. LSM/YSZ cathode electrochemistry is modeled using a global Butler-Volmer approach according to Zhu et al.[167] It is assumed that the presence of the sulfur-containing surface species does not have an influence on the kinetic parameters of $H_2$ oxidation. Thus, for the elementary reactions R1 – R5, R12 – R14 and C1, activation energy barriers along with pre-exponential factors are assumed to have the previously derived values. Up to this point, there is no validated reaction mechanism available in literature for sulfur formation and its removal. Hence, the extension of the validated reaction mechanism is based on elementary steps suggested in first-principles studies.[115,116,119,120] It consists of the following steps: $H_2S$ adsorption (R6), $H_2S$ dissociation (R7 – R8), $SO_2$ formation (R9 – R10), and $SO_2$ desorption (R11). The adsorption of $H_2S$ is assumed to be molecular and fast,[71] thus the sticking coefficient was set to 0.5 and the activation energy barrier was set to 0. For the activation energy barriers of the $H_2S$ dissociation and $SO_2$ formation reactions, the values calculated via DFT by Alfonso and Galea et al. were used.[115,120] Due to a lack of literature data about entropies of different adsorbed species used in the reactions R7 – R11, pre-exponential factors of surface reactions can be estimated based upon their hopping frequency and the hopped distance.[168] Therefore, the commonly accepted assumption that the attempt frequency at the surface is equal to the vibrational frequency of the adsorbate was used, which leads to a pre-exponential factor of $1 \cdot 10^{22}$ $cm^2 \cdot mol^{-1} \cdot s^{-1}$ for second order reactions.

Table 4.2. Reaction mechanism used in the present study. Ni and YSZ surface site densities are $6.1 \cdot 10^{-5}$ mol·m$^{-2}$ and $1.3 \cdot 10^{-5}$ mol·m$^{-2}$, respectively. Symmetry factor of the charge transfer reaction is set to 0.5. The parameters are: pre-exponential factor $k^0$, sticking coefficient $s_i^0$, activation energy barrier $E_{act}$. The symbols $\square_{Ni}$ and $\square_{YSZ}$ represent free active surface sites on Ni and YSZ, respectively. The table shows only the rate coefficients for the forward reaction. The respective rate coefficients for the reverse reactions are derived based on thermodynamic consistency using the data shown in Table 4.1.

| No. | Reaction | $k^0$ (or $s_i^0$) | $E_{act}$ (kJ·mol$^{-1}$) | Ref. |
|---|---|---|---|---|
| *Ni surface* | | | | |
| R1 | $H_{2,g} + 2\square_{Ni} \rightleftharpoons 2H_{Ni}$ | $9.80 \cdot 10^{17}$ cm$^4$·mol$^{-2}$·s$^{-1}$ | 0 | [34] |
| R2 | $H_2O_g + \square_{Ni} \rightleftharpoons H_2O_{Ni}$ | $1.4 \cdot 10^{10}$ cm$^2$·mol$^{-1}$·s$^{-1}$ | 0 | [34] |
| R3 | $H_{Ni} + O_{Ni} \rightleftharpoons OH_{Ni} + \square_{Ni}$ | $5.0 \cdot 10^{22}$ cm$^2$·mol$^{-1}$·s$^{-1}$ | 97.9 | [34] |
| R4 | $H_{Ni} + OH_{Ni} \rightleftharpoons H_2O_{Ni} + \square_{Ni}$ | $3.0 \cdot 10^{20}$ cm$^2$·mol$^{-1}$·s$^{-1}$ | 42.7 | [34] |
| R5 | $H_2O_{Ni} + O_{Ni} \rightleftharpoons 2OH_{Ni}$ | $5.42 \cdot 10^{23}$ cm$^2$·mol$^{-1}$·s$^{-1}$ | 209.4 | [34] |
| R6 | $H_2S_g + \square_{Ni} \rightleftharpoons H_2S_{Ni}$ | $s_i^0 = 0.5$ | 0 | Estimated |
| R7 | $H_2S_{Ni} + \square_{Ni} \rightleftharpoons HS_{Ni} + H_{Ni}$ | $1.0 \cdot 10^{22}$ cm$^2$·mol$^{-1}$·s$^{-1}$ | 14.5 | [115] |
| R8 | $HS_{Ni} + \square_{Ni} \rightleftharpoons H_{Ni} + S_{Ni}$ | $1.0 \cdot 10^{22}$ cm$^2$·mol$^{-1}$·s$^{-1}$ | 10.6 | [115] |
| R9 | $SO_{Ni} + \square_{Ni} \rightleftharpoons S_{Ni} + O_{Ni}$ | $1.0 \cdot 10^{22}$ cm$^2$·mol$^{-1}$·s$^{-1}$ | 158.2 | [166] |
| R10 | $SO_{Ni} + O_{Ni} \rightleftharpoons SO_{2,Ni} + \square_{Ni}$ | $1.0 \cdot 10^{22}$ cm$^2$·mol$^{-1}$·s$^{-1}$ | 61.8 | [166] |
| R11 | $SO_{2,Ni} \rightleftharpoons SO_{2,g} + \square_{Ni}$ | $1.0 \cdot 10^{10}$ s$^{-1}$ | 0 | [166] |
| *YSZ surface* | | | | |
| R12 | $H_2O_g + \square_{YSZ} \rightleftharpoons H_2O_{YSZ}$ | $6.6 \cdot 10^{11}$ cm$^2$·mol$^1$·s$^{-1}$ | 0 | [34] |
| R13 | $H_2O_{YSZ} + O^{2-}_{YSZ} \rightleftharpoons 2OH^-_{YSZ}$ | $1.6 \cdot 10^{25}$ cm$^2$·mol$^{-1}$·s$^{-1}$ | 164.0 | [34] |
| R14 | $O^x_{o\,YSZ} + \square_{YSZ} \rightleftharpoons V^{\cdot\cdot}_{YSZ} + O^{2-}_{YSZ}$ | $1.6 \cdot 10^{22}$ cm$^2$·mol$^{-1}$·s$^{-1}$ | 91.0 | [34] |
| *Charge transfer reaction* | | | | |
| C1 | $H_{Ni} + OH^-_{YSZ} \rightleftharpoons \square_{Ni} + e^- + H_2O_{YSZ}$ | $3.4 \cdot 10^{19}$ cm$^2$·mol$^{-1}$·s$^{-1}$ | 181.4 | [34] |

In the present reaction mechanism, possible direct electrochemical sulfur oxidation is not explicitly included due to only limited information in literature about its occurrence and kinetics. Moreover, electrochemical sulfur oxidation would require simultaneous mass and charge transfer and thus, could possibly be further resolved into additional processes. Moreover, electrochemical oxidation of sulfur would probably involve a twofold oxygen spillover charge transfer process which was shown to be significantly slower than hydrogen spillover during hydrogen oxidation, due to the large molar weight of the oxygen atom.[34] For this reason and also in order to reduce the number of fitting parameters, in the present model sulfur oxidation is modeled by a heterogeneous catalytic pathway.

In a different study, Appari et al. have reported four additional chemical reactions, in which different sulfur-containing species participate.[126] In their kinetic model of biogas steam reforming on Ni catalysts the following reactions are included:

$$HS_{Ni} + O_{Ni} \rightleftharpoons SO_{Ni} + H_{Ni}, \quad (32)$$

$$H_2S_{Ni} + O_{Ni} \rightleftharpoons HS_{Ni} + OH_{Ni}, \quad (33)$$

$$S_{Ni} + OH_{Ni} \rightleftharpoons SO_{Ni} + H_{Ni}, \quad (34)$$

$$S_{Ni} + H_2O_{Ni} \rightleftharpoons HS_{Ni} + OH_{Ni}. \quad (35)$$

All of these processes involve simultaneous bond-breaking and bond-making. However, they are not explicitly included in the model, since all of them are represented by the elementary reactions comprised in our mechanism if the bond-breaking and bond-making events are assumed to happen consecutively. For example, reaction (32) can be described by the dissociation of the HS radical (R8) and the subsequent recombination of atomic sulfur and oxygen (R9). The other reactions (33) – (35) can also be subdivided analogously. However, the extension of our developed chemical mechanism by the reactions (32) – (35) could be considered, when DFT calculations become available that show only one transition state along the respective minimum energy pathway in one of the reactions (32) – (35).

### *4.1.2 Heterogeneous chemistry on Ni surface and charge transfer process: Coverage dependence of the enthalpy of the adsorbed sulfur species*

The effect of the repulsive lateral interactions between the sulfur surface atoms becomes notable at high coverage that emerges due to the strong adsorbate-surface interactions of sulfur and nickel. To date, in most surface science modeling studies these predominantly repulsive lateral interactions were modeled by coverage-dependent activation energy barriers.[47,123,169] However, in the present work a coverage-dependent surface enthalpy $h(S_{Ni})$ is employed, as it

has already been suggested previously.[116,121,122] This approach has already been used in prior microkinetic modeling studies in which simple linear correlations have been employed to model adsorption enthalpies as a function of coverage.[170–173]

In order to determine the exact coverage dependence of $h(S_{Ni})$, experimental data published by Alstrup et al were reproduced.[122] In their paper, the authors measured the fractional coverage of sulfur on nickel for different gas phase concentrations of $H_2S$ in the temperature range between 800 K and 1150 K. As inlet gas, they used hydrogen with different trace amounts of $H_2S$. In order to compare the simulations with the experimental data, sulfur coverage on Ni was calculated at the experimental conditions described by Alstrup et al.[122] The originally given fractional sulfur coverage is converted into the real coverage by means of the sulfur saturation coverage $\theta_{max}(S)$ that was experimentally determined to be 0.5 ML.[9] The thermodynamic and kinetic data of all species and reactions (Table 4.1 and Table 4.2) are utilized as the base parameter set in the calculations. The value of $h(S_{Ni})$ was fitted to reproduce the given experimental data.

Figure 4.1a compares the computed equilibrium coverage of sulfur for a temperature range from 800 K to 1150 K with the experimental measurements by Alstrup et al. As illustrated in Figure 4.1a, the proposed surface reaction mechanism of sulfur formation matches the experimental observation well. The determined coverage-dependent values of $h(S_{Ni})$, based upon equilibrium calculations shown in Figure 4.1a, are plotted in Figure 4.1b. Based on the obtained results, a clear linear correlation between enthalpy and surface sulfur coverage can be perceived. This behavior is similar to the results of previous studies by Grabow et al.[171] and Miller et al.[172] who investigated the relation between binding energies and coverage for different adsorbate/metal systems. They have found that the binding energy of adsorbates increases linearly with surface coverage above a certain threshold coverage $\theta_0$. Based upon these findings, in the present work the following linear relation between the enthalpy of sulfur and its coverage was derived

$$h(S_{Ni}) = \begin{cases} -202 \text{ / kJ·mol}^{-1}, & \text{for } \theta_s < 0.28 \\ -202 + 370.99 \cdot (\theta_s - 0.28) \text{ / kJ·mol}^{-1}, & \text{for } \theta_s \geq 0.28 \end{cases} \quad (36)$$

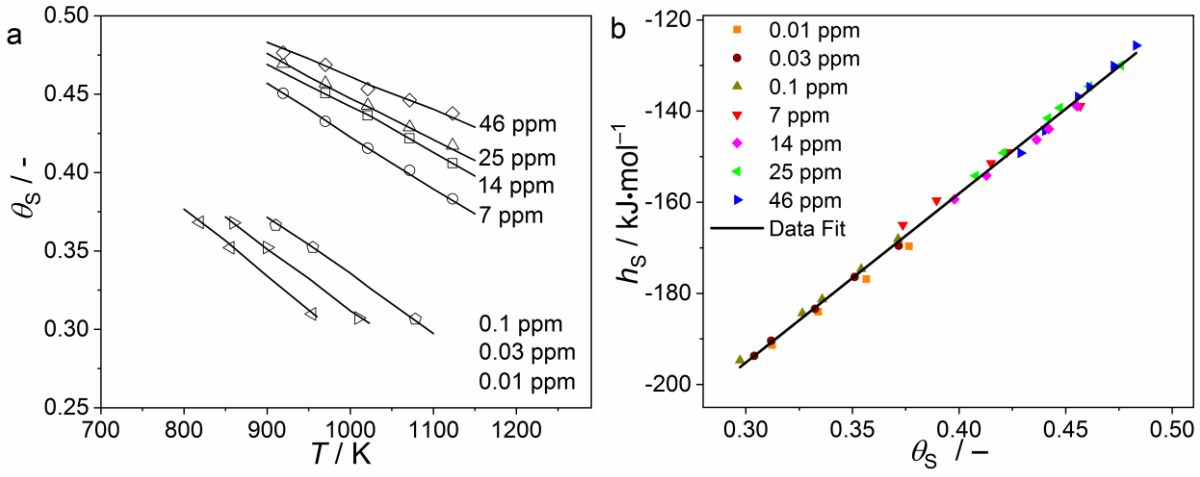


Figure 4.1: (a) Comparison between experimental and simulated sulfur surface coverage on Ni as a function of temperature for different $H_2S$ gas concentrations. Experimental data are taken by Alstrup et al.[122] (b) Values of the enthalpy of nickel-adsorbed sulfur obtained through fitting of the experimental results shown in (a). Different gas phase concentrations of $H_2S$ are represented by different colors and symbols. The resulting linear regression of the illustrated values is shown as a solid line. Coefficient of determination: $R^2 = 0.995$.

As it is revealed by Eq. 36, the threshold coverage is $\theta_0 = 0.28$. This is a physically meaningful description of the coverage dependence of sulfur, since in the limit of low coverage the lateral adsorbate-adsorbate interactions are weak and the adsorbates do not share any metal atoms, thus, below the threshold coverage $h(S_{Ni})$ should be constant.

The obtained enthalpy below the threshold coverage (–202 kJ·mol$^{-1}$) represents the value calculated using DFT for sulfur on a Ni(111) surface by Wang et al.[116] Based on a binding energy of –1.96 eV, the lowest reported value, a sulfur surface enthalpy of –202 kJ·mol$^{-1}$ can be derived. Furthermore, the authors reported an increase in binding energy starting at real sulfur coverage of 0.25 ML which is also in good agreement with the threshold coverage used in Eq. 36.

In summary, based on experimental results available in literature, a physically meaningful relation between the enthalpy of nickel-adsorbed sulfur and its coverage was derived. The validity of the developed reaction mechanism was demonstrated for a purely chemical system within the temperature range 800 K – 1150 K and for gas phase concentrations over more than three orders of magnitude (0.01 ppm – 46 ppm). In the following electrochemical simulations, $h(S_{Ni})$ is calculated accordingly to Eq. 7.

## *4.2 The influence of sulfur poisoning on the performance of Ni/YSZ anodes operating on $H_2/H_2O$ fuel gases*

To verify the developed model in $H_2/H_2O$ fuels, it was validated against various experimental literature data from the same research group under a wide range of conditions. First, impedance spectra of ASC recorded by Yang et al. were reproduced for a $H_2S$ gas concentration of 1 ppm at 750 °C.[79] These impedance spectra simulations also served as an initial calibration of the model parameters listed in Table 4.3. Subsequently, current density stability tests of ESC by Zha et al. were simulated for a higher temperature of 750 °C and $H_2S$ concentrations as high as 50 ppm.[75] Eventually, relative power output drops for ESC were calculated for $H_2S$ concentrations between 1 – 10 ppm published by Cheng et al. in order to reproduce the saturation effect and the different behavior in power output drop for galvanostatic and potentiostatic operation mode.[76]

### *4.2.1* Cell geometrical and electrochemical parameters

Table 4.3 lists geometrical and electrochemical parameters that have been utilized in the electrochemical simulations. Since different literature-based experimental results were used to validate our model, Table 4.3 gives basic geometrical/structural parameters. When geometrical parameters were changed (e.g. thickness of electrode and/or electrolyte), they are given in the respective subsections. Due to the lack of information about some structural parameters (e.g. porosity, pore radius, etc.), some assumptions based upon previous works[35,46,174,175] were made where these parameters have been shown to be valid for a wide range of operating conditions. Table 4.3 presents first the data for the Ni/YSZ phase including electrical double layer capacitance estimated based upon impedance simulations, second, data for the YSZ electrolyte (ionic conductivity, surface site density and bulk properties) and third, information about geometrical and electrical parameters of the mixed ionic-electronic conducting LSCF phase. The latter data was thoroughly described elsewhere.[35]

Table 4.3. Model parameters used for simulations.

| **Parameter** | **Value** | **Reference** |
|---|---|---|
| *Ni/YSZ Anode* | | |
| Anode porosity, $\varepsilon$ | 0.35 | Estimated |
| Anode/gas surface specific area | $2.0 \cdot 10^6\ \mathrm{m^2 \cdot m^{-3}}$ | Estimated |
| Anode tortuosity, $\tau$ | 2 | Estimated |
| Ni particle radius | 0.5 µm | Estimated |
| Anode pore size, $d_{\mathrm{P,A}}$ | 1 µm | Estimated |
| Surface site density, $\Gamma_{\mathrm{Ni}}$ | $6.1 \cdot 10^{-5}\ \mathrm{mol \cdot m^{-2}}$ | [34,46] |
| Interfacial DL capacitance, $C_{\mathrm{DL}}^{\mathrm{In}}$ | $1\ \mathrm{F \cdot m^{-2}}$ | Fit |
| *YSZ Electrolyte* | | |
| Ionic conductivity of bulk YSZ, $\sigma_{\mathrm{CGO}}$ | $T/(1.4 \cdot 10^7\ \mathrm{K}) \cdot \mathrm{e}^{(90000\ \mathrm{J}/k_{\mathrm{B}}T)}$ S/m | [46,174] |
| Surface site density, $\Gamma_{\mathrm{YSZ}}$ | $1.1 \cdot 10^{-5}\ \mathrm{mol \cdot m^{-2}}$ | [46,174] |
| Bulk density, $\rho_{\mathrm{YSZ}}$ | $6800\ \mathrm{kg \cdot m^{-3}}$ | [46,174] |
| Bulk vacancy/oxygen fraction | 0.0401/0.9599 | [46,174] |
| *LSCF Cathode* | | |
| LSCF/gas surface specific area, $A_{\mathrm{LSCF/Gas}}^{\mathrm{V}}$ | $1.2 \cdot 10^7\ \mathrm{m^2 \cdot m^{-3}}$ | [35] |
| Cathode porosity, $\varepsilon$ | 0.37 | Estimated |
| Cathode tortuosity, $\tau$ | 2 | Estimated |
| LSCF particle radius | 1 µm | Estimated |
| Pore size, $d_{\mathrm{P,C}}$ | 1 µm | Estimated |
| LSCF/gas phase DL capacitance, $C_{\mathrm{DL}}^{\mathrm{sur}}$ | $100\ \mathrm{F \cdot m^{-2}}$ | [35] |
| LSCF/YSZ Interfacial capacitance, $C_{\mathrm{DL}}^{\mathrm{int}}$ | $(0.245 \cdot T / \mathrm{K} - 185)\ \mathrm{F \cdot m^{-2}}$ | [35] |
| Surface site density, $\Gamma_{\mathrm{LSCF}}$ | $1.0 \cdot 10^{-5}\ \mathrm{mol \cdot m^{-2}}$ | [35] |
| Bulk density, $\rho_{\mathrm{LSCF}}$ | $6890\ \mathrm{kg \cdot m^{-3}}$ | [35] |
| Bulk vacancy/oxygen fraction | 0.01/0.99 | [35] |

*4.2.2 Modeling of anode-supported SOFC performance.*

First, in order to obtain a base parameter set for the consecutive simulations of sulfur poisoning, the polarization curve for a system without the presence of sulfur was simulated. As an example to illustrate the model, a particular membrane electrode assembly (MEA) structure used by Yang et al.[79] is adapted. Yang et al. have investigated anode-supported cells with a Ni/YSZ anode, LSCF cathode and a base anode fuel mixture of 50 % $H_2$, 1.5 % $H_2O$, 48.5 % $N_2$. Using the model with the parameter set shown in Table 4.1 – 4.4, the polarization curve as well as power density curve have been reproduced in Figure 4.2.

This particular cell shows relatively high transport resistance at voltages below 0.45 V leading to an asymmetric power density curve. Thus, in order to achieve the shown agreement, some parameters of the model have been tuned to represent this button cell, in particular, the TPB length of the anode, the interfacial double layer capacitance, and the geometrical parameters of the gas channel over the anode were fitted to the experimental results. As the interfacial double layer capacitance cannot be derived from the polarization curve, it was fitted to the non-sulfur impedance spectra shown in Figure 4.3. The same parameter set was subsequently used in all impedance spectra simulations in the presence of hydrogen sulfide.

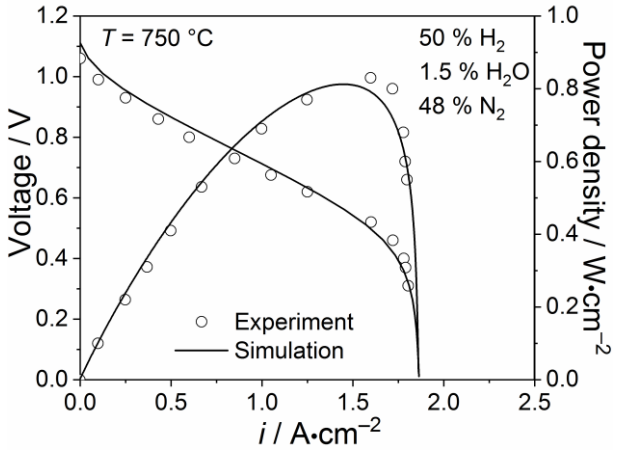


Figure 4.2: Comparison of the model (solid lines) and experimental measurements (open symbols) for a button cell operating on humidified hydrogen at $T$ = 750 °C. Experimental data are taken by Yang et al.[79]

Table 4.4. Model parameters used to reproduce the different electrochemical experiments.

| Parameter | Yang et al.[79] | Zha et al.[75] | Cheng et al.[76] |
|---|---|---|---|
| Anode thickness, $d_{Ni/YSZ}$ | 500 µm | 50 µm | 50 µm |
| Anode TPB length | $2.3 \cdot 10^{12}$ m·m$^{-2}$ | $2.5 \cdot 10^{12}$ m·m$^{-2}$ | $6.3 \cdot 10^{12}$ m·m$^{-2}$ |
| Electrolyte thickness, $d_{YSZ}$ | 10 µm | 250 µm | 250 µm |
| Cathode thickness, $d_{LSM}$ | 30 µm | 50 µm | 50 µm |

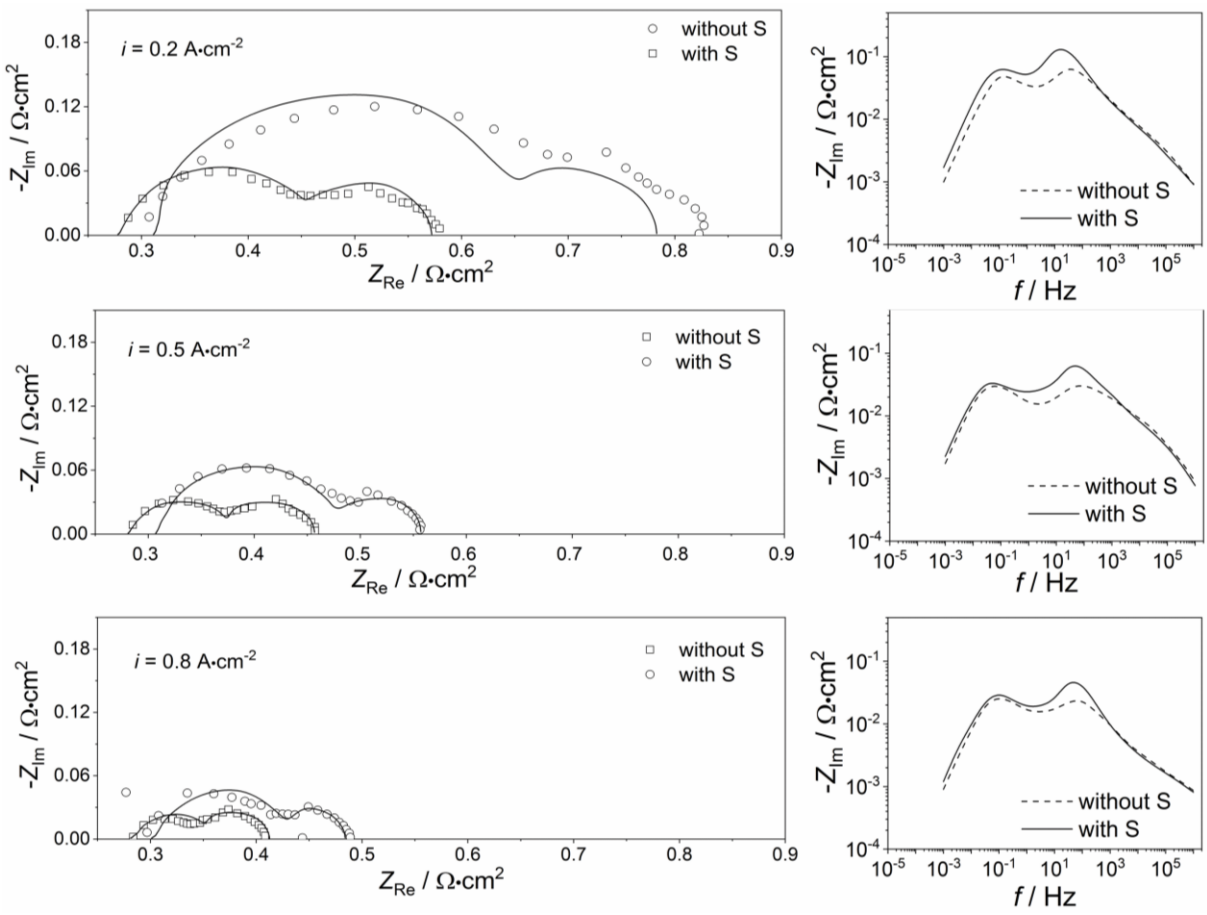


Figure 4.3: Nyquist (left panel) and imaginary impedance (right panel) plots of impedance spectra at a temperature of 750 °C, pressure of 1 atm before and after exposure to 1 ppm $H_2S$ at various current densities. The experimental results are taken from Yang et al.[79] The left panel of the figure represents Nyquist plots of experiments and simulations. The right panel shows imaginary impedance plots of the imaginary part of the simulated complex impedance. There is no experimental data given for the imaginary impedance plots, thus, only simulation results are depicted.

Figure 4.3 shows the comparison between experimental and simulated electrochemical impedance spectra for systems before and after exposure to 1 ppm $H_2S$ at various current densities and $T$ = 750 °C. The experimental results have shown the trend of a smaller relative increase in cell resistance for higher current densities.[76] As, the simulated Nyquist plots are in very good agreement with the experimental results, it can be concluded that our model is able to reproduce this characteristic poisoning behavior.

The influence of an exposure of the system to $H_2S$ is also clearly demonstrated by the imaginary impedance plots in Figure 4.3. At frequencies between $10^1 – 10^2$ Hz, where commonly surface processes take place,[176] the presence of $H_2S$ leads to a significant increase of the imaginary part of the impedance. This increase occurs at all current densities, however, the increase is most pronounced for $i$ = 0.2 A·cm$^{-2}$. Moreover, a small upwards shift of the initial imaginary impedance plot after exposure to $H_2S$ can be observed in the low frequency region between $10^{-3}$ and $10^{-1}$ Hz which corresponds to resistance due to gas transport over the anode surface in the supply volume, also referred to as gas conversion impedance.[39] Due to insufficient data about the increase of ohmic resistance in impedance spectra during the sulfur poisoning process it was modeled by employing additional contact resistance with $r_0$ equals to $7.8 \cdot 10^{-5}$ Ω·m$^2$ and a slope of $-1.03 \cdot 10^{-3}$ K$^{-1}$. This assumes no effect of sulfur on the ohmic resistance, since it was shown in recent experimental studies that even for considerably higher $H_2S$ concentrations (up to 100 ppm) sulfur poisoning does not have a significant influence on the ohmic resistance for short exposure times.[77]

### *4.2.3 Modeling of electrolyte-supported SOFC performance*

The following results are shown in order to demonstrate the capability of the model towards ESC performance. Zha et al. have examined Ni/YSZ-based cells with LSM cathodes in a fuel mixture of 50 % $H_2$, 1.5 % $H_2O$, 48.5 % $N_2$ and various trace amounts of $H_2S$ at 800 °C. The parameters used in the corresponding simulations are listed in Table 4.4. The base parameter set including TPB length and gas channel geometry was determined via the reproduction of a polarization curve of a non-sulfur system by Zha et al.[75] (not shown here). Since Zha et al. employed LSM as cathode of the investigated cell, in our study electrochemical oxygen reduction process was modeled by the Butler-Volmer equation. In Figure 4.4 comparisons between the experimental and simulated results of the current density stability during sulfur poisoning and recovery process are shown. In contrast to the study of Yang et al. who observed stable long-term performance for low $H_2S$ gas phase concentrations, Zha et al. reported slow-

er, irreversible long-term degradation. Recently, Kishimoto et al. used thermodynamic calculations to show that an increasing oxygen potential entails enhanced sulfur diffusion into nickel and can trigger sulfur-induced reversible degradation.[114] As a result, increased sintering of the nickel particles can lead to their detachment from the original position and an associated change in TPB length. This is investigated in more detail for Ni/CGO anodes in chapter 7. Due to limited data on the actual rate and type of the mentioned processes, the irrversible degradation was modeled via a continuous reduction of TPB length. In the present model the TPB of the anode is assumed to decrease by the following function

$$l^{V}_{Ni/YSZ} = l^{V}_{Ni/YSZ,0} \cdot e^{-t/\tau} \cdot (1 - 0.12 \cdot \theta_S) \quad (37)$$

where $l^{V}_{Ni/YSZ}$ is the TPB length of the Ni/YSZ/gas phase, a subscript $_0$ denotes the initial TPB length, $t$ is the time and $\tau$ is the time constant which is set to 3600 h. In Figure 4.4a, a $H_2S$ concentration of 2 ppm was introduced into the fuel at a cell voltage of 0.7 V, in Figure 4.4b 50 ppm $H_2S$ was added at a cell voltage of 0.6 V. At the beginning of the simulation, the cell is operating in steady state at a current density of about 0.25 $A \cdot cm^{-2}$. After a certain period of time (10 hours for 2 ppm and 25 hours for 50 ppm) $H_2S$ was introduced to the system, which leads to a decrease in current density from 0.25 $A \cdot cm^{-2}$ to 0.216 $A \cdot cm^{-2}$ (2 ppm) and to 0.207 $A \cdot cm^{-2}$ (50 ppm) with a subsequent slow decrease over the whole experimental monitoring time. In both cases the initial cell current density drop was successfully modeled by sulfur chemisorption at the nickel surface. The simulated initial drop is completed after approximately 10 min depending on the $H_2S$ concentration in the gas phase. The consecutive current density decrease is initiated by a TPB reduction described by Eq. 37. The model reveals the average degradation rate to be approximately 0.2 $mA \cdot cm^{-2} \cdot h^{-1}$.

The developed sulfur poisoning mechanism has been tested towards the recovery of the cell after operation with $H_2S$. Figure 4.4 also illustrates the recovery of the cell after operation with 2 ppm (after 30 h) and 50 ppm (after 145 h) of $H_2S$. In the case of lower hydrogen sulfide concentration slower recovery in comparison to the experimental data is obtained, and for 50 ppm the predicted recovery of the cell operation is slightly faster, however, after a certain period of time the simulated and experimental current densities match well for both concentrations. However, the deviation in Figure 4.4a demonstrates that further improvement of the thermodynamic and kinetic data will be necessary to obtain better predictive capabilities.

As it is reported in the prior literature section, the continuous decrease of SOFC performance could be observed over longer time periods as the anode is exposed to hydrogen sulfide.[105] Thus, in order to include the 2$^{nd}$ stage degradation over a longer period of exposure time, an

exponential function was included in Eq. 37. Ideally, the irreversible degradation should be modeled by anode microstructural changes, which lead to a decrease of TPB length. However, due to insufficient knowledge about the origin of the latter processes and the corresponding kinetic and thermodynamic data, a gradual reduction of TPB length was employed.

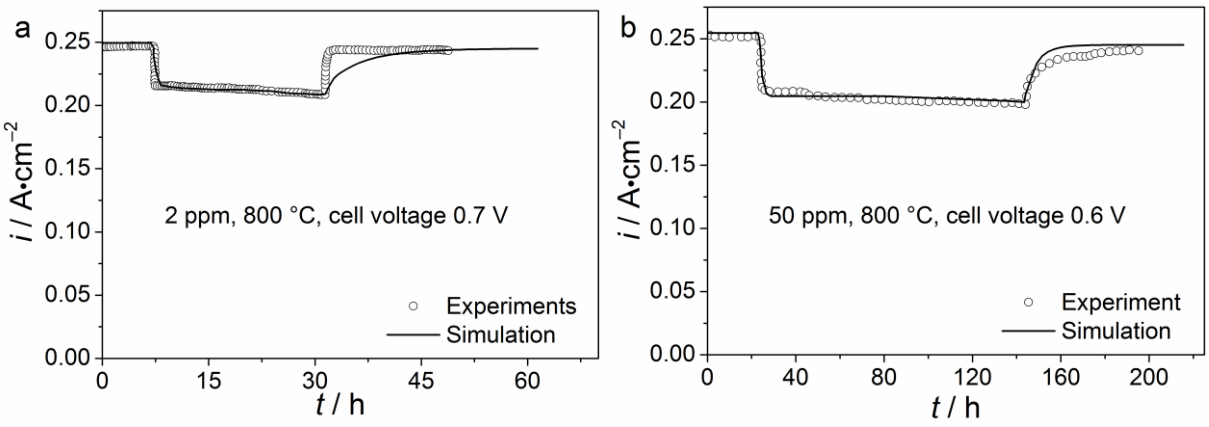


Figure 4.4: Simulated and experimental data for sulfur poisoning and regeneration processes of Ni/YSZ anodes in a fuel mixture with (a) 2 ppm (0.7 V) and (b) 50 ppm $H_2S$ (0.6 V).

For deeper insights into the mechanistic details of sulfur poisoning, the calculated equilibrium sulfur coverage on the Ni surface as a function of current density is shown in Figure 4.5. At a $H_2S$ gas phase concentration of 50 ppm a considerably higher sulfur surface coverage is achieved than at 2 ppm. This can be assumed to be the reason for the higher current density drop at the 50 ppm system. The sulfur coverage for both 2 ppm and 50 ppm $H_2S$ increase nearly exponentially with current density. This behavior is due to a reduced partial pressure of hydrogen in the anode compartment at high current densities, which shifts the thermodynamic equilibrium of Eq. 38 to the left.

$$S_{Ni} + H_{2,g} \rightleftharpoons H_2S + \square_{Ni} \tag{38}$$

This is an interesting finding, since it is contrary to previous studies, which suggest the increase of the sulfur removal rate via electrochemical oxidation caused by the larger oxygen ion flux at high current densities.[75,76,82,86,177] This reaction was postulated after observing decreasing relative anode resistance increase values upon sulfur exposure with current density. An alternative possible explanation for this behavior was indicated by Cheng et al.[105] In their study, the authors have used simple correlations based on the Tafel equation to show that the decreasing relative total anode resistance with current density is the inherent Tafel behavior and thus, is not related to the decreasing sulfur coverage on the Ni surface. As shown in Figure 4.3, in the present work this behavior is quantitatively reproduced while even showing

increasing sulfur coverage with current density. The decreasing anode resistance increase at high current densities can still be reproduced with the developed model as the charge transfer reaction rate increases at higher $pH_2O$ values, which are induced by high current densities. This counterintuitive behavior is caused by the participation of $OH^-_{YSZ}$ in the rate-limiting charge transfer reaction C1 and its generation via a molecular $H_2O$ precursor in R13.

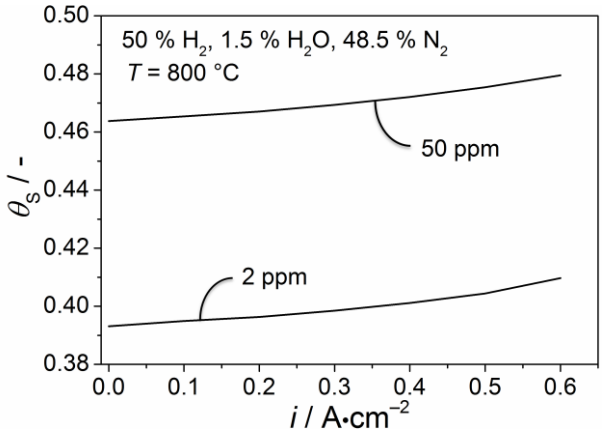


Figure 4.5: The change of sulfur coverage with cell current density for $H_2S$ gas phase concentrations of 2 ppm and 50 ppm corresponding to results shown in Figure 4.4.

### *4.2.4 Modeling of electrolyte-supported SOFC performance: Galvanostatic versus potentiostatic regime*

As it was briefly described above the relative power output drop caused by sulfur poisoning decreases as the cell voltage is lowered potentiostatically, however, it increases with current density in the galvanostatic mode. In order to verify these phenomena, potentiostatic and galvanostatic relative power drop calculations were carried out. Therefore, experimental results of Cheng et al. were used, who have investigated LSM-based ESC in a fuel mixture of 50 % $H_2$,1.5% $H_2O$, 48.5% $N_2$ and various trace amounts of $H_2S$ under both galvanostatic and potentiostatic conditions at 800 °C. Using the kinetic and thermodynamic parameter set developed and validated above and the cell-specific parameters listed in Table 4.4, Figure 4.6 shows the comparison between the model predictions and experimental data. In Figure 4.6a, the comparison of the relative voltage drops for different $H_2S$ concentrations under galvanostatic conditions is shown. Figure 4.6b shows the relative current density drops under potentiostatic conditions. In galvanostatic mode, the authors measured the relative voltage drops at constant current densities of $i$ = 0.241 A·cm$^{-2}$ and $i$ = 0.409 A·cm$^{-2}$, corresponding to initial cell voltages of 0.708 V and 0.534 V, respectively. They observed that the relative voltage drop curve was greater at higher current density for all tested $H_2S$ concentrations.

At potentiostatic mode, the relative current density drops were determined at the voltages $E = 0.7$ V and $E = 0.535$ V (corresponding to initial current densities of 0.26 A·cm$^{-2}$ and 0.432 A·cm$^{-2}$) consistent with the initial cell voltages from the galvanostatic measurements. In contrast to the results obtained for constant cell current densities, the relative current density drop was greater for the cell voltage of 0.7 V, that is, for the lower initial cell current density.

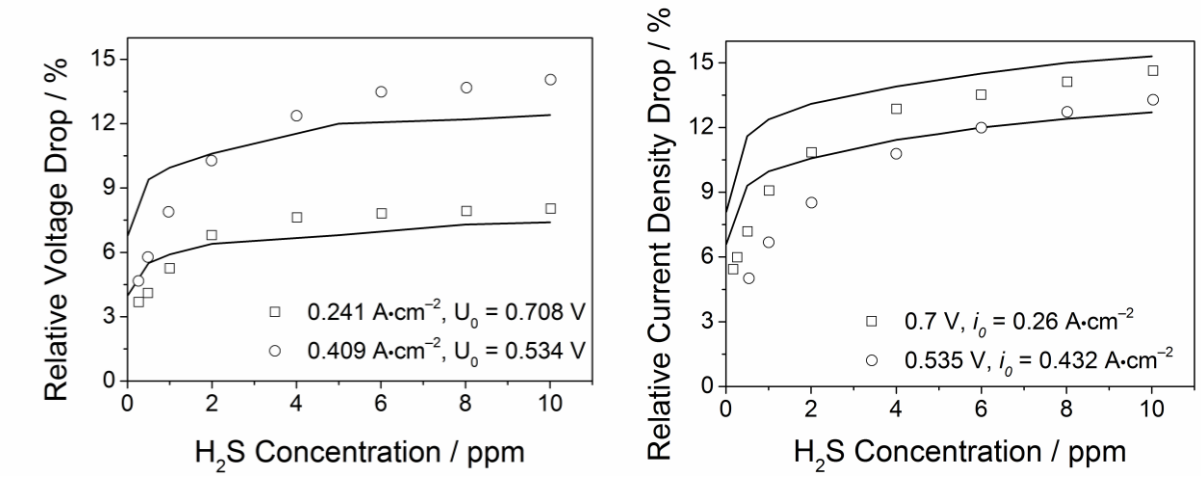


Figure 4.6: Comparison between the experimental and simulated values for the relative voltage drop (a) and current density drop (b) for different conditions at $T = 800$ °C.

There are two distinguished regions in the relative power output drop shown in Figure 4.6. At the beginning, the degree of poisoning increases drastically with increasing $H_2S$ concentrations (up to about 4 ppm), which is followed by almost constant performance drops at higher concentrations. As illustrated in Figure 4.6, the behavior of experimental measurements can be represented well by our model for a variety of $H_2S$ concentrations. There is a substantial discrepancy between simulated and experimental results for the relative current density drop at small $H_2S$ concentrations, however, the validity of our model for a $H_2S$ concentration of 2 ppm at 0.7 V under potentiostatic mode was already demonstrated in the previous subsection. Thus, the observed deviation with a relatively large calculated current density drop might be related to limited information about structure and geometry of the experimental cell taken from literature. However, the existence of an important physical process that is not represented by our model and influences the relative current density drop at small $H_2S$ concentrations cannot be excluded. Nevertheless, the overall simulation results show that the developed sulfur poisoning model provides a reasonable representation of the galvanostatic and potentiostatic behavior, especially at relatively high $H_2S$ concentrations.

*4.2.5 Sensitivity analyses*

The simulation results shown above have demonstrated the validity of the developed model for a wide range of operating conditions. In order to further investigate the sulfur poisoning behavior as a function of operational, geometrical and physicochemical parameters, sensitivity analyses were carried out. Sensitivity analysis is a tool used to quantitatively determine the dependencies of the macroscopic electrochemical behavior on model parameters. In the performed analyses the investigated parameters $P$ (geometrical, kinetic, thermodynamic, etc.) are varied separately by 5 % and their effect on the investigated macroscopic quantity is quantified by the relative sensitivity $s$. In the present paper, the relative sensitivities of the total anode resistance $R_p$ and sulfur coverage on Ni, $\theta(S_{Ni})$ are determined. The dimensionless relative sensitivity, in the example of the total anode resistance $R_p$, is calculated as $s(R_p) = (\Delta R_p/R_p)/(\Delta P/P)$. The same procedure is applied to test the effect of sulfur coverage change towards the change of physico-chemical parameters. In the following, a relative sensitivity of unity signifies a proportional impact of the parameter on the macroscopic quantity. Sensitivity values close to zero mean that the parameter has no influence on the quantity. Negative sensitivities represent a decrease of the investigated quantity. The sensitivity of all parameters used in the model was tested; in Figure 4.7a+b only the results for parameters are reported that actually have a significant influence on the respective macroscopic quantity. The sensitivity analysis towards the change of total anode resistance ($R_p$) shown in Figure 4.7a was performed based upon impedance spectra from Figure 4.3. As it is indicated in Figure 4.7a, for $R_p$, a sensitivity analysis was carried out at two different temperatures (650 °C and 750 °C). The results are divided into four different categories. These are (*i*) thermodynamic and kinetic parameters, (*ii*) the electrochemical double layer capacitance, (*iii*) geometrical parameters of the cell and (*iv*) physical parameters. The strong sensitivity of $\theta(S_{Ni})$ towards the enthalpy and entropy of sulfur demonstrates the difficulties associated with the modeling of sulfur poisoning. Already small deviations from the real thermodynamic data of sulfur lead to a strong divergence between experiments and simulation results. The analysis also reveals that the charge transfer reaction C1 has significant influence on total anode resistance for both temperatures. Another co-limiting reaction is the $H_2O$ adsorption on YSZ that is involved in providing the reactants for the charge transfer reaction. Moreover, $R_p$ is sensitive towards the enthalpies of $O^{2-}_{YSZ}$ and $H_2O_{YSZ}$, both involved in the rate co-limiting reactions. Furthermore, $R_p$ is sensitive to the change of several geometrical parameters that affect the gas diffusion and gas conversion resistance, the Ni/YSZ interfacial double layer capacitance and pressure.

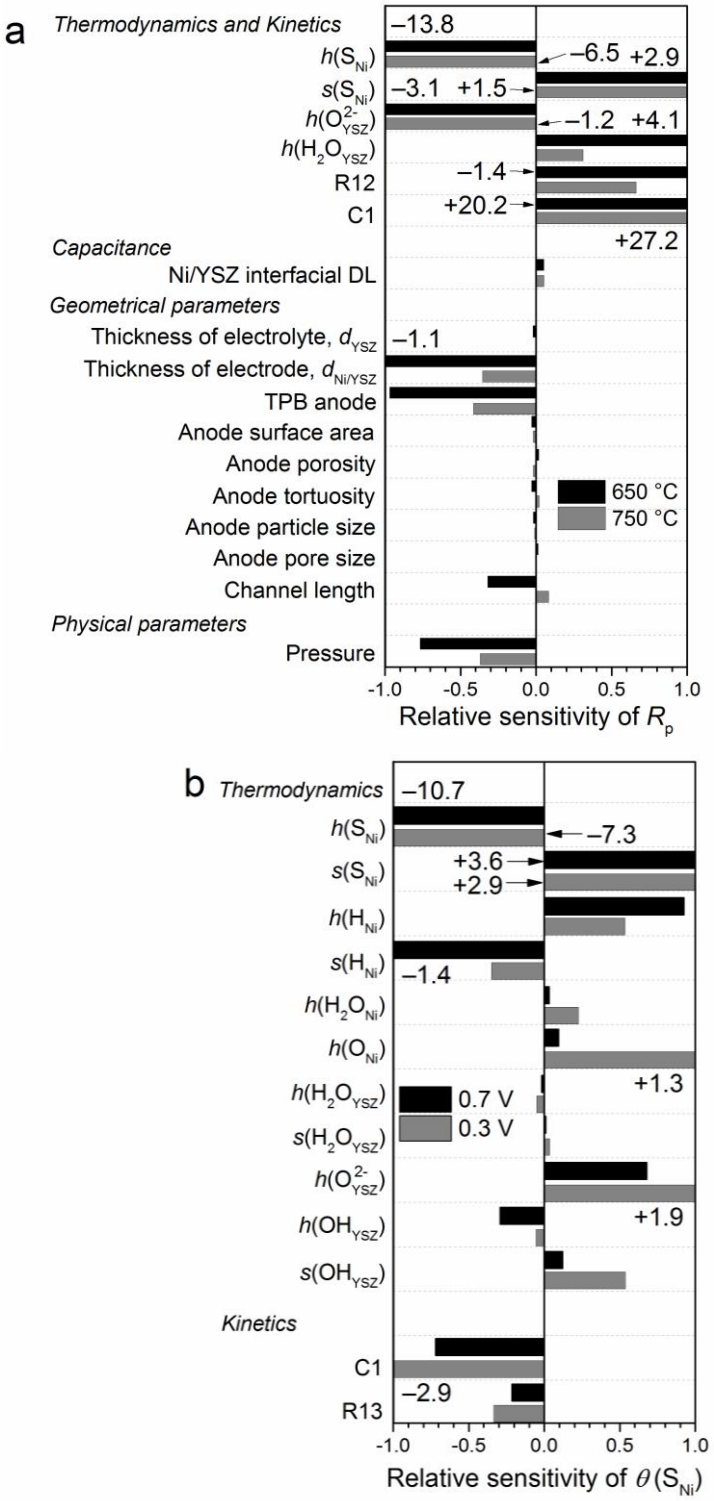


Figure 4.7: Sensitivity analysis of (a) the total anode resistance ($R_p$) at two different temperatures and (b) sulfur coverage $\theta(S_{Ni})$ at two different cell voltages. For further details see text.

Many of these parameters have also shown a significant effect on $R_p$ for systems without $H_2S$.[34] Hence, another sensitivity analysis towards $\theta(S_{Ni})$ was performed, since sulfur coverage was identified to be the key parameter dictating the performance loss in sulfur-containing systems. The sensitivity analyses towards the change of sulfur coverage were performed at two different cell voltages (0.7 V and 0.3 V) and a temperature of 750 °C. Again, the results are divided into two categories, namely thermodynamic and kinetic parameters. As expected, $\theta(S_{Ni})$ is very sensitive towards the enthalpy and entropy of sulfur. This sensitivity is decreasing for lower cell voltages (that is, higher current densities).

However, as already noted above this behavior is not due to increasing sulfur removal, but rather caused by the enhanced charge transfer reaction rate. $\theta(S_{Ni})$ also shows a significant sensitivity towards the thermodynamic data of adsorbed hydrogen atom on Ni surface. The strong coverage dependence of sulfur and its high surface coverage illustrate that its presence on the surface highly affects the surrounding adsorbates. Thus, the introduction of a coverage dependence for $h(H_{Ni})$ and/or $s(H_{Ni})$ might lead to an improvement of the simulation results. Although there are studies in literature,[121] which suggest the coverage-dependent modification of the hydrogen atom enthalpy on Ni, this value was kept constant in order to decrease the number of fitting parameters. However, if further thermodynamic data concerning the sulfur coverage dependence of the hydrogen atom enthalpy/entropy becomes available, the refinement of their values will be valuable.

Considering the influence of the physico-chemical processes on sulfur coverage, the performed sensitivity analysis shows that the charge transfer reaction C1 and reaction R13 which is delivering the reactants for C1 are the rate co-limiting steps. Correspondingly, the thermodynamic data of species involved in these reactions also have a high influence on coverage. All other reactions are fast and not co-limiting. Thus, their rate coefficients only have a minor influence on sulfur coverage. Neither the kinetics of the reactions leading to sulfur oxidation to $SO_2$ nor the thermodynamic data of the involved species have any impact on sulfur coverage. Thus, their accuracy has no significant impact on the simulation outcome.

Figure 4.7b shows that the coverage of sulfur is sensitive towards more thermodynamic parameters than kinetic parameters. Thus, as $\theta(S_{Ni})$ can be regarded to be the key parameter describing sulfur poisoning, it can be stated that sulfur poisoning is driven thermodynamically.

## *4.3 The influence of sulfur formation on performance and reforming chemistry of Ni/YSZ anodes operating on methane containing fuel*

As a next step, the developed elementary kinetic reaction mechanism for sulfur poisoning on Ni/YSZ in $H_2/H_2O$ fuel systems is extended to methane-containing fuels. As this involves numerous additional gas phase and surface species, a significantly more complex reaction mechanism is required as described in the following.

### *4.3.1 Heterogeneous chemistry in methane-containing systems.*

For SOFC fueled with methane, the inlet gas mixture at the anode side consists of $CH_4$, $H_2$, $H_2O$ and $H_2S$ gases, and after reforming on the Ni catalyst furthermore contains the four additional gas phase species CO, $CO_2$, $O_2$ and $SO_2$. In order to describe this complicated heterogeneous mechanism, two validated reaction mechanisms were combined: first, the full methane reforming mechanism on the nickel surface consisting of 42 surface reactions among 6 gas phase species and 14 surface-adsorbed species,[69,178] and second, the elementary kinetic mechanism of sulfur formation/oxidation on Ni/YSZ as described in the previous section. Since all relevant thermodynamic and kinetic data are thoroughly described in the references given above, it is not repeated here. However, a schematic illustration of the coupled mechanisms of methane reforming and sulfur poisoning is shown in Figure 4.8. In this figure the methane reforming steps are shown on the right in black, whereas $H_2S$ dissociation and $SO_2$ formation are shown in bold and blue on the left of the scheme.

The employed methane reforming mechanism was developed to describe methane steam reforming (MSR), partial oxidation and dry reforming (DR) of methane on the Ni surface. From an elementary kinetic point of view, all of these chemical processes are based on identical elementary steps.[169,179] Therefore, it is evident that MSR, CPOX and DR cannot be seen as three independent reaction pathways, and they are inherently coupled forming a complex heterogeneous chemical reaction mechanism. The dominating process among these three global reactions is determined by a number of factors, all of which are interdependent: (a) the gas phase composition and, therefore, the availability and ratio of surface species, (b) the reaction kinetics and mobility of the surface species, which depend on temperature and the materials, and (c) the location within the porous anode (close to the supply channel or to the electrolyte). For that reason, one of the aims of the present section is to establish the influence of sulfur formation on the heterogeneous chemistry.

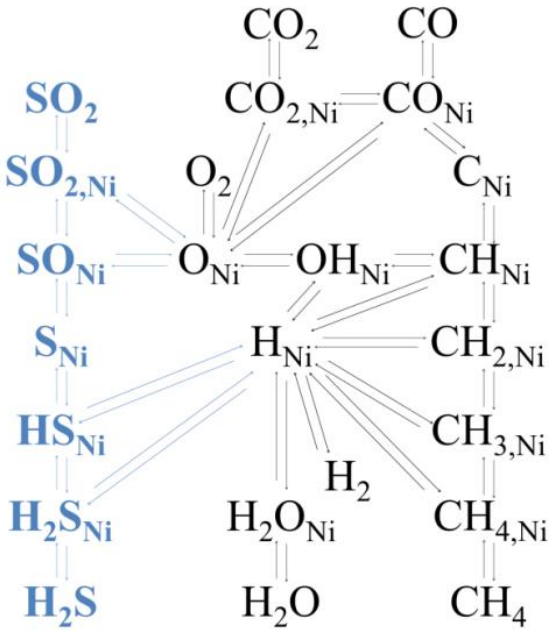


Figure 4.8: Schematic illustration of the combined methane reforming (in black to the right) and sulfur formation/oxidation reaction mechanism (in blue on the left).

As depicted in Figure 4.7, the total cell resistance in a $H_2/H_2O$ system is not sensitive towards the Ni surface area. However, as Ni acts as catalyst for methane steam reforming, modeling of sulfur poisoning of methane steam reforming must include an active surface area reduction depending on the sulfur coverage on Ni. In the present work, this dependency is assumed as follows

$$A_{\mathrm{Ni}}^{\mathrm{V}} = A_{\mathrm{Ni},0}^{\mathrm{V}} \cdot e^{-a \cdot \theta(\mathrm{S_{Ni}})}, \tag{39}$$

where $A_{\mathrm{Ni}}^{\mathrm{V}}$ describes the volume-specific surface area, $A_{\mathrm{Ni},0}^{\mathrm{V}}$ denotes the initial volume-specific surface area and $\theta(\mathrm{S_{Ni}})$ is the sulfur coverage on the Ni surface.

Since the adsorption of atomic sulfur on the Ni surface occurs on hexagonal closed packed (hcp) and face centered cubic (fcc) sites[120] with strong lateral repulsion, it reflects in significant active surface blockage. Experimental investigations of the sulfur surface structure on Ni catalysts have shown that the surface structure continuously changes with coverage and that especially for high sulfur surface coverages numerous complex surface patterns can be formed that are only stable in a small coverage range.[71,180] However, modeling this highly non-linear relationship between sulfur coverage and blocked surface area at such a high level of resolution would be extremely difficult. In this study, an inversely exponential approach is employed which has proven to capture this effect well for the whole investigated sulfur

coverage range. In order to account for the atomic level interaction between adsorbed sulfur and active surface area a steric coefficient *a* is used in equation 1, which is set to the constant value nine for all simulations.

### *4.3.2 Simulation of electrochemical experiments in methane-containing systems*

As a next step, the developed elementary reaction mechanism is applied to analyze experiments by Rasmussen et al.,[99] which were conducted using Ni/YSZ-based ASC operated on methane-containing fuel. These experiments stand for the most complete data set available and cover an extended range of operating conditions. The MEA used by Rasmussen et al. consists of five distinct layers: (*i*) a fuel chamber (4 cm width) in horizontal direction, (*ii*) a porous Ni/YSZ anode (315 μm), (*iii*) a dense YSZ electrolyte (15 μm), (*iv*) an LSM/YSZ porous cathode (25 μm), and (*v*) a cathode air supply channel. The detailed description of the used SOFC configuration is given by Rasmussen et al.[99] and briefly summarized in Table 4.5. Experiments were carried out at 750 °C. In order to verify the developed model and its base parameter set, it is validated against electrochemical measurements by Rasmussen et al.[99] by using the system without sulfur-containing gases with a fuel gas consisting of 13 % $H_2$, 29 % $CH_4$ and 58 % $H_2O$. First, the *i*-*V* curve was simulated and, subsequently, voltage stability tests at different conditions were reproduced. Figure 4.9 illustrates the predicted polarization features of the nominal MEA structure (see Table 4.5) operating on $CH_4$, $H_2$ and $H_2O$ at 750 °C. In the original paper there was no complete experimental polarization curve available, however, based upon comparisons to the given *i*-*V* data points by Rasmussen et al., as described further below, the predicted polarization characteristics describe the experimental cell well. The simulated OCV of 995 mV is in good agreement with the measured value of 984 mV. Also, a FU of 57 % for a current density of 1 $A \cdot cm^{-2}$ was reported for the experiments, which is in accordance with the simulated value as depicted in Figure 4.9. The peak power density of 0.8 $W \cdot cm^{-2}$ is reached for a current density of 1.5 $A \cdot cm^{-2}$ and a voltage of 0.55 V. At high current density the strong influence of transport limitations is apparent as the FU approaches 100 %.

In the following, two cases will be discussed. First, the comparison of the model predictions with the electrochemical results at OCV, and second, the comparison between simulated and experimental results for certain applied currents.

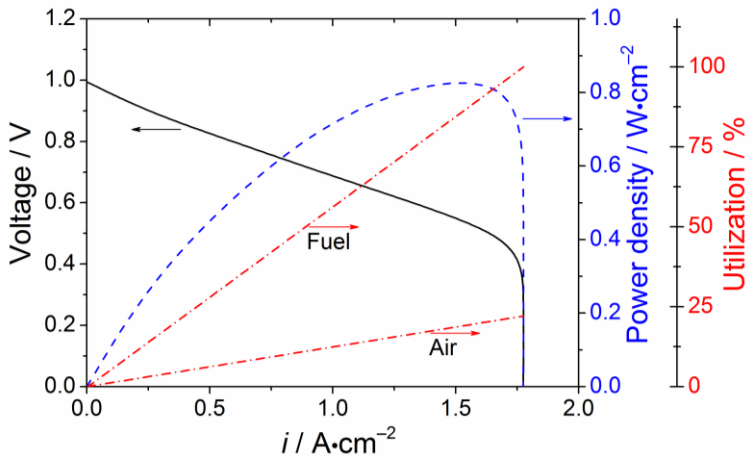


Figure 4.9: Predicted cell voltage (full, black line) and power density (dashed, blue line) as functions of current density at 750 °C for a gas mixture of 13 % $H_2$, 29 % $CH_4$, 58 % $H_2O$. The additional axis on the right shows fuel and air utilization (in percentage) as function of current density (red, dashed-dotted line).

*Cell operation at open circuit voltage*— In the following the comparison between simulations and sulfur poisoning experiments by Rasmussen et al.[99] at OCV is shown. First, the OCV stability tests over 270 hours are reproduced in which the model is run with time-varying inputs monitoring different electrochemical performance changes. Figure 4.10 shows the results of the transient simulations for a 29 % $CH_4$, 13 % $H_2$, 58 % $H_2O$ gas mixture containing 2, 4, 7, 9, 20 and 24 ppm of $H_2S$. At the beginning, up to 6 h, the OCV has a constant value of 0.995 V, as long as no $H_2S$ was added to the fuel. However, starting from 7 h the OCV gradually decreases over 43 h upon operation with a constant $H_2S$ concentration of 2 ppm. After about 30 – 40 h of $H_2S$ exposure the cell voltage reaches a constant value. In the following, the increase of $H_2S$ concentration initially leads to a further decrease of voltage, however, for $H_2S$ concentrations higher than 20 ppm the cell voltage stabilizes. Moreover, the initial decrease of cell voltage for 2 ppm $H_2S$ proceeds at a much lower rate than the consecutive drops. A removal of $H_2S$ from the feed gas results in a nearly complete voltage recovery in the experiments. All in all, Figure 4.10 shows a very good overall agreement between experiments and simulations over the whole investigated time period.

Table 4.5. Model parameters used for the simulations.

| **Parameter** | **Value/expression** | **Reference** |
|---|---|---|
| Anode Ni/YSZ | | |
| Thickness, $d_{\mathrm{Ni/YSZ}}$ | 315 µm | [99] |
| Anode/gas surface specific area | $3.0\cdot10^{6}\ \mathrm{m^2\cdot m^{-3}}$ | Estimated |
| Anode TPB length | $3.0\cdot10^{12}\ \mathrm{m\cdot m^{-2}}$ | Estimated |
| Anode porosity, $\varepsilon$ | 0.3 | Estimated |
| Anode tortuosity, $\tau$ | 2 | Estimated |
| Ni particle radius | 1 µm | Estimated |
| Pore size, $d_{\mathrm{P,A}}$ | 1 µm | Estimated |
| Interfacial DL capacitance, $C_{\mathrm{DL}}^{\mathrm{In}}$ | $0.02\ \mathrm{F\cdot m^{-2}}$ | Fit |
| Cathode LSM/YSZ | | |
| Thickness, $d_{\mathrm{LSM/YSZ}}$ | 25 µm | [99] |
| Cathode TPB length | $5.0\cdot10^{-5}\ \mathrm{m}$ | Estimated |
| Cathode porosity, $\varepsilon$ | 0.3 | Estimated |
| Cathode tortuosity, $\tau$ | 2 | Estimated |
| LSM particle radius | 1 µm | Estimated |
| Pore size, $d_{\mathrm{P,C}}$ | 1 µm | Estimated |
| Interfacial DL capacitance, $C_{\mathrm{DL}}^{\mathrm{In}}$ | $2\ \mathrm{F\cdot m^{-2}}$ | Fit |
| Electrolyte, YSZ | | |
| Thickness, $d_{\mathrm{YSZ}}$ | 15 µm | [99] |
| Ionic conductivity of bulk YSZ, $\sigma_{\mathrm{CGO}}$ | $T/(1.4\cdot10^{7}\ \mathrm{K})\cdot \mathrm{e}^{(9000\mathrm{K}/T)}$ S/m | [46,174] |
| Surface site density, $\Gamma_{\mathrm{YSZ}}$ | $1.1\cdot10^{-5}\ \mathrm{mol\cdot m^{-2}}$ | [46,174] |
| Bulk density, $\rho_{\mathrm{CGO}}$ | $6800\ \mathrm{kg\cdot m^{-3}}$ | [46,174] |
| Bulk vacancy/oxygen fraction | 0.0401/0.9599 | [46,174] |
| Gas channel | | |
| Length, $D_{\mathrm{ch}}$ | 0.04 m | [99] |
| Thickness, $d_{\mathrm{ch}}$ | $1.0\cdot10^{-4}\ \mathrm{m}$ | [99] |
| Inflow velocity | $10\ \mathrm{l\cdot h^{-1}}$ (fuel), $140\ \mathrm{l\cdot h^{-1}}$ (air) | [99] |

In the original paper, Rasmussen et al. indicated hindered methane steam reforming and the associated change of the gas phase composition to be the reasons for the cell voltage decrease and its stabilization to be due to the saturation of sulfur surface coverage. In order to allow for an in-depth analysis of this explanation, the evolution of the mean coverage of selected Ni surface species was simulated over 270 h corresponding to the OCV stability test from Figure 4.10. The results depicted in Figure 4.11 show that the initial addition of 2 ppm $H_2S$ leads to a significant increase in sulfur coverage and a simultaneous reduction of hydrogen and CO coverage. Subsequently, with a further increase in $H_2S$ concentration sulfur surface coverage approaches its saturation value of 0.5 ML[180] and the hydrogen and CO coverage stabilize. At this point, CO coverage on Ni is close to zero. It can be seen that after the introduction of 2 ppm $H_2S$ the cell voltage reduction and the increase of sulfur coverage happen simultaneously.

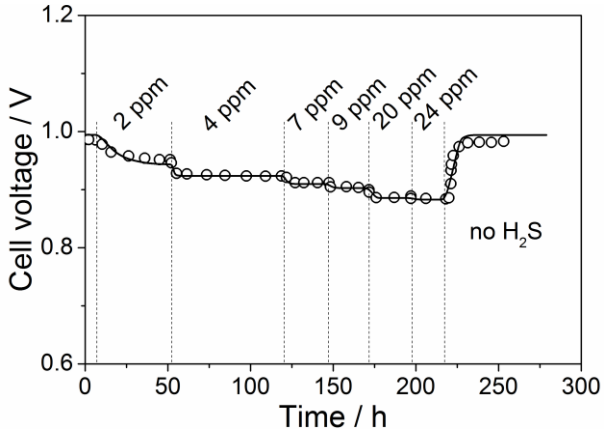


Figure 4.10: Comparison of the cell voltage (OCV) development at different $H_2S$ concentrations between simulation (solid line) and experiments (open symbols) at $T$ = 750 °C for 13 % $H_2$, 29 % $CH_4$, 58 % $H_2O$.

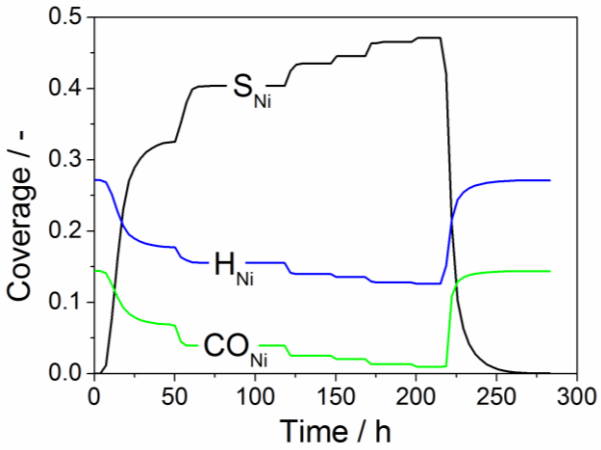


Figure 4.11: The coverage of selected species on the Ni surface during cell poisoning with 2, 4, 7, 9, 20 and 24 ppm of $H_2S$. Experimental conditions are the same as for the results in Figure 4.10.

For the non-sulfur system depicted in Figure 4.12a, full methane conversion (steam reforming) is reached quickly leading to equilibrated gas phase profiles along the channel after already about one third of its length. The analysis of the gas phase profiles in the channel shows that the dry reforming reaction rate is smaller than that of WGS, as there is a certain formation of $CO_2$ which was absent in the initial fuel gas mixture. However, the equilibrium partial pressure of $CO_2$ is comparatively low due to the high hydrogen gas phase concentration promoting the reverse water gas shift reaction (r-WGS). As shown in Figure 4.12b, the introduction of 2 ppm $H_2S$ particularly reduces methane conversion at the fuel inlet. At a channel length of approximately 0.75 cm, the methane conversion rate starts to increase strongly and the gas phase composition approaches the equilibrium composition as shown at the outlet of Figure 4.12a. It is known from catalysis that sulfur coverage on Ni can be described by the Temkin isotherm and was shown to be a function of hydrogen partial pressure.[37] Thus, the severe hindrance of methane conversion at the inlet of the channel can be explained with a comparatively high sulfur surface coverage on Ni at the channel inlet and the corresponding blockage of the active surface area.

The initial formation of $H_2$ gas from methane conversion is very slow, but initiates a domino effect where the sulfur coverage decreases with increasing $H_2$ partial pressure inducing an acceleration of methane conversion. Even though methane is nearly fully converted at the fuel outlet, the low $H_2$ concentration at the fuel inlet entails a smaller local electromotive force compared to Figure 4.12a leading to the measured cell voltage drop.

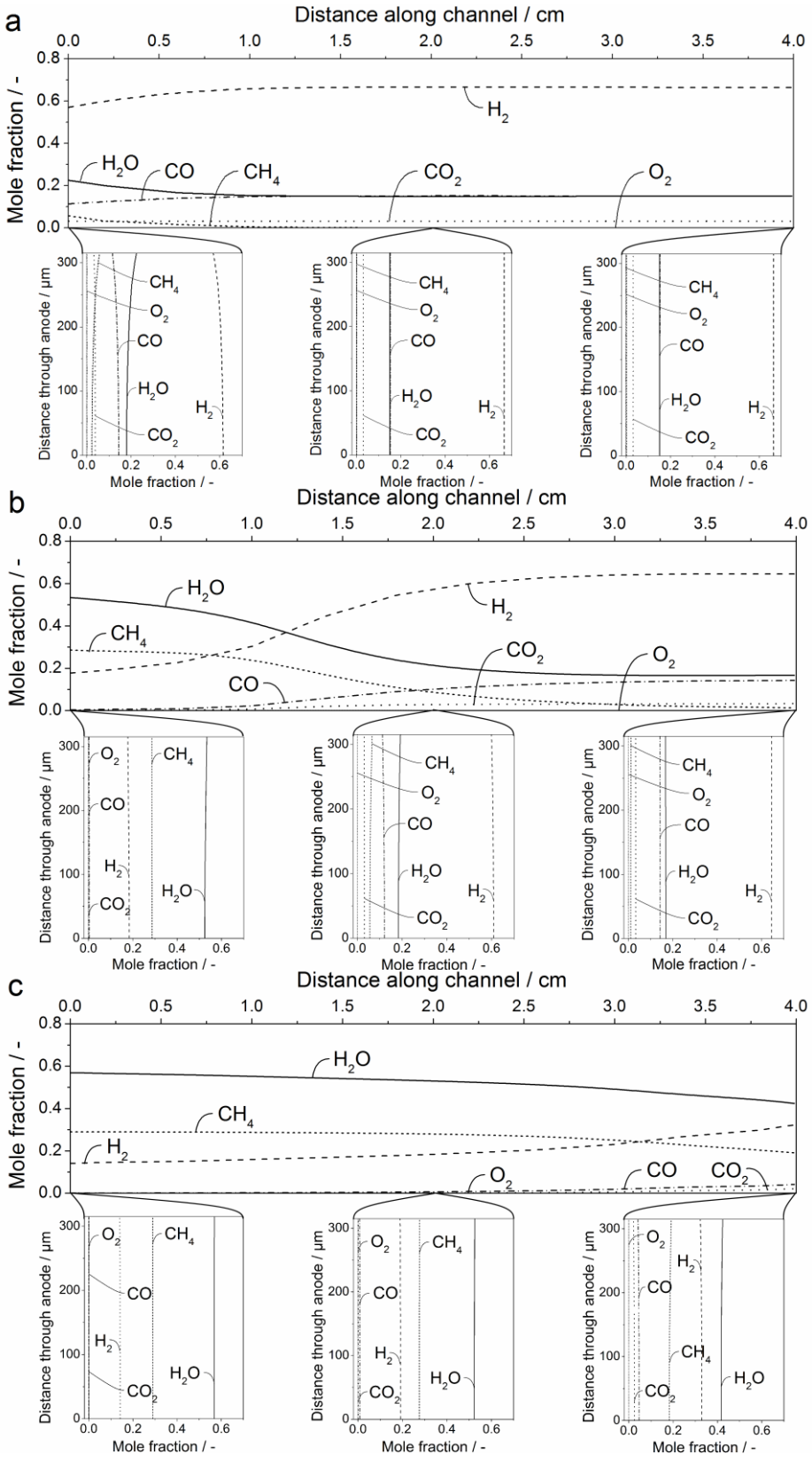


Figure 4.12: Spatial distribution of gas phase species along the anode channel (horizontal panel) and inside the porous anode at three different positions in the channel (vertical panel), and at the time of 6 h (a – no $H_2S$), 50 h (b – 2 ppm) and 220 h (c – 24 ppm).

With a further increase of $H_2S$ concentration to 24 ppm, the poisoning behavior becomes even more severe. The gas phase profile at the beginning resembles the imposed inlet gas phase concentration and only changes slowly along the channel. There is only a small formation of CO and $CO_2$ gases towards the end of the channel demonstrating strongly reduced reforming activity. The initiation of the domino effect described for the system exposed to 2 ppm $H_2S$ is now even further shifted toward the channel outlet as can be seen in Figure 4.12c. However, at the fuel outlet, the partial pressures of the gas phase species are still far-off from equilibrium. Thus, the local electromotive force is now reduced over the whole length of the channel causing an even more severe voltage drop.

In order to further understand the spatial evolution of the poisoning behavior, the methane conversion values at the channel inlet, channel outlet and an average over the whole cell were calculated and are depicted in Figure 4.13. The methane conversion given in the original paper determined based on the measured OCV is in good agreement with the averaged methane conversion values shown in Figure 4.13. However, to allow for a more spatially resolved analysis, it was additionally distinguished between methane conversion at the inlet and outlet. At the channel inlet methane conversion is dramatically reduced and nearly completely blocked already for the lowest $H_2S$ concentration of 2 ppm. As the $H_2S$ concentration is further increased methane conversion at the inlet approaches 0 %. However, there is still significant methane conversion at the outlet even for the largest investigated hydrogen sulfide concentrations. In the original paper, a methane conversion of 15 % was calculated for 24 ppm $H_2S$ based on OCV measurements. The more detailed calculations depicted in Figure 4.13 show that this value refers to the average conversion over the cell whereas the conversion at the outlet is considerably higher. Yet, its value is also decreasing with higher $H_2S$ concentrations which would ultimately lead to an almost complete blockage of methane steam reforming reactions. Previous studies have reported the increased sensitivity of methane reforming towards sulfur poisoning compared to the electrochemical hydrogen oxidation.[99,106] Based on the given analysis, this is indeed the case as even for a full monolayer of sulfur on Ni the electrochemical reactions are still active[75,77,104] whereas methane steam reforming is nearly completely blocked.

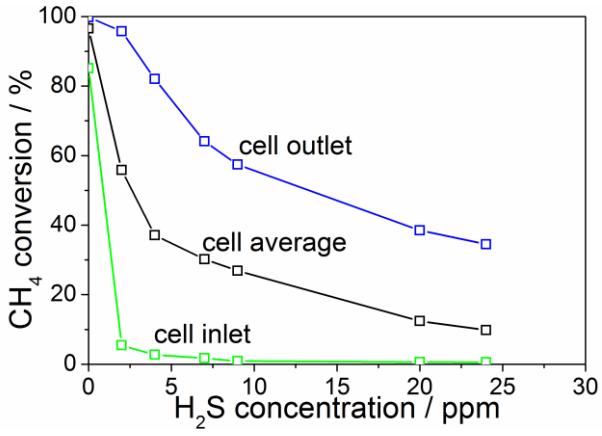


Figure 4.13: Methane conversion as the function of $H_2S$ concentration: green curve – at the cell inlet, blue curve – at the cell outlet and black curve – average across the cell.

*Cell operation under polarization* — In the second part of this subsection, SOFC performance degradation due to sulfur formation under current load is described. All parameters are the same as at OCV. First, three examples at constant current density of 1 $A \cdot cm^{-2}$ serve to demonstrate the capabilities of the model. Subsequently, the gas phase species distribution across the cell is shown to allow for a more detailed analysis of the poisoning behavior. Then, the reproduction of impedance spectra before and after $H_2S$ addition is shown in order to further establish the model's physically meaningful predictive capabilities.

As described by Rasmussen et al. three voltage stability tests were conducted for gas compositions of 46 % $H_2$, 17 % $CH_4$, 37 % $H_2O$ with $H_2S$ concentrations of 2 ppm, 4 ppm, 7 ppm and 2 ppm (Test 1), 13 % $H_2$, 29 % $CH_4$, 58 % $H_2O$ with an $H_2S$ concentration of 2 ppm (Test 2), 13 % $H_2$, 29 % $CH_4$, 58 % $H_2O$ with $H_2S$ concentrations of 4 ppm, 9 ppm and 7 ppm (Test 3). In test 3 the same fuel gas mixture as in test 2 was employed. However, the initial cell voltage was slightly higher which was accounted for by a higher initial TPB length in the model. A steam to carbon ratio equal or greater than 2 was maintained in all three tests, hence, preventing coke formation. Figure 4.14 illustrates the comparison between the model predictions and the experimental measurements for these three tests. There are two distinguished regions in the results shown in Figure 4.14. First, time periods with cell operation in the absence of $H_2S$, where constant slow cell degradation is observed and second, periods exhibiting the characteristic cell voltage reduction after introduction of different $H_2S$ concentrations to the anode gas. After switching off the $H_2S$ supply the cell voltage regenerates quickly to a level consistent with the overall degradation observed for operation without $H_2S$.

Already for cell operation in the absence of sulfur, a slow overall cell degradation can be observed. Similar to Eq. 37 in the previous section, the overall cell degradation was modeled via a continuous reduction of TPB length, according to the following function

$$l^{\mathrm{V}}_{\mathrm{Ni/YSZ}} = l^{\mathrm{V}}_{\mathrm{Ni/YSZ,0}} \cdot e^{-t/\tau}, \tag{40}$$

where $l^{\mathrm{V}}_{\mathrm{Ni/YSZ}}$ is the TPB length of the Ni/YSZ phase, a subscript $_0$ denotes the initial TPB length, $t$ is time and $\tau$ is the time constant which is set to 700 h. This can be considered as a reasonable approach for the present work, since it is not the primary aim of this study to investigate long-term non-sulfur related degradation.

In order to study the influence of the initial $CH_4$ concentration, in test 1 the fuel gas contained a significantly higher $H_2$ concentration than in tests 2 and 3. Figure 4.14 illustrates that the poisoning effect is less severe with larger initial $H_2$ concentrations. For example, in test 1 the cell tolerated exposure of 7 ppm $H_2S$ without the voltage falling below the current turn off voltage of 450 mV, whereas in test 3 the same concentration led to a drop below this value. The experimental conditions used to model the experimental results displayed in Figure 4.14b correspond to the results shown for OCV stability tests presented in the previous subsection. There is a good agreement between simulations and experiments for all three tests. The respective voltage drops could accurately be modeled by sulfur formation on the Ni surface. Thus, it can be concluded that their whole extent over a 24 h poisoning period is solely due to sulfur chemisorption on Ni and the associated surface site blockage. Rasmussen et al. explained the experimentally observed cell voltage breakdown and the associated cell failure in test 1 after the last period of anode exposure to $H_2S$ by nickel oxidation due to local fuel starvation at these conditions. Furthermore, the introduction of 9 ppm $H_2S$ to the fuel gas in test 3 led to an almost immediate cell voltage drop below 450 mV resulting in an automatic current turn off. Subsequently, after the same current load was applied again the anode exposure to 7 ppm $H_2S$ triggered a turn off of current as well. In accordance with the experiments in the simulations for 9 ppm $H_2S$ a cell voltage drop below 450 mV was calculated. However, the subsequent performance drop for 7 ppm $H_2S$ clearly results in a final voltage greater than 450 mV. The authors of the original paper have explained the experimental behavior by the high fuel utilization of >90% leading to Ni oxidation. It was not attempted to account for these Ni oxidation processes in the present model, thus, it comes to a deviation between experiment and simulation in the mentioned cases. Rasmussen et al. have observed the recovery of the cells in the methane-containing fuel to be faster than the recovery in $H_2/H_2O$ fuel indi-

cating a faster sulfur removal from the surface. This characteristic behavior was also successfully reproduced with the employed model. Taking into account the observation of the domino effect-like behavior illustrated in Figure 4.12, the rapid recovery in methane-containing fuel is suggested to be due to an increase of hydrogen partial pressure as the surface area becomes gradually available again for methane reforming.

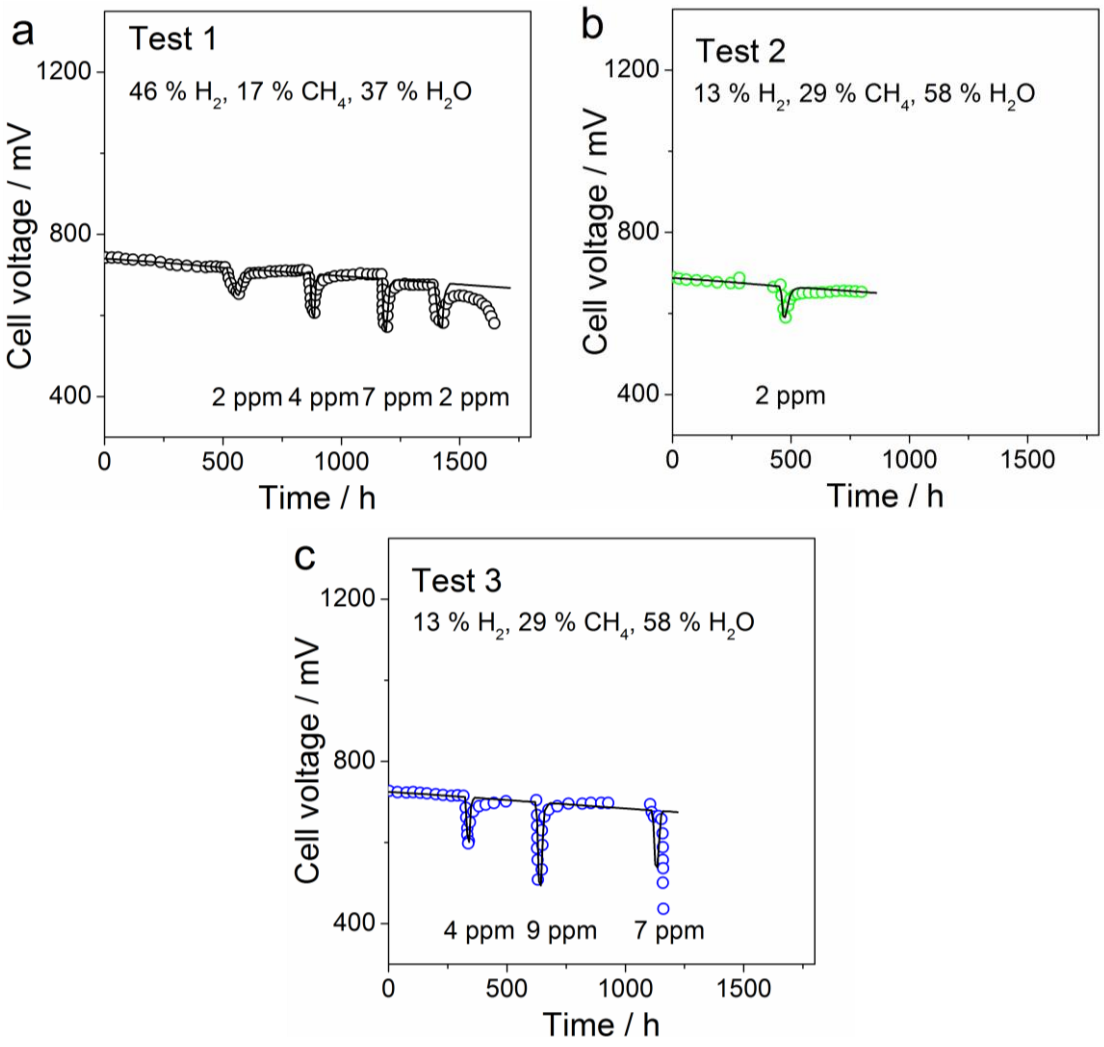


Figure 4.14: Comparison of the cell voltage development at different $H_2S$ concentrations and inlet gas mixture (test 1, 2, 3) between model (solid line) and experimental measurements (open symbols) at $T$ = 750 °C.

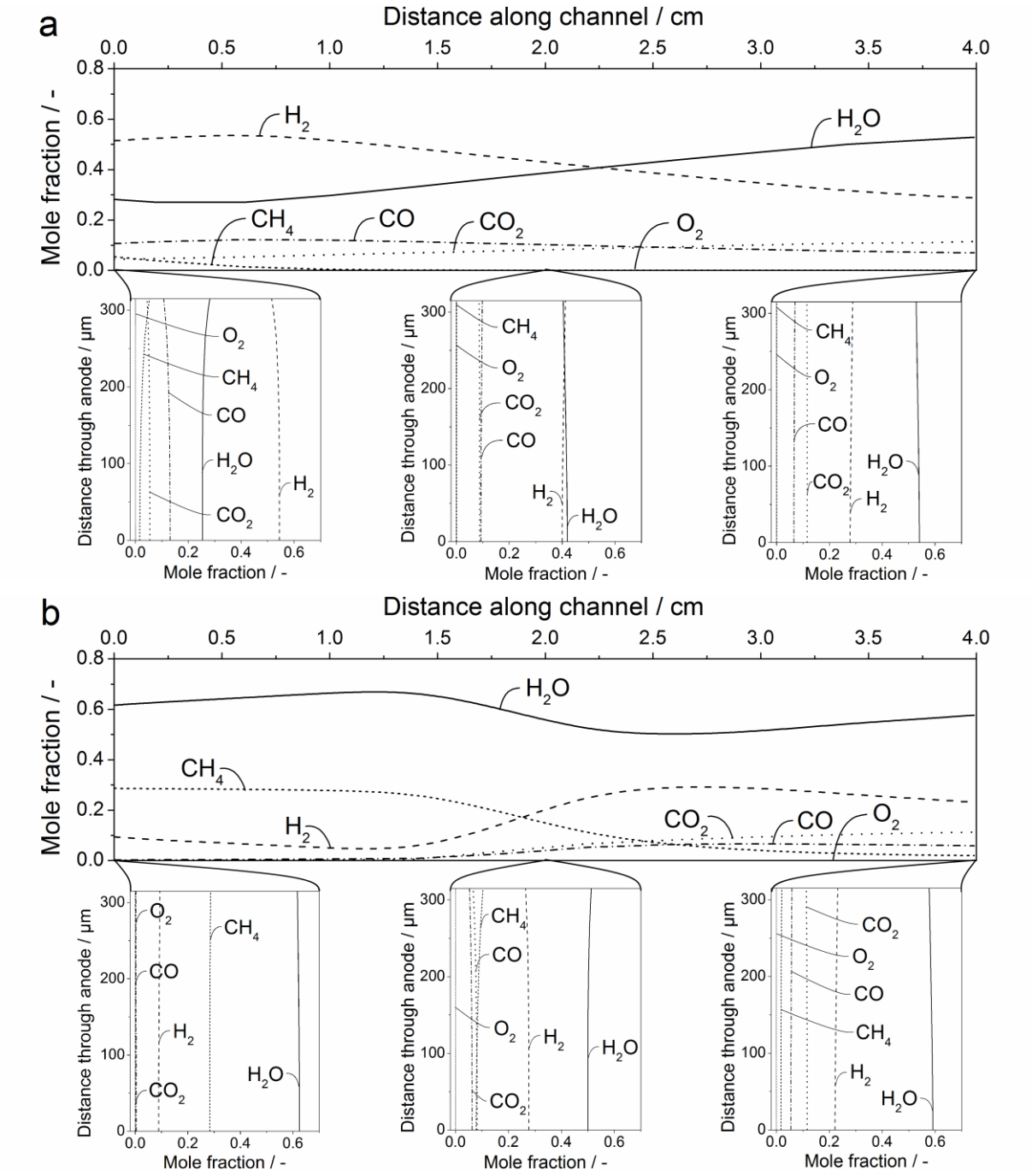


Figure 4.15: Spatial distribution of gas phase species along the channel (horizontal panel) and inside the porous anode for three different positions along the channel (vertical panel), at the time of 150 h (a – no $H_2S$), 460 h (b – 2 ppm). The corresponding voltage stability test is shown in Figure 4.14b.

A further analysis of the results presented in Figure 4.14b is shown in Figure 4.15. Similarly to the results in Figure 4.12, the gas species distribution is plotted for the channel and the porous anode. Figure 4.15a shows results for the system without the presence of $H_2S$ in the gas

phase, and Figure 4.15b illustrates the sulfur poisoning effect for an $H_2S$ gas phase concentration of 2 ppm. Figure 4.15a shows that as methane enters the channel, it is rapidly reformed to $H_2$ and CO. Two local maxima can be observed in the $H_2$ and CO mole fractions at approximately 0.5 cm after the channel inlet. These maxima can be attributed to a faster consumption of $CH_4$ via the reforming chemistry than $H_2$ consumption via electrochemical oxidation. As soon as methane is fully converted, the partial pressure of hydrogen starts to decrease due to its electrochemical oxidation. The accompanying accumulation of steam in the anode also leads to a promotion of the WGS reaction. Thus, the evolution of the concentrations of CO and $H_2$ display the same trends. In literature it was shown that even though it is possible to achieve stable SOFC performance with $CO/CO_2$ mixtures,[46,181] in reformate-fueled ASC only hydrogen is oxidized due to the rapid kinetics of the water gas shift reaction on Ni.[182] Hence, the evolution of the gas phase concentrations of CO and $CO_2$ is probably related to the reforming reactions. Along the whole length of the channel, as a result of the generally increased water content and thus, shifted WGS equilibrium, the mole fraction of $CO_2$ is higher and the mole fraction of CO is lower than at OCV.

Analogous to Figure 4.12, exposure of the anode to $H_2S$ shifts the main reaction zone of methane reforming towards the middle of the channel. As hydrogen is still electrochemically oxidized at the channel inlet, its mole fraction reaches a minimum at around one third of the channel length. The existence of this minimum clearly demonstrates the increased sensitivity of methane steam reforming towards sulfur poisoning in comparison to the electrochemical hydrogen oxidation reactions. It can be concluded that a further increase in $H_2S$ concentration would eventually lead to a nearly complete lack of hydrogen in some parts of the anode and thus, a corresponding oxidation of the Ni particles.

Once the reforming reactions are initiated, the hydrogen mole fraction increases and reaches a maximum at full methane conversion. As a consequence of the large water content in the system and the resulting promotion of the WGS reaction, the $CO_2$ mole fraction at the channel end is greater under polarization than at OCV conditions.

The formation of NiO is possible for the conditions observed in Figure 4.14c. As mentioned above, the exposure of the system to 7 ppm $H_2S$ (Test 3) leads to the failure of the cell, presumably due to Ni oxidation. Indeed at the time point of about 1150 h, when a significant voltage drop is observed, the local $pH_2/pH_2O$ ratio is very small (0.005) and fuel utilization reaches ~95 %. This is a strong indication that Ni could be oxidized in these conditions leading to a breakdown of the cell.

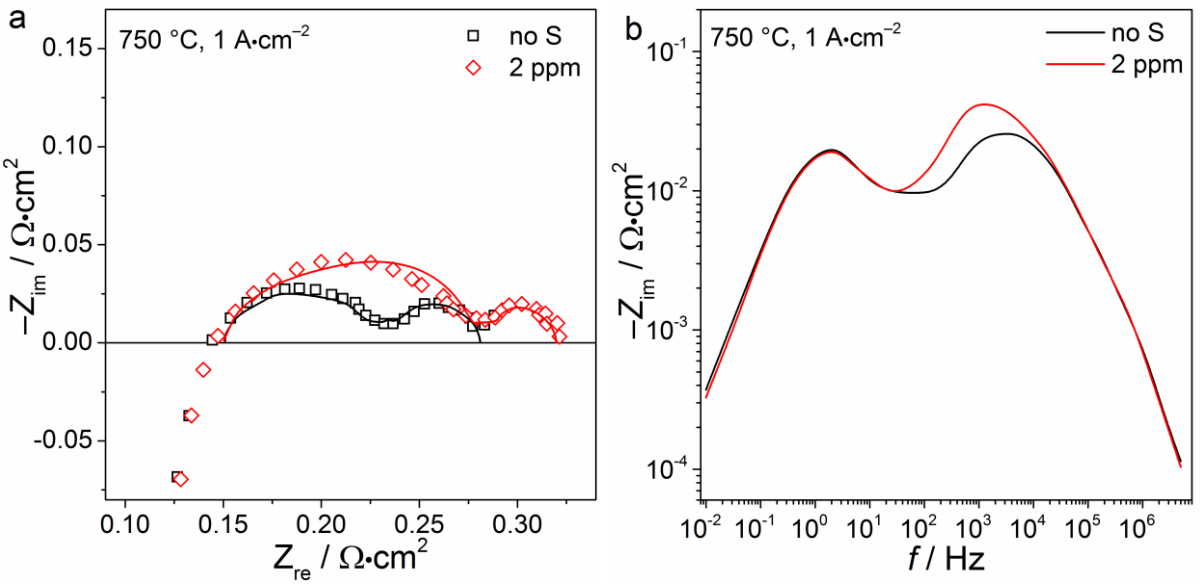


Figure 4.16: (a) Nyquist and (b) imaginary impedance plots of impedance spectra at a temperature of 750 °C before and after cell exposure to 2 ppm $H_2S$ at 1 A·cm$^{-2}$. Nyquist plots are depicted for experiments (open symbols) and simulations (solid lines). As there is no experimental data given for the Bode plots, only simulation results are shown. The black lines in the plots represent the non-sulfur system, the blue lines exhibit the impedance after $H_2S$ exposure.

In order to demonstrate the physical accuracy of the model and its parameters, impedance spectra were reproduced before and after exposure of the Ni/YSZ anode to $H_2S$. The corresponding Nyquist plot in Figure 4.16 shows the comparison between the experimental and simulated impedance responses. The experimental impedance spectra for the poisoned cell were measured for test 2 as shown in Figure 4.14 with an $H_2S$ concentration of 2 ppm after cell voltage stabilization. Simulations and experiments show very good agreement both before and after cell poisoning. Under $H_2S$ exposure a significant increase of cell resistance is observed accompanied by an increase of the high frequency arc. The sulfur poisoning effect is further demonstrated by the corresponding imaginary impedance plots in Figure 4.16b that, under sulfur exposure, exhibit an increase of the imaginary part of the impedance mainly in the frequency range between $10^2$ and $10^3$ Hz, consistent with the earlier shown behavior in $H_2/H_2O$ fuels and literature.[99,103]

To shed light on the mechanistic understanding of the surface processes leading to sulfur poisoning of SOFC operated with methane, the sulfur surface coverage on Ni depending on the cell current density is shown in Figure 4.17. The surface coverage values were obtained after the completion of the cell voltage drop as depicted in Figure 4.14b for steady-state conditions.

Analogous to the evolution in $H_2/H_2O$ fuels (Figure 4.5), sulfur surface coverage increases with current density. At high current densities, sulfur coverage is already close to saturation (0.5 ML) for 2 ppm demonstrating the high sensitivity of methane-fueled Ni/YSZ anodes towards sulfur poisoning. This is a similar behavior as observed in $H_2/H_2O$ fuels as described earlier and related to the enhanced electrochemical hydrogen oxidation rates at high current densities and the associated hydrogen removal from the surface and gas phase. In contrast to multiple experimental sources suggesting a decrease of sulfur coverage with current density the present work shows the opposite behavior while successfully reproducing experimental data over a wide range of operating conditions.

In both $H_2/H_2O$ and $CH_4/H_2O/H_2$ fuels, good agreement between experiments and simulation was achieved without the inclusion of an electrochemical sulfur oxidation reaction, hence, the macroscopic impact of this hypothetical process can be put into question. As shown in Figure 4.15b the increasing rate of hydrogen oxidation decreases the hydrogen partial pressure in the gas phase which lowers the driving force of sulfur removal as equilibrium in Eq. 38 is shifted to the side of gaseous hydrogen and adsorbed sulfur. In this regard, the reduced partial pressure of hydrogen in the gas phase has two convoluted effects: first, the increase of sulfur coverage as a result of a shifted equilibrium in the above reaction and second, the decrease of the local electromotive force between anode and cathode which appears due to the altered gas phase composition in the anode.

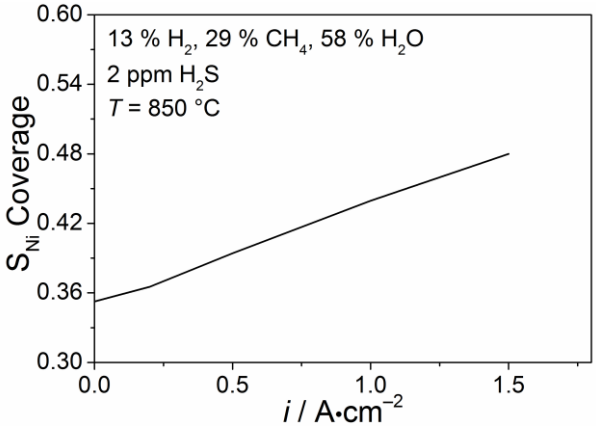


Figure 4.17: The change of sulfur coverage with cell current density for an $H_2S$ gas phase concentration of 2 ppm.

### *4.4 Conclusions*

In this chapter, an elementary kinetic model of sulfur poisoning of Ni/YSZ anodes was presented. A detailed multi-step reaction mechanism of sulfur formation and oxidation was developed for SOFC operation with trace amounts of hydrogen sulfide. The derived chemical model was validated against literature-based sulfur chemisorption isobars, and was used subsequently to analyze performance drops of anode- and electrolyte-supported SOFC in both $H_2/H_2O$ and methane-containing fuel systems. Throughout the present work, an elementary kinetic approach was used which allows for a mechanistic interpretation of the experimentally observed poisoning behavior. The underlying set of thermodynamic data for the relevant species and kinetic parameters for corresponding heterogeneous reactions was compiled from various literature sources.

Using literature experimental data including characteristic voltage drops under transient conditions and impedance spectra, sulfur-induced degradation was described under different operating conditions. Comparisons of model predictions with experiments showed that the developed model enables an accurate representation of the poisoning processes capturing their effect on methane conversion and selectivity.

In contrast to the widely spread assumption that an increasing current density leads to electrochemical oxidation of sulfur and thus, reduced sulfur surface coverage, it was shown that the coverage is actually increasing, despite decreasing anode resistance. The results of the simulations qualitatively confirm the hypothesis that decreasing anode resistance with current density is the consequence of enhanced fuel oxidation kinetics at increased water contents and, thus, cannot be explained by the sulfur coverage.

Furthermore, it was shown that atomically adsorbed sulfur significantly affects heterogeneous reforming chemistry, suppressing hydrogen and carbon monoxide production and causing a significant degradation of the cell voltage already at the open circuit voltage. The blockage of the reforming reaction is particularly pronounced at the fuel gas inlet and advances along the channel with increasing hydrogen sulfide concentration and current density. At constant current densities, the poisoning behavior of Ni/YSZ anode operated on methane-containing fuels is illustrated by a non-linear cell voltage decrease. Spatially resolved analyses of the gas phase distributions have shown the hazard of local fuel starvation already at low $H_2S$ concentrations potentially causing cell failure. Under polarization, the high susceptibility of Ni/YSZ anodes to sulfur poisoning in methane-containing fuels was explained by a restricted supply of fuel gases.

Although the developed mechanism was able to qualitatively and quantitatively reproduce a large set of experimental data both of chemical and electrochemical nature from different experimental literature sources under different operating conditions, it remains unclear how close the mechanism is to being the 'true' mechanism of sulfur poisoning of Ni/YSZ anodes. The physically meaningful elementary kinetic approach provides a large amount of mechanistic information, however, it naturally also requires a large amount of input data. Due to a lack of knowledge about microstructure, thermodynamics and kinetics, assumptions have to be taken and properties estimated, whose refinement could further improve the developed model.
In summary, the present chapter shows that due to the importance of the nickel phase in the fuel oxidation mechanism in Ni/YSZ, large performance drops upon sulfur exposure are inevitable due to high sulfur coverage on Ni, even at operation with high current densities. Although increased operating temperatures might alleviate this performance drop to a certain extent, increasing operating temperatures promote other degradation phenomena such as nickel agglomeration, and thus, are not a viable option to increase SOFC lifetimes. Another option to diminish the effect of sulfur poisoning on SOFC performance, is the use of more sulfur tolerant anodes. The viability of an alternative anode material is further explored in the subsequent chapters with the use of a Ni/CGO anode.

# 5 Evaluation of the effect of sulfur on Ni/CGO anodes in $H_2$/ $H_2O$ fuel gases

It was shown in the previous chapter that Ni/YSZ anodes are prone to large performance drops upon sulfur exposure, which promotes the academic and industrial interest in the exploration of alternative anode materials. While metal-free perovskites have been shown to display no performance drops at all upon sulfur exposure,[26] Ni/CGO anodes still exhibit performance drops upon sulfur exposure. However, under sulfur-free conditions they show high performance comparable to Ni/YSZ (or even better) and under sulfur exposure significantly lower performance drops in $H_2$/$H_2O$ fuels.[82,85,89–94,183] As only few studies have targeted the sulfur poisoning behavior of Ni/CGO anodes so far, the details of the underlying fuel oxidation mechanism remain unclear.

To shed more light on the sulfur poisoning process of Ni/CGO anodes, this chapter presents a detailed investigation of short-term sulfur poisoning behavior in $H_2$/$H_2O$ fuel gases. However, before the investigation of the poisoning phenomena, a fundamental understanding of the fuel oxidation mechanism on Ni/CGO-based anodes is necessary.

For this reason, this chapter first presents extensive electrochemical measurements of Ni/CGO-based cells (described in detail in chapter 3) in sulfur-free fuels. This includes symmetrical and full cell measurements of the most commonly used Ni/CGO10 anode (cell A) and full cell measurements of a Ni/CGO40 anode-based cell (cell B). These measurements will provide the basis for sulfur poisoning experiments with these cells, where the impact of hydrogen sulfide on Ni/CGO10 and Ni/CGO40-based anodes is investigated systematically with a variation of the temperature, current density, and $H_2S$ concentration. In order to give a more complete picture, selected electrochemical measurements are also shown for cell C (Ni/CGO10 anode) and cell E (Ni/YSZ anode), although these cells were characterized in less detail. Subsequently, the impact of sulfur poisoning is evaluated by taking into account findings published recently to give an insight into the corresponding fuel oxidation mechanism.

Most of the results presented in this chapter were already previously published.[184,185]

## *5.1 Identification of physico-chemical processes in non-sulfur systems*

### *5.1.1 Testing procedure*

In this chapter, symmetrical cell measurements are presented that were carried out in the symmetrical cell setup depicted in Figure 3.4. Hydrogen partial pressure, water partial pressure and temperature were varied independently of each other. The cell was tested in a temperature range between 550 – 975 °C at steps of 25 K and at $pH_2$ = 0.8 atm and $pH_2O$ =

0.2 atm. Hydrogen partial pressures were varied between 0.04 – 0.80 atm at constant $pH_2O$ = 0.2 atm and at 550 °C and the water partial pressured was varied between 0.04 – 0.6 atm at constant $pH_2$ = 0.4 atm and at 550 °C. The rest of the fuel gas consisted of nitrogen. Total gas flow rates were kept constant at 1 $L \cdot min^{-1}$.

Furthermore, full cell measurements with cell A (Ni/CGO10 anode; same anode as the symmetrical cell) and cell B (Ni/CGO40-based anode) were performed, which were operated with various $H_2/H_2O$ fuel mixtures. Initial cell characterization was performed by measuring *i-V* curves and by recording EIS at different temperatures and with a series of different gas compositions fed to the anode and cathode, respectively. The *i-V* curves and impedance spectra were measured between 650 °C and 950 °C (800 – 950 °C for cell B) at steps of 50 K and $pH_2/pH_2O$ (97:3) mixtures. Furthermore, impedance spectra were recorded at different $pH_2O$ between 0.03 and 0.5 atm. Subsequently, the sulfur poisoning experiments presented in the following subsection were carried out.

### *5.1.2 Symmetrical cell characterization of Ni/CGO10*

Process identification in EIS measurements of full cells is often hindered by a convolution of cathode, anode and mass transport contributions with similar relaxation frequencies. Therefore, to get a better understanding of electrode spectra, symmetrical cells are investigated. Small electrode areas, thin anodes and large gas flow rates are then used to minimize mass transport contributions, that is, gas diffusion and gas conversion resistances. Furthermore, symmetrical cell measurements can be used to derive the input parameters of the electrode exchange current density $i_0$. For anode operation with $H_2/H_2O$ fuels these parameters are the exponents *a, b* and the activation energy barrier $E_{act}$ (see Eq. 12), which can be determined by independently varying the parameters *T*, $pH_2$ and $pH_2O$. Electrode process contributions on Ni/CGO are calculated by means of a CNLS fit of an ECM to experimental data. The ECM is devised based on the calculated DRT. The corresponding experiments are shown in the following.

*Temperature dependence* — Figure 5.1 shows a typical EIS measurement at a temperature of 550 °C. The spectra show two distinguished arcs, one at ~0.5 Hz and one at ~10 Hz. Furthermore, the beginning of another arc is indicated at frequencies higher than $10^4$ Hz. This high frequency arc corresponds to the resistance within the electrolyte and thus, the interception with the y-axis at ~11.5 $\Omega \cdot cm^2$ represents the value of the Ohmic resistance. As polycrys-

talline electrolytes are employed, in the high frequency range, contributions of the YSZ grain bulk and YSZ grain boundaries appear at low temperatures such as 550 °C.[186] However, in the measured frequency range they cannot be fully resolved. These contributions become decreasingly visible at higher, more realistic temperatures, which is why they are typically not reported in literature. The two identified electrode contributions are represented by two nearly ideal semicircles and seem not to be coupled. For Ni/YSZ anodes, a transmission line model is sometimes employed to obtain a more physically meaningful description of the anode processes. However, in the present case, since the two processes are not coupled a transmission line model cannot be applied without further investigation of the electrode system.

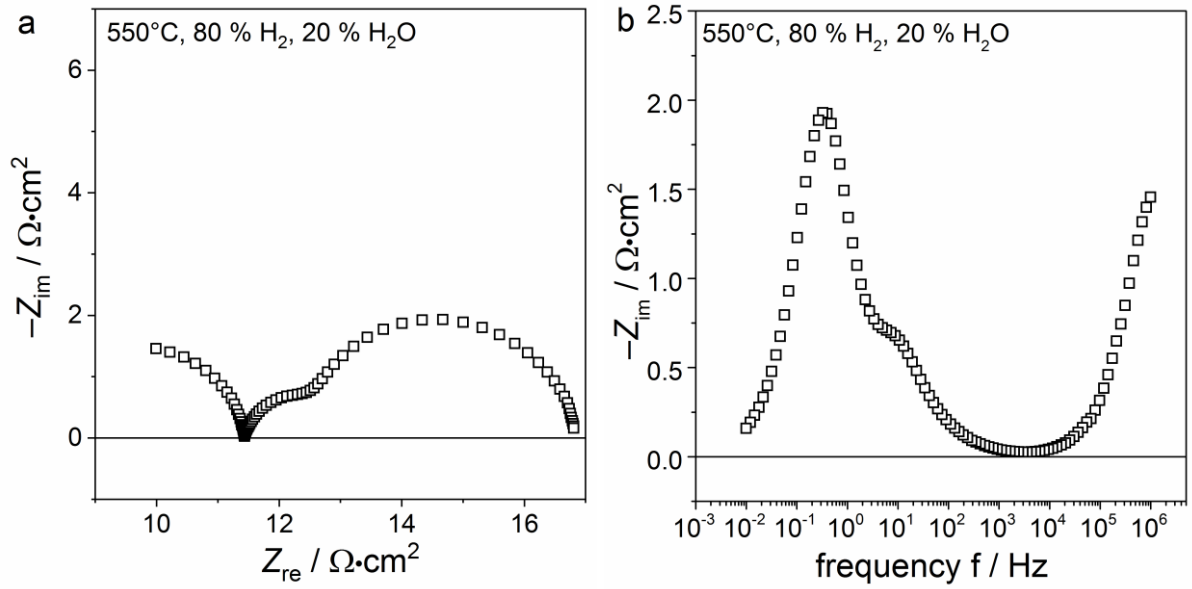


Figure 5.1. (a) Nyquist plot and (b) imaginary impedance plots at 550 °C. The gas phase composition was at $pH_2$ = 0.8 atm and $pH_2O$ = 0.2 atm.

Figure 5.2 shows the DRT calculated for the EIS measurements of the symmetrical cells at 0.8 atm $H_2$ and 0.2 atm $H_2O$ and between 575 – 725 °C. The discussion of DRT has been shown to reveal significantly more insight into the cell behavior than raw impedance data as demonstrated in numerous previous publications.[100,110,143,151] The calculated DRT show two main contributions, one at low frequencies (LF) around 1 Hz and another at middle frequencies (MF) around $10^2$ Hz, which is consistent with previous studies on Ni/CGO10 anodes.[187,188] No high frequency contribution >$10^3$ Hz is visible as it is generally observed for Ni/YSZ anodes (see Figure 4.16).[143,151] Both of the contributions are thermally activated and show a shift to lower frequencies with decreasing temperature, and thus, are related to

physico-chemical electrode processes. As a result, a simple ECM was applied that includes one inductance element, one resistance element (describing the ohmic resistance) and two RQ elements (describing the two electrode processes). Furthermore, at lower temperatures another middle frequency contribution is visible at $10^2$ – $10^3$ Hz. However, it is very small and the two middle frequency elements were therefore modeled with one RQ element during the CNLS fitting process.

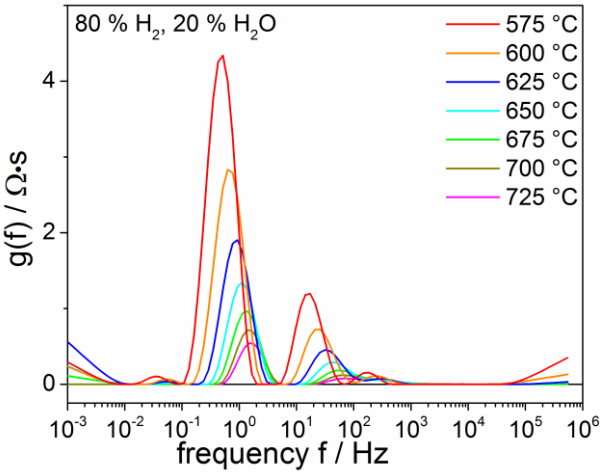


Figure 5.2. DRT for changing operating temperatures between 575 – 725 °C. Measurements at higher temperatures were omitted here to increase visibility of the remaining plots. The gas phase composition was kept constant at $p\mathrm{H_2}$ = 0.8 atm and $p\mathrm{H_2O}$ = 0.2 atm.

The obtained resistance values of the two processes as a function of temperature are depicted in Figure 5.3. Activation energy barriers for the processes can be extracted by fitting the data to the Arrhenius-type Eq. 41:

$$R_p(T) = B \exp(\frac{E_{act}}{\mathrm{R}T}), \tag{41}$$

where $R_p$ is the process resistance, $B$ the pre-exponential factor and $E_{act}$ the process activation energy barrier. The fit of the middle frequency process shows a high quality ($R^2$ >0.999) and yields an activation energy barrier of 1.04 eV. The fit for the low frequency process, however, shows a deviation for high temperatures, where the measured values suggest a change of slope of the fitted curve (Figure 5.3a). As the process was shown to be thermally activated, it is likely that at temperatures higher than 775 °C, mass transport processes start to significantly contribute to the low frequency resistance and thus, hinders the accurate determination of the low frequency anode resistance. Gas conversion was shown not to contribute to the impedance in the employed setup due to large gas flow rates and small cell size.[143] Even though the anode thickness is thin (< 30 µm) the likely present low frequency mass transport re-

sistance indicates that gas diffusion cannot be fully neglected. This could also include axial gas diffusion above the porous electrode and diffusion through the contacting mesh. Above 775 °C, the activation energy barrier is identified to be 0.61 eV, below 775 °C it is 1.14 eV.

To obtain a more accurate value, it is assumed that at the highest temperature of 975 °C, the low frequency process resistance (0.058 $\Omega \cdot cm^2$) is dominated by the gas diffusion, as, in contrast to the electrode process, it is not thermally activated.[39,189] Therefore a value of 0.05 $\Omega \cdot cm^2$ is subtracted from all resistance values which leads to the graph in Figure 5.3b. The corresponding fit shows a good agreement over the whole temperature range with an activation energy barrier of 1.18 eV.

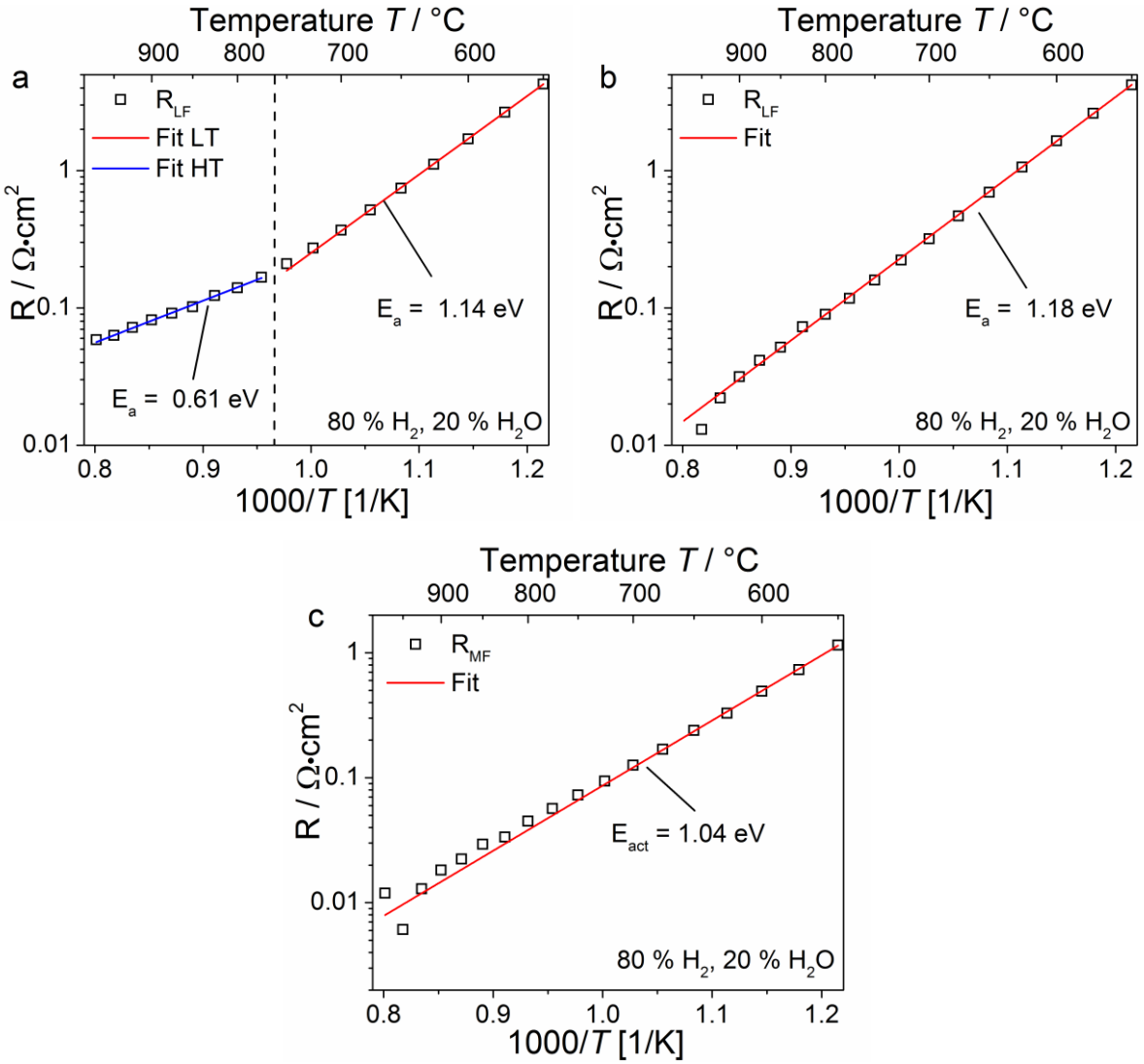


Figure 5.3. Resistance of the (a) low frequency, (b) the low frequency with a subtracted 0.05 $\Omega \cdot cm^2$to account for the gas diffusion and (c) the middle frequency anode process as a function of temperature *T*. All fits achieved values with $R^2 > 0.999$.

Figure 5.4a displays the capacitance values associated with the low frequency process. The values of about ~1 F·cm$^{-2}$ are significantly larger than the ones generally obtained for Ni/YSZ (~10$^{-4}$ F·cm$^{-2}$),[34,163] which clearly illustrates the different nature of the capacitance in Ni/CGO. The origin is likely a large chemical capacitance, which is associated with a changing $Ce^{3+}/Ce^{4+}$ (due to variation in the nonstoichiometric oxygen content between $Ce_2O_3$ and $CeO_2$) ratio in the CGO.[36,129,190] Although a convolution of the low frequency electrode process and the gas diffusion exists in the present study, at low temperatures the cell behavior is dominated by the electrode process. The calculated capacitance values increase with temperature. The curve exhibits plateaus at high and low temperatures. Thus, the possible values of this ratio determine the boundaries of the chemical capacitance values and stretch over a whole order of magnitude (0.1 – 1 F·cm$^{-2}$).

The capacitance of the middle frequency process also shows a similar dependence on the temperature with increasing values (0.02 – 0.04 F·cm$^{-2}$) at higher temperatures, however the change of capacitance is less pronounced.

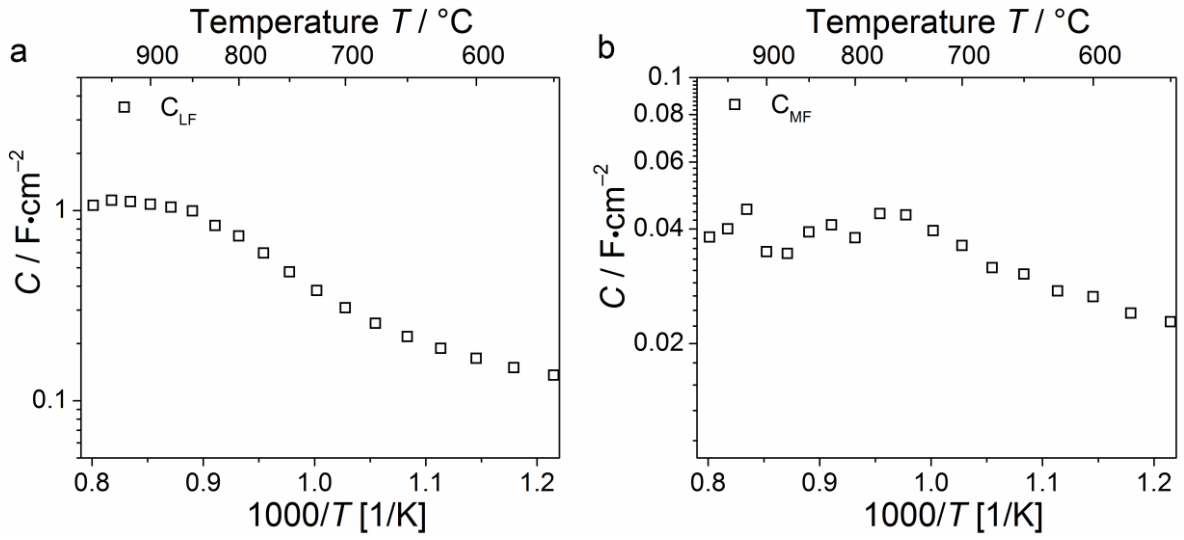


Figure 5.4. Capacitance of (a) the low frequency anode process and (b) the middle frequency anode process as a function of temperature.

*$pH_2O$ dependence* — In order to investigate the dependence of the anode process on the partial pressure of water, the water content was varied between 0.04 and 0.6 atm at a constant hydrogen partial pressure of 0.4 atm and at 550 °C. This comparatively low temperature was chosen to minimize the influence of the gas diffusion and gas conversion process on the low frequency contribution.[39,189] Based on the gas diffusion resistance estimated based on Figure

5.3, it will account for ~1.1 % (0.05 Ω·cm$^2$/4.25 Ω·cm$^2$) of the resistance of the low frequency process. Figure 5.5a shows the calculated DRT and reveals a significant dependence of the low frequency process on the water content, while the middle frequency contribution was only marginally affected. This is consistent with previous studies.[184,187,188] The clear reduction of the low frequency anode process resistance with increasing water content suggests an enhancing effect of water on the kinetics of the low frequency process, similar to the influence of $H_2O$ on the anode charge transfer process on Ni/YSZ.[34,151,163] This confirms that its origin is an anode surface process, probably the anode charge transfer process, as was already suggested in earlier publications.[129,132,138,188,191,192]

The small $pH_2O$ dependence of the middle frequency process points towards a bulk process as its origin. Specifically, oxide ion transport from bulk to surface or across the electrolyte/anode interface has been suggested before.[187,193] A dependence of the ionic conductivity on $pH_2O$ due to a change in oxygen vacancy concentration can explain the small dependence of this process on water.[194]

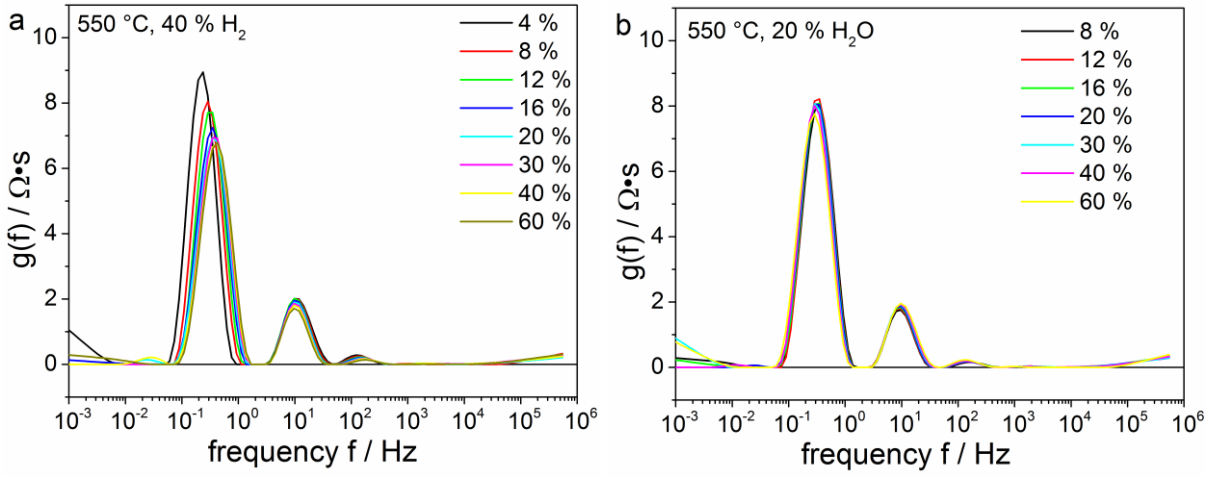


Figure 5.5. Dependence of the DRT on changing (a) water partial pressure (constant $pH_2$ = 0.4 atm) and (b) hydrogen partial pressure (constant $pH_2$ = 0.2 atm). The temperature was kept constant at $T$ = 550 °C.

For small overpotentials, the anode exchange current density can be calculated according to Eq. 13. By combining this equation with Eq. 15, a relation between the partial pressures $pH_2$ and $pH_2O$ including the parameters $a$ and $b$, and the electrode resistances is obtained. Thus, the resistance of the anode process is plotted over the respective partial pressures on a double-logarithmic scale, and the negative slope of the diagrams represent the parameters $a$ and $b$. In

Figure 5.6a, the resistance of the low frequency process is plotted over $pH_2O$. The slope of the fit to the low frequency resistance in the double-logarithmic plane leads to the identification of $b$ = 0.08. This is significantly smaller than the one calculated for the charge transfer process on Ni/YSZ ($b$ = 0.33). The poor quality of the fit ($R^2$ = 0.67) could possibly be related to the cell design, since based on the operating conditions, the electrochemically active zone can extend from the anode functional layer into the anode contact layer.[150] In addition, hydrogen oxidation could also occur in the not fully dense CGO adhesion layer. Thus, the interplay between the ionic conductivity in the matrix, the electrochemical hydrogen oxidation reaction and the gas diffusion can vary considerably. To determine more accurate power law exponents, an anode with a more homogeneous microstructure and a more sophisticated ECM are probably necessary. However, it is also possible that the convolution of different processes hinders the accurate determination of the exponents of the applied power law.

The capacitance values of the low frequency process obtained by the CNLS fit show a dependence on the water partial pressure as well (Figure 5.6b) with a decreasing value for increasing $pH_2O$. The relationship at this temperature can be described with a power law as well according to $C_{LF} \sim pH_2O^{-0.16}$.

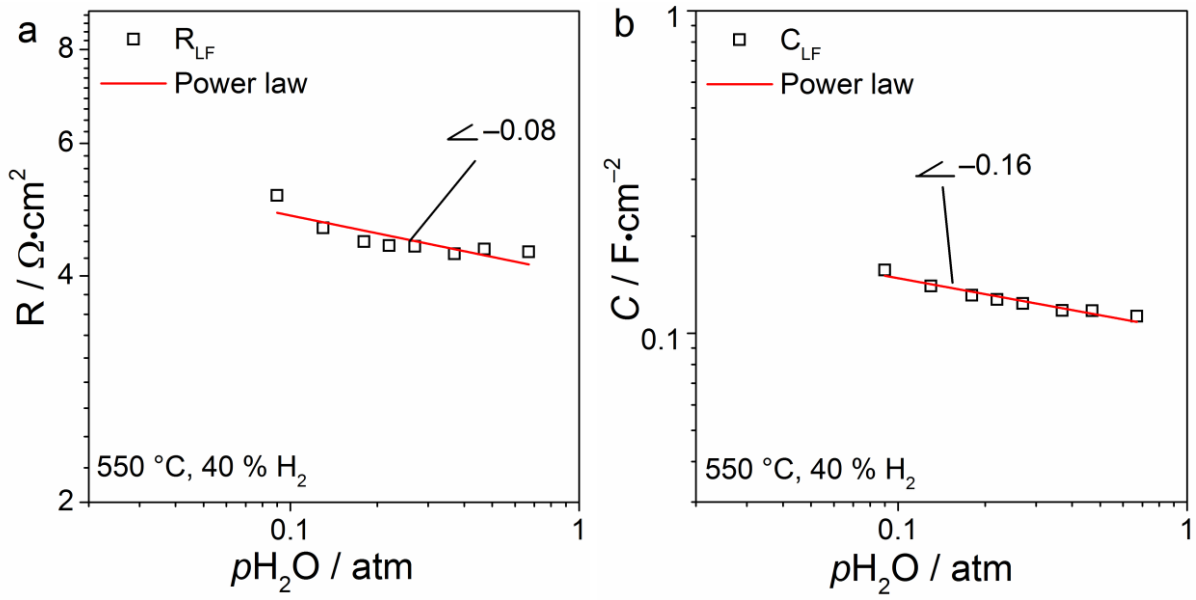


Figure 5.6. (a) Resistance and (b) capacitance of the low frequency anode process as a function of $pH_2O$. The linear fits achieve (a) $R^2$ = 0.67 and (b) $R^2$ = 0.92.

*$pH_2$ dependence* — Eventually, to investigate the dependence of the anode process on the hydrogen partial pressure, $pH_2$ was varied between 0.08 and 0.6 atm at a constant water content of 0.2 atm and at 550 °C. The DRT corresponding to the recorded impedance spectra are depicted in Figure 5.5b. Again, the middle frequency contribution shows no dependence on the gas phase composition. Moreover, the low frequency peak also only shows a very small change upon hydrogen variation.

The resistance and capacitance values of the process are depicted in Figure 5.7. Based on the fit in the double-logarithmic plot in Figure 7a, an $a$ value of 0.01 could be derived. Although the fit quality is poor ($R^2$ = 0.47), Figure 5.7 shows the nearly negligible influence of $pH_2$ on the charge transfer resistance. As the rate-determining step is probably the charge transfer reaction,[138] this means that independently of the hydrogen inlet content, hydrogen is always readily available on the surface as a reactant. Thus, hydrogen adsorption and dissociation are fast and probably do not strongly influence the hydrogen oxidation rate.

Furthermore, Figure 5.7b shows that the capacitance of the low frequency anode process is also dependent on $pH_2$, with $C_{LF} \sim pH_2^{0.11}$. Thus, a dependence of the low frequency process on both temperature and $pO_2$ is confirmed. This can be correlated with previous investigations of CGO10, where the $Ce^{3+}$ concentration in the CGO bulk was shown to change with both temperature and $pO_2$. This confirms the source of the capacitance to be related to the $Ce^{3+}/Ce^{4+}$ ratio.

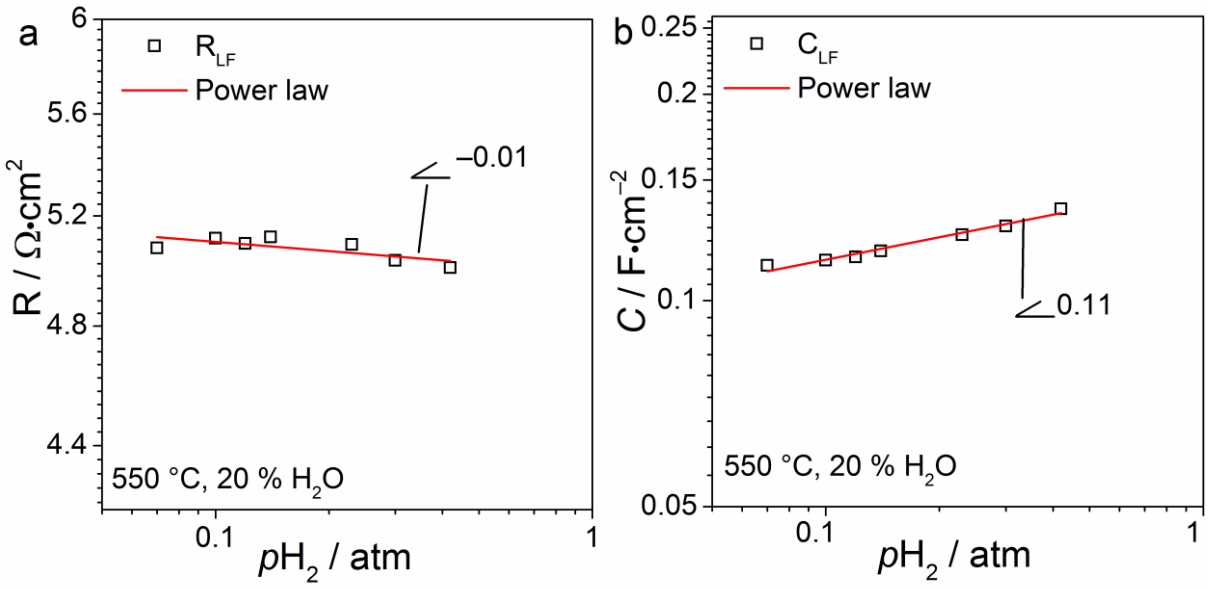


Figure 5.7. (a) Resistance and (b) capacitance of the low frequency anode process as a function of $pH_2$. The linear fits achieve (a) $R^2$ = 0.47 and (b) $R^2$ = 0.97.

### *5.1.3 Full cell characterization of the Ni/CGO10-based cell*

In this subsection, full cell measurements of cell A are presented, that is based on the same Ni/CGO10 anode as the symmetrical cells in the previous subsection. Comprehensive *i-V* curves of cell A in a $H_2/H_2O$ (97:3) mixture at different temperatures between 650 to 950 °C are shown in Figure S1. The Nyquist plot of the impedance spectra measured at different operating temperatures is shown in Figure 5.8a, and the corresponding imaginary impedance plot is shown in Figure 5.8b. Analogously, the Nyquist and imaginary impedance plots of data recorded at different humidity levels at 850 °C are presented in Figure 5.8c and d. Clearly, the Nyquist plots at higher temperatures show two separated arcs. The peak frequency of the middle frequency arc lies at approximately 200 Hz at 850 °C, whereas the low frequency peak is at approximately 0.2 Hz (Figure 5.8b). This is in agreement with the two identified peaks in the symmetrical cell measurements. However, the existence of a cathode and a more pronounced gas conversion process leads to the convolution of the different contributions.

This is demonstrated by the emergence of two distinguished peaks in the middle frequency contribution at decreasing temperature. For example, at 700 °C, one contribution is visible at approximately 35 Hz and the other is at 5 Hz. Both contributions show thermal activation and, thus, can be interpreted as physicochemical electrode processes.

A temperature dependence in the low frequency region is also observed in the data shown in Figure 5.8a and b, which indicates the existence of a thermally activated electrode process in addition to a gas conversion process, which is expected to have only a small temperature dependence.[39,189] The peak frequency of the low frequency contribution shifts to higher frequency values between 750 and 650 °C. This is unusual for thermally activated processes, which usually exhibit a peak shift to lower frequencies caused by an increase in resistance under these conditions. Consequently, the observed behavior must be caused by a significant decrease of capacitance with decreasing temperature, which is consistent with the temperature dependence of the capacitance shown in the last subsection for the symmetrical cell.

At temperatures above 800 °C, the peak frequency and peak intensity stay constant, which indicates a less temperature-dependent behavior of the low frequency arc in this region. This suggests that at higher temperatures, the gas conversion dominates the low frequency arc, whereas at lower temperatures the physicochemical anode process prevails. In the present study, thin anodes (<30 µm) are employed, for which resistances caused by porous transport are generally assumed to be small.[195] However, the previous subsection showed that they are not fully negligible, also possibly caused by increased resistance due to the gas diffusion

through the contacting mesh.

The replacement of the air supply with pure oxygen at 850 °C leads to a reduction of the middle frequency peak mainly in a frequency range of approximately 50 – 100 Hz (Figure S2). This confirms the existence of a cathode surface process in this region, which is also in accordance with previous studies on LSM/YSZ cathodes.[196–198] However, the reduction of the cathode contribution in the impedance spectra still leaves a significant middle peak contribution in the impedance spectra at a frequency of approximately 200 Hz. This confirms the existence of the anode bulk process in this region, which is in agreement with the symmetrical cell measurements in Figure 5.2.

In summary, the two processes identified in the symmetrical cell measurements could also be observed at the same frequencies in the impedance spectra of full cell A.

### *5.1.4 Full cell characterization of the Ni/CGO40-based cell*

The *i-V* curves of the Ni/CGO-based cell B at different temperatures are presented in Figure S3. The Nyquist plot of the impedance spectra measured at different operating temperatures of 700 – 950 °C is shown in Figure 5.9a, and the corresponding imaginary impedance representation is shown in Figure 5.9b. Analogously, Nyquist and imaginary impedance plots for different $pH_2O$ at 850 °C are shown in Figure 5.9c and d. In the Nyquist plots, two clearly separated arcs can be distinguished. The peak frequencies of the middle frequency arc lie between $10^1$ and $10^2$ Hz at common ESC operating temperatures above 800 °C (Figure 5.9b). Notably, there is also a cathode process present at frequencies of approximately 50 Hz (Figure S4). The influence of the changing water partial pressure at $10^1$ – $10^2$ Hz on the imaginary impedance plot presented in Figure 5.9d indicates clearly the existence of an anode surface process.

The intensity of the peak of this anode process is decreased and its characteristic frequency peak is slightly shifted to higher values with increasing $pH_2O$, which reflects the decreasing process resistance caused by the enhanced kinetics. This is the same seemingly counterintuitive behavior, which was also observed for the Ni/CGO10 anode in Figure 5.5a and Figure 5.8d. The existence of an anode surface process at approximately 100 Hz is contrary to the results shown in Figure 5.8d for a Ni/CGO10-based cell, which did not show a significant influence of water in this frequency range. This gives rise to the assumption that the same anode surface process appears in completely different frequency ranges for different cells.

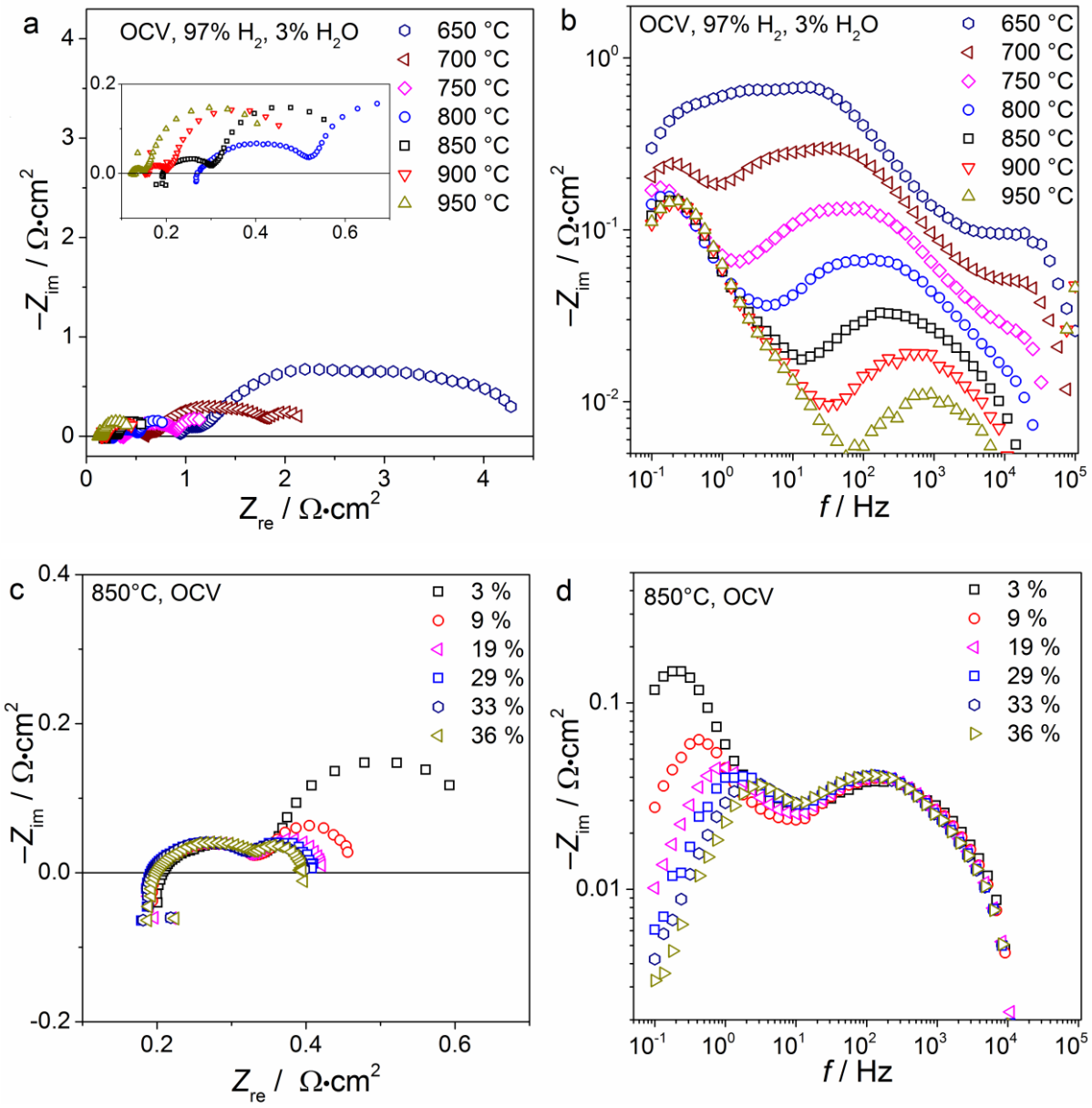


Figure 5.8. (a) Nyquist and (b) imaginary impedance plots of EIS of Ni/CGO10-based SOFC measured at different temperatures $T$ = 650 – 950 °C, OCV, $pO_2$ = 0.21 atm, $pH_2$ = 0.97 atm, $pH_2O$ = 0.03 atm, (c) Nyquist and (d) imaginary impedance plots of EIS measured at $T$ = 850 °C, OCV, $pO_2$ = 0.21 atm, varying $pH_2O$ = 0.03 – 0.36 atm.

In symmetrical cell measurements of Ni/CGO40-based anodes with the same design as in the present study, Iwanschitz et al. observed two anode processes: one middle frequency process at 50 – 100 Hz and one low frequency process at 1 – 2 Hz.[130] Although they admit that gas conversion could contribute to the low frequency process, on the basis of the observation that redox cycling was observed to have an effect on this process and a comparison to other literature sources, they interpreted it as an actual electrode process rather than a gas transport process. In the present study, upon a decrease of temperature in Figure 5.9b, a small effect on the low frequency impedance spectra is visible by a peak shift to higher frequencies at 750 °C. However, the increase of $pH_2O$ in the fuel gas leads to a stepwise decrease of the intensity of the low frequency peak shown in Figure 5.9d, which is the typical behavior of a gas conversion process. At a humidity level of 0.3 atm, the low frequency peak has nearly disappeared. In the present study, the same anode design was used as in the work of Iwanschitz et al., except for the addition of small amounts of Cu in the metallic phase. The observation of anode processes at the same frequency in the impedance spectra is a strong indication that the influence of Cu on the hydrogen oxidation mechanism is indeed negligible. However, the alloying of Ni with Cu has been shown to lower the sulfur adsorption energy for $Ni_{0.5}Cu_{0.5}$.[[199,200] Thus, although the amount of Cu in the present study is small, a minor influence of Cu on the magnitude of the sulfur-poisoning-related resistance increase cannot be excluded.

In summary, two low frequency processes could be identified in the impedance spectra of cell B as well. However, in contrast to that observed for cell A, the middle frequency process is affected by humidity, and therefore, is assigned to a surface process. Additionally, one low frequency process with an unclear origin was observed. No bulk anode process in the middle frequency range was observed, however, because of the possible convolution of processes in this region, its existence cannot be excluded.

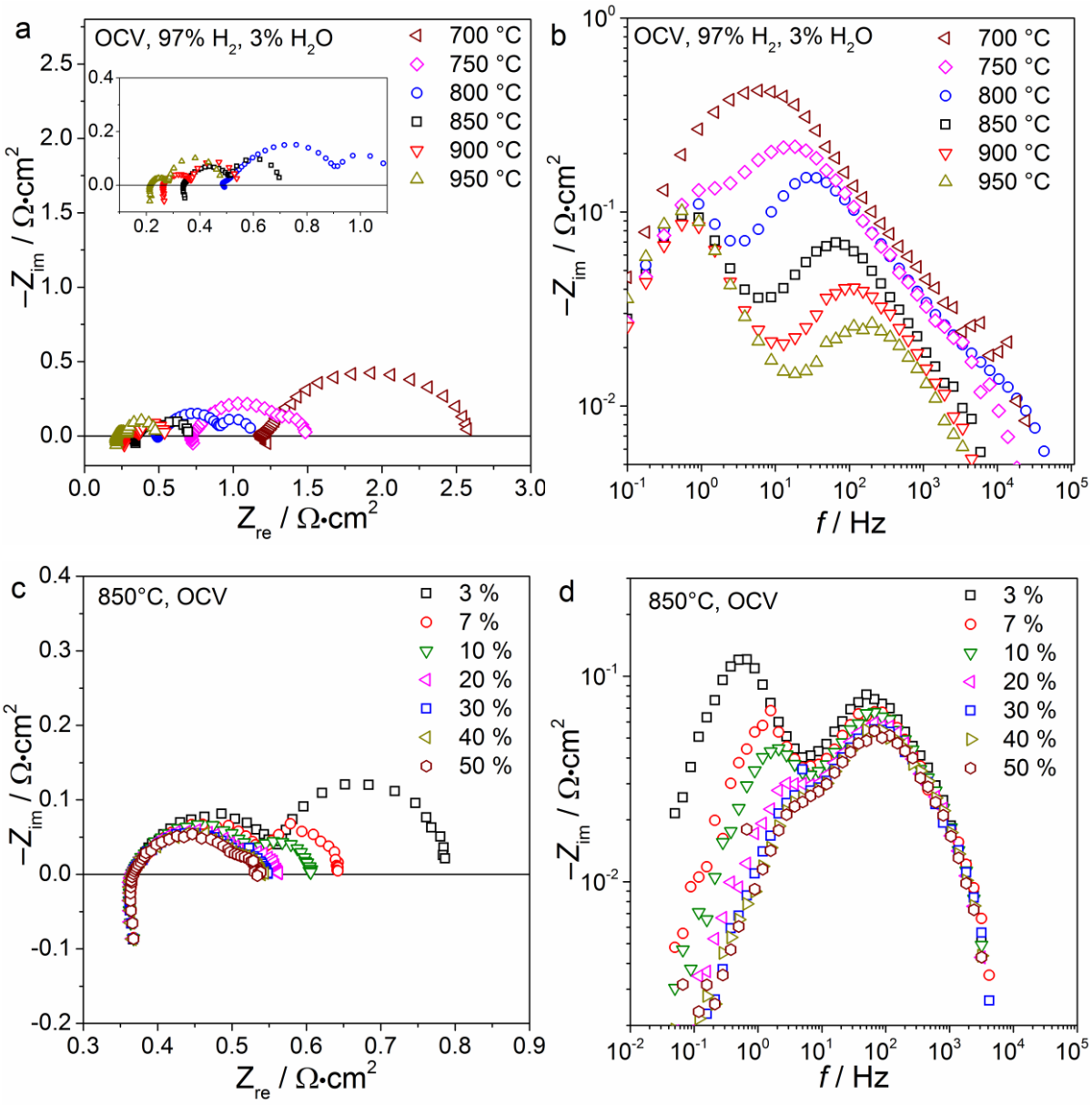


Figure 5.9. (a) Nyquist and (b) imaginary impedance plots of EIS of a Ni/CGO40-based SOFC recorded at different temperatures $T$ = 700 °C – 950 °C, OCV, $pO_2$ = 0.21 atm, $pH_2O$ = 0.03 atm, (c) Nyquist and (d) imaginary impedance plots of EIS of the cell recorded at $T$ = 850 °C, OCV, $pO_2$ = 0.21 atm, varying $pH_2O$ = 0.03 – 0.5 atm.

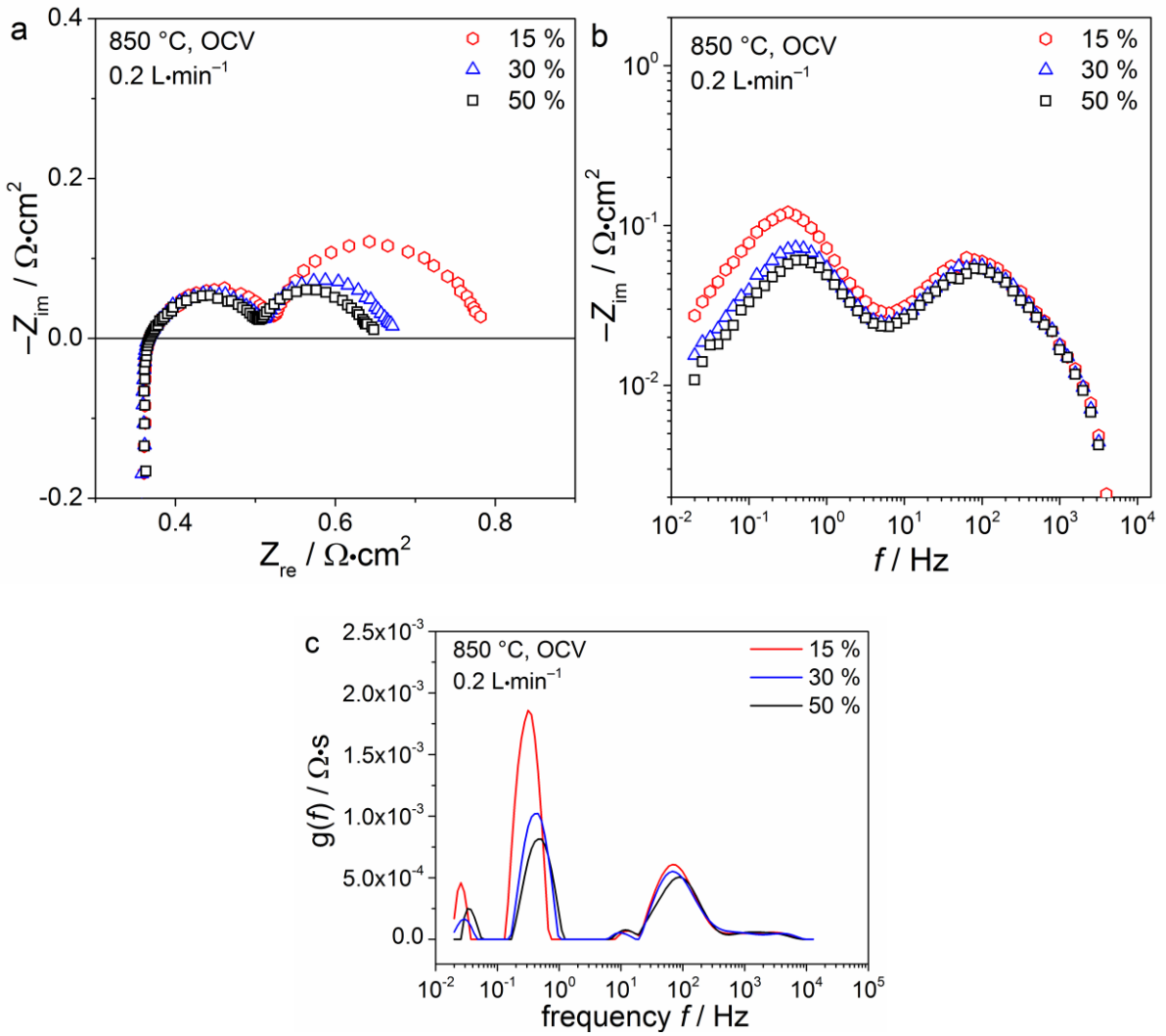


Figure 5.10. (a) Nyquist and (b) imaginary impedance plots of impedance spectra of a Ni/CGO40-based SOFC recorded at $T$ = 850 °C, OCV, $pO_2$ = 0.21 atm, 0.2 L·min$^{-1}$ with varying $pH_2O$ = 0.15 – 0.5 atm. (c) shows the calculated DRT.

## *5.2 Short-time sulfur poisoning of Ni/CGO anodes in $H_2/H_2O$ fuels*

In this section, the systematic investigation of sulfur poisoning of the two different anodes is presented. To facilitate the comparison of the poisoning behavior of each cell under the different operating conditions, all sulfur poisoning experiments were conducted with the same cell, as this approach avoids problems with regard to slightly different performance, tightness, and contacting. As the sulfur poisoning behavior on Ni/CGO anodes is expected to be mainly reversible, this approach should be viable (as shown in the following). To avoid sulfur-related irreversible degradation, after the saturation of the respective performance drop was reached, the poisoning intervals were kept as short as possible.

### *5.2.1 Testing procedure*

After initial characterization of cell A (Ni/CGO10-based) and cell B (Ni/CGO40-based) as shown in the previous section, the temperature was set to 850 °C where sulfur poisoning experiments were conducted for different current densities. The investigated current densities were 0.5 $A \cdot cm^{-2}$, 0.75 $A \cdot cm^{-2}$, 0.25 $A \cdot cm^{-2}$, and OCV, in this order. In addition, subsequently, the operating temperature was varied to 900 °C, 950 °C (only for cell B) and 800 °C where poisoning experiments were performed at 0.5 $A \cdot cm^{-2}$. For cell A, the poisoning experiments for 800 °C and 900 °C were carried out with a different cell of same specifications from the same batch. Also the experiment at 850 °C with 0.5 $A \cdot cm^{-2}$ was repeated with this cell. The poisoning experiments were carried out for a $H_2/H_2O$ ratio of 97/3. For a systematic investigation of the sulfur poisoning behavior the $H_2S$ concentration was increased stepwise and set to 1, 2, 5, 10, and 20 ppm at each operating point until saturation occurred. After saturation of the last performance drop related to 20 ppm $H_2S$, its supply was switched off, the gas flow was substituted with pure $H_2$ and the anode was regenerated until full recovery of the SOFC performance was achieved. In addition, sulfur poisoning experiments with 1 – 20 ppm $H_2S$ at 850 °C and 0.5 $A \cdot cm^{-2}$ were also carried out with cell C and cell D to allow a comparison between the cells.

Furthermore, ESC with pure CGO electrodes were prepared based on a commercial half-cell substrate with the same composition and geometry as cell D. The half-cell did not have a functional and contact layer, however, the CGO10 adhesion layer was still present. First, a screen-printing ink consisting of CGO10 was prepared, which was in a next step screen-printed onto the half-cell. Subsequently, the cell was calcinated at 1150 °C for 3 h in air. The CGO10-based cell was contacted with gold meshes on both cathode and anode side. Sulfur

poisoning experiments were carried out at OCV. The SEM image of a manufactured cell with CGO electrode is depicted in Figure 5.11. The average CGO particle size in the applied electrode is approximately ~200 nm and thus, significantly smaller than the one in the adhesion layer (~500 nm). Thus, the microstructure is fine and should give rise to a good anode performance. The anode functional layer is 20 µm thick, similar as the ones of the commercial cells in Figure 3.3.

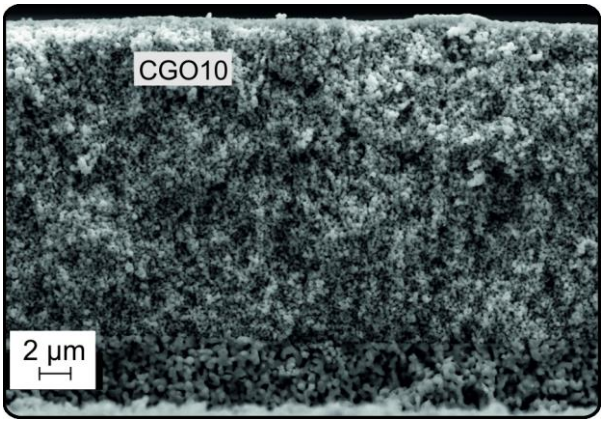


Figure 5.11. Cross-section SEM image of the manufactured CGO electrode. The lower layer (approximately 4 µm thick) shows the CGO adhesion layer already applied by the supplier. The upper layer shows the screen-printed anode layer (approximately 20 µm thick).

### *5.2.2 Sulfur poisoning of Ni/CGO10-based anodes*

The voltage stability tests over time are depicted in Figure 5.12 for temperature variations between 800 and 900 °C at 0.5 $A \cdot cm^{-2}$ and for current density variations at constant $T$ = 850 °C between OCV and 0.75 $A \cdot cm^{-2}$. In all cases, the overall voltage drop is stepwise increasing along with the $H_2S$ concentration. The initial performance drop associated with the exposure of 1 ppm $H_2S$ is the largest, and a further increase of the $H_2S$ concentration only leads to smaller performance losses. For the exposure times investigated in the present study, full recovery was reached within 22 h after the sulfur supply was switched off at all operation points. As the introduction of $H_2S$ did not lead to a voltage drop at OCV, the poisoning characteristics were captured by impedance spectroscopy. The corresponding recorded spectra are illustrated in Figure 5.13. Although sulfur exposure has no influence on the identified bulk processes in the middle frequency region, it leads to an increase in the low frequency arc associated with an influenced frequency range at around 0.1 Hz, which is consistent with the identification of an anode process at this frequency in Figure 5.5 and Figure 5.8. The effect of sulfur on this process further confirms that this process is likely to be a surface process.

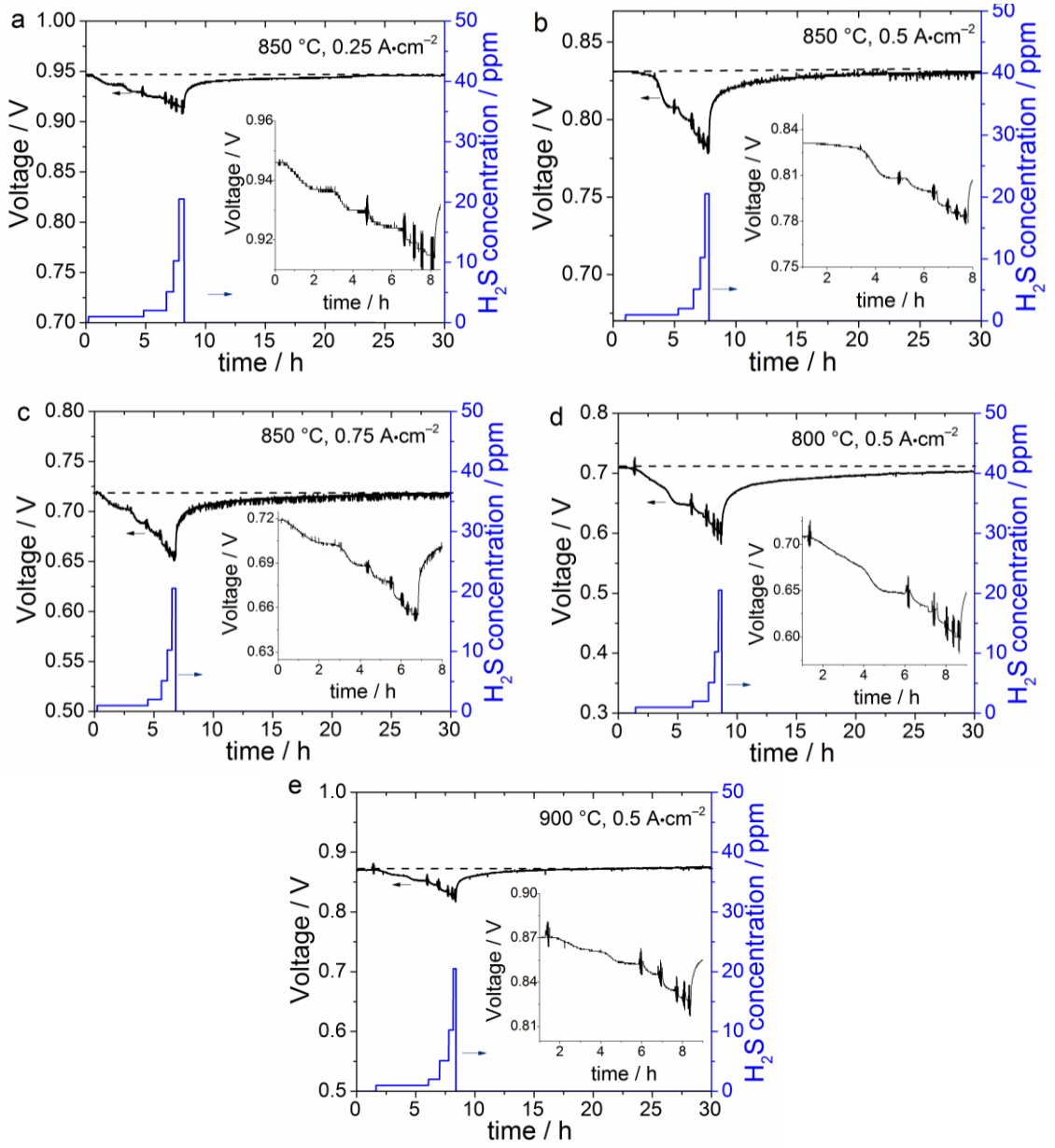


Figure 5.12. Transient sulfur poisoning tests of cell A at $pO_2$ = 0.21 atm, $pH_2$ = 0.97 atm, $pH_2O$ = 0.03 atm with a stepwise increase of $H_2S$ concentration between 0 – 20 ppm. At $T$ = 850 °C the different current densities a) 0.25 A·cm$^{-2}$, b) 0.5 A·cm$^{-2}$ and c) 0.75 A·cm$^{-2}$ are shown. At a constant current density of 0.5 A·cm$^{-2}$, the operating temperatures d) 800 °C and e) 900 °C are depicted. The left y-axis shows the voltage behavior (black) during poisoning and recovery phase and the right y-axis the imposed $H_2S$ concentration (blue). Dotted lines indicate the value of the initial voltage before poisoning and are for guiding the eye. The inset in the figures is a magnification of the voltage evolution during the poisoning phase. The oscillation of the cell voltage in the figures is caused by electrochemical impedance measurements that were recorded after the saturation of each performance drop.

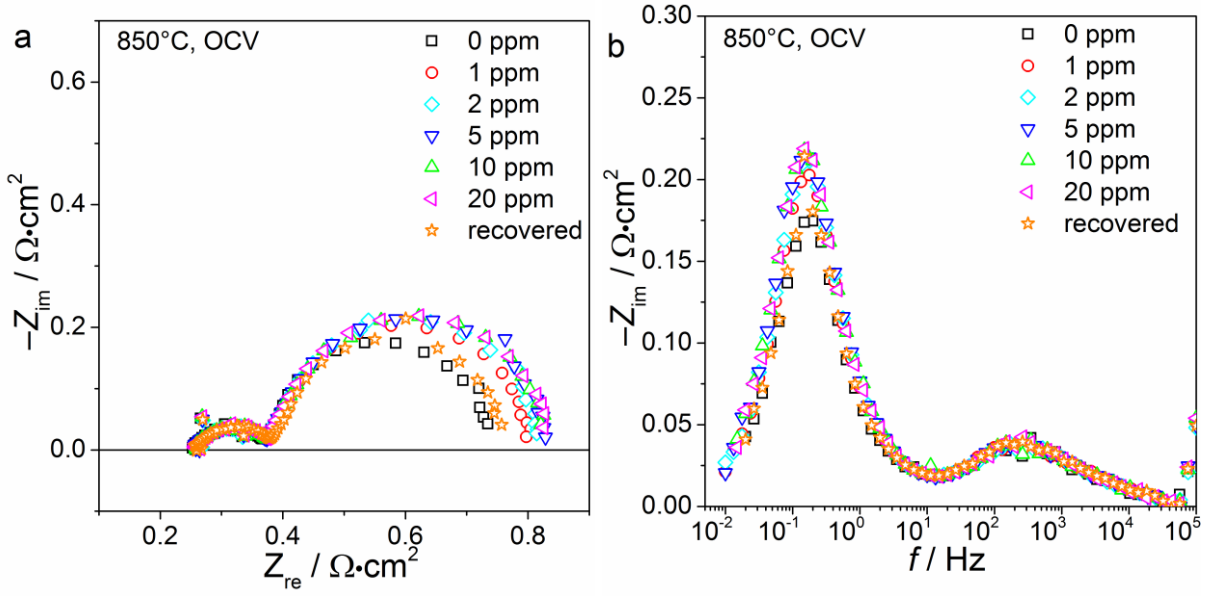


Figure 5.13. a) Nyquist and (b) imaginary impedance plots of impedance spectra of cell A recorded at temperature $T$ = 850 °C, OCV, $pO_2$ = 0.21 atm, $pH_2$ = 0.97 atm, $pH_2O$ = 0.03 atm, with different $H_2S$ concentrations between 0 – 20 ppm.

*The influence of current density and temperature* — Recent studies on sulfur poisoning of Ni/YSZ have demonstrated the difficulties of finding an appropriate descriptor in order to quantify the extent of sulfur poisoning in full cell measurements as cathode and gas diffusion/concentration resistance contributions might superimpose the anode poisoning behavior in a full cell configuration.[76,103,105] As it was not possible to deconvolute the anode surface process from the gas conversion process at low frequencies to calculate the relative resistance increase upon poisoning, in the present work the absolute decrease in voltage and the absolute increase of total ASR are employed to evaluate the extent of sulfur poisoning. The values of the voltage drops in Figure 5.14a show the same characteristic behavior for all current densities with a sharp drop for low $H_2S$ concentrations and a saturation effect at higher concentrations. This strongly resembles the saturation effect also observed for Ni/YSZ as shown in chapter 4, which was related to the saturation of S on the Ni surface.[74,80] The sulfur coverage on Ni can be estimated by means of a Temkin isotherm as shown by Alstrup et al.[122] The respective calculated values for the conditions employed in the present study are depicted on the right y-axis in Figure 5.14a. The behavior of the sulfur coverage on Ni and the voltage drop is indeed strikingly similar, which indicates that the observed Ni/CGO sulfur poisoning is likely to be caused by Ni surface poisoning. This clearly suggests an active involvement of

Ni in the hydrogen oxidation process. This is consistent with previous studies in which Ni infiltration enhanced the low frequency process,[193] and contradicts reports about the mere role of Ni as electronic conductor in Ni/CGO anodes.[132]

In comparison to earlier reports on sulfur poisoning of Ni/CGO, the voltage drops in the present study demonstrate that sulfur poisoning of Ni/CGO-based anodes can significantly decrease SOFC performance.[85,90,91] The reason for this behavior is further explored in the microstructural analysis in chapter 7. A comparison of the different curves presented in Figure 5.14a reveals that increasing current densities lead to larger performance drops. Although this behavior itself is not surprising, the increase of ASR observed in Figure 5.14b shows the opposite behavior and indeed indicates some kind of mitigation effect at high current densities. However, interestingly, the increased ASR values for the experiments at the OCV are not in accordance with this trend as they are significantly smaller than the ASR increase values for 0.25 $A \cdot cm^{-2}$. Although the reason for this behavior is still elusive, it should be mentioned that it could be reproduced with different cells of the same type.

Previous investigations of sulfur poisoning of Ni/YSZ anodes revealed that the relative increase in ASR tends to decrease with increasing current density, which gave rise to the hypothesis that large oxygen ion flows lead to a reduced sulfur surface coverage on Ni by means of S oxidation reaction to $SO_2$.[76] However, as suggested in chapter 4, this behavior is probably rather caused by enhanced hydrogen oxidation kinetics at higher humidity content. The macroscopic influence of $SO_2$ was also questioned in other studies.[103,105,125] However, hydrogen oxidation mechanisms of Ni/CGO and Ni/YSZ might differ significantly. For example, it was shown that the nickel surface in a operated Ni/CGO-based cell was mainly covered by oxygen in contrast to Ni/YSZ, which could indicate an oxygen spillover reaction and opens up the possibility of $SO_2$ formation on the Ni surface.[201,202]

However, the increase of the ASR values in the OCV experiment is lower than at an applied current density of 0.25 $A \cdot cm^{-2}$, which is inconsistent with the hypothesis of $SO_2$ formation. Furthermore, an enhancing effect of water on the hydrogen oxidation kinetics was also shown in the impedance spectra in Figure 5.5a.

Both Figure 5.14c and Figure 5.14d show the same trend of a lower voltage drop, respectively lower ASR increase with increasing temperature, indicating a mitigating effect of temperature on the extent of sulfur poisoning. A similar behavior has also already been observed for sulfur poisoning of Ni/YSZ and was related to an increasing desorption of $H_2S$ from the Ni surface with increasing temperature and thus, a reduced sulfur surface coverage.[77] This could also be

the case in the present study, as desorption processes are generally endothermic and, hence, energetically more favorable with increasing temperature.

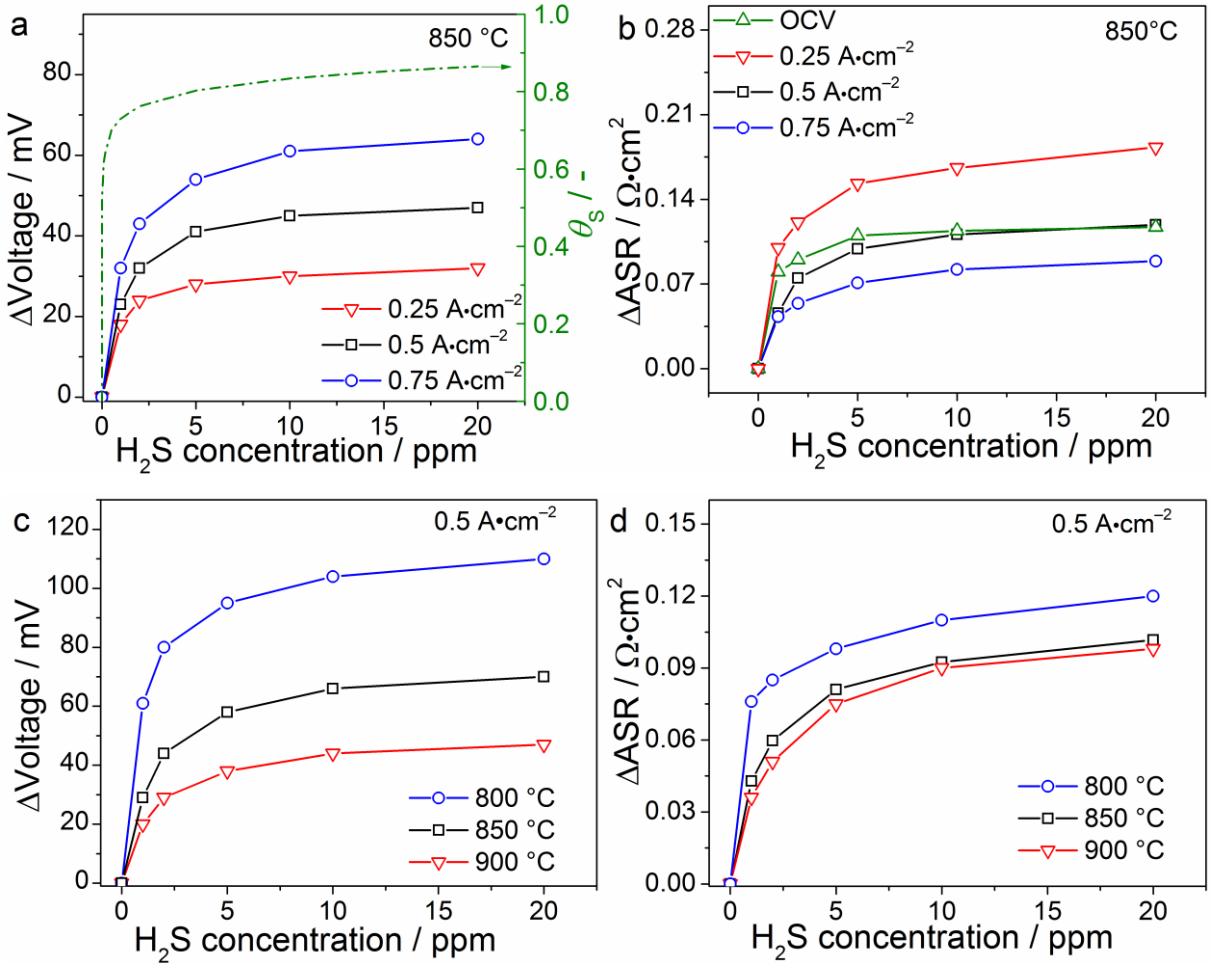


Figure 5.14. (a) Accumulated voltage drop and (b) accumulated total resistance increase at temperature $T$ = 850 °C, $pO_2$ = 0.21 atm, $pH_2$ = 0.97 atm, $pH_2O$ = 0.03 atm, as a function of $H_2S$ concentration at different current densities. (c) Accumulated voltage drop and (d) accumulated ASR increase at a current density of 0.5 A·cm$^{-2}$, $pO_2$ = 0.21 atm, $pH_2$ = 0.97 atm, $pH_2O$ = 0.03 atm, as a function of $H_2S$ concentration at temperatures. The right y-axis in a) shows the calculated sulfur coverage on Ni according to the Temkin isotherm derived by Alstrup et al.[122]. The experiments in (c) and (d) were conducted with a different cell from the same batch as the cell in (a) and (b). Thus, the values do not coincide completely.

The observed voltage drops for higher $H_2S$ concentrations at 800 °C reach values of over 100 mV. These voltage drops already approach the magnitude of values observed for Ni/YSZ.[80] This is a lot more severe than that in earlier studies of Ni/CGO10 anodes.[85,90]

The reason for the significantly larger performance drops in the present study will be further explored in chapter 7 about sulfur-induced long-term degradation. At this point it is only noted that the reason lies in a non-optimized microstructure of Ni/CGO anodes, which apparently plays an important role to determine the sulfur tolerance of such electrodes.

The differential imaginary impedance spectra in Figure 5.15a confirm the behavior observed in Figure 5.14d with a more pronounced increase of the imaginary impedance peak at higher temperatures after exposure of the anode to 1 ppm $H_2S$. Interestingly, however, the peak frequency of the differential impedance spectra increases with decreasing temperature, which implies that the characteristic frequency of the low frequency anode surface process changes as well. This is rarely observed for SOFC as thermally activated processes generally exhibit higher resistances at lower temperatures and cause the corresponding characteristic frequencies to shift to lower values. Hence, the observed behavior must be caused by a significant decrease of capacitance with decreasing temperature, which was shown to be the case for the symmetrical cell measurements in Figure 5.4a. This is also confirmed by the results of a CNLS fit of a reduced ECM to the experimental data. The ECM is depicted in Figure S5, and the corresponding results are shown in Table S1.

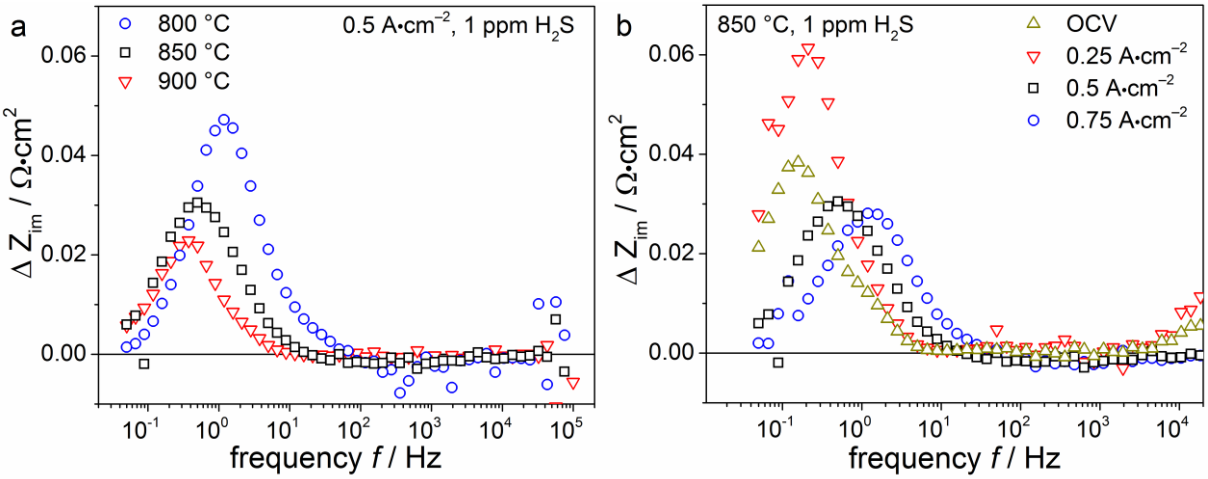


Figure 5.15. Differential impedance spectra (subtraction of imaginary impedance of 0 ppm $H_2S$ spectra from 1 ppm $H_2S$) for a) different temperatures at constant $i$ = 0.5 A·cm$^{-2}$ and b) different current densities at constant $T$ = 850 °C.

A similar analysis can be performed based on the differential imaginary impedance spectra for varying current densities (Figure 5.15b). The peak intensities confirm the trends observed in Figure 5.14b, with the test at 0.25 A·cm$^{-2}$ being the most severely poisoned by 1 ppm $H_2S$.

Again, it is interesting to see that the increase in current density leads to a peak frequency shift from 0.1 Hz at OCV to 1.4 Hz. Although a certain shift to higher frequencies can be expected due to the possibly accelerated kinetics at higher $pH_2O$, a shift of more than one order of magnitude is comparatively large.[151] Thus, the change of the chemical capacitance of the surface anode process with $pO_2$ observed in Figure 5.4 can also be observed in full cells.

### *5.2.3 Sulfur poisoning of Ni/CGO40-based anodes*

In the following, the electrochemical results for the sulfur poisoning of cell B are presented with a systematic variation of current density and temperature. All sulfur poisoning experiments are shown in Figure 5.16. The overall poisoning behavior of cell B resembles that of cell A strongly with a significant voltage drop after exposure to 1 ppm $H_2S$ and a subsequent saturation of the voltage drop. However, although the regeneration of cell B between 850 and 950 °C leads to a complete voltage recovery under all operating conditions, this is not the case at 800 °C (Figure 5.16b). At this operating temperature, the voltage stabilizes after approximately 20 h of poisoning, but at a value 10 mV lower than the initial one. This indicates that sulfur exposure can cause irreversible degradation on Ni/CGO anodes. The analysis of sulfur-induced long-term degradation will further explore this behavior in chapter 7.

Impedance spectra at OCV are affected by sulfur exposure by an increase of the middle frequency arc in the Nyquist plot at a frequency range between $10^1$ and $10^2$ Hz (Figure 5.17). The plots of the initial and the recovered impedance spectra overlap at each recorded frequency point, which indicates a full recovery also at OCV. The low frequency range of the spectra remains unaltered, which indicates the absence of an anode surface process. Interestingly, the frequencies of the impedance spectra affected by sulfur are more than two orders of magnitude higher than those for cell A, which indicates significant differences between the behavior of Ni/CGO10 and Ni/CGO40-based anodes. However, the affected process lies at a frequency 2 – 3 orders of magnitude lower than that of Ni/YSZ, which is caused by the double layer capacitance at the interface between Ni and YSZ.

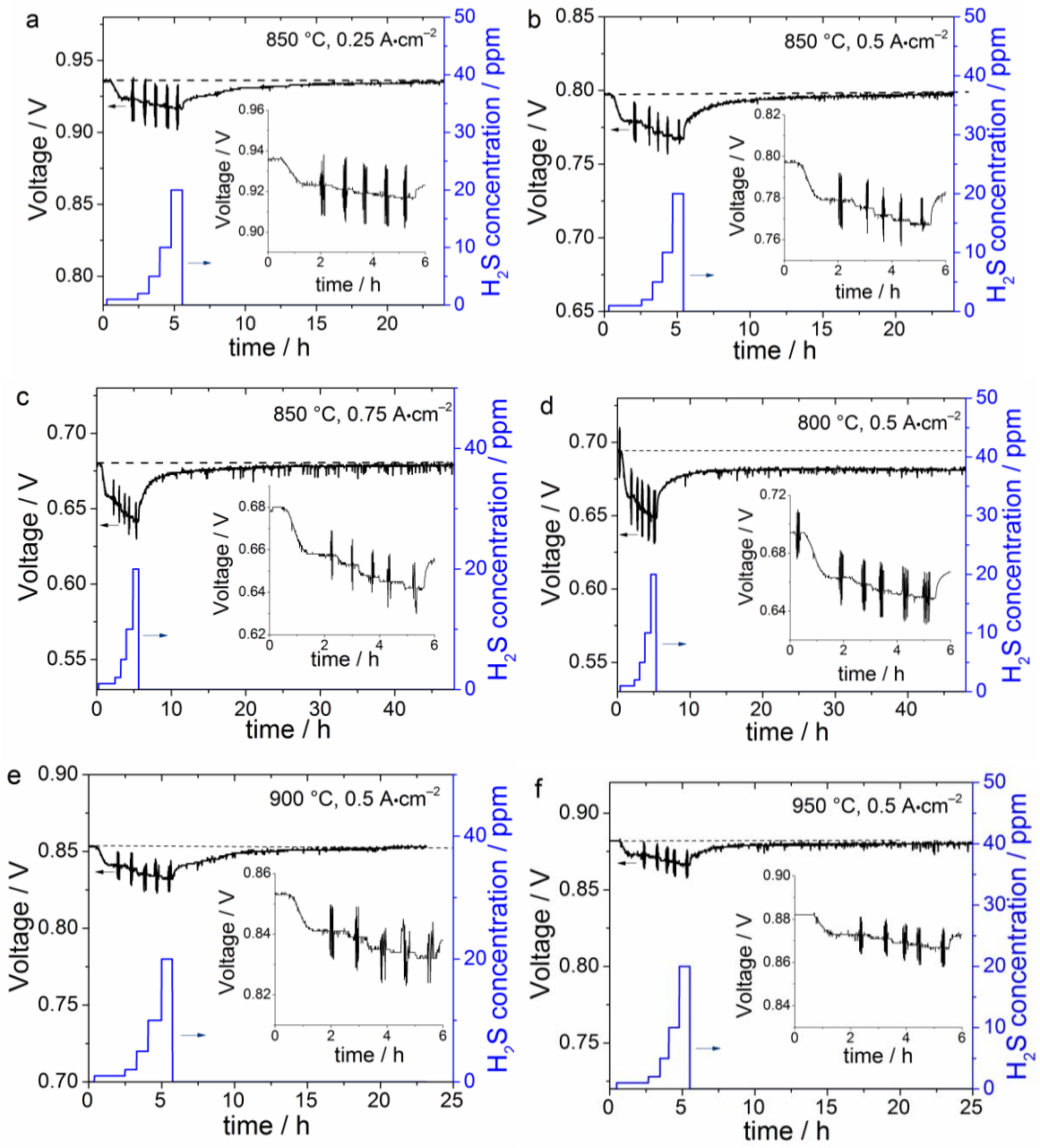


Figure 5.16. Transient sulfur poisoning tests of cell B at (a–c) 850 °C, $pO_2$ = 0.21 atm, $pH_2$ = 0.97 atm, $pH_2O$ = 0.03 atm with a stepwise increase of $H_2S$ concentration between 0 – 20 ppm at the different current densities a) 0.25 A·cm$^{-2}$, b) 0.5 A·cm$^{-2}$ and c) 0.75 A·cm$^{-2}$. (d–f) show the poisoning transient sulfur poisoning tests at 0.5 A·cm$^{-2}$ with a varying temperature (d) 800 °C, (e) 900 °C and (f) 950 °C. The left y-axes show the voltage behavior (black) during poisoning and recovery phase and the right y-axes the imposed $H_2S$ concentration (blue). Dotted lines indicate the value of the initial voltage before poisoning and are for guiding the eye. The inset in the figures is a magnification of the voltage evolution during the poisoning phase. The oscillation of the cell voltage in the figures is caused by electrochemical impedance measurements that were recorded after the saturation of each performance drop.

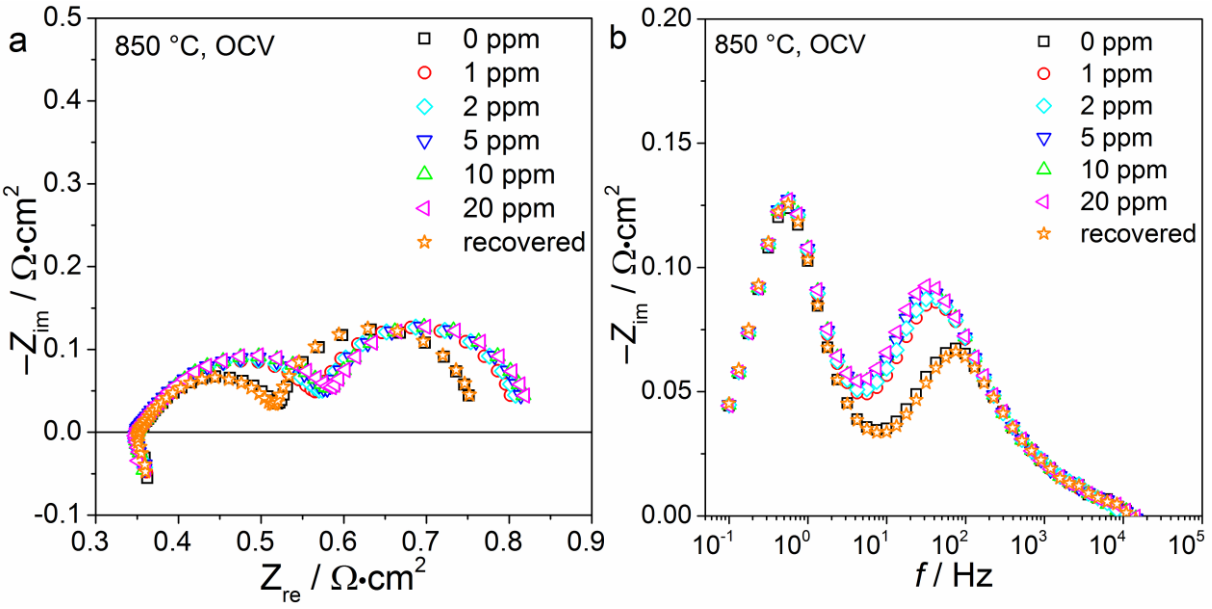


Figure 5.17. a) Nyquist and (b) imaginary impedance plots of impedance spectra of cell B recorded at temperature $T$ = 850 °C, OCV, $p$O$_2$ = 0.21 atm, $p$H$_2$ = 0.97 atm, $p$H$_2$O = 0.03 atm, with different H$_2$S concentrations between 0 – 20 ppm.

Although the peak frequency of the affected process is significantly higher for cell B than for cell A, the overall sulfur poisoning behavior remains similar both in regard to the magnitude of the performance drops and their evolution with H$_2$S concentration and current density. Under the assumption that the resistances of both anode processes are approximately the same, the capacitance of the sulfur-affected process for the Ni/CGO40-based anode can be estimated to be twice that of Ni/CGO10. SEM images of the respective anodes are shown in Figure 3.3. The microstructure of cell B (Ni/CGO40-based) is finer and less porous than that of cell A (Ni/CGO10-based). This leads to an increased TPB length (also confirmed by FIB/SEM tomography in chapter 7) and a larger CGO surface and therefore, probably to a faster charge transfer reaction, which could be reflected by a shift of the anode charge transfer reaction to higher frequencies. However, as a result of the similarity of the performance with respect to the *i*-*V* curves (Figure S1 and Figure S3) and the polarization resistances derived from impedance measurements (e.g., Figure 5.13 and Figure 5.17), a frequency shift as high as two orders of magnitude could not be expected. However, a minor influence of the different microstructures cannot be excluded.

Previously, it has been shown that the amount of $Ce^{3+}$ in CGO is affected by the Gd-doping concentration as the introduction of a trivalent dopant enhances the stability of $Ce^{4+}$.[32] It has also been reported that Gd doping higher than 25 % can lead to the surface segregation of the

Gd phase and, consequently, to a more tortuous Ce network within the CGO phase.[203] This is reflected by a significantly lower electronic conductivity of CGO at higher Gd contents.[32] Thus, as the capacitance of CGO is determined by the amount of available $Ce^{3+}$, this value can be expected to be significantly lower for CGO40 than for CGO10, which leads to a substantial shift of the surface process to higher frequencies in the impedance spectra. Although similar relaxation frequencies impede the direct separation of the anode surface process, the results of equivalent circuit modeling summarized in Table S2 confirm the significantly lower capacitance value in the case of the CGO40-based anode (~0.1 $F \cdot cm^{-2}$, in comparison to ~1 $F \cdot cm^{-2}$ for Ni/CGO10). This large shift in capacitance could also be interpreted as a reduced electrochemically active surface area on CGO40, if CGO is assumed to be the catalytically active phase.[132] However, the actual role of CGO in the hydrogen oxidation process is still unclear.[204]

In their attribution of the low frequency peak of Ni/CGO40 to a charge transfer process, an important argument in the work of Iwanschitz et al. is the comparison to other experimental data published previously, among which are many studies based on Ni/CGO anodes with a lower Gd content.[130] Although the low frequency process of the Ni/CGO40-based anode was also observed in the present work (Figure 5.10), it is not affected visibly by sulfur exposure, which makes a charge transfer process as its origin unlikely.

Throughout this section it was shown that the anode surface process observed at frequencies around 0.1 Hz in Ni/CGO10 anodes is observed at significant higher frequencies for Ni/CGO40-based anodes. Thus, it can be concluded that the impedance spectra of Ni/CGO anodes with different Gd contents have to be handled with caution as processes might be subject to significant frequency shifts, which can lead to misinterpretations. The physicochemical origin of the observed low frequency process in Ni/CGO40 anodes and if it is present in Ni/CGO10-based anodes so far remains unclear. It could possibly be related to a surface diffusion process as suggested previously.[187]

*The influence of current density and temperature* — To compare the dependence of the degradation behavior on the current density, voltage drops and ASR changes are depicted over the imposed $H_2S$ concentrations in Figure 5.18a and Figure 5.18b. Furthermore, the influence of temperature is shown in Figure 5.18c and Figure 5.18d. All curves show a similar characteristic saturation behavior as in Figure 5.14, which indicates that the underlying poisoning mechanism is probably the same. Similar to that shown in Figure 5.14, the increasing

current density shows a mitigating effect on the sulfur poisoning behavior, which is reflected by a decreasing ASR increase with current density. In contrast to that shown in Figure 5.14, even the increased ASR values for the OCV experiments obey this trend.

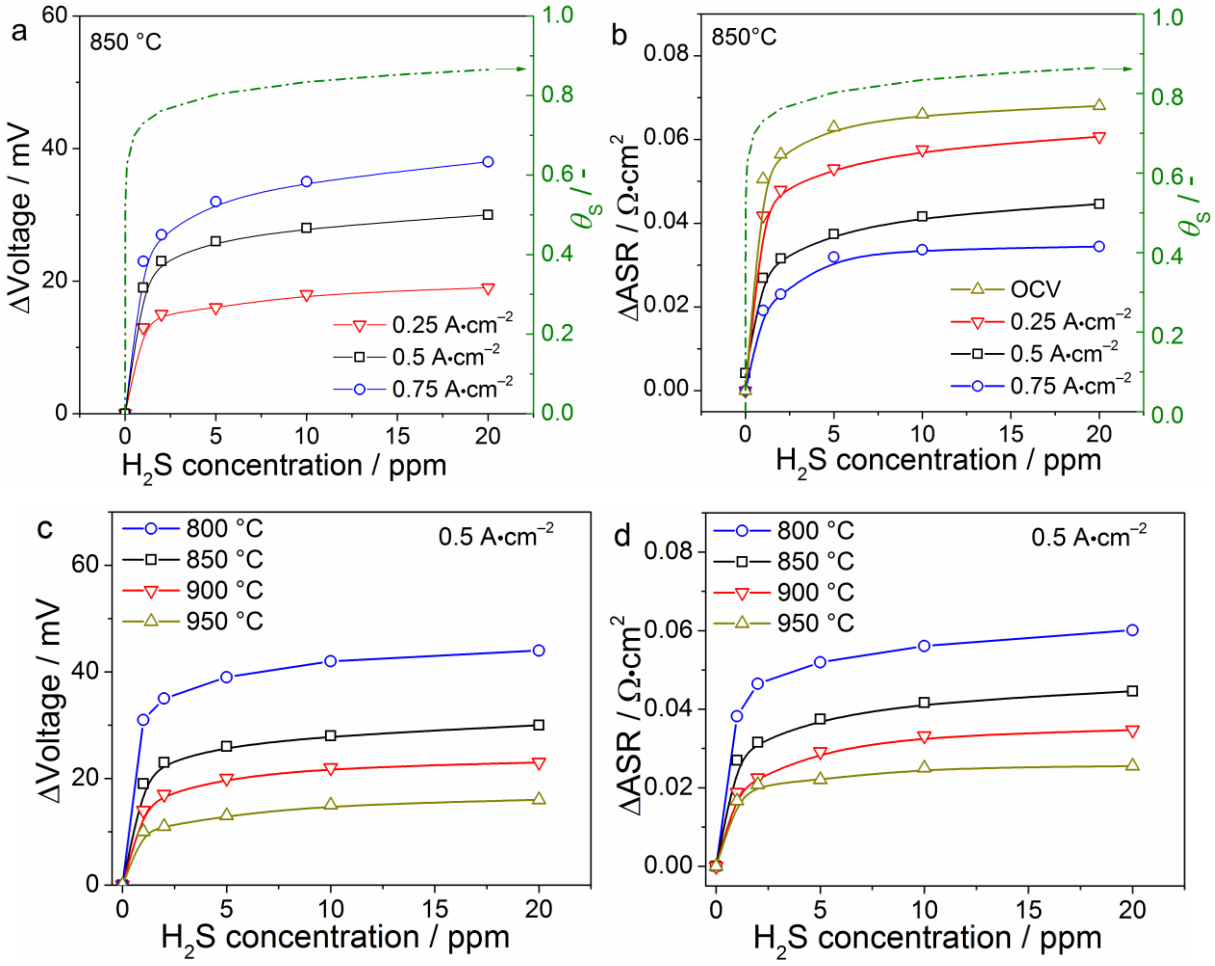


Figure 5.18. (a) Accumulated voltage drop and (b) accumulated ASR increase at temperature T = 850 °C, OCV, $pO_2$ = 0.21 atm, $pH_2$ = 0.97 atm, $pH_2O$ = 0.03 atm, as a function of $H_2S$ concentration at different current densities. (c) Accumulated voltage drop and (d) accumulated ASR increase at a current density of 0.5 A·cm$^{-2}$, OCV, $pO_2$ = 0.21 atm, $pH_2$ = 0.97 atm, $pH_2O$ = 0.03 atm, as a function of $H_2S$ concentration at temperatures. The right y-axes in (a) and (b) show the calculated sulfur coverage on Ni according to the Temkin isotherm derived by Alstrup et al.[122]

Both Figure 5.18c and Figure 5.18d show the same trend of a lower voltage drop, respectively lower ASR increase with increasing temperature analogous to the behavior of cell A shown in Figure 5.14. The increasing sulfur desorption could also occur for sulfur surface poisoning of the CGO surface, which was confirmed by a combined temperature-programmed desorption (TPD) and X-ray photoelectron spectroscopy (XPS) analysis by Mullins and McDonald.[136]

In that study the adsorption and dissociation of hydrogen sulfide was investigated on reduced ceria surfaces that resemble a gadolinium-doped ceria surface with regard to their high $Ce^{3+}$ surface concentration to show that the sulfur coverage decreases with temperature. Even for temperatures as high as 700 °C, the authors could detect sulfur on the reduced ceria surface. However, they also mention that above 500 °C sulfur could diffuse into bulk ceria to lower the surface coverage, which could possibly give rise to long-term degradation effects. The incorporation of sulfur into the CGO10 bulk phase at 10 ppm $H_2S$ exposure under cathodic polarization was also shown recently to be higher at increased temperatures by using TOF-SIMS.[137] In the present study, by using EDX, no traces of sulfur could be detected postmortem. Long-term experiments in chapter 7 will shed more light on the sulfur–CGO interactions in SOFC operation.

The behavior observed in Figure 5.18 is conformed in Figure 5.19, with a more pronounced increase of the imaginary impedance at higher temperatures and lower current densities. In contrast to that of the Ni/CGO10-based cells, however, the peak frequencies of the differential impedance spectra decrease with decreasing temperature and thus, exhibit the typical behavior of thermally activated processes. Furthermore, the change from OCV conditions to 0.75 $A \cdot cm^{-2}$ leads to a peak frequency shift from 23 to 37 Hz, which is a lot smaller than that observed in Figure 5.15. This is an indication that, in contrast to Ni/CGO10, the capacitance of the anode surface process on the Ni/CGO40-based anode is significantly less dependent on temperature and gas phase composition, which is probably related to the stabilization of the $Ce^{3+}/Ce^{4+}$ ratio by the high gadolinium content.

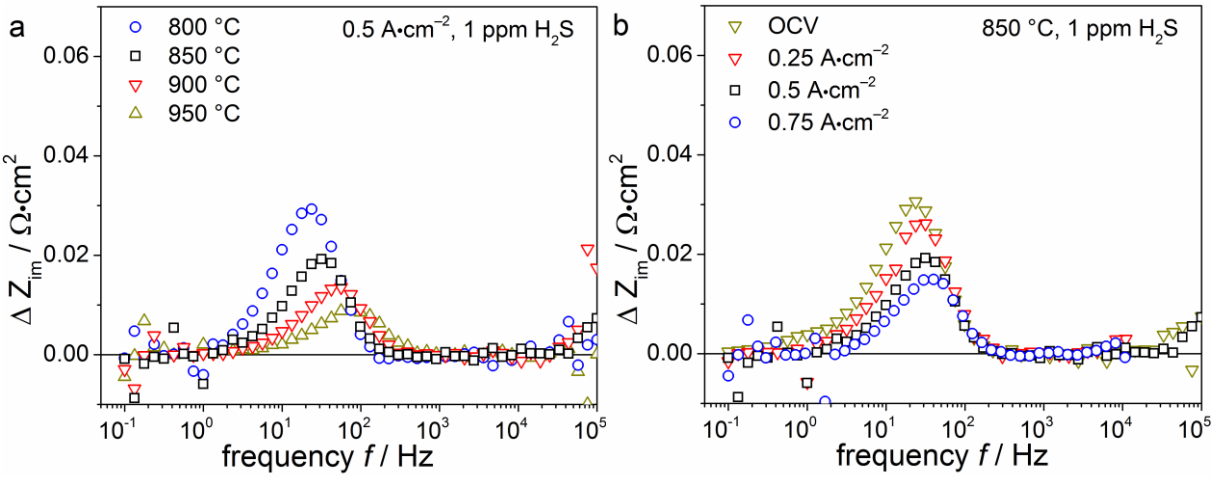


Figure 5.19. Differential impedance spectra (subtraction of imaginary impedance of 0 ppm $H_2S$ spectra from 1 ppm $H_2S$) for a) different temperatures at constant $i$ = 0.5 $A \cdot cm^{-2}$ and b) different current densities at constant $T$ = 850 °C.

### *5.2.4 Comparison of sulfur poisoning of cells with different Ni-based anodes*

While the last subsections have focused on a detailed investigation and comparison of cell A and cell B in order to identify the influence of Gd-doping level on the electrode performance, the present subsection exhibits additional experimental data for cell C (Ni/CGO10-based cell from a different supplier) and cell E (Ni/YSZ-based cell) and compares all investigated cells.

The current-voltage characteristics of all four cells in a $H_2/H_2O$ (97/3) fuel gas mixture at 850 °C are shown in Figure 5.20. The Ni/YSZ-based cell reaches 0.63 $A \cdot cm^{-2}$ at 0.7 V, while the Ni/CGO10-based cell C achieves 0.88 $A \cdot cm^{-2}$ at the same voltage.

The analysis of the electrochemical impedance spectra in Figure S7 shows that the lower performance of the Ni/YSZ-based cell is mainly due to an increased ohmic resistance (0.16 $\Omega \cdot cm^2$ for the Ni/CGO-based cell C and 0.25 $\Omega \cdot cm^2$ for the Ni/YSZ-based cell), while the polarization resistance of the two cells is approximately the same (0.23 $\Omega \cdot cm^2$). As the electrolyte has the same phase composition and thickness in both cells, the increased ohmic resistance of the Ni/YSZ-based cells is probably due to the YSZ adhesion layer, which shows a significantly lower ionic conductivity than the CGO10 adhesion layer of the Ni/CGO-based cell.[19] This is also reflected in a lower overall performance. The Ni/CGO10-based cell A shows a similar performance as the Ni/CGO10-based cell C, with a current density of 0.94 $A \cdot cm^{-2}$ at 0.7 V. The Ni/CGO40-based cell B is slightly worse than the ones based on Ni/CGO10 anodes with 0.68 $A \cdot cm^{-2}$ at 0.7 V.

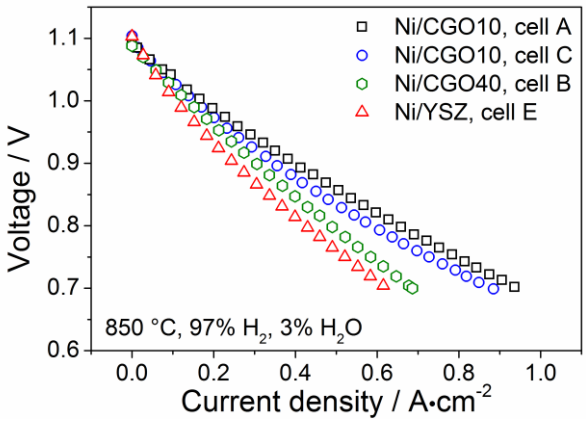


Figure 5.20: *i–V* curves of the four cells investigated in the present chapter at $T$ = 850 °C, $pO_2$ = 0.21 atm, and $pH_2O$ = 0.03 atm. The four characterized cells are cell A (Ni/CGO10), cell B (Ni/CGO40), cell C (Ni/CGO10) and cell E (Ni/YSZ).

Figure 5.21a+b shows the systematic variation of the $H_2S$ level between 0 and 20 ppm in the $H_2/H_2O$ fuel for cell C (Ni/CGO10) and cell E (Ni/YSZ) operating at 0.5 $A \cdot cm^{-2}$. Interesting-

ly, the successive sulfur poisoning did not have a significant effect on the cell voltage of the Ni/CGO10-based cell C and caused a maximum cell voltage drop of only 9 mV (Figure 5.21a). Moreover, the cell voltage recovered quickly back to the initial cell voltage after stopping the hydrogen sulfide supply. Sulfur exposure to Ni/YSZ led to a voltage drop of 172 mV at 20 ppm $H_2S$ and thus, was a lot more severe than for the Ni/CGO cells. This is also reflected in a higher ASR resistance increase for Ni/YSZ. Furthermore, the Ni/YSZ anode showed a significant extent of irreversible degradation and lost 29 mV of cell voltage within only one poisoning cycle (Figure 5.21b). Regeneration of Ni/YSZ anodes is an extensively investigated topic and the process was frequently shown to extend over hundreds of hours and, nevertheless, displayed irreversible degradation in most cases.[75,80,102,103] Thus, the value for the irreversible voltage drop could possibly further diminish with time. However, as recently shown the irreversible long-term degradation mechanism for Ni/YSZ is probably related to the anode overpotential.[112] Irreversible long-term degradation of Ni/CGO anodes is investigated in detail in chapter 7.

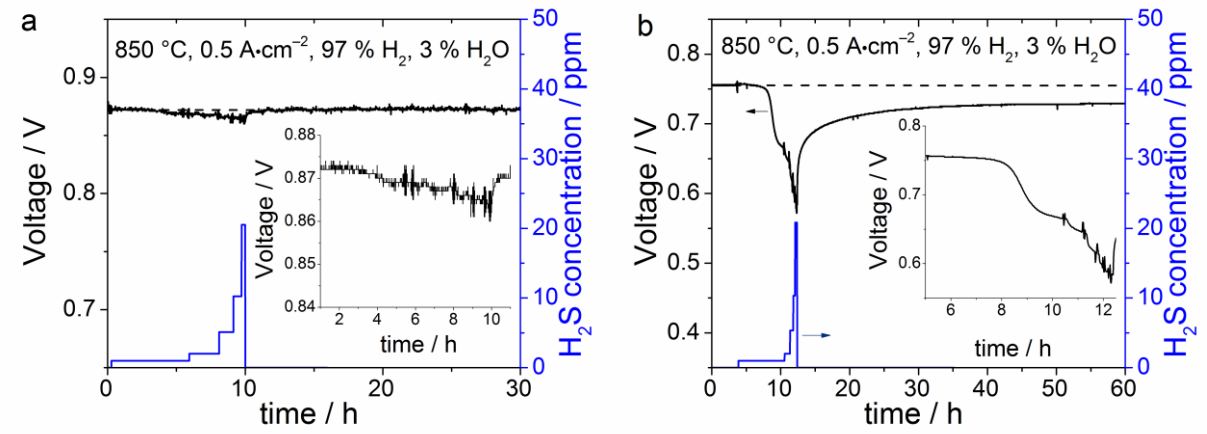


Figure 5.21: Transient sulfur poisoning tests of the two cells at $pO_2$ = 0.21 atm, $pH_2$ = 0.97 atm, $pH_2O$ = 0.03 atm, and current density of $i$ = 0.5 A·cm$^{-2}$. (a) The $H_2S$ concentration was increased stepwise for the Ni/CGO10-based cell C between 0 – 20 ppm. (b) The $H_2S$ concentration was increased stepwise for the Ni/YSZ-based cell between 0 – 20 ppm. The left y-axis shows the voltage behavior (black) during poisoning and recovery phase and the right y-axis the imposed $H_2S$ concentration (blue). Dotted lines indicate the value of the initial voltage before poisoning and are for guiding the eye. The insets in the figures are a magnification of the voltage evolution during the poisoning phase. The oscillation of the cell voltage in the figures is caused by electrochemical impedance measurements that were recorded after the saturation of each performance drop.

Impedance spectroscopy measurements of cell C (Ni/CGO, Figure S7a+b) and cell E (Ni/YSZ, Figure S7c+d) with and without addition of 20 ppm hydrogen sulfide have been carried out. The spectra are influenced by sulfur at the respective opposite ends. Cell C is affected at frequencies around 1 Hz, in agreement with the results on cell A. Ni/YSZ is affected at frequencies between $10^3$ and $10^4$ Hz, which is consistent with earlier studies. This can be related to the much smaller interfacial double-layer capacitance between Ni and YSZ.[85,93]

Voltage drop and ASR increase values of all Ni-based cells are summarized in Figure 5.22. Interestingly, considerably different voltage drops were observed for the two different Ni/CGO10 anodes (cell A and cell C). The cell voltage drop of the in detail investigated cell A (Ni/CGO10) was 47 mV, and therefore was more than five times higher than the 9 mV of cell C (Ni/CGO10). This also holds true for the increase in ASR resistance and is unexpected in view of the similar overall performance shown in Figure 5.20. This behavior could also be reproduced for each cell type with several different cells from the same batch.

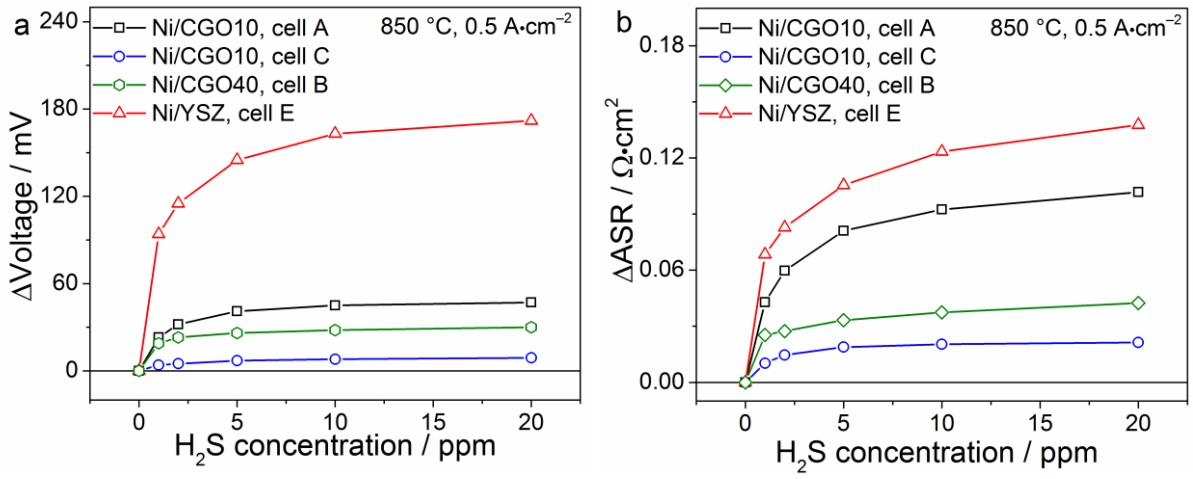


Figure 5.22: (a) Accumulated voltage drops and (b) accumulated total resistance increase at temperature $T$ = 850 °C, $pO_2$ = 0.21 atm, $pH_2$ = 0.97 atm, $pH_2O$ = 0.03 atm, as a function of $H_2S$ concentration.

To improve the understanding of the different behavior of these two cells, impedance spectroscopy measurements under the same conditions were carried out (OCV, 850 °C, 97 % $H_2$ and 3 % $H_2O$ in the anode gas; depicted in Figure S8) and were analyzed by means of ECM. The results of a CNLS fit showed that the resistance of the low frequency arc related to anode charge transfer of cell C (0.2 Ω·cm$^2$) is smaller than the resistance of cell A (0.28 Ω·cm$^2$). As the two Ni/CGO-based cells employ different cathodes, the respective cathode charge transfer processes lie at different frequencies (Ni/CGO: ~5 Hz, Ni/CGO-Ref: ~100 Hz), which is also

evident from the different shapes of the impedance spectra. However, despite the difference in frequencies, neither of these processes are part of the low frequency arc, and thus, the comparison of the low frequency arc resistance values should be valid since they only comprise the anode charge transfer and the gas conversion/diffusion processes in both cases. However, in general the separation of the different process resistances from impedance spectra of full cells with Ni/CGO anode is complicated, due to the occurrence of the anode charge transfer resistance at low frequencies, which causes its convolution with other processes in many cases. Thus, the derived values above can only be considered as a rough assessment.

However, differences in the anode microstructure are also visible in the SEM images of the Ni/YSZ and the two Ni/CGO10 anodes in Figure 3.3. The SEM images show that the microstructure of cell C is finer and the CGO particles are better distributed than in cell A, which represents a more optimized microstructure and indicates a faster charge transfer reaction and therefore also a higher sulfur resistivity. However, the demonstrated difference in sulfur tolerance between the two different Ni/CGO-based cells is surprisingly large for two cells of nominally equivalent cell architecture, despite differences in the anode charge transfer resistance.

In a number of studies, the reason for the high sulfur tolerance of Ni/CGO was speculated to be due to the MIEC characteristics of CGO.[85,90,91] Moreover, in other fundamental studies Ni was shown to only assume the role of a pure electronic conductor during hydrogen oxidation, which would extend the electrochemical reaction zone to the DPB interface.[132] On the basis of these studies, the sulfur adsorption on the Ni surface would not be expected to have a major influence on SOFC performance. Thus, it can be speculated that the hydrogen oxidation mechanism on Ni/CGO is a convolution of a DPB process on the CGO surface and a spillover process at the TPB between Ni/CGO/gas phase. As a consequence, it is possible that the role of the Ni phase in Ni/CGO anodes differs depending on the exact composition of the electrode, as a function of TPB length, double phase boundary, DPB area, and other microstructural parameters. The hydrogen oxidation mechanism on Ni/CGO is discussed in detail in the following.

### *5.2.5 Performance of pure CGO electrodes*

In order to shed more light on the electro-catalytic activity of CGO, sulfur poisoning measurements were carried out on a pure CGO electrode. *i-V* curves were recorded for the cell at 850 °C in a fuel consisting of 97 % $H_2$, 3 % $H_2O$ and one containing 50 % CO, 50% $CO_2$. The results are depicted in Figure 5.23 and demonstrate that CGO anodes are indeed capable of

oxidizing hydrogen on the DPB without the addition of a metal catalyst. Furthermore, electrochemical carbon monoxide oxidation is possible, which will be further investigated in the following chapter. The performance of the cell (0.25 $A \cdot cm^{-2}$ at 0.5 V) is comparatively low, which can be related to a non-optimized manufacturing process. The low performance is mainly related to a large ohmic resistance (see Figure 5.24). This could be caused by a low electronic conductivity in the anode and demonstrates the necessity of a metal phase as electronic conductor in a cermet electrode.

To explore the possibility of CGO surface poisoning with sulfur, the CGO-based cell was exposed to 20 ppm $H_2S$ while operated with the 97 % $H_2$, 3 % $H_2O$ fuel at OCV. Corresponding EIS measurements of the cell are depicted in Figure 5.24. The measurements reveal that the addition of hydrogen sulfide does not negatively affect the cell performance at OCV. Interestingly, the exposure of sulfur rather even slightly increases the cell performance due to the decrease in the middle frequency peak at ~10 Hz. This increase in performance is restored after the $H_2S$ supply is switched off. To identify the origin of this performance increase, a more detailed investigation of CGO electrodes has to be carried out. However, it can be concluded that the performance drops of Ni/CGO anodes upon sulfur exposure are related to the surface poisoning of the Ni phase, while the CGO phase remains sulfur-free.

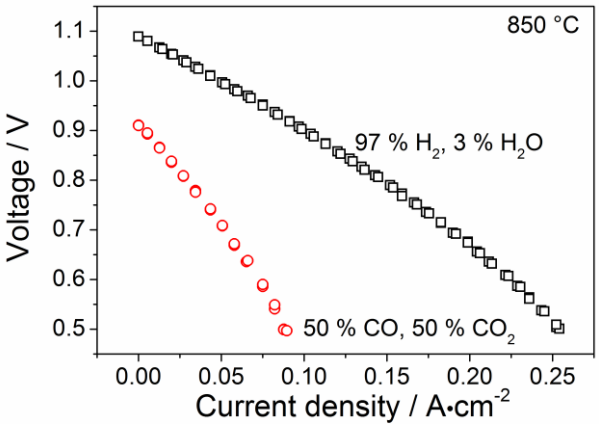


Figure 5.23. *i-V* curve of the cell with CGO electrode at 850 °C and with 97 % $H_2$, 3 % $H_2O$ (black squares) and 50 % CO, 50 % $CO_2$ (red circles) fuel gas.

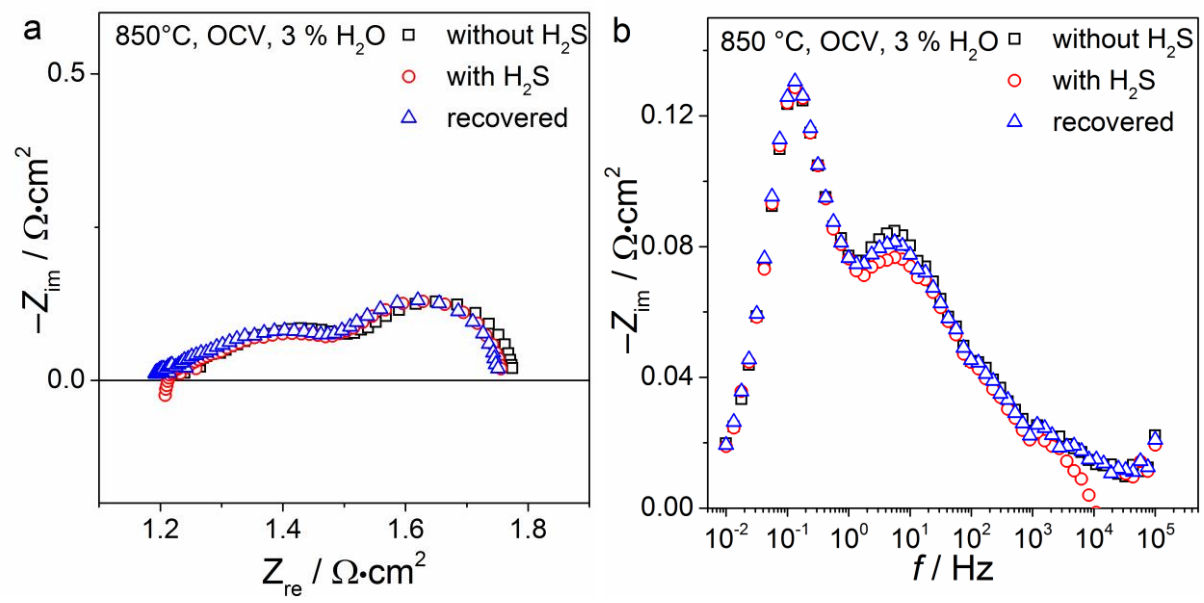


Figure 5.24. (a) Nyquist and (b) imaginary plots of the EIS measurements of the cell with CGO electrode at 850 °C, OCV and with 97 % $H_2$, 3 % $H_2O$ fuel gas before (black squares) and after the exposure to 20 ppm $H_2S$ (red circles), and after recovery (blue triangle).

### *5.2.6 The influence of $H_2S$ on the hydrogen oxidation mechanism on Ni/CGO*

Early investigations have attributed the high sulfur tolerance of Ni/CGO to the high ionic conductivity of CGO in comparison to YSZ and a corresponding spatial extension of the hydrogen oxidation location in the porous electrode. This might play a certain role, as Ni/ScSZ have been shown to display a higher sulfur tolerance than Ni/YSZ due to their increased ionic conductivity, which is similar to CGO.[19,74,102,106,112] However, the differences obtained by increasing the ionic conductivity were by far not as pronounced as the ones observed in the present study. Therefore, it seems to be clear that the different behavior of Ni/CGO is caused by a different underlying hydrogen oxidation mechanisms.

It was suggested before that fuel oxidation on Ni/CGO-based anodes of SOFC proceeds essentially through the so-called bulk-surface path, in which oxygen anions first migrate through the electrolyte/electrode boundary (YSZ/CGO) and then through the electrode-bulk/electrode-surface interface (CGO–bulk/CGO–surface).[190] Finally, at the surface of CGO, oxygen atoms are oxidized by hydrogen to form $H_2O$.

The electro-catalytic activity of CGO originates from its MIEC characteristics and was given as a reason for high sulfur tolerance of Ni/CGO in several studies.[85,90,91,129–134] Some studies have even suggested that Ni primarily assumes the role of a pure electronic conductor in Ni/CGO anodes, which improves the comparatively low electronic conductivity of CGO and

extends the electrochemical reaction zone to the gas/ceria interface.[132] Thus, oxidation could occur on CGO through a Mars-van-Krevelen mechanism as suggested for CO oxidation on ceria catalysts:[205]

$$H_2O_{CGO} + O^{2-}_{CGO} \rightleftharpoons 2OH^{-}_{CGO} \quad (42)$$

$$\frac{1}{2} H_{2(g)} + OH^{-}_{CGO} \rightleftharpoons H_2O_{(g)} + \square_{CGO} + e^{-} \quad (43)$$

The previous formation of $OH^{-}_{CGO}$ via water dissociation (Eq. 42) was shown to explain the dependence of the charge transfer reaction on $pH_2O$ on Ni/YSZ. Due to the similar dependence of the hydrogen oxidation process on $pH_2O$ on both anodes, a similar activation process possibly occurs on Ni/CGO as well. Moreover, the charge transfer reaction (Eq. 43) could be further resolved into more elementary steps. Electron transfer from $OH^{-}_{CGO}$ to ceria was suggested to be the rate-limiting step on ceria before:[138]

$$OH^{-}_{CGO} + Ce^{4+} \rightleftharpoons Ce^{3+} + OH_{CGO} \quad (44)$$

According to these studies, the sulfur adsorption on the Ni surface would not be expected to have a major influence on SOFC performance, which is in contrast to the sulfur poisoning behavior presented in this work.

Hydrogen dissociation on reduced ceria was suggested to be associated with a rather large activation energy barrier of ~1 eV by means of DFT.[206] However, hydrogen dissociation on Ni can be assumed to occur spontaneously.[34] Therefore, the addition of nickel to a CGO electrode is likely to facilitate the kinetics of hydrogen dissociation, which is also in agreement with studies in which catalytic amounts of Ni were infiltrated into a CGO backbone and a reduced low frequency resistance was observed.[193]

Therefore, the observed sulfur poisoning of Ni/CGO anodes is probably caused by the surface poisoning of the Ni surface as illustrated in Figure 5.25. The spillover of hydrogen from nickel to CGO can either occur via a surface (hydrogen or oxygen spillover) or an interstitial bulk pathway. In the hydrogen spillover pathway, hydrogen is dissociated on Ni and jumps to the CGO surface at the TPB (Eq. 45).

$$H_{Ni} + OH^{-}_{CGO} \rightleftharpoons \square_{Ni} + e^{-} + H_2O_{CGO} \quad (45)$$

This would be the same hydrogen oxidation mechanism as on Ni/YSZ and probably cannot sufficiently describe the higher sulfur tolerance of Ni/CGO alone.[34,195]

Moreover, an oxygen spillover from CGO to Ni could occur (Eq. 46), possibly coupled to a previous oxygen discharge mechanism (Eq. 47).

$$O^{2-}_{CGO} + 2Ce^{4+} \rightleftharpoons 2Ce^{3+} + O_{CGO} \quad (46)$$

$$2H_{Ni} + O_{CGO} \rightleftharpoons H_2O_{(g)} + \square_{CGO} \quad (47)$$

Oxygen spillover was also proposed to be the reason for possible $SO_2$ formation on Ni and thus, increased sulfur tolerance. Both a hydrogen and an oxygen spillover pathway have been shown to be energetically feasible by means of DFT calculations.[207]

Another possibility is the charge transfer of hydrogen via an interstitial hydrogen spillover (Eq. 48), which occurs at the DPB between CGO and Ni (Eqs. 48 + 49; in Kröger-Vink notation) and is followed by a subsequent water desorption from the CGO surface:

$$H^{x}_{i,\,Ni} \rightleftharpoons H^{\bullet}_{CGO} + e^{-}. \quad (48)$$

$$H^{\cdot}_{CGO} + OH^{-}_{CGO} \rightleftharpoons H_2O_{(g)} \quad (49)$$

This was considered to be unlikely to happen on Ni/YSZ due to low hydrogen diffusivity in YSZ.[208] However, it was shown that proton solubility in CGO is two orders of magnitude higher, which is why this pathway was proposed to occur on Ni/CGO.[201,202,209,210] This reaction mechanism is also capable to explain to the higher sulfur tolerance of Ni/CGO, since under sulfur exposure the nickel surface area active for hydrogen dissociation would still be larger than for Ni/YSZ where only the nickel close to the TPB is active.

Moreover, previously sulfur atoms were observed in the CGO bulk phase of CGO electrodes under cathodic polarization and in monocrystalline reduced ceria, which could indicate sulfur transport from the Ni surface to the CGO bulk.[136,137]

It is also possible that the presented mechanisms are competitive, and the nature and location (TPB or DPB) of the prevailing hydrogen oxidation mechanism depend on the microstructure of the respective electrode. This is supported by the considerable differences between the voltage drops observed in the present study for different Ni/CGO10 anodes of the nominally same composition. As a consequence, the role of the Ni phase in Ni/CGO anodes could differ depending on the exact composition of the electrode, as a function of TPB length, CGO surface area and other microstructural parameters.

Although the impedance spectra of Ni/CGO10 and Ni/CGO40-based anodes exhibit significant differences, the similarity of their sulfur poisoning behavior indicates that their underlying mechanisms are probably the same. The large differences in the capacitance of the identified anode surface processes are likely to be caused by the lower availability of $Ce^{3+}$ in CGO40, which could also be interpreted as a reduced electrochemically active region on CGO40.

As shown above, sulfur adsorbs on the Ni surface and blocks active surface sites of the electrode to deteriorate fuel oxidation. As a result, the electrostatic surface potential step ($\Delta\chi$), shown in red in Figure 5.25, diminishes. The interfacial potential step ($\Delta\phi$) stays constant during our experiments, which indicates the lack of significant influence of sulfur on the CGO bulk/surface transport for the exposure times investigated.

However, the identification of the real fuel oxidation mechanism cannot be achieved within the framework of the present study. Detailed studies on point or patterned electrodes combined with elementary kinetic modeling could help to unravel the hydrogen oxidation mechanism in the future.

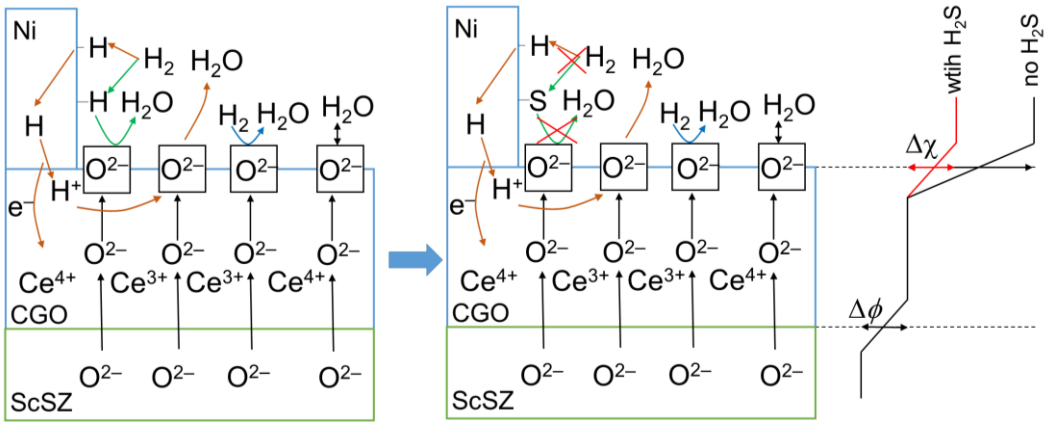


Figure 5.25. Schematic illustration of reaction mechanism of fuel oxidation and sulfur poisoning mechanisms in Ni/CGO-based anodes of SOFC. The first block represents the normal operation upon exposure to $H_2/H_2O$, the second block shows the influence of sulfur on the (electro-)chemical processes and the third diagram demonstrates the potentials drop at different interfaces. In the illustration of the mechanism, different hypothetical hydrogen oxidation mechanisms are shown. The brown arrows denote an interstitial hydrogen charge transfer, the green arrows hydrogen spillover and the blue arrows hydrogen oxidation on the CGO surface. All structural details and scaling are exaggerated merely for illustration purposes.

### *5.3 Conclusions*

This chapter aims to advance the understanding of the electrochemical processes that occur during the sulfur poisoning of Ni/CGO based anodes in $H_2/H_2O$ fuel gases. Therefore, electrolyte-supported Ni/CGO10 and Ni/CGO40-based SOFC were characterized extensively by analyzing their current-voltage curves and impedance spectra. Moreover, the short-term sulfur poisoning behavior of the SOFC was investigated systematically under a wide range of oper-

ating conditions at various temperatures and current densities with different $H_2S$ concentrations (1 – 20 ppm). The investigated cells displayed a different magnitude of performance losses, which were lower than the ones of a Ni/YSZ-based cell. While one of the Ni/CGO10-based cells showed voltage drops of less than 10 mV at 20 ppm $H_2S$ and 0.5 $A \cdot cm^{-2}$, another cell of similar overall performance and geometry exhibited a voltage drop which was more than five times larger (47 mV). This demonstrates a considerable effect of the microstructure of Ni/CGO anodes on sulfur tolerance.

The analysis of the ASR increase values after sulfur exposure displayed a sulfur mitigation effect at high current loads and temperatures. The poisoning behavior was shown to be reversible for short exposure times. The sulfur poisoning behavior of the different anodes was observed to be similar in both the magnitude of the cell voltage drops and the saturation behavior.

However, the analysis of comparable impedance spectra revealed that the sulfur-affected processes can be found at substantially different relaxation frequencies that depend on the Gd-doping level of the CGO-based anode. Ni/CGO40-based anodes were affected at frequencies of approximately 50 Hz, whereas the impedance spectra of the Ni/CGO10-based anodes showed an increase at 0.1 Hz. Moreover, the capacitance of the anode surface process in Ni/CGO10 was shown to exhibit a significant dependence on both the operating temperature and gas phase composition, which reflects a changing $Ce^{3+}$ concentration in CGO, although this was not the case for Ni/CGO40-based anodes. From these differences, it could be demonstrated that the capacitance of Ni/CGO-based anodes is strongly dependent on multiple parameters and thus, a direct comparison between the impedance spectra of different Ni/CGO-based anodes, which is performed frequently in the literature, should be avoided.

The observed reversible degradation and voltage drops are encouraging with regard to the operation of Ni/CGO anodes with sulfur-containing $H_2/H_2O$ fuel gases. As a next step, the subsequent chapter will extend the investigation of sulfur poisoning of Ni/CGO anodes to more realistic conditions with reformate fuels.

# 6 Sulfur poisoning of electrochemical reformate conversion on Ni/CGO anodes

As shown in the previous chapter, Ni/CGO anodes show a promising high resistivity against sulfur poisoning in $H_2/H_2O$ fuel systems. Hypothetical explanations of this superior sulfur tolerance include the activity of CGO as a hydrogen oxidation catalyst in the Ni/CGO system,[129–134] the oxidation of sulfur to $SO_2$ involving an oxygen spillover from CGO to Ni,[85,92,135] and sulfur diffusion from the surface to the CGO bulk phase.[136,137] While the actual reason still needs to be identified, it is clear that the influence of sulfur on Ni/CGO anodes has to be reevaluated under the assumption that the underlying mechanism is fundamentally different from that of Ni/YSZ.

The present chapter evaluates the effect of hydrogen sulfide on the performance of Ni/CGO-based SOFC operating on a number of different reformate fuels and compares the observed behavior with Ni/YSZ anodes. This allows the decoupling of the different (electro-)catalytic reactions shown in Eq. 21 – 23 and to draw several mechanistic conclusions about the behavior of Ni/CGO anodes. First, Ni/YSZ and Ni/CGO anodes were characterized in a model reformate containing $H_2$, $H_2O$, CO and $CO_2$ in order to represent realistic operating conditions. Subsequently, in order to answer mechanistic questions, the influence of sulfur on electrochemical CO oxidation and finally, on methane steam reforming is investigated.

Most of the results presented in this chapter were already published.[185]

## *6.1 Testing procedure*

In this chapter, cell C and cell E (see Table 3.1) were investigated, both based on a 10Sc1CeSZ electrolyte. Cell C employs a Ni/CGO10 anode and showed the highest sulfur tolerance of all cells in chapter 5. Cell E is based on a Ni/YSZ anode and displayed the lowest sulfur tolerance.

Electrochemical experiments were carried out in a number of different fuel gas mixtures (Table 6.1). Two different synthetic reformate gas mixtures were used (mixtures I and III), which correspond to the equilibrium gas compositions at the operating temperature of 850 °C. The equilibrium gas phase compositions and the theoretical open circuit voltage according to the Nernst voltage were calculated with CANTERA.[211] Furthermore, to identify the influence of sulfur on the conversion of carbon monoxide, for both gas mixtures $CO/CO_2$-free reference gases were used (gas mixture II and IV). Moreover, the sulfur poisoning effect on CO oxidation (mixture V) and methane steam reforming (mixture VI) was investigated.

Table 6.1. Inlet gas phase compositions in the different experiments and indications with which cell they were performed.

| Number of fuel gas mixture | $H_2$ | $H_2O$ | CO | $CO_2$ | $N_2$ | $CH_4$ | Ni/YSZ | Ni/CGO |
|---|---|---|---|---|---|---|---|---|
| I | 16 | 14 | 16 | 14 | 40 | - | - | Yes |
| II | 32 | 14 | - | - | 54 | | - | Yes |
| III | 7 | 7 | 20 | 20 | 46 | - | Yes | Yes[a] |
| IV | 7 | 7 | - | - | 86 | - | Yes[a] | Yes[a] |
| V | - | - | 20 | 20 | 60 | - | Yes | Yes[a] |
| VI | 16 | 23 | - | - | 50 | 11 | - | Yes |

[a]Experiments in gas mixtures III, IV and V were carried out with a different cell from the same batch than the other experiments. However, performance of the commercial SOFC was shown to be highly reproducible.

The conducted experiments include a systematic investigation of the effect of the hydrogen sulfide concentration on the extent of sulfur poisoning on Ni/CGO operated with fuel gas mixture I. This has been carried out with stepwise increasing $H_2S$ concentration analogous to the previous chapter at the different current densities $i$ = OCV, 0.25, 0.5 and 0.75 $A \cdot cm^{-2}$.
Throughout this chapter, the hydrogen utilization ($FU_{H2}$) is used. This value is calculated by dividing the number of electrons going through the external electrical circuit with the maximum number of electrons that can be generated by the hydrogen inlet. Frequently, overall fuel utilization values are used that include both the hydrogen and carbon monoxide inlet gases. However, in the present chapter $FU_{H2}$ is preferred, since this descriptor can state more clearly if carbon monoxide is oxidized at a given operating point. As illustrated in Figure 3.2, a bypass of the fuel gas around the anode is possible within the ceramic cell housing in the employed setup. Moreover, the cell housing has not been optimized to deliver an equally distributed gas profile across the cell. Thus, the values of the fuel utilization ($FU$) reported in this study are influenced by the setup. However, as the same cell housing is used for all investigated cells, the magnitude of the bypass flow rate is the same in all experiments.

## *6.2 Sulfur poisoning in reformate-fueled systems*

Since most commercial SOFC systems so far are operated with an external fuel gas reformer, the present section aims to explore sulfur poisoning under more realistic operating conditions with $H_2/H_2O/CO/CO_2/N_2$-based fuels. Therefore, first the effect of increasing $H_2S$ concentrations and current density on the performance of a Ni/CGO-based SOFC operated on a synthetic diesel reformate gas mixture is investigated. Subsequently, the hydrogen content in the gas is lowered in order to reach operating points where CO conversion inevitably must occur.

### *6.2.1 The effect of $H_2S$ concentration and current density on Ni/CGO anodes operated on reformate fuels*

The voltage stability tests over time are illustrated in Figure 6.1 for gas mixture I (see Table 6.1) at varying current densities of $i$ = 0.25, 0.5, and 0.75 $A \cdot cm^{-2}$. In all cases, the overall voltage drop increases stepwise along with the hydrogen sulfide concentration. The initial performance drop that is caused by 1 ppm $H_2S$, is the largest, and a further increase of the hydrogen sulfide concentration only leads to smaller performance losses. The sulfur poisoning for all investigated current densities was again observed to be completely reversible, as full voltage regeneration was achieved after less than 20 h of sulfur-free operation.

Overall voltage drops and ASR increase values for all current densities are depicted in Figure 6.2. For current densities until 0.5 $A \cdot cm^{-2}$, all curves show the same characteristic behavior with a drastic change at low $H_2S$ concentrations and a saturation effect at higher concentrations. This behavior is similar to the evolution of the estimated sulfur coverage on Ni, calculated according to the Temkin isotherm.[122] Interestingly, the poisoning behavior at 0.75 $A \cdot cm^{-2}$ no longer follows this characteristic behavior anymore. At this current density, voltage drop and ASR increase values do not show a saturation effect but continue increasing. As with increasing current densities the fuel utilization increases ($FU_{H2}$ = 52 %) as well, this behavior could indicate the influence of the inhibited water gas shift reaction or CO oxidation. This could entail mass transport limitations in addition to the poisoned hydrogen oxidation reaction, which leads to a higher sensitivity of the ASR towards small variations of $H_2S$ concentrations. Hence, the observed behavior is likely to be associated with the conversion of CO.

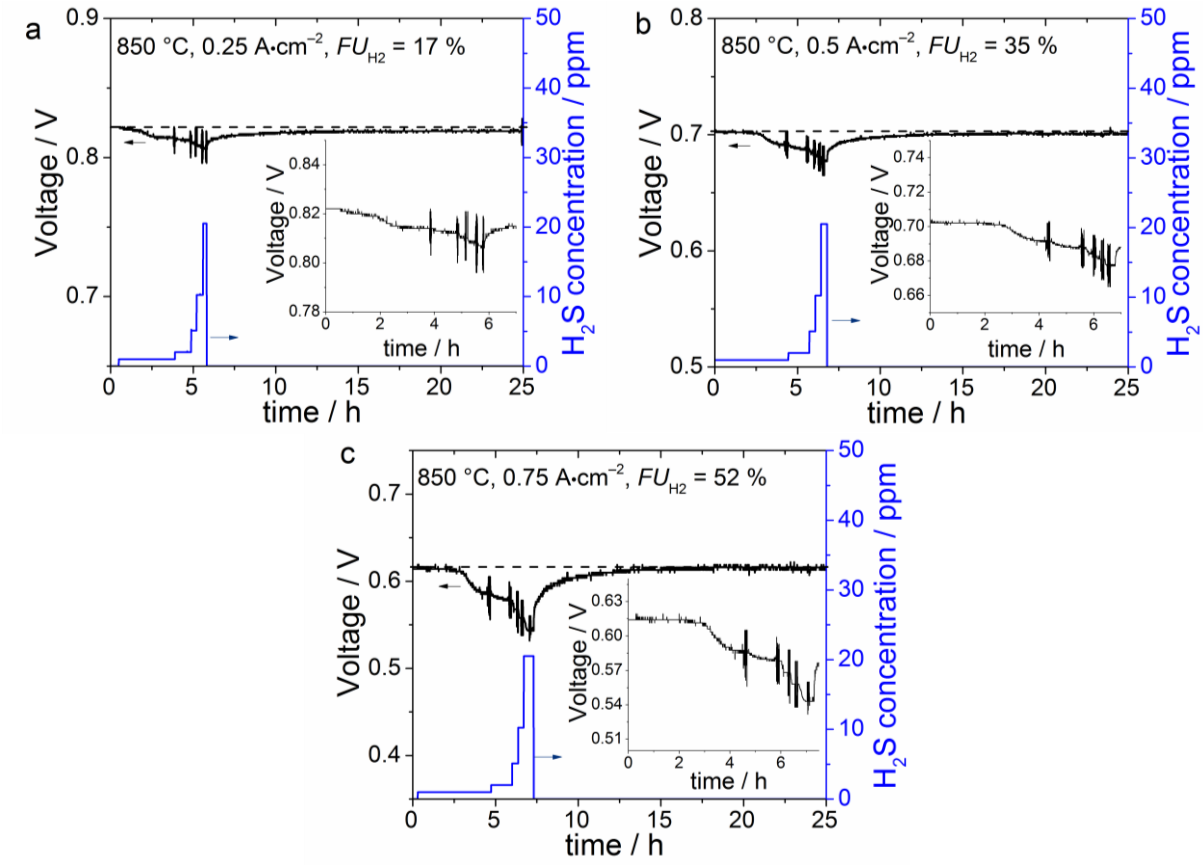


Figure 6.1. Transient sulfur poisoning tests of the Ni/CGO-based cell fueled with gas mixture I and with a stepwise increase of $H_2S$ concentration between 0 – 20 ppm. The different current densities a) 0.25 A·cm$^{-2}$, b) 0.5 A·cm$^{-2}$ and c) 0.75 A·cm$^{-2}$ are shown. The left y-axis shows the voltage behavior (black) during poisoning and recovery phase and the right y-axis the imposed $H_2S$ concentration (blue). Dotted lines indicate the value of the initial voltage before poisoning and are for guiding the eye. The inset in the figures is a magnification of the voltage evolution during the poisoning phase. The oscillation of the cell voltage in the figures is caused by electrochemical impedance measurements that were recorded after the saturation of each performance drop.

The ASR increase curves show the lowest values for the sulfur poisoning test at 0.5 A·cm$^{-2}$. This indicates a general mitigation effect of current density, in agreement with Figure 5.14 in the previous section and as reported for Ni/YSZ anodes.[76] However, the test at OCV displays lower ASR increase values in comparison to the 0.25 A·cm$^{-2}$ test, which is also in agreement with the sulfur poisoning behavior of Ni/CGO10 anodes in $H_2/H_2O$ fuel gases (Figure 5.14b). The similarity of this behavior in both fuels indicates that sulfur poisoning at low current densities is governed by its effect on electrochemical hydrogen oxidation. However, the reason

for particularly low ASR increase at OCV is still unclear. The highest ASR increase values of the test at 0.75 $A \cdot cm^{-2}$ further suggest that, at the corresponding fuel utilization values, the sulfur poisoning of CO conversion has a strong effect on the performance losses.

However, already the ASR increase of 0.06 $\Omega \cdot cm^2$ at 0.5 $A \cdot cm^{-2}$ in reformate fuel is considerably larger than the 0.02 $\Omega \cdot cm^2$ value (also at 0.5 $A \cdot cm^{-2}$) for the pure $H_2/H_2O$ fuel system in Figure 5.22. In order to check if this is a result of the changed $pH_2S/pH_2$ ratio or of additional resistances due to CO conversion, a reference experiment without $CO/CO_2$ was conducted. In this poisoning experiment, a fuel gas mixture consisting of 32 % $H_2$, 14 % $H_2O$ and 54 % $N_2$ was employed. This corresponds to the reformate with CO replaced by hydrogen and $CO_2$ replaced by nitrogen and represents the ideal case where all carbon monoxide can readily be converted to hydrogen via the water gas shift reaction. In the corresponding reformate, such high hydrogen contents will not be reached, as it already represents the equilibrium composition under this operating conditions and conversion of CO into hydrogen via the water gas shift reaction will only occur after hydrogen is consumed by the electrochemical reaction in the first place. However, small variations in the hydrogen partial pressure might occur during operation. Therefore, and as the sulfur coverage on Ni is a function of $pH_2S/pH_2$,[122] the reference fuel mixture IV was considered to represent a "best-case scenario": that is, the highest dilution of $H_2S$ in $H_2$, with the lowest possible resistance increase.

Judging from the voltage drop and ASR increase (Figure 6.2a+b), the reference test in the $H_2/H_2O$ fuel system does not result in a considerably lower extent of sulfur poisoning, since these values nearly coincide with the corresponding values for reformate operation. Therefore, it can be concluded that sulfur poisoning on Ni/CGO anodes at low fuel utilization is largely governed by the effect of sulfur on hydrogen oxidation. Thus, the defining parameter responsible for large performance drops in reformate fuel at low current densities is the $pH_2S/pH_2$ ratio.

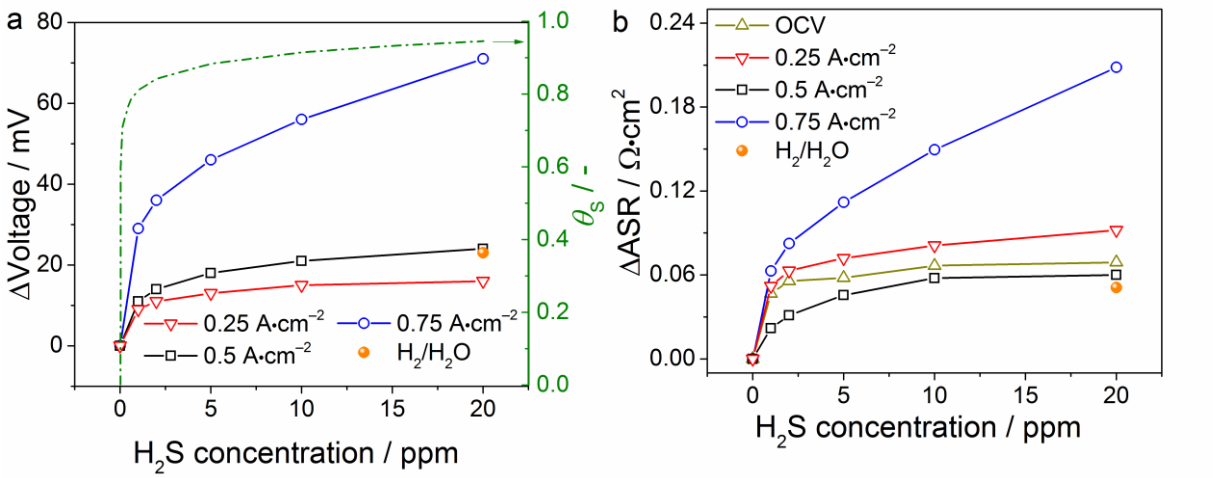


Figure 6.2. (a) Accumulated voltage drop and (b) accumulated ASR increase for fuel gas mixture I (Table 6.1) at $T$ = 850 °C, as a function of $H_2S$ concentration at different current densities. The $H_2/H_2O$ measurement (gas mixture II) represents a reference measurement at 0.5 A·cm$^{-2}$ with a fuel consisting of 32 % $H_2$, 14 % $H_2O$ and 54 % $N_2$ (orange cross). The right y-axis in a) shows the calculated sulfur coverage on Ni according to the Temkin isotherm derived by Alstrup et al.[122]

The introduction of hydrogen sulfide did not cause a voltage change at OCV, thus, the influence of sulfur was captured by electrochemical impedance spectroscopy. The corresponding spectra are illustrated in Figure 6.3a+b. Additionally, impedance spectra at 0.75 A·cm$^{-2}$ are displayed in Figure 6.3c+d. The Nyquist plots highlight the reported ASR increase, which is a lot more significant for 0.75 A·cm$^{-2}$. At both current densities, this is reflected by an increase of the imaginary impedance at frequencies between 1 – 10 Hz. In chapter 5, an anode surface process was identified at this frequency. This process was shown to depend on temperature and anode gas phase composition, and interpreted to correspond to the anode charge transfer reaction. Its low frequency is due to the large chemical capacitance caused by the oxygen nonstoichiometry of CGO.

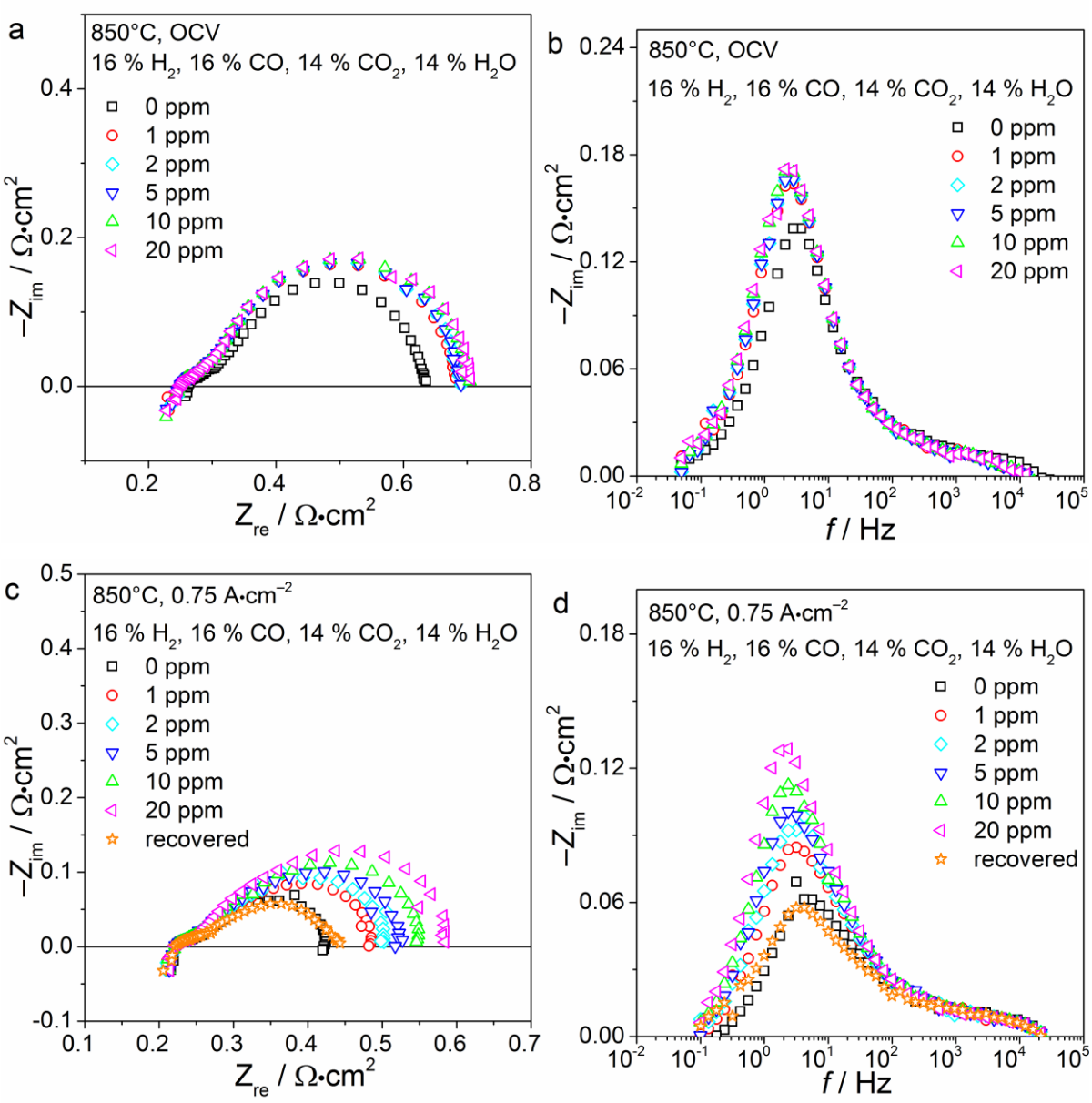


Figure 6.3. (a) Nyquist and (b) imaginary impedance plots of impedance spectra of the Ni/CGO10-based cell recorded for gas mixture I (see Table 6.1) at temperature $T$ = 850 °C, OCV and different $H_2S$ concentrations between 0 and 20 ppm. (c) and (d) show Nyquist and imaginary impedance plots for $i$ = 0.75 A·cm$^{-2}$.

In addition to the influence at this frequency, no further change in the impedance spectra at 0.75 A·cm$^{-2}$ could be observed. However, earlier studies on the sulfur poisoning of the water gas shift reaction on Ni/YSZ anode-supported cells have witnessed a mass transport limitation at similar frequencies of ~1 Hz, which overlaps the Ni/CGO anode process in the present work.[100,102,110] This mass transport limitation is caused by the deactivation of the water gas shift reaction and causes changes in the impedance spectra due to effects on $CO/CO_2$ diffu-

sion, $H_2/H_2O$ diffusion and gas conversion. In addition to that, the cathode charge transfer process lies in the frequency range between 1 and 10 Hz as well, as the variation in $pO_2$ affects the impedance response at this frequency range (Figure S9). Therefore, the different processes cannot be separated.

### *6.2.2 Influence of sulfur on carbon monoxide conversion on Ni/CGO and Ni/YSZ*

To obtain further information about the sulfur poisoning behavior of CO conversion on Ni/CGO, a number of *i-V* curves were recorded for both the Ni/CGO- and the Ni/YSZ-based cells. The fuel gas was changed to mixture III (see Table 6.1) with a reduced hydrogen content in order to make the sulfur influence on the CO oxidation more clearly visible. As the sulfur poisoning on Ni/YSZ has been extensively investigated in numerous fuel systems over the years,[74,77,80,100,102,110] a comparison between the different anodes can give important insights into the different underlying reaction mechanisms. Figure 6.4a shows the comparison between the data of the Ni/CGO anode fueled with the reformate and those for a reference gas (gas mixture IV) consisting of 7 % $H_2$, 7 % $H_2O$ and 86 % $N_2$, both of them with and without the addition of 20 ppm $H_2S$. The reference fuel was chosen in order to represent a system in which the oxidation of CO is completely disabled and the gases CO and $CO_2$ are assumed to be inert. Analogous data are depicted for Ni/YSZ in Figure 6.4b.

The Ni/CGO-based cell is operated on a maximum hydrogen utilization of 181 % at a current density of 1.14 $A \cdot cm^{-2}$ and a voltage of 0.47 V. Thus, at this operating point a significant amount of CO is converted. The sulfur poisoning of this anode results in a severe performance loss and only leads to a maximum current density of 0.64 $A \cdot cm^{-2}$ at 0.3 V. The reference fuel consisting of $H_2$ and $H_2O$ only displays a small performance drop from 0.44 $A \cdot cm^{-2}$ to 0.39 $A \cdot cm^{-2}$, which again demonstrates the high sulfur tolerance of Ni/CGO anodes towards hydrogen oxidation. The maximum fuel utilization in the case of $H_2/H_2O$ operation reaches around 70 %. Therefore, losses due to bypasses and a nonoptimized gas flow profile can amount to up to 30 %. Still, under poisoning conditions a hydrogen fuel utilization of 101 % is obtained with the reformate fuel without reaching the limiting current density. Moreover, a comparison between the two *i-V* curves under sulfur exposure clearly shows a significantly better performance of the reformate-fueled cell. Therefore, it can be concluded that CO oxidation is still active under reformate operation and exposure to 20 ppm $H_2S$.

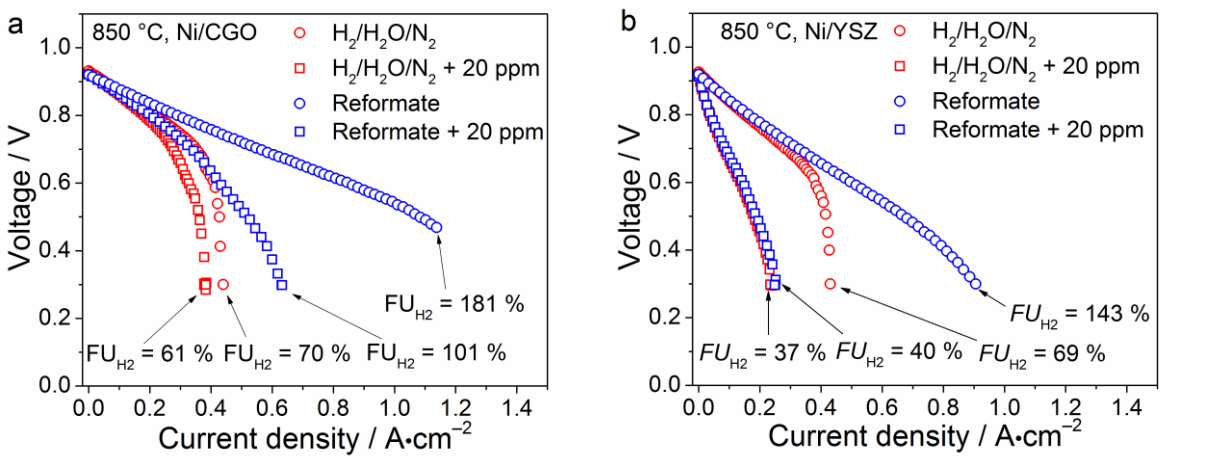


Figure 6.4. *i-V* curves of the (a) Ni/CGO- and (b) Ni/YSZ-based cells. Experiments were conducted at 850 °C. The reformate consisted of gas mixture III (blue) containing 7 % $H_2$, 7 % $H_2O$, 20 % CO, 20 % $CO_2$, and 46 % $N_2$, and the reference mixture IV(red) containing 7 % $H_2$, 7 % $H_2O$, 86 % $N_2$. *i-V* curves were recorded with (squares) and without (circles) the addition of 20 ppm $H_2S$.

The Ni/YSZ-based cell fueled with reformate is initially also operated in a regime where CO is oxidized ($FU_{H2}$ = 143 %) and shows a better performance than in the experiment without $CO/CO_2$. However, after exposure to 20 ppm $H_2S$ the *i-V* curves of both fuel gas mixtures coincide. This is a clear indication that CO conversion is fully deactivated on these cells, implying that both the water gas shift reaction and electrochemical CO oxidation are completely blocked under these conditions. Furthermore, these experiments demonstrate that the increased sulfur tolerance of Ni/CGO anodes not only is limited to systems with $H_2/H_2O$ fuel gases but also extends to reformate operation. However, so far it is unclear if the reason for this increased sulfur tolerance in reformate-operation is the activity of the water gas shift reaction or the electrochemical CO oxidation reaction, or possibly both. Therefore, sulfur poisoning experiments of Ni/CGO and Ni/YSZ in $CO/CO_2/N_2$ fuels are shown in the following subsection.

### *6.3 Sulfur poisoning of electrochemical CO oxidation on Ni/CGO and Ni/YSZ*

Similarly to the previous section, *i-V* curves were measured in order to assess the effect of sulfur poisoning on CO oxidation. Experiments under the same conditions were carried out for Ni/CGO (Figure 6.5a) and Ni/YSZ (Figure 6.5b) with a gas phase composition of 20 % CO, 20 % $CO_2$, and 60 % $N_2$ with and without addition of 20 ppm hydrogen sulfide. This is the equilibrium gas composition at 850 °C; thus, catalytic reactions at OCV are avoided.

Moreover, coke formation under the operating conditions was ensured not to be favorable by thermodynamic calculations. A comparison of the maximum current density at a cell voltage of 0.4 V demonstrates that the Ni/CGO-based cell (0.91 $A \cdot cm^{-2}$) shows a significantly better performance than Ni/YSZ (0.38 $A \cdot cm^{-2}$). Due to different processing conditions and previous poisoning experiments, which caused irreversible degradation on Ni/YSZ, this difference in performance is no proof of an inherently higher activity of Ni/CGO towards CO oxidation. However, exposure of the two cells to hydrogen sulfide reveals interesting mechanistic details about the behavior of the electrodes. Sulfur poisoning of Ni/YSZ with 2 ppm $H_2S$ leads to a nearly immediate breakdown of the cell voltage after the beginning of the voltage variation. The maximum achieved current density is 0.002 $A \cdot cm^{-2}$, which clearly illustrates that CO oxidation is fully deactivated under these conditions. This also leads to the observation of an interesting phenomenon during the sulfur poisoning process at OCV (Figure 6.6). While the cell voltage of the Ni/CGO-based cell stays constant throughout the experiment, the cell voltage of the Ni/YSZ-based cell quickly drops from 0.922 V over 0.771 V (2 ppm) and 0.727 V (10 ppm) to 0.712 V (20 ppm). After the hydrogen sulfide supply is switched off, the OCV slowly recovers back to the initial value within 24 h.

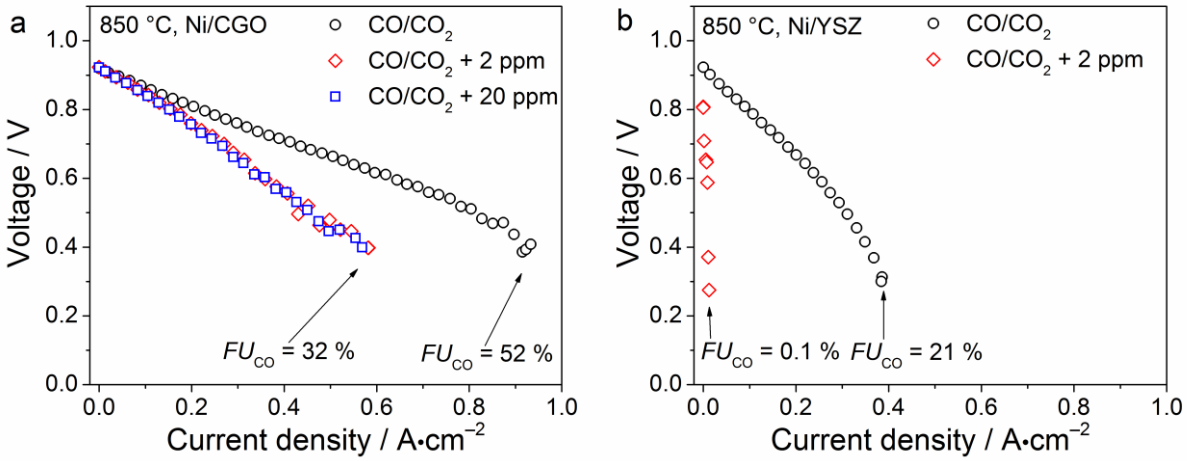


Figure 6.5. *i-V* curves of the (a) Ni/CGO and the (b) Ni/YSZ-based cell. Experiments were conducted at 850 °C. The fuel gas mixture consisted of gas mixture V (see Table 6.1). *i-V* curves were recorded with (squares) and without (circles) the addition of 20 ppm $H_2S$.

So far, an influence of sulfur poisoning on OCV values has only been observed for internal methane steam reforming on Ni/YSZ, since in this case the blockage of the Ni surface hinders $CH_4$ conversion.[99] Thus, the gas composition is altered during the poisoning process and the

Nernst voltage changes. However, this should not be the case for pure CO oxidation since the gas phase composition is already in equilibrium. Another reason for the change in OCV could be the complete blockage of the Ni surface for CO adsorption as it has already been indicated in the literature.[102] This is consistent with more fundamental studies of Ni(111) surfaces, which indicated that CO adsorption is entirely inhibited for surface coverages higher than 0.3 monolayer (ML).[212] This is also in agreement with the calculations in chapter 4 (Figure 4.11), where CO coverage on Ni was shown to approach 0. Recent elementary kinetic modeling studies indeed showed that CO oxidation proceeds via CO adsorption on Ni.[46,47] Hence, complete surface blockage would result in the disappearance of the corresponding electromotive force. Consequently, the OCV must be related to a different galvanic chain. Ni oxidation is a common phenomenon in fuel gases with low hydrogen content. However, in a reference measurement where the entire anode gas supply was substituted with pure nitrogen, an OCV of 0.655 V was observed. This is consistent with previously reported OCV values for nickel oxidation around 0.7 V.[213] As the observed voltage of the poisoned Ni/YSZ anode is considerably larger, it is likely not to be caused by Ni oxidation. In further experiments (not shown here), the OCV of Ni/YSZ under $CO/CO_2$ operation was observed to increase with carbon monoxide and decrease with carbon dioxide gas phase concentration after sulfur poisoning. Consequently, the OCV is still associated with a carbon monoxide oxidation process with carbon dioxide as product. Since the OCV is changing only under sulfur exposure, it is postulated that carbonyl sulfide (COS) is formed on the surface, which was shown to be the second most thermodynamically stable sulfur-containing species in CO-rich gas phase mixtures.[214] The lowered OCV could then correspond to the reaction

$$COS_{Ni} + 3O^{2-} \rightleftharpoons CO_{2,g} + SO_{2,g} + 6e^{-} \quad (50)$$

Furthermore, it was shown that $Ni_3S_2$ formation can occur for $pH_2S/pH_2$ values above $10^{-3}$ (100 ppm).[71] Hence, as hydrogen is absent in gas mixture V, it is possible that Ni sulfide is created upon anode sulfur exposure, which could cause the $CO_2$ and $SO_2$ to form via reaction of CO and $Ni_3S_2$. Since the processes on Ni at OCV occur under equilibrium conditions in the absence of current, Ni sulfide formation can also reasonably be expected on Ni/CGO. Therefore, neither a full Ni surface blockage with sulfur nor Ni sulfide formation can solely explain the different electrode behaviors at OCV. Whatever the underlying mechanism of the OCV decrease in the case of Ni/YSZ is, the negligible maximum current density at 0.4 V shows that the kinetics of the corresponding carbon monoxide oxidation reaction are slow and a concurrent surface reaction such as that of Eq. 50 can lead to significant OCV mixed potential for-

mation.

Although the influence of sulfur poisoning of the Ni/CGO electrode on CO oxidation is significant as well and leads to a reduction in the maximum current density to 0.56 $A \cdot cm^{-2}$ at 20 ppm, the CO oxidation process is still active. The impedance spectra in Figure S10 conducted at OCV show a considerable ASR increase after sulfur exposure as well, which is reflected by an increased intensity in the imaginary impedance at around 1 Hz. Thus, carbon monoxide oxidation on Ni/CGO displays the same relaxation time as hydrogen oxidation (see Figure 6.3b). An increase in $H_2S$ concentration from 2 to 20 ppm does not have a significant influence on the maximum current density.

Due to the unavailability of water and hydrogen in these experiments, the carbon monoxide must be electrochemically oxidized. This demonstrates that electrochemical CO oxidation on Ni/CGO shows high reaction rates even under severe sulfur exposure and is likely to bear the main responsibility for the comparatively high performance under reformate operation in the previous section. Sulfur removal from the Ni surface via $SO_2$ formation can be excluded to be the reason for the stable voltage of Ni/CGO in Figure 6.6 due to the absence of current. This shows that the CGO surface is dominating the electrochemial carbon monoxide oxidation at least close to OCV conditions, due to its intrinsic electro-catalytic activity which was also demonstrated in Figure 5.23.[92,129–134,215,216] As pure CGO electrodes do not show a performance drop upon sulfur exposure (Figure 5.24), performance drops in Figure 6.5a are not related to CGO surface poisoning. Moreover, it has been demonstrated that sulfur diffuses into the CGO bulk at high temperatures, at least for cathodic polarization and in single crystal reduced ceria.[136,137] However, so far this diffusion process has not yet been proven to occur under realistic SOFC operating conditions.

Although removal does not occur at OCV, sulfur could still be removed from the Ni surface at higher current densities. However, according to DFT calculations the binding energy of CO to the Ni surface is considerably more positive than that of sulfur, making a preferred sulfur oxidation via oxygen spillover unlikely.[115,217] Nonetheless, the hypothesis of a rapid oxygen spillover from CGO to Ni and a corresponding $SO_2$ formation cannot definitely be discarded. This would still enable the adsorption of CO on the Ni surface and includes the possibility of an active water gas shift reaction, which could represent the major difference between the two electrodes. In order to investigate this mechanistic hypothesis, methane steam reforming experiments were carried out and are shown in the next section.

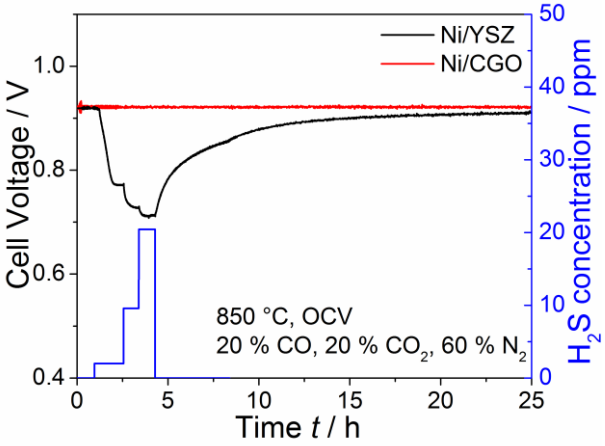


Figure 6.6. Transient sulfur poisoning tests of the Ni/CGO-based (red) and Ni/YSZ-based (black) cells fueled with gas mixture V and an $H_2S$ concentration of 20 ppm. The experiment was carried out at 850 °C and OCV. The left axis shows the voltage behavior during poisoning and recovery phase and the right axis the imposed $H_2S$ concentration (blue).

### *6.4 Sulfur poisoning of methane steam reforming*

Methane steam reforming experiments on Ni/CGO were carried out at OCV with fuel gas mixture VI (Figure 6.7a). Sulfur poisoning of this anode leads to a fast voltage drop from 0.998 to 0.908 V at 20 ppm $H_2S$, which is similar to the behavior observed for Ni/YSZ anodes.[99,103,106] The final cell voltage nearly exactly coincides with the theoretical cell voltage that is obtained under the assumption that no methane is converted (0.907 V). This is also reflected in a low overall performance of the poisoned cell as illustrated in the *i-V* curve in Figure 6.7b. At a current density of 0.84 A·cm$^{-2}$ the cell already shows mass transport limitations as indicated by the declining slope of the curve. The hydrogen utilization of 58 % suggests that, if at all, only a small amount of methane is converted to hydrogen. At the same time, the curve of the sulfur-free sample still exhibits a stable slope at current densities of more than 1.1 A·cm$^{-2}$ ($FU_{H2}$ = 81 %) and no indications of mass transport problems, demonstrating that methane is converted under these conditions. From these experiments, it can be deduced that methane steam reforming on Ni/CGO is fully blocked after exposure to 20 ppm $H_2S$.

This is probably related to the sulfur poisoning of the Ni surface, since Ni is an effective methane steam reforming catalyst. Since close to 0 % methane conversion could be observed at 20 ppm $H_2S$, it is also improbable that the CGO surface plays a significant role in the methane reforming process. Although sulfur was suggested to adsorb on CGO, it is unlikely to block

the full surface as it tends to diffuse into the bulk at high temperatures.[135–137] Thus, the inactivity of CGO towards methane reforming probably also holds for non-sulfur conditions. This is consistent with investigations, which showed that ceria is almost inactive with respect to C-H bond cracking.[218]

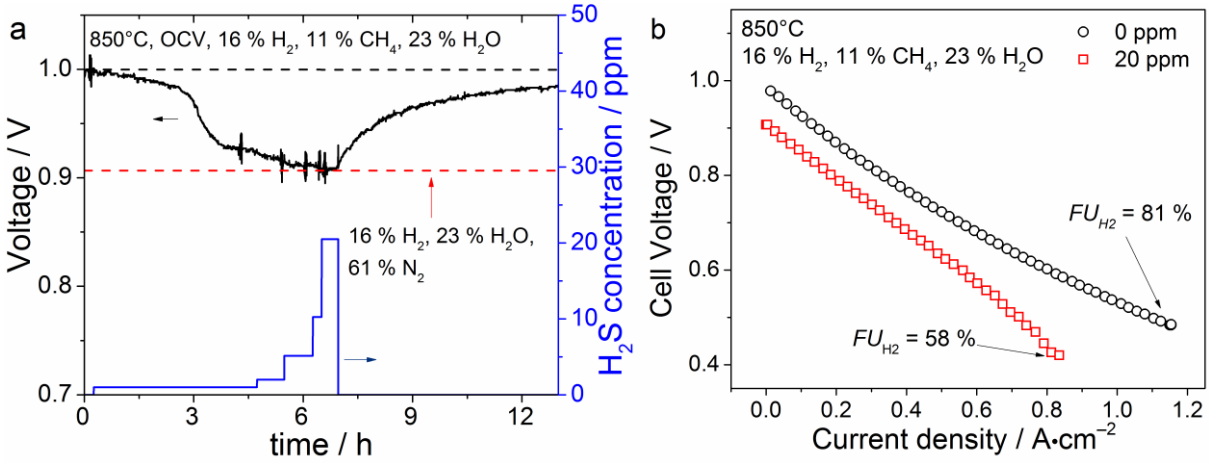


Figure 6.7. (a) Transient sulfur poisoning tests of the Ni/CGO-based cell fueled with gas mixture VI and with a stepwise increase of $H_2S$ concentration between 0 – 20 ppm. The experiment was carried out at 850 °C and OCV. The left axis shows the voltage behavior (black) during the poisoning and recovery phase and the right axis the imposed $H_2S$ concentration (blue). The dotted black line indicates the value of the initial voltage before poisoning and is for guiding the eye. Moreover, the dotted red line represents the theoretical Nernst voltage of a gas mixture with 16 % $H_2$, 23 % $H_2O$, and 61 % $N_2$. The oscillation of the cell voltage in the figure is caused by electrochemical impedance measurements that were recorded after the saturation of each performance drop. (b) *i-V* curve of the Ni/CGO-based cell before and after exposure to 20 ppm $H_2S$.

The water gas shift reaction and methane steam reforming have been shown to display the same sulfur poisoning behavior on Ni/YSZ anodes with a complete deactivation already at an $H_2S$ concentration of about 20 ppm.[99,102,106,111,219] This similar behavior has been attributed to the participation of water in both reactions.[111] Moreover, it was suggested that these two catalytic reactions occur on the same active sites.[86] If this analogy is transferred to the Ni/CGO electrode, it can be considered to be highly likely that the water gas shift reaction on Ni is fully deactivated as well for $H_2S$ concentrations as low as 20 ppm.

### *6.5 Discussion of sulfur poisoning of Ni/CGO under reformate operation*

The experiments in the present chapter have clearly demonstrated that the high sulfur tolerance of Ni/CGO anodes not only is limited to hydrogen oxidation, but also extends to the oxidation of carbon monoxide. As explained earlier, hypothetical explanations of the high sulfur tolerance of Ni/CGO include the inherent electro-catalytic activity of CGO,[129–134] the oxidation of nickel-adsorbed sulfur to $SO_2$ involving an oxygen spillover from CGO to Ni,[85,92,135] and sulfur diffusion from the surface to the CGO bulk phase.[136,137] However, on the basis of the present experiments, the first explanation can be considered as the most likely one. The electrochemical CO oxidation at the TPB, methane steam reforming and the water gas shift reaction seem to be fully deactivated due to nickel-adsorbed sulfur; thus, the electro-catalytic activity of CGO is concluded to be the reason for continued carbon monoxide oxidation.

A schematic illustration of the proposed underlying mechanism is depicted in Figure 6.8a+b. It is likely that under sulfur-free operation, the water gas shift reaction on Ni (Eq. 22) is the dominating pathway for CO conversion into hydrogen and $CO_2$ due to its rapid kinetics.[182] After sulfur exposure, the water gas shift reaction on nickel is probably fully deactivated for an $H_2S$ concentration of approximately 20 ppm, which is concluded based on the analogy between the WGS and MSR reactions.[102,111] As the nickel surface is likely to be completely blocked for CO adsorption (also shown by the calculated coverage values in Figure 4.11), an electrochemical oxidation of CO on Ni at the TPB via oxygen spillover as described by Eq. 51 is also unlikely.

$$CO_{Ni} + O^{2-}_{CGO} \rightleftharpoons CO_{2,Ni} + 2e^- \tag{51}$$

Instead, CO oxidation then proceeds via an electrochemical pathway on the CGO surface:

$$CO_{(g)} + O^{2-}_{CGO} + Ce^{4+} \rightleftharpoons CO_{2,(g)} + Ce^{3+} + \square_{CGO}, \tag{52}$$

where $\square_{CGO}$ represents a free active surface site on CGO. During the reaction, similar to the case for hydrogen oxidation,[138,220] the surface cerium atoms change their valence state from $Ce^{4+}$ to $Ce^{3+}$.[221] Under reformate operation and sulfur exposure, carbon monoxide oxidation on CGO allows higher fuel utilization values in comparison to that on Ni/YSZ anodes. Although this surface charge transfer process still proceeds under sulfur exposure, the significant poisoning of pure CO oxidation on Ni/CGO (Figure 6.5a) indicates that the oxidation at the TPB (Eq. 51) probably occurs with a faster reaction rate in sulfur-free fuel gases.

While electrochemical CO oxidation is often completely neglected in SOFC modeling literature,[69,222] the present study shows that this is not the case for Ni/CGO anodes under sulfur

exposure since CO can also be electrochemically oxidized on the CGO surface. The possibility of high CO oxidation rates on doped ceria was already indicated earlier.[90,221,223] Recently, it was reported that CGO model electrodes with CGO nanoparticles can even show higher electrocatalytic activity towards $CO/CO_2$ in comparison to that towards $H_2/H_2O$ reactions.[223] CO oxidation on CGO was shown to probably proceed via a Mars-van-Krevelen mechanism.[205] Therefore, the global reaction described in Eq. 52 could possibly be further resolved into an oxygen discharge (Eq. 53)[35] and a catalytic CO oxidation reaction (Eq. 54).

$$O^{2-}_{CGO,b} + 2Ce^{4+} \rightleftharpoons 2Ce^{3+} + O_{CGO} \quad (53)$$

$$CO_{(g)} + O_{CGO} \rightleftharpoons CO_{2,(g)} + \square_{CGO} \quad (54)$$

At a lower temperatures of 500 °C, Feng et al. suggested CO oxidation on CGO to occur via a carbonate molecule.[221] However, this might change at higher temperatures. Thus, the dominating mechanism of CO oxidation on ceria is still unclear.

In general, the rate of the methane steam reforming reaction on Ni depends on the sulfur coverage to the third power, $(1 - \theta_S)^3$, and thus, is more severely affected than the rate of the electrochemical hydrogen oxidation on Ni/YSZ that follows the dependence $(1 - \theta_S)$.[87,88,108] Kuhn et al. have demonstrated a similar sulfur dependency also for the water gas shift reaction.[111] Russner et al. even showed a stronger deactivation of the WGS in comparison to the MSR reaction.[219] Thus, hydrogen oxidation can still be active under operating conditions where methane steam reforming and the water gas shift reaction are fully deactivated. This origin of this behavior is that hydrogen is still able to adsorb on Ni in conditions where CO adsorption is blocked (Figure 4.11).

Ceria is easily oxidized by $H_2O$ as shown in the literature (Eq. 55).[224] This is also reflected by the dependence of the capacitance on the operating conditions ($pO_2$, $T$).

$$H_2O + 2Ce^{3+} \rightleftharpoons 2Ce^{4+} + O_{CGO} + H_2 \quad (55)$$

Since reaction 52 was shown to be possible on the CGO surface via experiments in $CO/CO_2$ fuels, the combination of the reactions (7) + (11) is the water gas shift reaction, which proceeds essentially via a redox mechanism. This was already proposed in the literature for ceria-supported precious metal.[225]

In this case, the oxygen necessary for the reaction can also be supplied from the water in the gas phase. Accordingly, under the present operating conditions the water gas shift reaction should still be active due to the high activity of CGO towards CO oxidation. Furthermore, as proposed in the previous chapter, on Ni/CGO hydrogen could either be dissociated on Ni or also be directly oxidized on CGO. However, hydrogen oxidation on the CGO surface was

shown not to be poisoned by sulfur. As indicated earlier, under sulfur-free conditions it is possible that the TPB and DPB processes are competitive and the prevailing pathway varies depending on the microstructure.

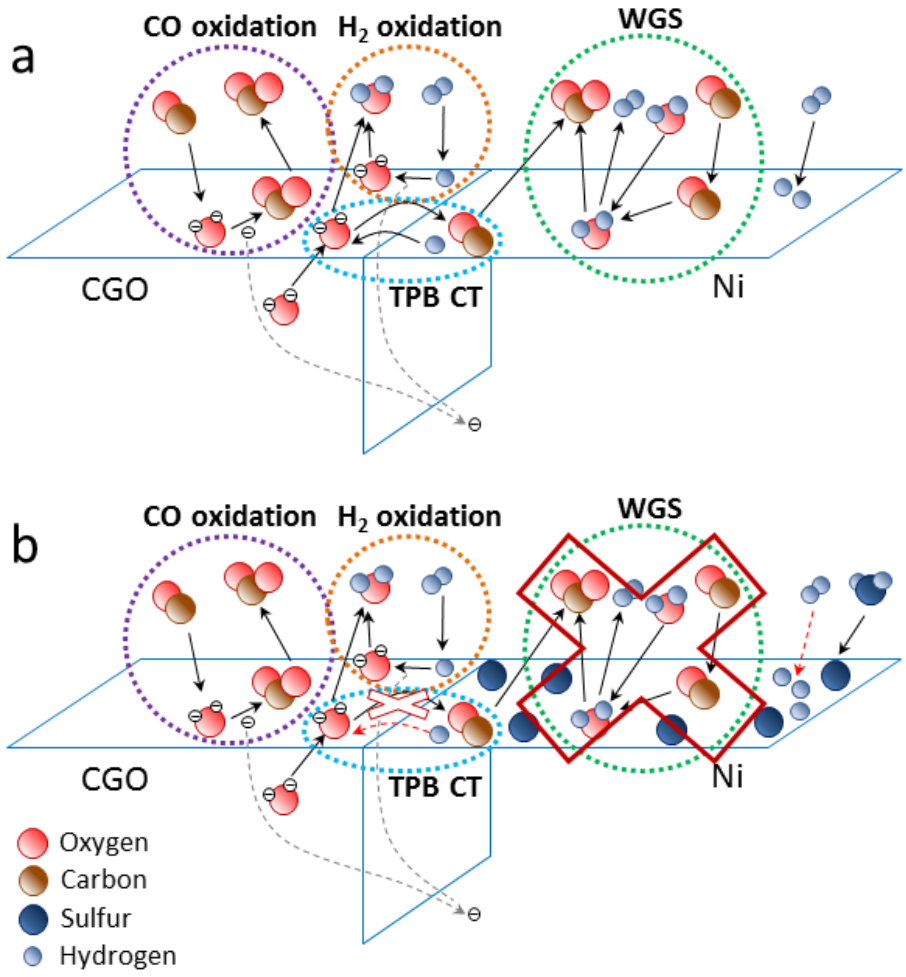


Figure 6.8. Schematic illustration of the reaction mechanism of the fuel oxidation (a) without and (b) with sulfur poisoning on Ni/CGO-based anodes operated on reformate mixtures. Reactions fully blocked by sulfur are signified by a red cross. Reactions that still proceed, but at a lower reaction rate are illustrated with dashed red lines. Dashed gray lines indicate the pathway of electron transfer. Dashed circles signify the WGS, the charge transfer reactions at the triple phase boundary (TPB CT), electrochemical oxidation on CGO, and electrochemical hydrogen oxidation on CGO.

### *6.6 Conclusions*

The sulfur poisoning behavior of ESC with Ni/CGO10 anodes operating on reformate fuels was investigated by means of current-voltage characteristics and electrochemical impedance

spectroscopy. In order to draw mechanistic conclusions, a variety of different fuels including methane and carbon monoxide containing reformates were used and a comparison to Ni/YSZ-based SOFC was carried out. It was revealed that the poisoning behavior is mainly governed by a hindered hydrogen oxidation reaction at low current densities in $H_2/H_2O/CO/CO_2$ fuel gas mixtures. At higher current densities, the poisoning becomes more pronounced, indicating a particularly severe poisoning effect on the carbon monoxide conversion reactions. However, the ability of Ni/CGO anodes to convert CO at $H_2S$ concentrations up to 20 ppm was demonstrated, which was shown not to be the case for Ni/YSZ. The sulfur poisoning behavior of Ni/CGO anodes was reversible for the investigated short exposure times. Sulfur poisoning experiments of methane steam reforming suggest that the Ni surface is entirely blocked and the water gas shift reaction is fully deactivated. However, electrochemical CO oxidation on the CGO surface was shown to be still active for hydrogen sulfide concentrations of 20 ppm. The present results clearly demonstrate that the high sulfur tolerance of Ni/CGO not only is limited to $H_2/H_2O$ fuel systems but also extends to CO-containing gases.

In order to further explore the potential use of Ni/CGO anodes under operation in sulfur-containing fuel gases, in the following chapter their long-term stability is investigated.

# 7 Sulfur poisoning of Ni/CGO: A long-term study outlining stable SOFC operation

In chapter 5, the sulfur poisoning behavior of Ni/CGO in $H_2/H_2O$ fuels was found to be promising due to the observed lower performance drops and complete reversibility of the poisoning. In chapter 6, it was shown that, in contrast to Ni/YSZ, Ni/CGO anodes are even able to convert carbon monoxide on the CGO surface under severe sulfur poisoning conditions, which further underlines their potential use in sulfur poisoning conditions. However, there are no reports about the long-term degradation effects on Ni/CGO in literature although this is vital in determining the acceptable limits of sulfur impurities in carbon-containing fuels. The few long-term sulfur poisoning studies existing in literature have focused on Ni/YSZ anodes, whose poor long-term stability was demonstrated for the exposure to $H_2S$ over a couple hundreds of hours.[106,112]

This chapter presents the results of long-term degradation experiments of Ni/CGO-based anodes exposed to a variety of $H_2S$-containing $H_2/H_2O/N_2$ fuel mixtures at 900 °C. The degradation behavior is monitored *operando* by means of electrochemical impedance spectroscopy. Furthermore, a 3D reconstruction technique using FIB-SEM tomography is applied for quantitative characterization of the microstructural evolution of the Ni/CGO composite anode during the long-term tests, which is then correlated to the anode performance degradation.

Most of the results presented in this chapter were already previously published.[226]

## *7.1 Testing procedure*

In the present chapter, SOFC with different anode compositions are tested. The tested cells are cell C and D, both based on Ni/CGO10 anodes and an additional 5 µm thick CGO10 adhesion layer between electrolyte and functional anode layer. Further details about their geometry and composition are given in Table 3.1 and SEM images of the initial microstructure are shown in Figure 3.3.

In the present chapter, four long-term experiments are presented with different sulfur exposure times between 200 and 1500 h. All tested cells and the corresponding testing conditions are shown in Table 7.1. All cells were operated at 900 °C with $H_2/H_2O/N_2$ fuel mixtures and different $H_2S$ concentrations. The comparatively high operating temperature was chosen to enable higher operating current densities and to accelerate possible thermally activated changes in the anode microstructure.

Table 7.1. Overview of test specifications of all four long-term tests.

| | Test acronym | Cell | Anode gas | $H_2S$ concentration [ppm] | Overall duration of experiment [h] | Current density [$A \cdot cm^{-2}$] |
|---|---|---|---|---|---|---|
| 1500 h test | 1500h-0ppm | D | 100 % $H_2$ | 0 | 1500 | 0.5 |
| | 1500h-1ppm | D | 100 % $H_2$ | 1 | 1500 | 0.5 |
| | 1500h-10ppm | D | 100 % $H_2$ | 10 | 1500 | 0.5 |
| 200 h test | 90h-8A-0ppm | D | 25 % $H_2$, 75 % $N_2$ | 0 | 90 | 0.5 |
| | 90h-12A-0ppm | D | 25 % $H_2$, 75 % $N_2$ | 0 | 90 | 0.75 |
| | 200h-2A-0ppm | D | 25 % $H_2$, 75 % $N_2$ | 0 | 200 | 0.125 |
| | 200h-2A-10ppm | D | 25 % $H_2$, 75 % $N_2$ | 10 | 200 | 0.125 |
| | 200h-8A-10ppm | D | 25 % $H_2$, 75 % $N_2$ | 10 | 200 | 0.5 |
| | 200h-12A-10ppm | D | 25 % $H_2$, 75 % $N_2$ | 10 | 200 | 0.75 |
| 915 h test | 915h-0ppm | C | 25 % $H_2$, 75 % $N_2$ | 0 | 915 | 0.75 (675 h), 0.5 (240 h) |
| | 915h-10ppm | C | 25 % $H_2$, 75 % $N_2$ | 10 | 915 | 0.75 (675 h), 0.5 (240 h) |
| 500 h test | 170h-0ppm | D | 25 % $H_2$, 75 % $N_2$ (0.5 $L \cdot min^{-1}$) | 0 | 170 | 0.5 |
| | 500h-2.5ppm | D | 25 % $H_2$, 75 % $N_2$ (0.5 $L \cdot min^{-1}$) | 2.5 | 500 | 0.5 |
| | 500h-10ppm | C | 25 % $H_2$, 75 % $N_2$ (0.5 $L \cdot min^{-1}$) | 10 | 500 | 0.5 |

## *7.2 Results*

Figure 7.1 shows the four long-term experiments listed in Table 7.1. In Table 7.2, a summary of the results is provided. The experiments reveal important insights into the nature of sulfur-induced degradation of Ni/CGO anodes and will be discussed in detail in the following sub-sections.

### *7.2.1 Sulfur poisoning in hydrogen-rich fuels – A 1500 h test*

The longest sulfur poisoning test in the present work was conducted on Ni/CGO10 anodes (cell D) and ran in pure hydrogen inlet gas at 0.5 $A \cdot cm^{-2}$ for a sulfur poisoning period of 1500 h (Figure 7.1a). Figure S19 depicts initial EIS measurements before start of the poisoning. The 1500h-1ppm test shows a slightly larger cell resistance, probably due to an increased gas conversion resistance, which could be caused by a slight variation in the total anode gas flow rate of the cells. However, the similar overall shape and resistance of the measurements in Figure S19 establishes a general good reproducibility of the measured cells and the employed test rig. The slightly increased initial total resistance of the 1500h-1ppm cell is the reason why the cell voltage of the 1500h-10ppm test is larger than the one of the 1500h-1ppm test during the course of the experiment. However, the 1500h-10ppm experiment still shows a larger initial voltage drop (25 mV) than the 1500h-1ppm cell (16 mV), due to an increased sulfur coverage on Ni at higher $H_2S$ concentrations. When the hydrogen sulfide supply was switched off after 1500 h, this initial voltage drop was fully recovered for both cells. The overall long-term voltage degradation values of 23 mV (1500h-10ppm test), that is a degradation rate of 15 mV/1000 h, and 25 mV (1500h-1ppm test; degradation rate of 17 mV/1000 h), are only slightly larger than the sulfur-free reference value of 14 mV (9 mV/1000 h), demonstrating that Ni/CGO anodes can indeed be operated at low degradation rates under sulfur exposure.

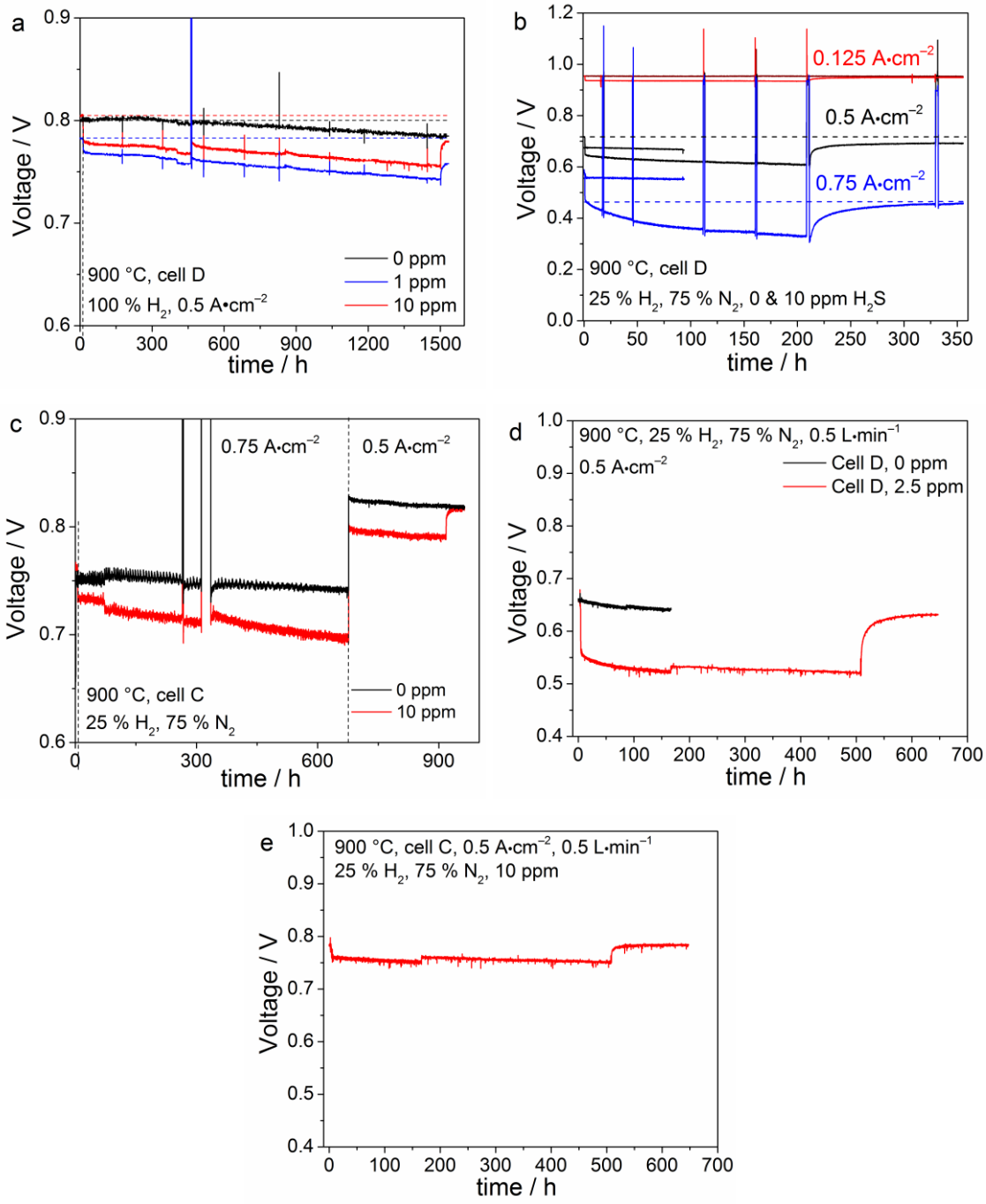


Figure 7.1. Cell voltage curves as a function of time at temperature $T$ = 900 °C and $pO_2$ = 0.21 atm. (a) Cells of type D operated at $i$ = 0.5 A·cm$^{-2}$, $pH_2$ = 1.0 atm, and with 0, 1 and 10 ppm $H_2S$. (b) Cells of type D operated at $i$ = 0.125 A·cm$^{-2}$ (red), 0.5 A·cm$^{-2}$ (black) and 0.75 A•cm$^{-2}$ (blue), $pH_2$ = 0.25 atm, $pN_2$ = 0.75 atm, and 0 & 10 ppm $H_2S$. (c) Cells of type C operated at $i$ = 0.75 A·cm$^{-2}$ (first 675 h) and 0.5 A·cm$^{-2}$ (subsequent 240 h), $pH_2$ = 0.25 atm, $pN_2$ = 0.75 atm, and with 0 (black) and 10 ppm $H_2S$ (red). (d) Cells of type D operated at $i$ = 0.5 A•cm$^{-2}$, $pH_2$ = 0.25 atm, $pN_2$ = 0.75 atm, 0.5 L•min$^{-1}$ and 0 (black) and 2.5 ppm (red). (e) One cell of type C operated at $i$ = 0.5 A·cm$^{-2}$, $pH_2$ = 0.25 atm, $pN_2$ = 0.75 atm, 10 ppm $H_2S$.

Table 7.2. Overview of the cell voltage changes for the long-term measurements. Initial and final voltages denote the cell voltages before the start of $H_2S$ exposure and after regeneration, respectively. The overpotential is calculated based upon the observed OCV and the cell voltage after the initial voltage drop.

| | Test acronym | Irreversible degradation [mV] | Initial voltage drop [mV] | Regenerated voltage [mV] | Overpotential $\eta$ [mV] |
|---|---|---|---|---|---|
| 1500 h test | 1500h-0ppm | 14 | - | - | 419 |
| | 1500h-1ppm | 25 | 16 | 15 | 455 |
| | 1500h-10ppm | 23 | 25 | 23 | 439 |
| 200 h test | 90h-8A-0ppm | 7 | - | - | 505 |
| | 90h-12A-0ppm | 5 | - | - | 622 |
| | 200h-2A-0ppm | 1 | - | - | 226 |
| | 200h-2A-10ppm | 7 | 11 | 13 | 236 |
| | 200h-8A-10ppm | 24 | 71 | 81 | 534 |
| | 200h-12A-10ppm | 122 | 116 | 128 | 717 |
| 915 h test | 915h-0ppm (0.75 $A \cdot cm^{-2}$ / 0.5 $A \cdot cm^{-2}$) | 14 / 7 | - / - | - / - | 425 / 355 |
| | 915h-10ppm (0.75 $A \cdot cm^{-2}$ / 0.5 $A \cdot cm^{-2}$) | 27 [a] / 5 | 29 / - | - / 25 | 456 / 384 |
| 500 h test | 170h-0ppm | 22[b] | 110 | 110 | 490 |
| | 500h-2.5ppm | 28 (0 - 170 h)[b]/ 12 (170 - 330 h) | 110 | 110 | 600 |
| | 500h-10ppm | 10 (0 - 170 h)[b]/ 10 (170 - 330 h ) | 23 | 30 | 389 |

[a] Technical problems occurred at $t$ = 72 h and slightly changed the anode gas flow rates to the two cells which led to small voltage changes. Therefore, initial and final voltages are given at $t$ =75 h and $t$ = 674 h, respectively. Also, at $t$ = 30 h the applied current was switched off for 24 h due to maintenance works in the lab.

[b] Due to technical problems at $t$ = 170 h, the gas to 170 h-0ppm was shut off and the test was finished. As the gas supply of all cell positions in the test bench are connected, this led to a slight gas variation for the two other cells, reflected by a slight increase in cell voltage.

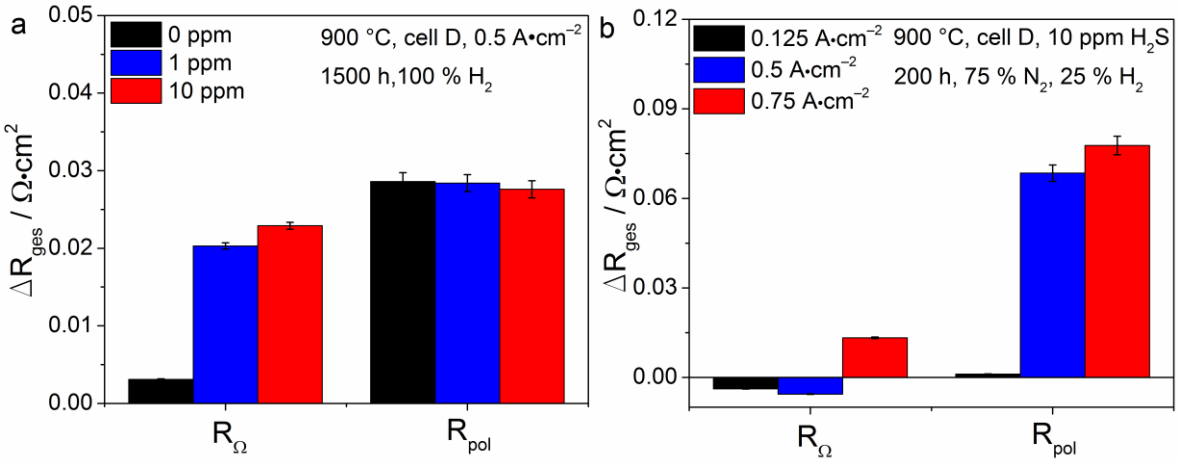


Figure 7.2. Analysis of ohmic and polarization resistance changes during the (a) 1500 h and the (b) 200 h experiment. Resistance changes were calculated from electrochemical impedance spectra based on measurements after completion of the initial voltage drop and before start of the recovery phase. (b) In order to allow a comparison between the cells operated at different current densities, the displayed data is derived from impedance spectra recorded at 0.125 A·cm$^{-2}$ for all cells. Afterwards, the current density was set back to the operating point.

A more detailed assessment of the origin of the observed degradation can be carried out by calculating the change in ohmic and polarization resistance based upon the recorded impedance spectra after completion of the initial poisoning and before the begin of the recovery phase as depicted in Figure 7.2a. The small degradation of the sulfur-exposed samples is reflected by an increase of the ohmic resistance (Figure 7.2a), which could not be observed for the reference test. The increase of the polarization resistance, however, is the same for all three samples (Figure 7.2a). As shown in the Nyquist and imaginary impedance spectra of the EIS measurements of the 1500h-10ppm test in Figure 7.3a and Figure 7.3b, this resistance increase is mainly due to an increase in intensity of the imaginary impedance at approximately 100 Hz, where the cathode charge transfer process is located. The frequency region at approximately 1 Hz is influenced by the initial sulfur exposure, which confirms the existence of an anode charge transfer process at this frequency, in agreement with the assignment in chapter 5. In the following, this frequency range remains completely unaffected by hydrogen sulfide exposure even after 1494 h. After the hydrogen sulfide supply is switched off, the low frequency impedance goes back to the intensity of the initial spectra. This clearly demonstrates the absence of any irreversible degradation of the anode charge transfer process. All other electrochemical impedance measurements that were used to create Figure 7.2a are dis-

played in Figure S20.

A likely explanation for the sulfur-induced ohmic resistance increase is a decrease in ionic or electronic conductivity in the Ni/CGO10 electrode, since electrolyte and cathode do not directly get into contact with sulfur. However, analysis of the different samples by means of XRD has not given conclusive evidence of a large-scale phase transformation of CGO during sulfur exposure (see Figure S21).

In long-term sulfur poisoning tests of Ni/YSZ anodes, Hauch et al. have observed Ni depletion at the electrode/electrolyte interface in their study of long-term degradation of Ni/YSZ anodes, which also led to a small increase of the ohmic resistance in the impedance spectra.[227] However, this increase was accompanied by a significant irreversible increase of the Ni/YSZ charge transfer resistance, which is not observed in the present study of Ni/CGO. Moreover, on the SEM images of the anodes of the 1500h-0ppm and the 1500h-10ppm test in Figure 7.4a+b, no obvious microstructural differences can be detected, indicating the absence of Ni depletion. Thus, the observed increased ohmic resistance is probably caused by a different degradation phenomenon. Hauch et al. have observed the irreversible degradation of the Ni/YSZ charge transfer resistance to be initiated by combined sulfur exposure and high cell overpotential.[227] They found that significant irreversible long-term degradation occurred at cell overpotentials of 300 mV or higher. Since this threshold value is already exceeded in the 1500h-1ppm and the 1500h-10ppm (see Table 7.2) experiments without the onset of considerable sulfur-induced irreversible degradation, this value of 300 mV is rather unlikely to hold for the degrading Ni/CGO anodes. However, as the resistance of the ESC investigated in the present study is largely governed by the ohmic resistance, that is, most of the cell overpotential originates from the ohmic resistance of the thick electrolyte, the electrostatic (Galvani) potential steps at the anode are likely to be higher under polarization than the ones of Ni/YSZ anode-supported cells investigated by Hauch et al. Thus, degradation could be triggered when a minimum value of the electrostatic anode surface (Galvani) potential step is gone below, that is, when a certain anode overpotential value is exceeded. This hypothesis is further investigated in the subsequent subsections.

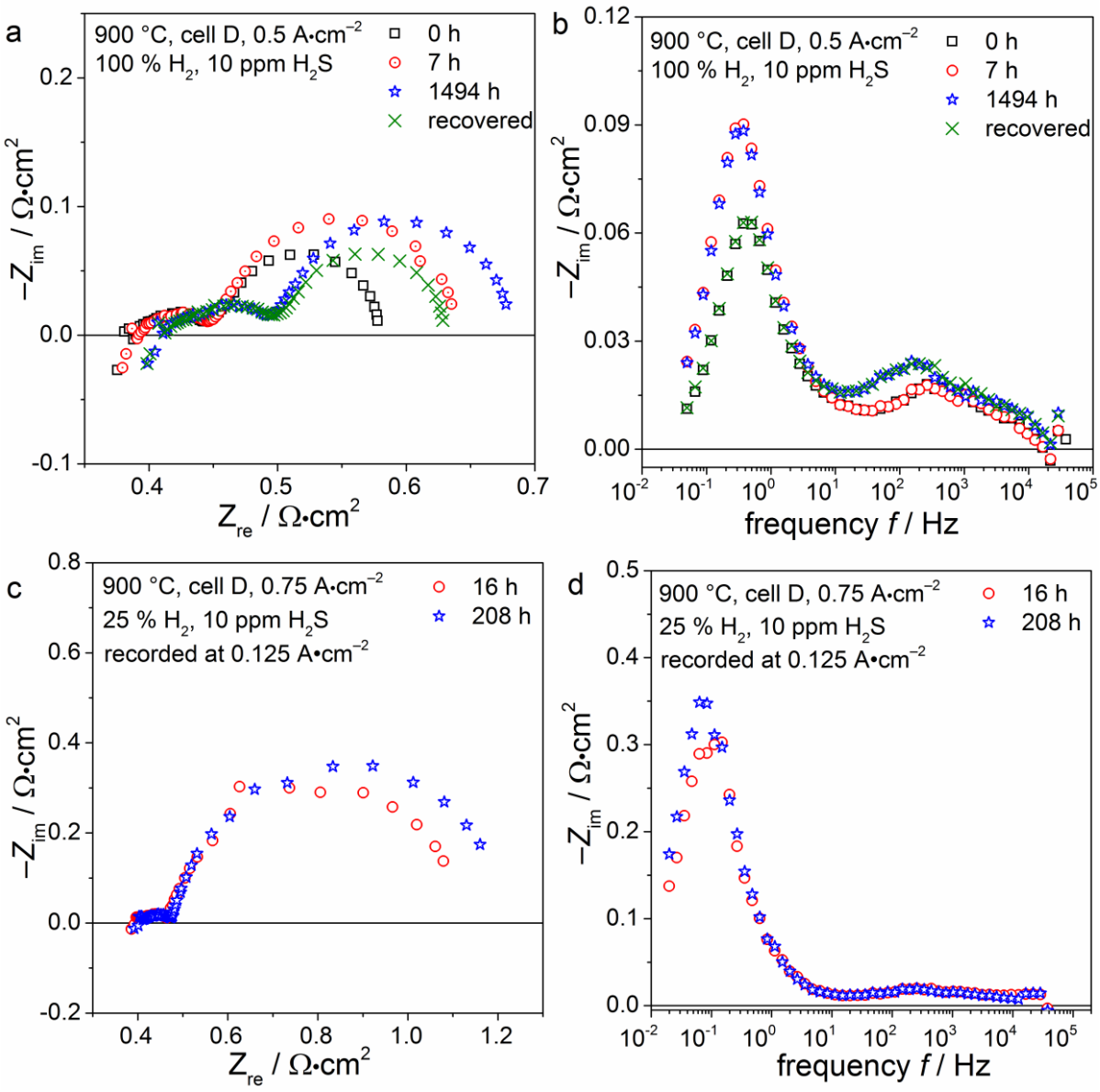


Figure 7.3. (a) Nyquist and (b) imaginary impedance plots of impedance spectra of the 1500h-10ppm test recorded. (c) and (d) show Nyquist and imaginary impedance plots for the 200h-12A-10ppm test. However, the shown impedance spectra were recorded at 0.125 A·cm$^{-2}$ to allow a comparison to other cells.

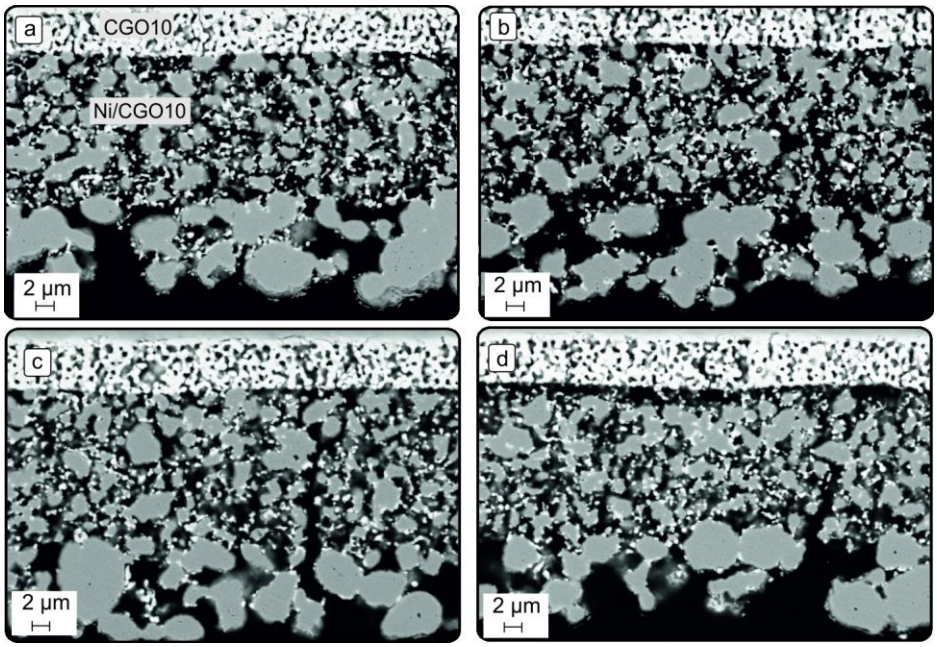


Figure 7.4. Scanning electron microscopy cross section image of the anodes of cell D of (a) the 1500h-0ppm test, (b) the 1500h-10ppm test, (c) the 200h-2A-0ppm and the (d) 200h-12A-10ppm test.

### *7.2.2 Long-term testing of other Ni-based anodes in hydrogen-rich fuels*

Although the aim of the present chapter is the investigation of Ni/CGO10-based anodes, further long-term tests under sulfur exposure were carried out for cells with NiCu5/CGO40 and Ni/YSZ-based cells for comparison (specifications of cells and tests in Table S3, Table S4). Details of the cells and comprehensive description of the experiments and their analysis are given in the supplementary information ("Long-term sulfur poisoning of other Ni-based anodes"). In the present section, only a brief summary is given.

Three NiCu5/CGO40-based cells were operated for 900 h at similar conditions as the 1500 h test with Ni/CGO10 anodes in the previous subsection with 0, 1 and 10 ppm $H_2S$ (Figure S12). The experiment showed the same extent of degradation for the 0 and 1 ppm $H_2S$ experiment and significant voltage degradation for 10 ppm $H_2S$ mainly via ohmic resistance increase (Figure S13 + Figure S14). Investigations via SEM and FIB/SEM did not show any sulfur-induced microstructural changes (Table S5, Figure S15 + Figure S16). This observed degradation phenomenon is consistent with the Ni/CGO10 anodes in the 1500 h test, however, it seems to be triggered at higher $H_2S$ concentrations for the NiCu5/CGO40 anodes. This suggests that the degradation is indeed caused by strong sulfur-CGO interactions, since the main difference between the two anodes (Ni/CGO10 and NiCu5/CGO40) is the different ce-

ramic composition. Moreover, XRF and TEM/EDX measurements were employed to investigate the 10 ppm $H_2S$ exposed sample towards sulfur traces. However, no traces could be found (Figure S17 + Figure S18).

Furthermore, the Ni/YSZ-based cell was used for a 200 h sulfur poisoning test under the same condition as the Ni/CGO10-based cell in the previous section and showed both a considerably larger initial performance drop and a rapid irreversible degradation of the anode charge transfer resistance (Figure S12b). This confirms that the investigated Ni/CGO10 anodes show a higher long-term sulfur tolerance than Ni/YSZ.

### *7.2.3 Long-term testing in hydrogen-lean fuels*

In order to further investigate the long-term sulfur resistivity of Ni/CGO anodes, this subsection shows three different long-term sulfur poisoning tests at more critical operating conditions with hydrogen-lean fuels. In the Temkin isotherm derived by Alstrup et al., sulfur coverage on Ni was shown to be linearly dependent on $\ln(\frac{p\mathrm{H_2S}}{p\mathrm{H_2}})$.[122] As in realistic SOFC system operation, pure hydrogen is rarely used, the hydrogen content in the inlet fuel gas was decreased to 25 % to increase the $\frac{p\mathrm{H_2S}}{p\mathrm{H_2}}$ ratio and the fuel utilization of the tests.

*The 200 h test - A parameter study with varying current density*—The present subsection shows the results of a 200 h test of Ni/CGO10 anodes (cell D, same batch as the 1500 h test) at varying current densities of 0.125 (200h-2A-10ppm), 0.5 (200h-8A-10ppm) and 0.75 $A \cdot cm^{-2}$ (200h-12A-10ppm) with and without the addition of a constant $H_2S$ concentration of 10 ppm (Figure 7.1b). The fuel gas composition was 25 % $H_2$ and 75 % $N_2$. This experiment was devised to reveal if sulfur-induced degradation is dependent on the electrostatic surface (Galvani) potential step at the anode, which can readily be adjusted by a variation in current density. The cell voltage curves of the experiment clearly shows that both the 200h-12A-10ppm and the 200h-8A-10ppm test show significant and rapid sulfur-induced irreversible degradation in contrast to the sulfur-free reference experiments. No voltage degradation is visible for the 200h-2A-10ppm test. To facilitate a comparison between the different current densities, EIS measurements of all cells in the experiment were regularly conducted at 0.125 $A \cdot cm^{-2}$. To conduct these measurements the operating voltage of the 200h-8A-10ppm and the 200h-12A-10ppm cells were changed to 0.125 $A \cdot cm^{-2}$ for the measurements and set back after their completion. The extracted resistance values show a strong increase of the polarization resistance of the 200h-8A-10ppm and the 200h-12A-10ppm tests. This increase is

reflected by an increase of the intensity of the imaginary impedance peak at frequencies around 1 Hz (Figure 7.3c+d), which were shown to be related to the anode charge transfer process in chapter 5. Additionally, the ohmic resistance of the 200h-12A-10ppm test increased slightly as well. As the ohmic resistance of the 200h-8A-10ppm test stayed constant, it is suggested that the ohmic resistance increase in the 200h-12A-10ppm test has a different origin than the one observed for all sulfur-exposed samples during the 1500 h test. The 200h-2A-10ppm showed a stable operation during the test with both constant ohmic and polarization resistance.

The comparison of the SEM images of the 200h-12A-10ppm (Figure 7.4d) and the 200h-2A-0ppm reference test (Figure 7.4c) shows a clear impact of the sulfur exposure on the anode microstructure, particularly at the interface between CGO adhesion layer and functional anode layer. At this region within the anode, Ni depletion is visible, which indicates a loss of Ni percolation. The SEM image even suggests that no Ni particles are connected to the CGO adhesion layer anymore. Other SEM images (not shown here) clearly show that Ni and CGO particles are still connected to the adhesion layer. Thus, delamination of the anode is unlikely. This is also consistent with the only small ohmic resistance increase, as delamination should have a significantly more severe effect on this value. For Ni/YSZ, Ni depletion was already reported to occur and to lead to an "extension" of the electrolyte material. This was reflected by an increased ohmic resistance, which is in agreement with the 200h-12A-10ppm test.[112]

Microstructural 3D reconstruction was carried out by means of FIB/SEM tomography for a reduced reference cell, the 200h-2A-2ppm, and the 200h-12A-10ppm in order to quantify the microstructural changes of sulfur-exposed Ni/CGO anodes. The variation of the microstructural parameters over the analyzed volume is shown in Figure S22. The analyzed volume was increased until the RVE was reached for all microstructural quantities. The obtained microstructural information about phase proportions and phase percolation are listed in Table 7.3. Furthermore, the TPB length is quantified. This parameter was considered to be the location of the charge transfer reaction in a first approximation. This might not be necessarily true as shown in the previous chapters, since the DPB between CGO surface and gas phase or the DPB between CGO and Ni could contribute to the charge transfer reaction rate. However, as the Ni phase is most likely involved in the hydrogen adsorption and dissociation, the TPB length is probably a good descriptor for the anode charge transfer rate. Table 7.3 and the visual representation of the TPB density in Figure 7.5 clearly show a decreased TPB length, a decreased Ni content, an increased porosity and a decreased Ni percolation for the 200h-12A-

10ppm test. The decreased Ni content in the 200h-12A-10ppm cell correlates well with an increased pore content and indicates a Ni removal from the anode functional layer, which is in agreement with the observed Ni depleted layer in the SEM image and the increase in both ohmic and anode charge transfer resistance. The CGO content is similar in all three cells. Furthermore, the lower Ni percolation value in the 200h-12A-10ppm sample could be the reason for the slightly increased ohmic resistance of the cell, but could also have an influence on the increased polarization resistance.

Table 7.3. Microstructural properties of the three cells calculated based on the post-mortem FIB-SEM measurements and corresponding 3D reconstruction.

| Test | TPB density [µm·µm$^{-3}$] | Ni proportion [%] | CGO proportion [%] | Pore proportion [%] | Percolation Ni [%] | Percolation CGO [%] | Percolation pore [%] |
|---|---|---|---|---|---|---|---|
| CellA-Ref | 4.6 | 28.5 | 15.3 | 56.2 | 92.7 | 47.2 | 99.8 |
| 200h-2A-10ppm | 3.1 | 28.5 | 14.8 | 56.7 | 93.4 | 61.9 | 99.7 |
| 200h-12A-10ppm | 2.8 | 24.4 | 14.8 | 60.8 | 90.9 | 75.5 | 99.7 |

The TPB length (2.8 µm·µm$^{-3}$) of the strongly degraded 200h-12A-10ppm sample is shorter than the one for the 200h-2A-10ppm cell (3.1 µm·µm$^{-3}$). However, both values are significantly smaller than the one for the reduced reference cell (4.6 µm·µm$^{-3}$). The TPB length was calculated without accounting for non-percolated Ni and CGO particles. Thus, its real reduction in the 200h-12A-10ppm sample is probably even more pronounced than reflected by the given values and mainly responsible for the increased anode charge transfer resistance. It has to be pointed out that the cells in the 200h experiment were operated at 900 °C and OCV for approximately 170 h before the start of the experiment. Thus, the process leading to the reduced TPB length of the tested cells in comparison with the reference cell could have happened during this initial time period. The lower TPB value is also consistent with the Ni parti-

cle size distribution (PSD; Figure S23), which shows small shifts to larger particle diameters for both the 200h-2A-10ppm and the 200h-12A-10ppm sample. Interestingly, this shift is particularly pronounced for the 200h-2A-10ppm sample, whereas the change of particle size in the 200h-12A-10ppm sample is very small. Still, this sample shows the lowest TPB value. This suggests that the observed Ni depletion is not related to a previous sulfur-induced Ni agglomeration process. It is also possible that the differences in PSD and TPB density are due to heterogeneities caused in the manufacturing process. However, the initial characterization of the cells in Figure S19 shows excellent reproducibility, indicating also a reproducible initial microstructure of cells within the same batch.

In the investigated volume, a constant mean value was found for all microstructural parameters except for CGO percolation (Figure S22e), although the RVE for CGO-related values should even be smaller than the one for Ni percolation due to the smaller CGO particle size.[160] Therefore, the values shown for CGO percolation in Table 7.3 cannot be considered representative for the whole anode volume. This is probably due to a generally low CGO phase proportion in cell type D (~15 vol %, see Table 7.3). In chapter 5 (Figure 5.22), it was shown that, although the overall performance of cell D (or rather cell A, which is based on the exact same anode) is excellent, its anode charge transfer resistance and susceptibility towards sulfur poisoning is rather large. Based on the 3D reconstruction, this observed behavior can now related to an insufficiently low CGO percolation and the corresponding inactivity of a large part of the TPB (or also the DPB between CGO and gas phase) in these cells.

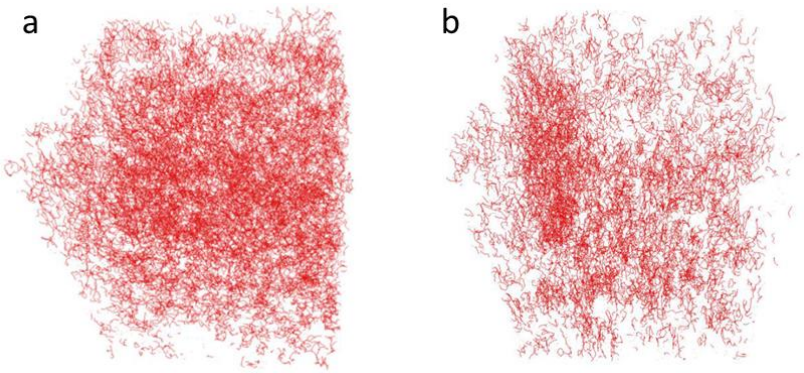


Figure 7.5. 3D visual representation of the TPB in (a) the reference sample and (b) the 200h-12A-10ppm sample.

In order to make more spatially resolved statements about the occurring microstructural changes, the initially investigated anode volume was separated into four equally sized compartments of 2.8 µm length ranging from the adhesion layer/anode functional layer interface to the anode functional layer/current collector interface and are labeled 1 – 4. The different phase proportions and TPB lengths in the different compartments are depicted in Figure 7.6. Percolation values are not given, as the decreased investigated volumes are smaller than the required RVE. This might also hold true for the different zones depicted in Figure 7.6, however, several general trends can still be deduced. The 200h-12A-10ppm sample shows a lower Ni phase proportion in all zones, which is accompanied by a larger pore fraction. This indicates that Ni depletion does not only occur close to the adhesion layer but throughout the whole anode functional layer. This is also reflected by a decreased TPB length in all zones. No clear trend for CGO phase proportion changes could be observed.

These microstructural changes were observed for the 200h-12A-10ppm sample, however, based on the resistance changes in Figure 7.2b, it is likely that the same degradation mechanism also occurred in the 200h-8A-10ppm cell, just with a slower rate. In this test, the polarization resistance degraded to a lower extent than in the 200h-12A-10ppm test and at the end of the experiment no ohmic resistance increase was observed. This behavior can be explained with that the removal of the first Ni particles from the electrolyte/electrode interface still leaves an intact Ni percolation network behind and therefore, the effective electrolyte thickness is not extended. The increase of ohmic resistance will only be later observed when the Ni at the interface is mostly depleted.

As the 200h-8A-10ppm showed significant degradation of the anode charge transfer process and the 1500h-8A-10ppm test did not, the combination of high current density and overall $H_2S$ concentration cannot be the reason for the irreversible degradation, as these parameters were the same in both tests. However, the hydrogen content in the fuel inlet gas differed in the two experiments. In the Temkin isotherm derived by Alstrup et al., sulfur coverage on Ni was shown to be linearly dependent on $\ln(\frac{p\mathrm{H_2S}}{p\mathrm{H_2}})$.[122] That is, sulfur coverage on Ni can be expected to be significantly higher in the 200 h test compared to the 1500 h test due to a change in hydrogen partial pressure. Thus, sulfur coverage on Ni probably has a crucial influence on the onset of irreversible degradation. However, irreversible degradation was not observed for the 200h-2A-10ppm test, which indicates that the anode charge transfer process degradation might also be influenced by the anodic electrostatic (Galvani) potential step.

To exclude electrochemical Ni oxidation as the source of irreversible degradation, an *i-V*

curve was recorded (Figure S24) for the 200h-8A-10ppm test under sulfur exposure after finishing the experiment shown in Figure 7.1d. The curve has a completely linear shape and no kink is visible at low cell voltages, as it has been observed before during electrochemical nickel oxidation.[228] Due to the low fuel utilization values (33 % for 0.75 A·cm$^{-2}$ and 25 % $H_2$) in the present experiment, chemical nickel oxidation can be excluded as well.[213]

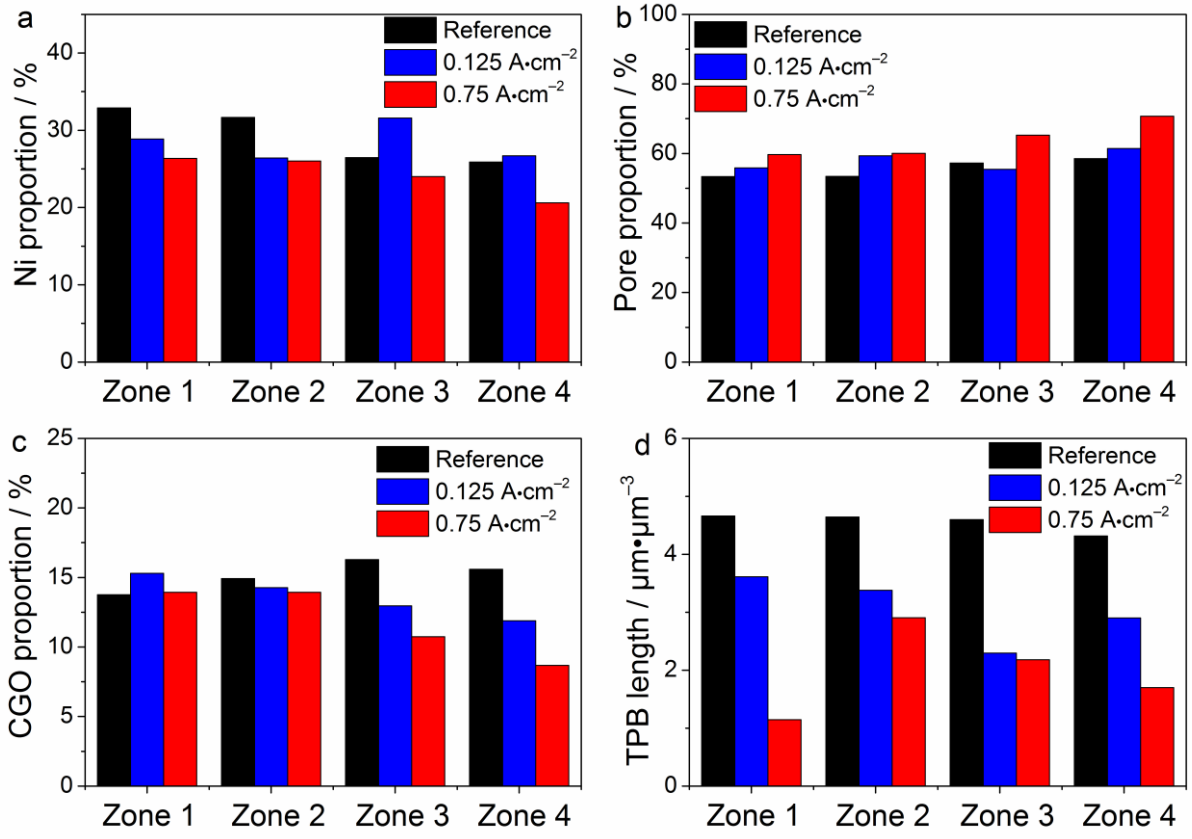


Figure 7.6. Microstructural quantities of a reduced reference sample, the 200h-2A-10ppm ("0.125 A·cm$^{-2}$") and the 200h-12A-10ppm ("0.75 A·cm$^{-2}$") sample in the zones 1 – 4 of the anode functional layer with 1 being adjacent to the CGO barrier layer and 4 adjacent to the anode contact layer. (a) Ni proportion, (b) Pore proportion, (c) CGO proportion and (d) TPB length.

*The 915 h test – A more sulfur tolerant SOFC*—The short-term sulfur poisoning behavior of the two cells C and D (cell A was investigated, however, anode composition and performance of cell A and D were exactly the same, as they were from the same supplier) was comprehensively investigated in chapter 5. Surprisingly large differences in the resistance increase values of the cells were observed. Cell C was shown to be significantly more re-

sistant towards sulfur exposure than cell D. To investigate if the increased short-term sulfur tolerance of cell C also entails increase long-term tolerance, another long-term test over 915 h was carried out with the Ni/CGO10-based cell of type C. The corresponding voltage evolution is displayed in Figure 7.1c. This test was divided into two phases. During the first phase of 675 h length, the cells were operated at 0.75 $A \cdot cm^{-2}$, afterwards the current density was set to 0.5 $A \cdot cm^{-2}$ for 240 h. During both phases, one of the cells was exposed to 10 ppm $H_2S$, the other cell was operated in a sulfur-free fuel. At 0.75 $A \cdot cm^{-2}$, the sulfur-exposed cell showed a cell voltage degradation of 27 mV, which is considerably higher than 14 mV for the reference cell. The second phase of the test was carried out at the same conditions as the 200h-8A-10ppm test, which displayed severe anode degradation of cell D. However, in the present test of cell C, the voltage degradation (5 mV) is comparable to the observed value of the reference test (7 mV). Hence, cell C displays sulfur-tolerant long-term behavior in conditions where cell D strongly degrades. The only difference between the experiments is that due to increased short-term sulfur tolerance of cell C, it was operated under formation of a significantly larger anodic (Galvani) potential step (or smaller anodic overpotential, respectively). Therefore, the presented results confirm the hypothesis that sulfur-induced irreversible degradation occurs at larger anodic overpotentials. Moreover, as both cells were exposed to the exactly same operation conditions, a purely chemical degradation mechanism can be excluded.

*The 500 h test – The influence of higher fuel utilization*—In order to investigate the dependency of irreversible long-term degradation on $\frac{p\mathrm{H_2S}}{p\mathrm{H_2}}$, a 500 h sulfur poisoning test of cell D was carried out (Figure 7.1d) with a decreased hydrogen sulfide concentration of 2.5 ppm, which results in the same $\frac{p\mathrm{H_2S}}{p\mathrm{H_2}}$ ratio as the 1500h-10ppm test. A reference test without sulfur exposure was conducted as well, however, it had to be ended after 170 h due to technical problems. Moreover, a cell of type C was exposed to 10 ppm $H_2S$. . This experiment was carried out simultaneously to the experiments with cell A, and is depicted in Figure 7.1e. The maximum fuel gas flow rates of the cells was decreased to 0.5 $L \cdot min^{-1}$ (in contrast to 1 $L \cdot min^{-1}$ in the experiments in the previous subsections) in order to obtain more realistic fuel utilization values. The nominal fuel utilization was 45 %, however, as described before a bypass in the cell housing amounts to approximately 30 %, leading to real fuel utilization values of approximately 65 % which already approaches realistic operating conditions. Only slightly increased overall degradation could be observed for the 500h-2.5ppm test in comparison to

the sulfur-free reference test in the first 170 h (28 mV vs. 22 mV). Furthermore, the voltage degradation of 500h-2.5ppm in the following 330 h is low with a decrease of only 12 mV which corresponds to a degradation rate of 36 mV/1000 h (i.e., smaller than the degradation rate of the reference test in the first 170 h of 129 mV/1000 h). This demonstrates low degradation rates under sulfur exposure and indicates a fully reversible sulfur poisoning behavior. This is consistent with the observations during the 1500h-10ppm test, that did not show irreversible degradation of the anode charge transfer process. As both tests were conducted at the same $\frac{p\mathrm{H_2S}}{p\mathrm{H_2}}$ ratio, the absence of degradation underscores the importance of this parameter in triggering sulfur-induced irreversible anode degradation. However, as demonstrated in the previous experiments irreversible degradation is not solely caused by the sulfur coverage on Ni. Nevertheless, increasing sulfur coverage also means a decreasing anodic potential step and thus, is an important parameter that determines the onset of irreversible degradation processes.

The 500h-10ppm loses 10 mV in the first 170 h (degradation rate of 58 mV/1000 h), and further 10 mV in the subsequent 330 h (degradation rate of 30 mV/1000 h). There is no reference experiment available. However, the degradation rate is not significantly higher than the one of the 915h-10ppm test (same cell type), which displayed a similar voltage decrease value of 7 mV in 240 h (29 mV/1000 h). Moreover, the test in the previous subsection was carried out with a larger anode gas flow rate and thus, at only half the $p\mathrm{H_2O}$ values in the anode compartment, which is expected to entail significantly lower degradation rates due to slower Ni agglomeration processes.[229,230] This indicates the absence of sulfur-induced irreversible degradation in the case of the 500h-10ppm test and demonstrates that Ni/CGO anodes can be stably operated at realistic hydrogen sulfide concentration, current density and fuel utilization.

### *7.2.4 Discussion of the mechanism*

Based on the results presented in the previous subsections, two different degradation phenomena can be identified: the degradation of the ohmic and the degradation of the anode charge transfer resistance.

The ohmic resistance increase is small and only visible for long sulfur exposure times around 1000 hours. As the increasing of ohmic resistance is not necessarily accompanied by an increasing anode charge transfer resistance, the degradation is likely to be related to a loss of ionic or electronic conductivity of the anode or possibly the CGO adhesion layer. As it was recently shown for sulfur poisoning experiments of CGO10 electrodes, sulfur quickly diffuses

into the CGO phase after $H_2S$ exposure, at least for cathodic polarization.[136,137] This could possibly be the reason for a decreased ionic conductivity of CGO due to a possible change in oxygen vacancy concentration. Furthermore, several fundamental studies have outlined the electro-catalytic role of CGO in Ni/CGO anodes.[132–134] These studies demonstrate significant physicochemical interactions between sulfur and CGO. This suggests that the presence of larger quantities of $H_2S$ might lead to a drop in the electronic conductivity as observed for redox cycling by Iwanschitz et al., who related this change to the ceramic transition from the CGO40 with MIEC behavior to a pure ionic conductor during the experiment.[130] This could play a role if hydrogen is, at least partially, oxidized on the DPB between CGO surface and the gas phase and the formed electrons need to migrate to the Ni phase.

Regarding the increase in anode charge transfer resistance, it is proposed that the combination of a small anodic potential step (that is, large anode overpotential) and high sulfur coverage on Ni is responsible for sulfur-induced irreversible degradation. The onset of this anode charge transfer process degradation in turn, can lead to a further degradation of the ohmic resistance, which seems to have a different origin than the one reported in the last paragraph. This behavior is in agreement with what was observed by Hauch et al. for Ni/YSZ anodes.[112] Furthermore, FIB/SEM experiments confirmed in 3D the Ni depletion and porosity increase, that Hauch et al. reported based on 2D analysis of SEM images. Thus, although the underlying hydrogen oxidation mechanisms of Ni/CGO and Ni/YSZ are likely to be different, it can be assumed that the Ni depletion is caused by the same mechanism in both cases and the electro-catalytic role of CGO cannot prevent the observed degradation. However, the present work showed that Ni/CGO is more resistant towards irreversible degradation than Ni/YSZ, probably due to its increased short-term sulfur tolerance and thus, larger anodic (Galvani) potential steps during operation.

The Ni depletion in the anode functional layer is probably caused by Ni diffusion, either in the solid state or in the gas phase as evaporated Ni species. In general, possible drivers of these diffusion processes are the $pH_2O$ and the potential gradient perpendicular to the electrode/electrolyte interface within the porous electrode. In the following, several possible mechanisms are discussed.

In general, Ni depletion of Ni/CGO anodes has been observed before also in sulfur-free $H_2/H_2O$ fuels for operation times over 1000 hours and was related to the evaporation of Ni particles via $Ni(OH)_x$ formation.[62,231] However, in the present study Ni depletion occurs for significantly shorter testing times due to sulfur exposure. Thus, the mechanism is either a dif-

ferent one, or its kinetics are accelerated by the presence of sulfur. Furthermore, Ni depletion is a common degradation phenomenon in Ni/YSZ anodes during solid oxide electrolysis cells (SOEC) operation.[232–234] The process of Ni depletion in both SOFC and SOEC mode was recently suggested to start with a loss of Ni-YSZ contact, and in the following a loss of Ni percolation as a precursor to a subsequent evaporation via $Ni(OH)_x$ formation.[235] The contact loss between Ni and YSZ and Ni-Ni particles was related to the strongly negative Ni potential (in SOEC mode), which leads to minimization of the Ni surface energy and therefore to a coarsening and rounding of Ni particles. The $Ni(OH)_x$ formation was suggested to start only after the contact loss, when there is no more Ni polarization and the Ni potential is much more positive. In the present work the Ni is operated at a completely different potential, however, it was suggested that the surface energy of Ni varies symmetrically around the "zero charge" potential and thus, the loss of Ni-Ni and Ni-YSZ contact could occur in the same way in both SOEC and SOFC operation.[235,236] Hence, as the introduction of sulfur significantly increases the anode overpotential and therefore, the Ni potential changes to more positive values, the sulfur exposure could be the reason for the loss of Ni percolation observed in the present study. However, while in SOEC mode the loss of Ni-Ni particles is a prerequisite for $Ni(OH)_x$ formation, this does not necessarily have to be the case in SOFC mode since the percolated Ni particles display an even more positive potential than the non-percolated Ni particles. Thus, the loss of Ni percolation is probably not a precursor for $Ni(OH)_x$ formation but a side effect of the increased anode overpotential. As sulfur exposure leads to a more positive Ni potential, its oxidation to $Ni(OH)_x$ species becomes favorable and the Ni migration away from the electrolyte could occur.

In the present study, the irreversible degradation was observed to be more pronounced for higher current densities where higher $pH_2O$ values and also larger $pH_2O$ and potential gradients perpendicular to the electrolyte occur. Thus, $Ni(OH)_x$ formation could play a role in the Ni migration process away from the electrolyte, which is also promoted at higher temperatures. However, the $pH_2O$ values in the anode compartments are relatively small in all of the presented experiments (approximately maximum 0.47 atm for 0.75 $A \cdot cm^{-2}$ and 0.25 atm hydrogen inlet gas pressure under consideration of the bypass in the testing setup) and lead to a maximum partial pressure of Ni gas phase species of about $10^{-10}$ atm.[237] This is smaller than in SOEC experiments that showed Ni depletion (~$10^{-9}$ in a 9000 h experiment at $pH_2O$ = 0.9 atm and 800 °C[235]), however, it was suggested that the electrochemical potential gradient is more important for the Ni migration than the steam gradient is.[235] In addition to physically

blocking the adsorption sites, adsorbed sulfur atoms also alter the electronic structure of the Ni surface.[9,71] Thus, a modification of the surface charge of Ni could accelerate the formation of volatile Ni species.

At higher $H_2S$ concentrations than investigated in the present study, bulk nickel sulfide species can be formed (e.g. $Ni_3S_2$). However, in situ Raman measurements and thermodynamic calculations have shown that their formation does not occur below 100 ppm for typical SOFC operating conditions.[74,113,114,238] Thus, long-term degradation cannot be simply explained by such chemical Ni sulfide formation. Recently, surface reconstruction of Ni to less active planes and increased Ni diffusion rates, due to the dissolution of sulfur atoms into the Ni bulk phase in the vicinity of TPB have been suggested to occur at $H_2S$ concentrations below 100 ppm for high chemical oxygen potentials.[75,114] Such changes could lead to enhanced sintering of Ni particles resulting in destruction of the Ni percolation network. Furthermore, Ivey et al. observed increased formation of terraces which occurs on the Ni surface and which increases with $H_2S$ concentration, but is independent of the applied current load.[239] This appears to be a precursor to Ni agglomeration and can lead to an eventual detachment of Ni from the YSZ phase.[94,114,239]

However, in the present work no clear trend of Ni agglomeration could be observed. This suggests that the observed Ni depletion is not related to a previous Ni agglomeration. This was also indicated for SOEC mode, where the increase of the Ni/YSZ charge transfer resistance was shown not to be due to a changed PSD.[240]

Furthermore, this work indicates that a purely chemical reaction mechanism is not sufficient to describe the observed microstructural changes, since the magnitude of the anode potential step has a critical influence on the onset of sulfur-induced degradation. However, the local electrochemical formation of Ni sulfide at comparatively positive nickel potentials (i.e., low anode (Galvani) potential steps close to the electrolyte/electrode interface) could be a possible explanation. A potential dependency of Ni sulfide formation was, for example, suggested in reference.[241] Since the melting temperature of Ni sulfide is 797 °C and thus, lower than the operating temperature in the present work, this could lead to the evaporation of Ni sulfide and its transport away from the electrolyte/electrode interface.

Diffusion may also be driven by electrical forces, which is known as electro-migration and is caused by transfer of momentum from electrons to ions. Generally, electro-migration is reported to occur at very high current densities $>10^4$ $A \cdot cm^{-2}$,[242,243] however due to the promoting effect of high temperature, moisture and contaminant concentrations on the metal surface,

it has recently also been suggested as a degradation mechanism during SOFC operation.[244,245] In particular, electro-migration was suggested to be one of the responsible mechanisms for the redistribution of nickel in Ni/YSZ anodes under applied current,[246,247] especially for phosphine-induced nickel migration away from the electrolyte.[245] Thus, electro-migration could also contribute to nickel depletion in the present study and might be accelerated under sulfur poisoning conditions due to the mentioned increased Ni mobility under sulfur dissolution in Ni. However, the actual underlying mechanism responsible for sulfur-induced irreversible long-term degradation cannot definitely be identified in the framework of this work.

In the present study, experiments were only carried out a single operating temperature, that is, at 900 °C. While experiments at lower temperatures could lead to further interesting insights, based on the proposed mechanisms, the effect of decreasing the operating temperature can be anticipated. Both the anode hydrogen oxidation kinetics and the formation of volatile Ni hydroxide or Ni sulfide species are thermally activated processes. Therefore, a decreased temperature will lead to an increased anode overpotential (at the same current density) but also to a lower formation rate of Ni gas phase species. While the first process will increase the extent of Ni depletion, the latter will mitigate it. Thus, the present study could lay the foundation for further cell investigations with systematic parameter variations and the aim to determine the operating conditions most suitable for low sulfur-induced degradation rates. As a lower operating temperature will also lead to an increased sulfur coverage on Ni, the onset of irreversible sulfur-induced degradation is always dependent on the interplay of the parameters temperature, anode overpotential and sulfur coverage.

Nevertheless, on the basis of the present results it can be concluded that the design of Ni/CGO anodes with a very fine microstructure can mitigate the sulfur-induced irreversible degradation effects by minimizing the anode overpotential values. However, after a certain period of cell operation, an increased anode overpotential due to non-sulfur-related anode degradation could lead to the onset of sulfur-induced degradation and, thus, start a self-accelerating degradation process.

The present results are promising with regard to the possible stable operation of Ni/CGO anodes under sulfur exposure. However, it has to be pointed out that this work has only investigated their use in $H_2/H_2O/N_2$ fuel systems in model cell geometries. Therefore, future work should focus on the operation of Ni/CGO-based stacks with representative fuels under sulfur exposure in order to fully assess the potential of Ni/CGO anode use in realistic SOFC sys-

tems. Furthermore, the present work has demonstrated that Ni/CGO possesses an increased long-term stability under sulfur exposure than Ni/YSZ. However, when operated under operating conditions at large anode overpotential values, both anodes will inevitably display Ni depletion. By further optimization of Ni/CGO anodes, the critical operating regime could be further pushed to higher current densities. However, the risk of Ni depletion will always limit the possible maximum SOFC performance. Thus, to fully prevent the occurrence of this degradation process, Ni-free anodes will have to be developed.

### *7.3 Conclusions*

In the present chapter the promising long-term stability of Ni/CGO anodes under realistic operating conditions was established. Furthermore, the existence of a critical operating regime is shown, that is governed by the combined influence of the sulfur coverage on Ni and the anodic (Galvani) potential step. Ni/CGO anodes were shown to display higher long-term stability under sulfur exposure than Ni/YSZ due to smaller initial sulfur-induced performance drops.

By means of electrochemical impedance spectroscopy, two degradation phenomena were observed: One is related to the increase of the ohmic and one to the increase of the anode charge transfer resistance. While the process related to the increase of the anode charge transfer resistance can be prevented by safe operating conditions at low anode overpotentials, the increase in ohmic resistance was observed to be inherently coupled to sulfur exposure. However, its magnitude was small in the present experiments and only becomes visible for testing times around 1000 h.

Based on SEM analysis, the increase of the anode charge transfer resistance under critical operating conditions was related to the evolution of a Ni depleted layer close to the electrolyte was established. By means of FIB/SEM and 3D reconstruction the microstructural changes could be quantified and showed a Ni depletion and simultaneous increase in porosity throughout the whole anode functional layer, which also leads to a decreased TPB. The present work shows that short-term sulfur poisoning behavior can be used to assess long-term stability.

# 8 Conclusions

The SOFC promises high electrical efficiencies, low emissions and fuel flexibility. One of the degradation processes that limit SOFC lifetime and thus, hinders its commercialization is sulfur poisoning of the state-of-the-art Ni-based anodes due to impurities in the fuel. Since the underlying mechanisms are still not fully understood, the present thesis focuses on the measurement and the fundamental understanding of sulfur poisoning phenomena on Ni-based anodes to enable their optimized operation and design.

An elementary kinetic model was developed to predict the influence of sulfur poisoning on the behavior of Ni/YSZ anodes. A detailed multi-step reaction mechanism of sulfur formation and oxidation at Ni/YSZ anodes coupled with channel gas-flow, porous-media transport and elementary charge transfer chemistry was established for SOFC operating with trace amounts of $H_2S$. A thermodynamic and kinetic data set of sulfur formation and oxidation was derived based upon various literature sources including a coverage-dependent description of the enthalpy of surface-adsorbed sulfur. The validity of the model was demonstrated for SOFC at different operating conditions operating both on $H_2/H_2O/H_2S$ and $CH_4/H_2/H_2O/H_2S$ fuel mixtures using various electrochemical literature experiments. The results reveal that sulfur surface coverage increases with current density which demonstrates a low sulfur oxidation rate. This implies that operation at high current densities is not a viable option for sulfur-poisoned Ni/YSZ-based SOFC.

As a result, the behavior of the more sulfur-resistant, but less understood Ni/CGO anodes was experimentally investigated to advance their understanding and explore their full potential when operated with sulfur-containing fuels. Therefore, experiments of various commercial, high-performance ESC with Ni/CGO anodes were performed in fuels with and without the addition of hydrogen sulfide. Different SOFC with Ni/CGO-based anodes were characterized by means of electrochemical impedance spectroscopy and current-voltage characteristics at different temperatures and in $H_2/H_2O$ and reformate fuels. Using symmetrical cells, different anode contributions in the impedance spectra of Ni/CGO10 anodes were identified and the parameters required to calculate the corresponding anode exchange current density in $H_2/H_2O$ fuels were determined by varying temperature, $pH_2$ and $pH_2O$. Moreover, it was demonstrated that the capacitance of Ni/CGO10 anode surface process is strongly dependent on temperature and gas phase composition reflecting a changing $Ce^{3+}/Ce^{4+}$ ratio.

The short-time sulfur poisoning behavior was systematically investigated for varying temperatures of 800 – 950 °C and current densities of 0 – 0.75 $A \cdot cm^{-2}$ with $H_2S$ concentrations

between 1 – 20 ppm. A sulfur poisoning mitigation effect was observed at high current loads and temperatures. The poisoning behavior was shown to be reversible for short exposure times. It was observed that the sulfur-affected processes exhibited significant different relaxation times depending on the Gd content in the CGO phase.

To explore the sulfur tolerance of Ni/CGO anodes in more realistic fuels, the sulfur poisoning behavior of Ni/CGO10 anodes in reformate fuels was compared with Ni/YSZ anodes. Various methane and carbon monoxide containing fuels were used to elucidate the underlying reaction mechanism. The analysis of the cell resistance increase in $H_2/H_2O/CO/CO_2$ fuel gas mixtures revealed that the poisoning behavior is mainly governed by an inhibited hydrogen oxidation reaction at low current densities. At higher current densities, the resistance increase becomes increasingly large, indicating a particularly severe poisoning effect on the carbon monoxide conversion reactions. However, the ability of Ni/CGO anodes to convert carbon monoxide even at $H_2S$ concentrations up to 20 ppm was demonstrated, while this was not possible for Ni/YSZ. From methane steam reforming experiments, it is deduced that the Ni surface is blocked and thus, the water gas shift reaction on Ni is fully deactivated as well. However, electrochemical CO oxidation on the CGO surface was shown to be still active. These results clearly demonstrated that the superior sulfur tolerance of Ni/CGO not only is limited to $H_2/H_2O$ fuel systems, but also extends to CO-containing gases.

Moreover, an in-depth analysis of long-term degradation due to sulfur poisoning of Ni/CGO anodes was presented. A parameter study of sulfur-induced irreversible long-term degradation Ni/CGO-based cells was carried out at 900 °C for different $H_2S$ concentrations, varying $H_2/N_2$ fuel gas atmospheres, current densities and different Ni/CGO anodes. The sulfur poisoning periods of the different cells varied from 200 to 1500 h. The possibility of stable long-term Ni/CGO anode operation under sulfur exposure was established and the critical operating regime was outlined. Degradation was observed to be triggered by a combination of a small anode (Galvani) potential step and high sulfur coverage on Ni and was accompanied by an increase in anode charge transfer and ohmic resistance. The microstructural evolution of altered Ni/CGO anodes was examined post-mortem by means of SEM and FIB-SEM, and was correlated to the anode performance degradation, establishing Ni depletion in the anode functional layer. It was shown that short-term sulfur poisoning behavior of Ni-based anodes is a good predictor for their long-term stability. Based on this finding it can be concluded that (i) a further optimization of Ni/CGO anode performance and (ii) an increased tolerance against

short-term sulfur poisoning will both lead to an increased long-term stability, since both measures will increase the anode potential step during operation.

The present investigation shows that under less harsh operating conditions, the initial sulfur-induced performance drop of Ni/CGO can be recovered quickly after switching off the sulfur supply. This implies that even if the desulfurization unit is not omitted, these anodes are capable of handling a sulfur breakthrough after the full capacity of the desulfurization unit is reached, without irreversible damage, which already represents valuable information for SOFC system manufacturers.

For stacks based on ESC with low electrolyte ionic conductivity, the operation without desulfurization unit could indeed become a viable option, since the contribution of the anode to the overall overpotential is relatively small and such systems are generally operated at low current densities. However, initial performance drops will probably always occur, which has to be compensated by oversizing the SOFC stack. If such performance drops can be accepted, has to be decided by industrial system manufacturers based on economic arguments.

# 9 Future perspectives

As the electrostatic anode potential step cannot be measured directly, an elementary kinetic model describing fuel oxidation and sulfur poisoning processes on Ni/CGO, similar to the one developed for Ni/YSZ in chapter 4, could yield valuable predictive information about the onset of sulfur-induced long-term degradation. However, the fuel oxidation mechanism is still elusive and more fundamental knowledge about its nature and the interplay between the Ni and the CGO phase has to be acquired before an elementary kinetic model can be developed. Therefore, experiments on electrodes with a defined microstructure and geometry such as point or patterned electrodes would be helpful to identify the nature and location of the rate-limiting charge transfer reaction. Especially, more information about the mechanistic role of CGO is required to steer efforts to optimize Ni/CGO electrodes into the right direction.

So far, Ni/CGO anodes were developed to display high performance in sulfur-free fuels, in which the Ni phase is fully catalytically active towards the reforming reactions. However, under sulfur poisoning conditions, the water gas shift reaction on nickel is blocked, and CO conversion occurs via electrochemical oxidation on the CGO surface. These mechanistic conclusions suggest that the optimization of Ni/CGO anodes with regard to increased electrocatalytic and reforming activity of the CGO phase could further increase the Ni/CGO performance under sulfur poisoning conditions.

In general, it has been shown that the search for sulfur tolerance in SOFC is exemplified by the properties of nickel. While it has excellent electro-catalytic properties, it is also extremely susceptible to the electron-withdrawing effects of sulfur. While Ni/CGO anodes display a superior sulfur tolerance than Ni/YSZ anodes, more investigations of stacks under realistic operating conditions are required to assess if the increased sulfur tolerance is sufficient for commercial use of Ni/CGO anodes without a desulfurization unit.

Another possibility to decrease the initial performance drop is the alloying of nickel with other less sulfur prone metals such as Rh, Mo, Sn, W and Cu.[248,249]. This was shown to decrease the metal-sulfur bond and thus, increase sulfur tolerance. However, since nickel is an excellent catalyst for the reforming reactions, alloying may reduce the activity towards these reactions. However, further investigations have to be performed to explore the full potential of nickel alloys.

In order to omit the desulfurization unit in SOFC systems and ensure stable long-term degradation for the whole range of possible sulfur contaminant concentrations in the fuel, the safest way would be to develop a nickel-free anode. Therefore, future work has to focus on finding

materials, which combine the activity and cost of nickel with a low susceptibility toward sulfur poisoning. Although metal-free anodes such as strontium titanates and its derivatives show essentially no performance drops after sulfur exposure, their overall performance has to be significantly improved in order to become a viable alternative.[250–252]

## Supplementary information

## S1 Cell characterization for short-term poisoning

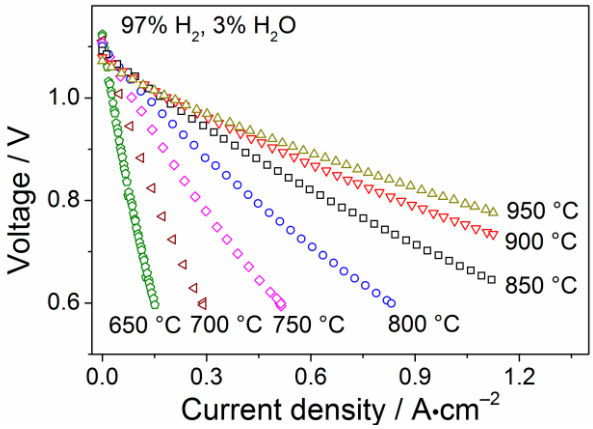


Figure S1. *i*–*V* curves of cell A at different temperatures $T$ = 650 – 950 °C, $pO_2$ = 0.21 atm, and $pH_2O$ = 0.03 atm.

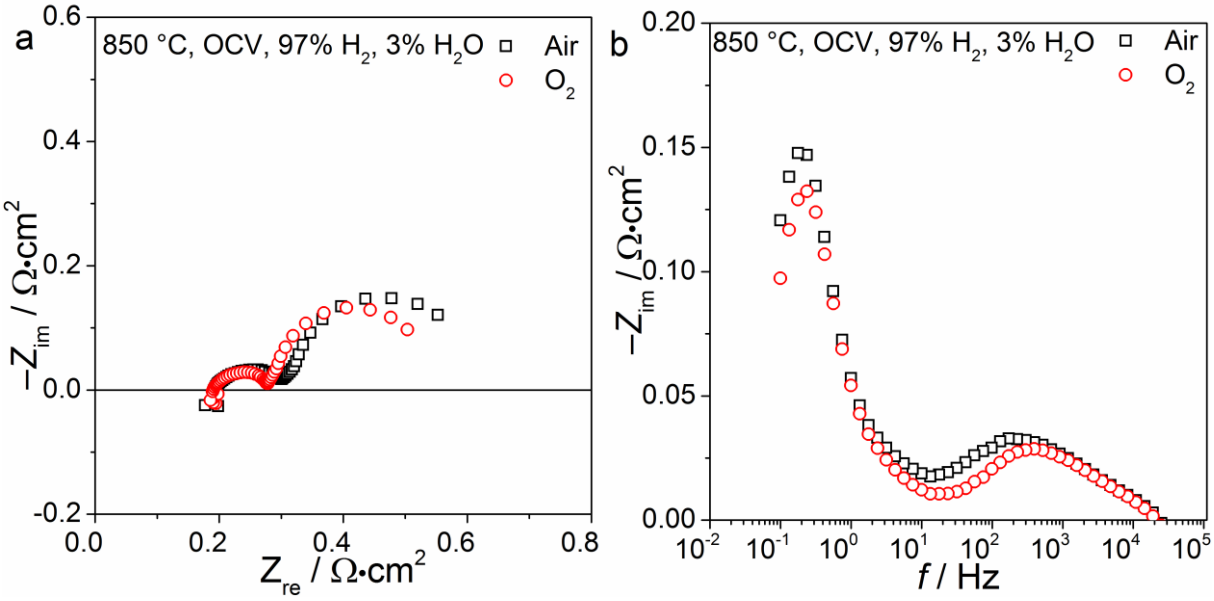


Figure S2. a) Nyquist and (b) imaginary impedance plots of impedance spectra of cell A recorded at temperature $T$ = 850 °C, OCV, $pH_2$ = 0.97 atm, $pH_2O$ = 0.03 atm with different $pO_2$ = 0.21 atm (black squares) and $pO_2$ = 1 atm (red circles).

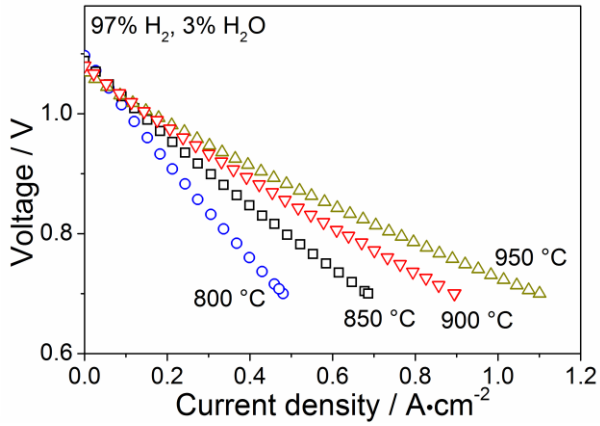


Figure S3. *i-V* curves of cell B at different temperatures $T$ = 800 – 950 °C, $pO_2$ = 0.21 atm, and $pH_2O$ = 0.03 atm.

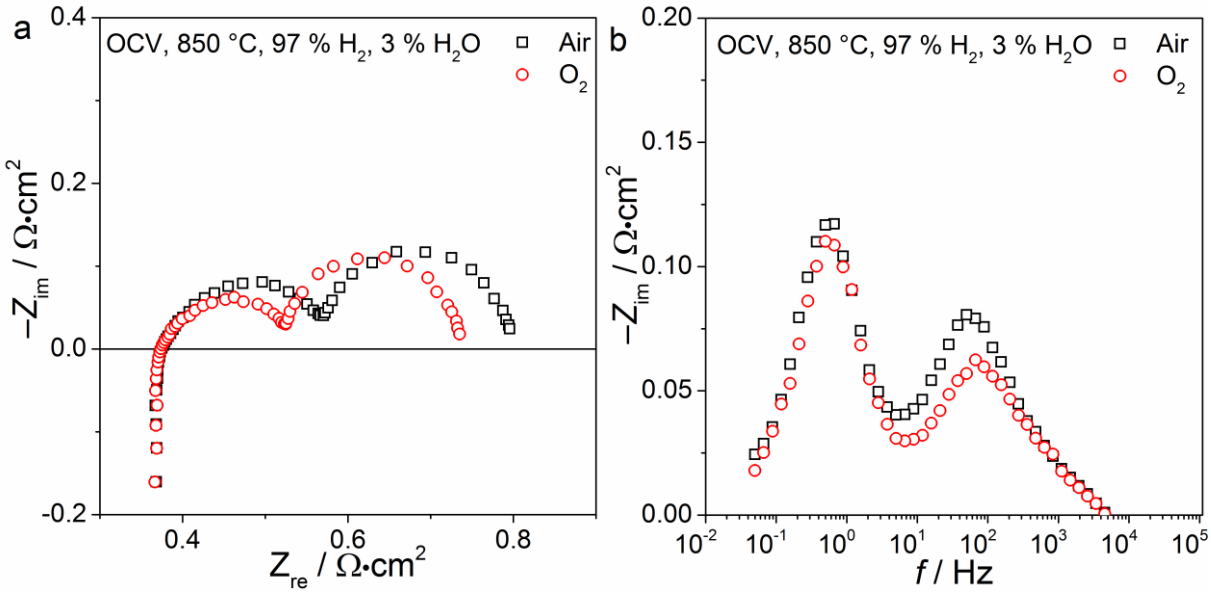


Figure S4. a) Nyquist and (b) imaginary impedance plots of impedance spectra of cell B recorded at temperature $T$ = 850 °C, OCV, $pH_2$ = 0.97 atm, $pH_2O$ = 0.03 atm with different $pO_2$ = 0.21 atm (black squares) and $pO_2$ = 1 atm (red circles).

In order to further understand the influence of the LSM cathode on the overall behavior of cell A and cell B, impedance spectroscopy measurements were recorded for the operation of the cathode with both air und pure oxygen. The respective spectra for cell A are illustrated in Figure S2. The recorded spectra for cell B are shown in Figure S4. The reduction of $pO_2$ influences the frequency range of both impedance spectra between 40 – 60 Hz causing a strong

reduction of the high frequency contribution indicating the presence of a cathode surface process at these frequencies. The reduction of the cathode contribution is not visible at frequencies higher than $10^3$ Hz. Thus, the peak visible at these frequencies is probably not cathode-related and caused by the anode bulk process as described earlier. In addition, a minor influence is visible upon $pO_2$ increase between $10^{-1}$ and $10^0$ Hz, which can be related to the cathode gas concentration impedance as reported by Kornely et al.[197] In earlier studies of SOFC with LSM/YSZ cathodes two distinct peaks significantly contributing to the overall cell resistance have been identified.[196–198] The low frequency contribution between 10 – 1000 Hz was related to the dissociative adsorption and diffusion of oxygen on the LSM surface which is most likely the contribution observed in the present study. Moreover, a high frequency contribution at about 10 kHz was identified and attributed to oxygen ion migration and diffusion into the electrolyte. This contribution cannot clearly be distinguished in the present study as it is probably obscured by the anode bulk process and/or inductance caused by wiring. In literature, the low frequency contribution was shown to be $pO_2$ dependent, while the high frequency contribution remained constant.[253] This is in good agreement with our observed results. In the present study, the peak observed at approximately 10 kHz is also neither dependent on $pH_2O$ nor on $pO_2$, hence, it is assigned to oxygen ion migration in the electrolyte.[254]

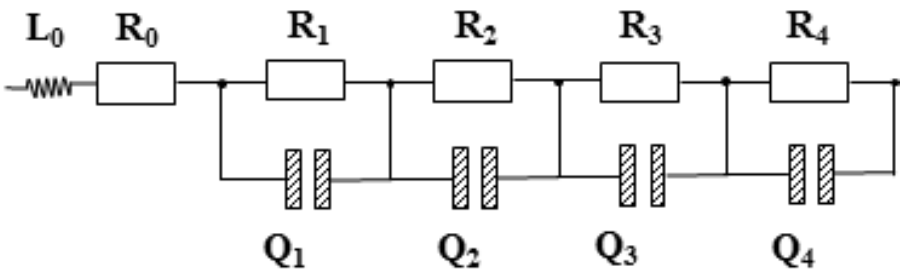


Figure S5. Equivalent circuit model, consisting of the inductance $L_0$, the Ohmic resistance $R_0$, and four resistance (R)/constant phase elements (Q), describing a high frequency cathode process ($R_1/Q_1$), a middle frequency anode bulk process ($R_2/Q_2$), a cathode surface process ($R_3/Q_3$) and an effective process containing an anode surface process and gas conversion ($R_4/Q_4$).

Table S1. Resistance and capacitance values calculated with equivalent circuit modeling and the equivalent circuit shown above. The ECM was used to fit the original impedance spectra with and without sulfur exposure used to calculate the differential impedance spectra in Figure 5.15.

| Test | $R_0$ [Ω·$cm^2$] | $R_1$ [Ω·$cm^2$] | $Q_1$ [mF·$cm^{-2}$] | $R_2$ [Ω·$cm^2$] | $Q_2$ [mF·$cm^{-2}$] | $R_3$ [Ω·$cm^2$] | $Q_3$ [mF·$cm^{-2}$] | **$R_4$ [Ω·$cm^2$]** | **$Q_4$ [F·$cm^{-2}$]** |
|---|---|---|---|---|---|---|---|---|---|
| 800 °C, 0 ppm | 0.23 | 0.09 | 0.08 | 0.09 | 4.28 | 0.15 | 7.09 | **0.13** | **1.07** |
| 850 °C, 0 ppm | 0.18 | 0.07 | 0.09 | 0.05 | 5.85 | 0.07 | 8.46 | **0.1** | **1.65** |
| 900 °C, 0 ppm | 0.15 | 0.04 | 0.25 | 0.06 | 5.2 | 0.02 | 394.69 | **0.1** | **2.57** |
| 800 °C, 1 ppm | 0.23 | 0.09 | 0.08 | 0.07 | 4.39 | 0.13 | 11.25 | **0.24** | **0.36** |
| 850 °C, 1 ppm | 0.2 | 0.04 | 0.25 | 0.06 | 5.58 | 0.06 | 22.04 | **0.17** | **1.16** |
| 900 °C, 1 ppm | 0.15 | 0.04 | 0.19 | 0.06 | 5.46 | 0.02 | 172 | **0.14** | **1.69** |

The results of the CNLS fit in Table S1 clearly show increasing capacitance values with increasing temperatures for both cases with and without the exposure to sulfur. However, it has to be emphasized that calculated capacitance and resistance values are still lumped parameters that contain both the gas conversion and the anode surface process. Upon a change of temperature, the ratio between the two contributions will invariably change, causing a frequency shift and thus, a change in capacitance of the lumped low frequency arc. However, the observed significant changes in capacitance of this lumped process can still be considered as clear indication for changes of the anode surface process capacitance.

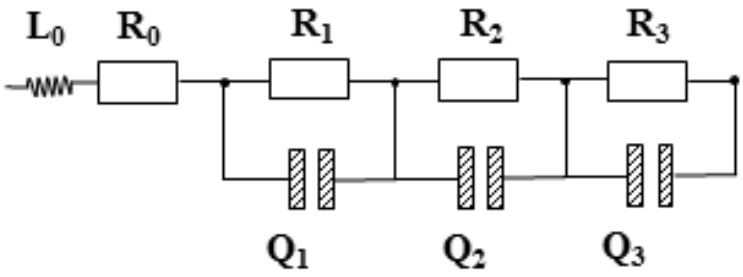


Figure S6. Equivalent circuit model, consisting of the inductance $L_0$, the Ohmic resistance $R_0$, and three resistance (R)/constant phase elements (Q), describing a high frequency cathode process ($R_1/Q_1$), an effective middle frequency process containing anode and cathode charge transfer processes ($R_2/Q_2$), and an effective process containing an anode process and gas conversion ($R_3/Q_3$).

Table S2. Resistance and capacitance values calculated with equivalent circuit modeling and the equivalent circuit shown in Figure S6. The ECM was used to fit the original impedance spectra with and without sulfur exposure used to calculate the differential impedance spectra in Figure 5.19.

| Test | $R_0$ [$\Omega\cdot cm^2$] | $R_1$ [$\Omega\cdot cm^2$] | $Q_1$ [$mF\cdot cm^{-2}$] | **$R_2$ [$\Omega\cdot cm^2$]** | **$Q_2$ [$F\cdot cm^{-2}$]** | $R_3$ [$\Omega\cdot cm^2$] | $Q_3$ [$F\cdot cm^{-2}$] |
|---|---|---|---|---|---|---|---|
| 800 °C, 0 ppm | 0.47 | 0.03 | 39.65 | **0.17** | **0.18** | 0.07 | 76.66 |
| 850 °C, 0 ppm | 0.34 | 0.02 | 74.29 | **0.11** | **0.18** | 0.07 | 1.05 |
| 900 °C, 0 ppm | 0.26 | 0.01 | 49.41 | **0.07** | **0.18** | 0.08 | 11.5 |
| 800 °C, 1 ppm | 0.46 | 0.03 | 61.13 | **0.22** | **0.21** | 0.06 | 8.44 |
| 850 °C, 1 ppm | 0.34 | 0.02 | 83.7 | **0.14** | **0.22** | 0.07 | 10.66 |
| 900 °C, 1 ppm | 0.26 | 0.01 | 78.89 | **0.08** | **0.23** | 0.07 | 11.17 |

The results of the CNLS fit in Table S2 clearly show constant capacitance values of the effective process 2 containing the sulfur-affected anode surface process ($Q_2$) for both cases with and without the exposure to sulfur. However, the calculated capacitance and resistance values are still effective parameters containing both a cathode and an anode surface process. Upon a change of temperature, the ratio between the two contributions will change, preventing the extraction of the respective capacitance values and hampering a comparison of the sulfur-affected anode surface processes. The capacitance of the effective process $Q_2$ is related to the single processes according to

$$Q_2 = \frac{C_{cat} C_{an}}{C_{cat} + C_{an}}, \qquad [56]$$

with $C_{cat}$ being the capacitance of the cathode charge transfer process and $C_{an}$ the capacitance of the anode charge transfer process.[144] The changes of resistance upon $pO_2$ variation on cathode (Figure S4) and anode side (Figure 5.9) indicate that both processes contribute significantly to the high frequency resistance and thus, can be estimated to be in the same order of magnitude. The cathode and anode processes in the high frequency contribution cannot even be separated by calculation of the DRT as shown in Figure 5.10 due to similar relaxation times. Therefore, the capacitance values also are in the same order of magnitude and according to Eq. 56, can be estimated to be close to the calculated value of $Q_2$. This value, is one order of magnitude smaller than the one of the corresponding value $Q_3$ of cell A in some cases (e.g. 850 °C, 1 ppm $H_2S$: 1.16 $F \cdot cm^{-2}$ vs. 0.22 $F \cdot cm^{-2}$) indicating a lower capacitance due to high Gd doping in the case of the Ni/CGO40-based anode. However, it has to be emphasized that such a comparison is done under simplified assumptions and thus, only provides a rough estimate.

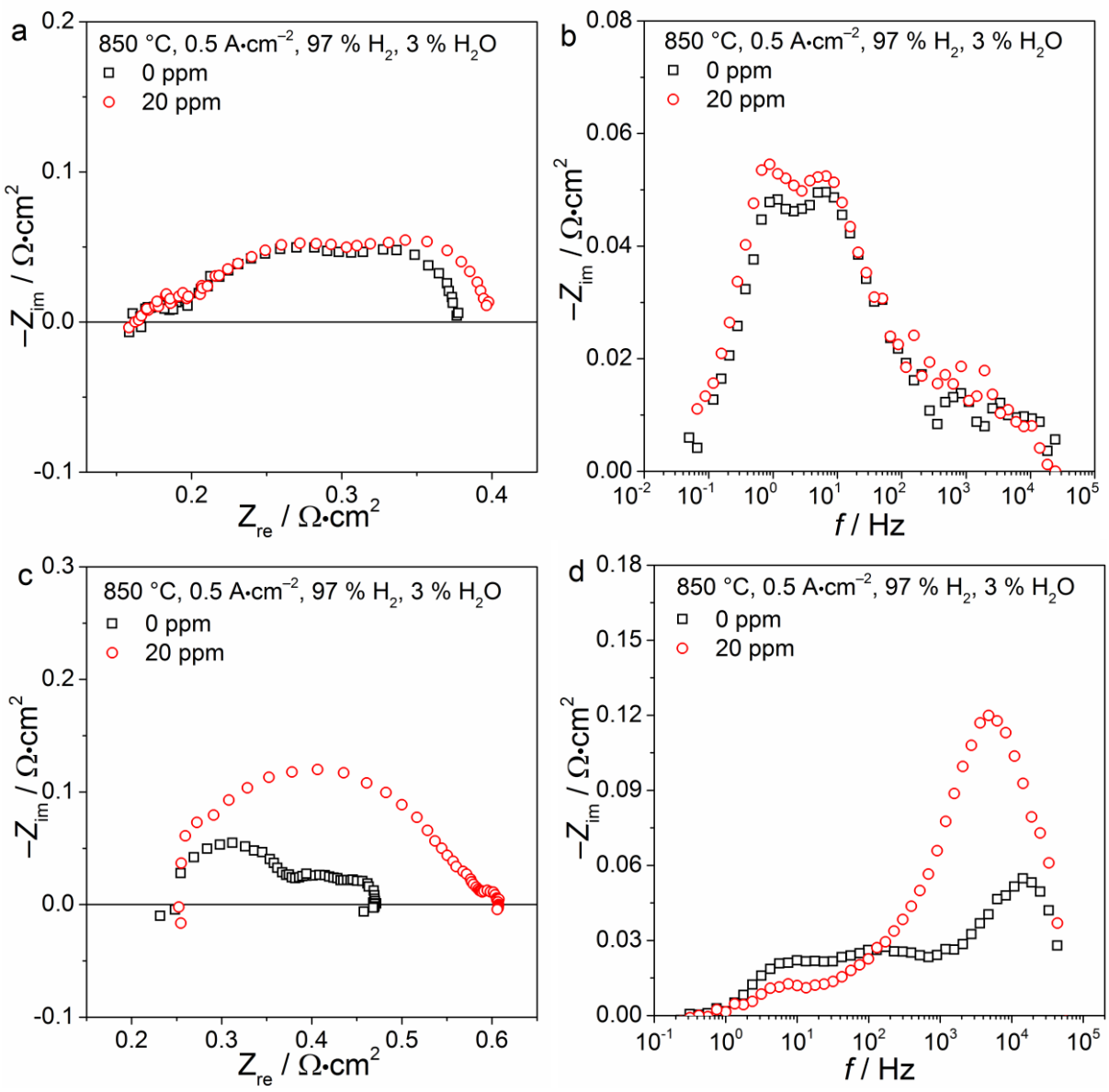


Figure S7. Nyquist and imaginary impedance plots of impedance spectra of (a + b) the Ni/CGO-based cell C and (c + d) the Ni/YSZ-based cell E recorded at temperature $T$ = 850 °C, 0.5 A·cm$^{-2}$, $p$H$_2$ = 0.97 atm, $p$H$_2$O = 0.03 atm with $p$O$_2$ = 0.21 atm. The graphs show measurements with (red circles) and without the addition of 20 ppm $H_2S$ (black squares).

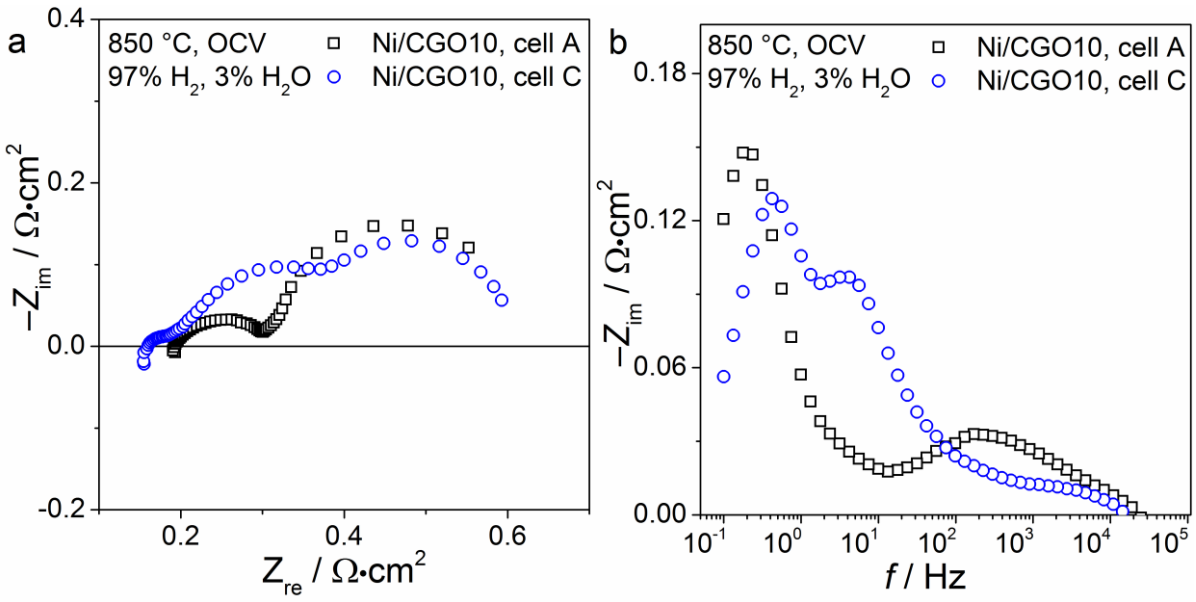


Figure S8. a) Nyquist and (b) imaginary impedance plots of impedance spectra of the Ni/CGO-based cell A (black squares) and Ni/CGO10-based cell C (blue circles) recorded at temperature $T$ = 850 °C, OCV, $p\mathrm{H_2}$ = 0.97 atm, $p\mathrm{H_2O}$ = 0.03 atm with $p\mathrm{O_2}$ = 0.21 atm.

In order to quantify the contribution of the anode charge transfer resistance, an equivalent circuit model was adopted. The model employs four R-Q elements to represent the overall cell behavior. By means of a non-linear square fit, resistance values of the anode charge transfer could be extracted (0.20 Ω·cm$^2$ for Ni/CGO10, cell C and 0.28 Ω·cm$^2$ for Ni/CGO10, cell A).

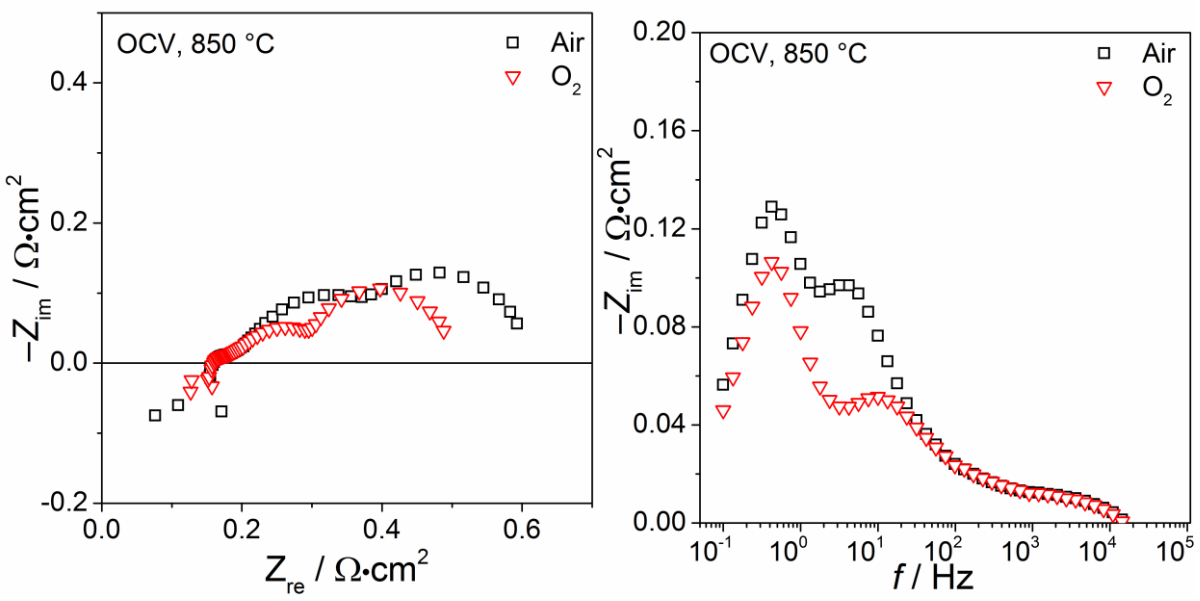


Figure S9. a) Nyquist and (b) imaginary impedance plots of impedance spectra of the two cells recorded at temperature $T$ = 850 °C, OCV, $pH_2$ = 0.97 atm, $pH_2O$ = 0.03 atm with $pO_2$ = 0.21 atm (red triangles) and 1 atm (black squares).

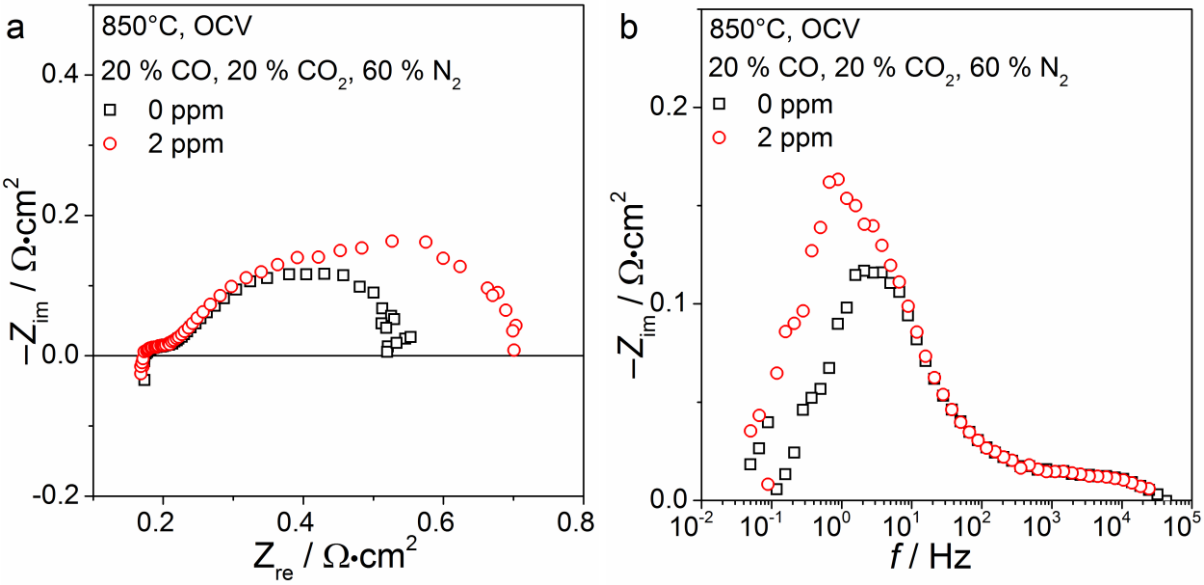


Figure S10. a) Nyquist and (b) imaginary impedance plots of impedance spectra of the two cells recorded at temperature $T$ = 850 °C, OCV, $pCO$ = 0.20 atm, $pCO_2$ = 0.20 atm $pN_2$ = 0.60 atm with $pO_2$ = 0.21 atm. The graphs show the Ni/CGO-based cell with (red circles) and without (black squares) the addition of 2 ppm $H_2S$.

## S2 Long-term sulfur poisoning of other Ni-based anodes in hydrogen-rich fuels

### *S2.1 Solid oxide cell testing*

Two other cells with Ni-based anodes have been investigated towards their long-term stability under sulfur exposure. Their geometries and employed materials are listed in Table 3.1. Cell B used a NiCu5/CGO40 anode and cell E a Ni/8YSZ anode. In cell B the functional anode layer was directly printed onto the electrolyte. In cell E, a 5 µm thick 8YSZ layer was applied between electrolyte and functional anode. Both cells were characterized in detail by means of current-voltage characteristics, electrochemical impedance spectroscopy and SEM in chaoters. Long-term experiments were performed with different sulfur concentrations and the test specifications described in Table S3.

Table S3. Overview of test specifications of the two long-term tests.

| | Test acronym | Cell | Anode gas | $H_2S$ concentration [ppm] | Overall duration of experiment [h] | Current density [$A \cdot cm^{-2}$] |
|---|---|---|---|---|---|---|
| 900 h test | 900h-0ppm | B | 97 % $H_2$, 3 % $H_2O$ | 0 | 900 | 0.75 |
| | 900h-1ppm | B | 97 % $H_2$, 3 % $H_2O$ | 1 | 900 | 0.75 |
| | 900h-10ppm | B | 97 % $H_2$, 3 % $H_2O$ | 10 | 900 | 0.75 |
| Ni/YSZ test | NiYSZ | E | 100 % $H_2$ | 20 (48 h), 10 (143 h) | 191 | 0.25 (118 h), 0.5 (73 h) |

### *S2.2 FIB/SEM tomography*

3D reconstruction of the anode microstructure of cells of type B was carried out via FIB/SEM tomography. The respective volumes were reconstructed right next to the anode/electrolyte. The metallic part in the anodes consists of two elements (95 wt. % nickel (atomic number $Z$ = 28) and 5 wt. % copper ($Z$ = 29)). As the 3D reconstruction can be carried out only for volumes consisting of three phases, it has to be assured that under the electronic beam the two elements are considered as one metallic part. Based on the grey level and using the backscat-

tered electron (BSE) detector at 3 kV, only three phases could be distinguished. For this reason, a Monte Carlo simulation[161] was carried out to compare the backscattering coefficient between the two elements by varying the acceleration voltage. The results presented in Figure S11 show that Ni and Cu have the same backscattering coefficient in the range 0.1 kV – 5kV, which confirms the SEM observation. Thus, it is concluded that based on the grey level and backscattering coefficient the two elements can be evaluated as one metallic part.

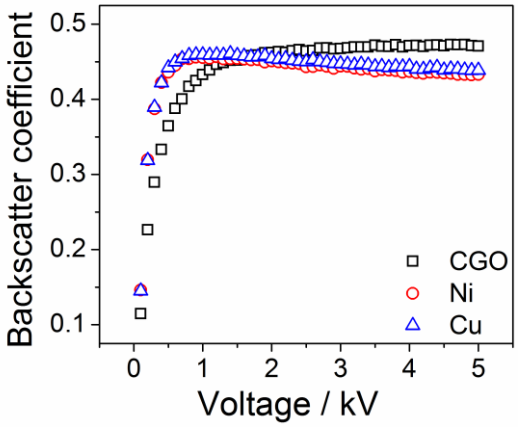


Figure S11. A Monte Carlo simulation carried out for the three phases Ni, Cu and CGO present in anodes of cell B.

*S2.3 The 900 h test – Ni/CGO40-based SOFC*

Another test with hydrogen-rich fuel gas was carried out for SOFC based on NiCu5/CGO40 anodes at similar conditions as the 1500 h test of the Ni/CGO10-based cell (cell D, see main text). Since the ionic conductivity of the 6ScSZ electrolyte is significantly higher than the one of 3YSZ (used in the cells D of the 1500 h test), it was possible to increase the current density to 0.75 $A \cdot cm^{-2}$ to obtain similar operating voltages as in the 1500 h test (see Table 7.2 and Table S4). Over the course of the experiment, both the two tests at 0 and 10 ppm $H_2S$ exposure show periods of steadily increasing voltage. However, the 900h-1ppm test does not exhibit this behavior. As all tests are mounted in the same test rig and are supplied with the same gas mixture, except for the sulfur-containing gas stream, the witnessed behavior could not be caused by variations in the gas supply. Rather likely is a cathode activation effect as reported in literature.[255,256] The reason why this did not occur for the 900h-1ppm sample, is unclear.

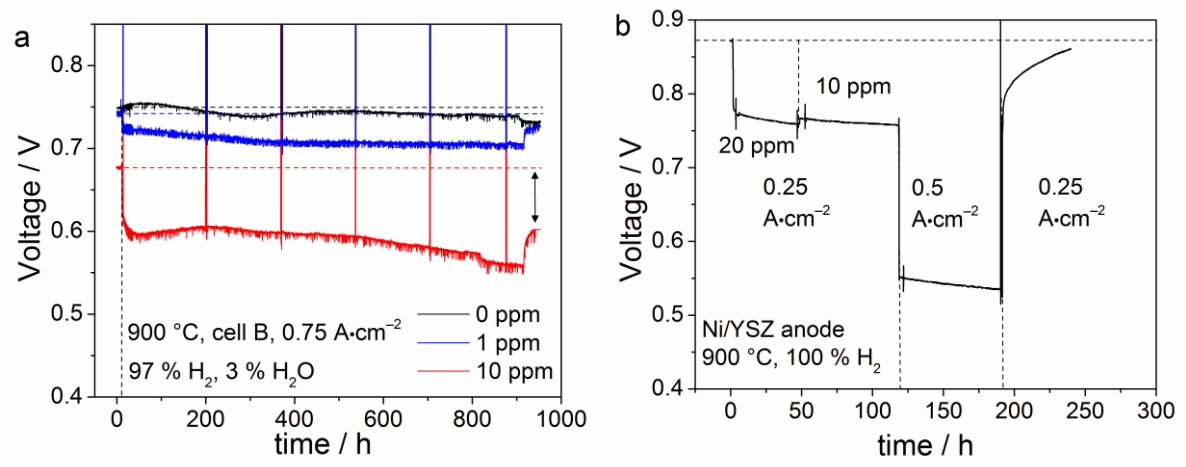


Figure S12. Cell voltage curves as a function of time at temperature $T$ = 900 °C and $pO_2$ = 0.21 atm. (b) Ni/CGO40-based cells of type B are operated at $i$ = 0.75 A·cm$^{-2}$, $pH_2$ = 0.97 atm, $pH_2O$ = 0.03 atm, with $H_2S$ concentrations of 0, 1 and 10 ppm. (c) A Ni/YSZ-based cell of type E is operated at $i$ = 0.25 A·cm$^{-2}$ (first 120 h) and 0.5 A·cm$^{-2}$ (subsequent 70 h) with 20 (first 40 hours) and 10 ppm $H_2S$ (subsequent 150 h) at $pH_2$ = 1.0 atm.

The initial voltage of the 0 ppm (0.748 V) and 1 ppm test (0.744 V) were approximately the same, however, the value for the 10 ppm test was significantly lower (0.677 V). The voltage evolution of the 900-1ppm test showed a similar trend as the sulfur-free reference test with an irreversible voltage decrease of 16 mV (900h-0ppm) compared to 17 mV (900h-1ppm). Moreover, the 900h-1ppm test displays the same change in both ohmic and polarization resistance over the course of the experiment (Figure S13, calculated based on EIS measurements in Figure S14) as the 900h-0ppm, which confirms the absence of sulfur-induced irreversible degradation. For exposure to 10 ppm $H_2S$, higher irreversible degradation of 65 mV was observed. The analysis of the cell resistance of the 900h-10ppm test shows that its degradation is mainly caused by an increase in ohmic resistance with a small contribution of an increased polarization resistance, which is consistent with the results shown in Figure 7.2.

Table S4. Overview of the cell voltage changes for the three long-term measurements. Initial and final voltages denote the cell voltages before the start of $H_2S$ exposure and after regeneration, respectively. The overpotential is calculated based upon the observed OCV and the cell voltage after the initial voltage drop.

| | Test acronym | Initial voltage [V] | Final voltage [V] | Irreversible degradation [mV] | Initial voltage drop [mV] | Regenerated voltage [mV] | Overpotential $\eta$ [mV] |
|---|---|---|---|---|---|---|---|
| 900 h test | 900h-0ppm | 0.748 | 0.732 | 16 | - | - | 340 |
| | 900h-1ppm | 0.744 | 0.727 | 17 | 20 | 23 | 364 |
| | 900h-10ppm | 0.677 | 0.602 | 65 | 76 | 64 | 486 |
| Ni/YSZ test | NiYSZ (Phase 1, 20 ppm, 0.25 A·cm$^{-2}$) | 0.872 | [a] | 13 | 100 | [a] | 448 |
| | NiYSZ (Phase 1, 10ppm, 0.25 A·cm$^{-2}$) | 0.766 | 0.759 | 7 | 92[b] | - | 454 |
| | NiYSZ (Phase 1, 10 ppm, 0.5 A·cm$^{-2}$) | 0.552 | 0.535 | 17 | - | - | 668 |

[a]The recovery phase of these experiments could not be completed due to technical problems.

[b]With regard to initial voltage before Phase 1.

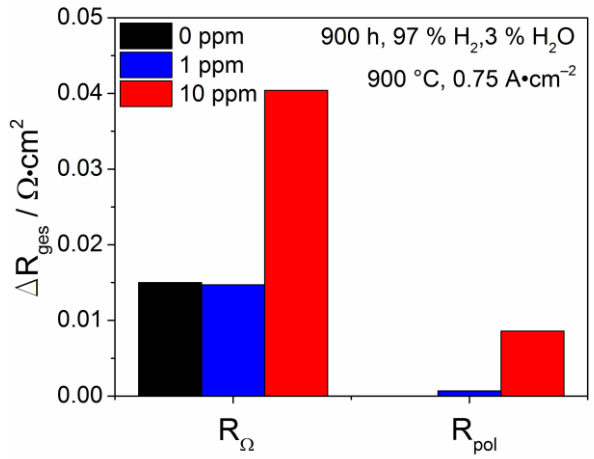


Figure S13. Analysis of ohmic and polarization resistance changes during the 900 h experiment with cells of type B. Resistance changes were calculated from electrochemical impedance spectra based on measurements after completion of the initial voltage drop and before start of the recovery phase.

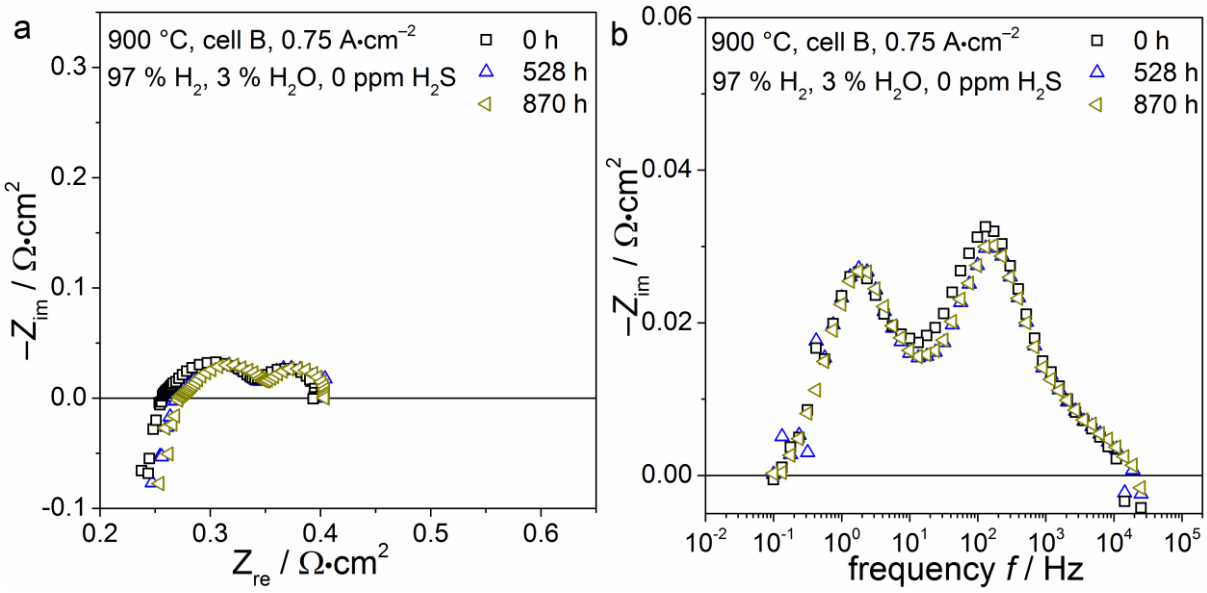

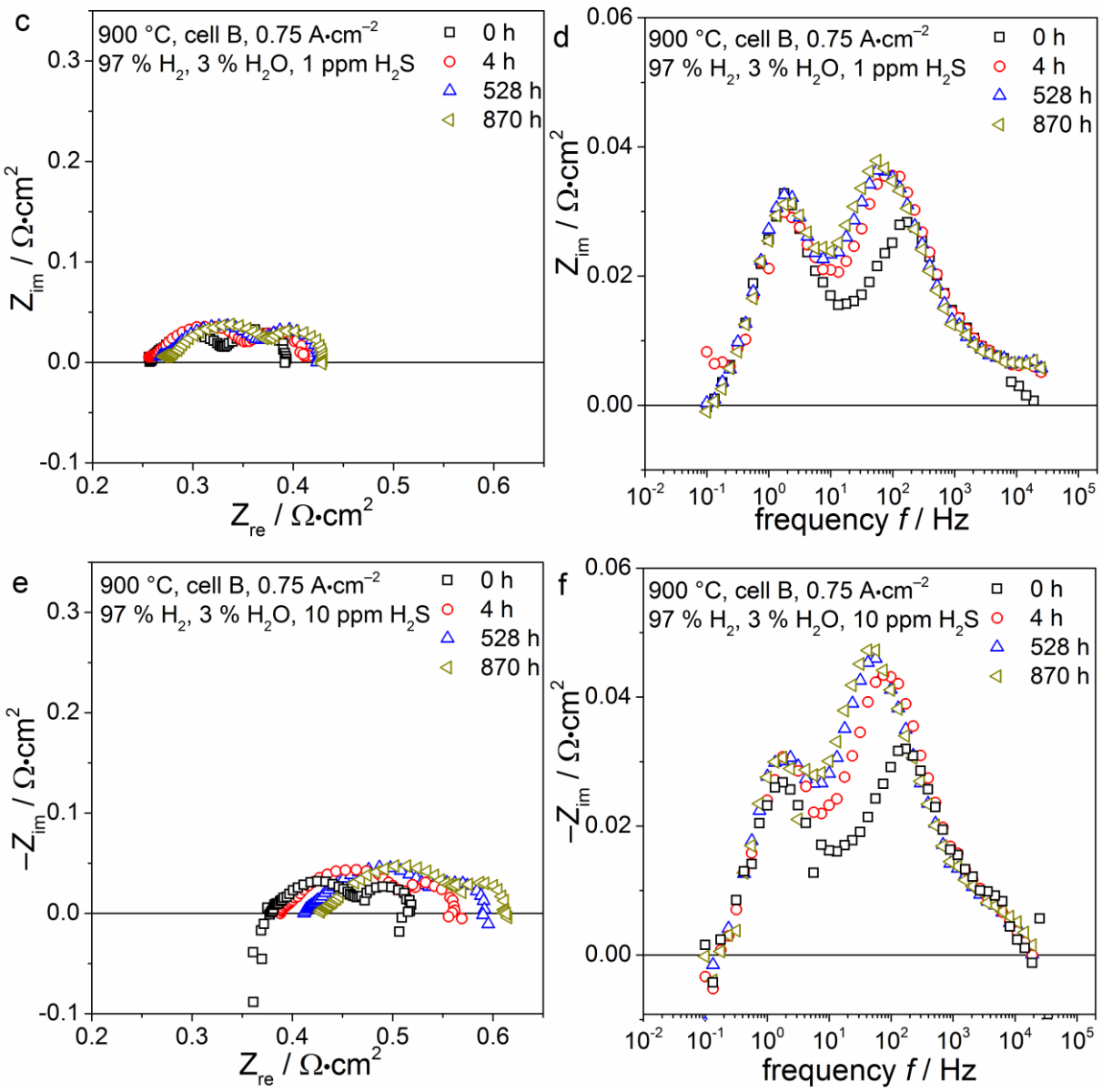


Figure S14. Nyquist and imaginary impedance plots of impedance spectra of the 900h test cells of type B recorded at temperature $T$ = 900 °C, $i$ = 0.75 A·cm$^{-2}$, $p$H$_2$ = 0.97 atm, $p$H$_2$O = 0.03 atm, $p$O$_2$ = 0.21 atm, with different H$_2$S concentrations of (a + b) 0, (c + d) 1, (e + f) 10 ppm. Impedance spectra are shown at different times $t$ = 0 h (black squares), 4 h (red circles), 528 h (blue up-pointing triangle) and 870 h (dark-green left-pointing triangle).

Microstructural analysis by means of FIB-SEM was carried out on all three tested cells. The variation of the microstructural parameters over the analyzed volume is shown in Figure S15. The results reveal no significant difference in TPB density and phase proportion in the anode functional layers between the three tested cells (Table S5). However, the percolation values of

the metallic and ceramic phase are lower for both of the sulfur-exposed samples by 1 – 3 % in comparison with the 900h-0ppm test. Especially the Ni percolation value of the 900h-10ppm test has decreased to 94.8 % (compared to 97.8 % for 900h-0ppm) and could possibly be the cause for the increased ohmic resistance. In contrast to YSZ, the agglomeration of CGO particles was shown to be a common degradation phenomenon during SOFC operation.[62,160,231] Although neither CGO nor Ni show a significantly changed particle size distribution (Figure S16), this could reflect a loss of CGO percolation, which is visible for both sulfur-exposed cells possibly contributing to the ohmic resistance increase of the 900h-10ppm cell.

Table S5. Microstructural properties of the three cells of type B after long-term testing with 0, 1, and 10 ppm $H_2S$ exposure. The given values are calculated based on the post-mortem FIB-SEM measurements and corresponding 3D reconstructions.

| Test | TPB density [µm·µm$^{-3}$] | Ni proportion [%] | CGO proportion [%] | Pore proportion [%] | Percolation [%] | | |
|---|---|---|---|---|---|---|---|
| | | | | | Ni | CGO | pore |
| 900h-0ppm | 13.7 | 32.9 | 25.2 | 41.9 | 97.8 | 98.11 | 99.3 |
| 900h-1ppm | 13.7 | 33.3 | 24.1 | 42.6 | 96.8 | 95.25 | 99.8 |
| 900h-10ppm | 14.0 | 33.1 | 24.2 | 42.7 | 94.8 | 96.35 | 99.6 |

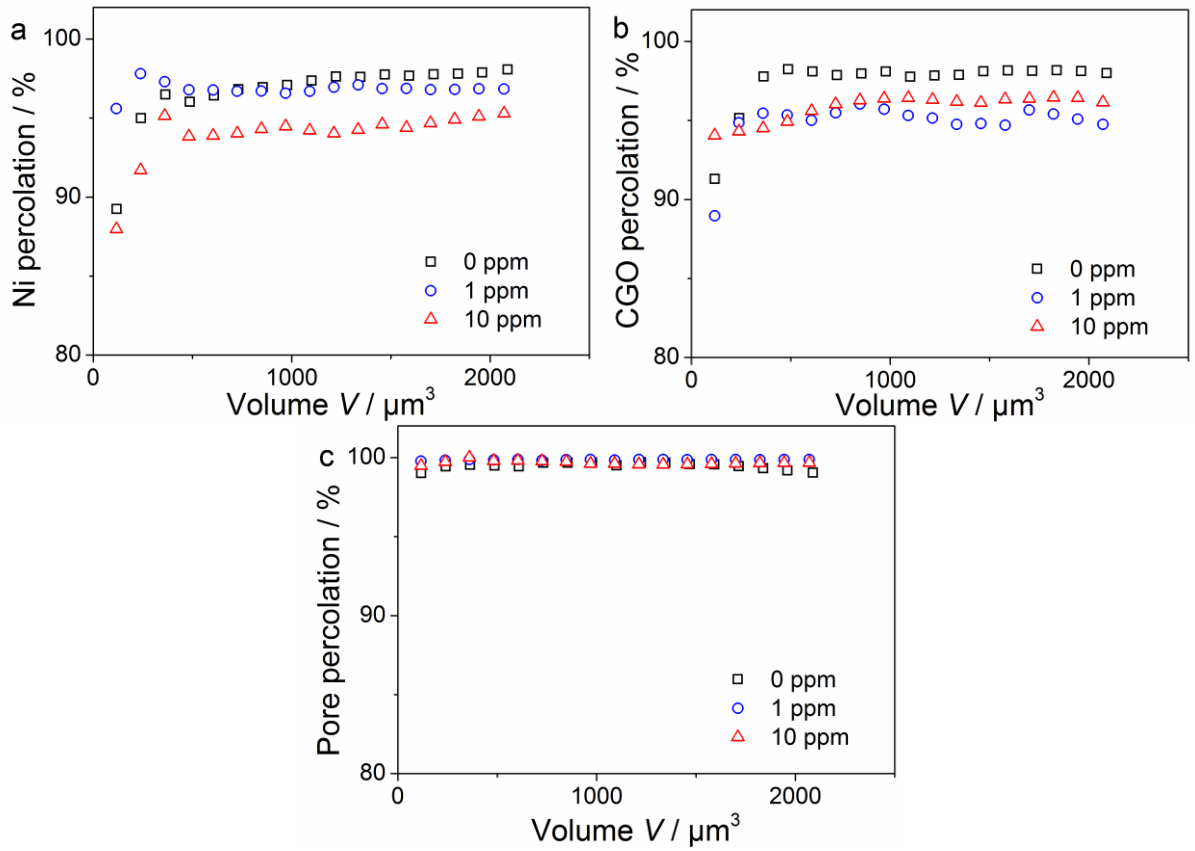


Figure S15. (a) Ni percolation, (b) CGO percolation and (c) pore percolation values according to 3D reconstruction via FIB-SEM tomography over the reconstructed volume of cells of type B in the 900 h test. The data points signify the values at the different subvolumes.

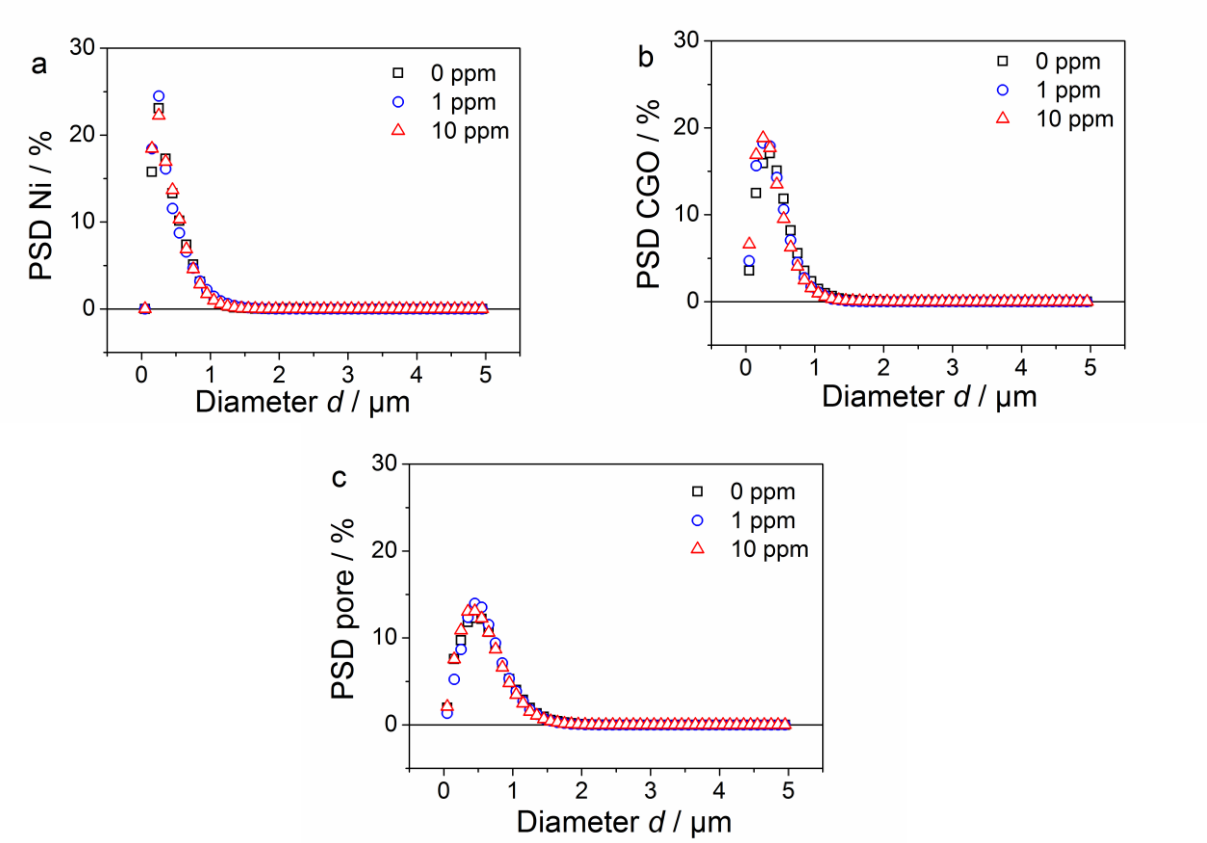


Figure S16. Particle size distribution (PSD) of cells of type B after the 900 h test for (a) the Ni phase, (b) the CGO phase and (c) the pore phase.

According to post mortem EDX measurements, both the 900h-0ppm and the 900h-10ppm test have lost approximately 60 % of the originally present copper over the course of the experiment due to the high operating temperature and comparatively low copper melting point of 1085 °C. Therefore, a certain loss of percolation of the metallic phase can be expected, which is likely accompanied by an increase in ohmic resistance. However, the loss of overall volume content of the metallic phase is maximum 1 % (based on an initial content of the metallic phase of 33 %). Moreover, the loss of copper occurred for both samples to the same extent, thus, the Cu loss cannot explain the sulfur-induced irreversible degradation in the 900h-10ppm test.

In order to possibly detect remaining trace amounts of sulfur in the anode, the 900h-10ppm sample was analyzed by means of TEM/EDX and XRF. Two different regions were imaged by means of TEM: the first at the interface between the Au layer and the surface of the anode (see Figure S17a) and the second one at Ni-CGO interface (see Figure S17b) The contrast of the EDX maps in Figure S17 is strongly enhanced to visualize the possible sulfur-enriched regions in the overlay images. However, in none of the investigated regions sulfur could be

detected. As the TEM/EDX resolution is about 0.2 wt. % and the scanning area of TEM/EDX is very small (0.85 x 0.85 µm$^2$), *post mortem* XRF measurements were also carried out. The results (Figure S18) show a similar low signal intensity for all three samples which is increased in comparison with an unreduced reference cell, probably caused by interactions of the anode with the fuel gas. Thus, neither high resolution TEM/EDX nor XRF measurements can conclusively confirm the presence of small amounts of sulfur in the anode layer. However, the present measurements represent the first efforts in literature to investigate sulfur-poisoned Ni/CGO anodes with those techniques.

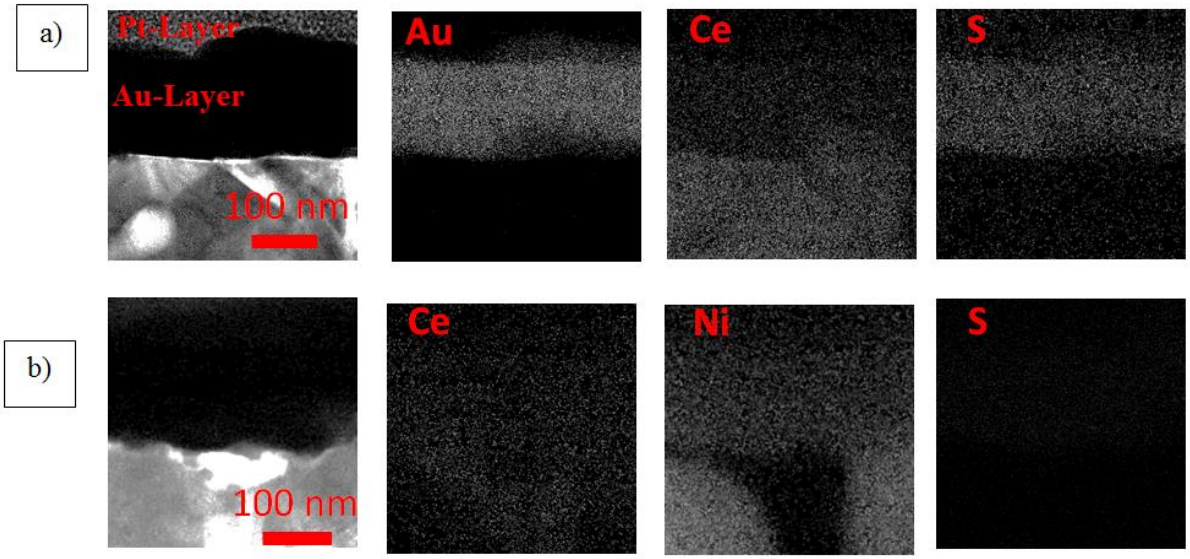


Figure S17. TEM/EDX analysis of the 900h-10ppm $H_2S$ sample carried out in two different areas: (a) at the interface Au-anode, (b) at a CGO-Ni interface. No sulfur traces could be detected.

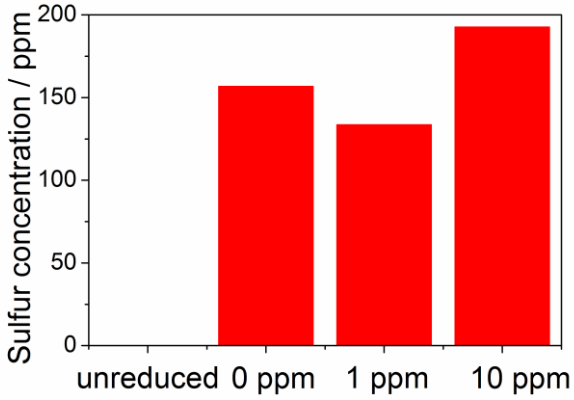


Figure S18. Results of XRF analysis of the 900h-10ppm $H_2S$ sample. Measured sulfur concentration in the Ni/CGO anode for the tests 900h-0ppm, 900h-1ppm and 900h-10ppm.

*S2.4 The Ni/YSZ test*

Although the irreversible degradation behavior of Ni/YSZ anodes has been extensively investigated before, a 200 h sulfur poisoning test was carried out (Figure S12b) in pure hydrogen to allow a comparison to Ni/CGO in similar conditions. The poisoning period was divided into three phases: a first one with 0.25 $A \cdot cm^{-2}$ and 20 ppm $H_2S$, a second one with hydrogen sulfide concentration reduced to 10 ppm and a third one with 0.5 $A \cdot cm^{-2}$ and 10 ppm $H_2S$ (comparable to the 1500 h test). The initial voltage drop reaches already 100 mV at 0.25 $A \cdot cm^{-2}$ demonstrating the considerably more severe short-time poisoning behavior of Ni/YSZ. Furthermore, poisoning phase 3 only lasted for about 70 h and resulted in a similar voltage decrease (17 mV) as the 1500h-10ppm test (23 mV). Although the two cells consist of different cell architectures, both are commercially available from the same supplier and show low degradation rates in sulfur-free atmospheres. Thus, it can be concluded that in the same sulfur-containing fuel gas atmosphere Ni/CGO anodes indeed show lower long-term degradation rates than Ni/YSZ. The decrease of $H_2S$ concentration from 20 to 10 ppm has an effect on the degradation rate as well since the voltage decrease drops from 13 mV (in 40 h) to 7 mV (80 h). In agreement with literature, the degradation is caused by an increase in the high frequency ($10^3 – 10^4$ Hz) charge transfer resistance.[112] Probably due to the short testing time, no increase in ohmic resistance was observed. It is possible that the less pronounced long-term degradation of Ni/CGO is caused by the increased (electro-)catalytic role of CGO. However, it might also be an indirect effect as the increased short-term sulfur resistivity also entails a smaller anode overpotential and thus, a larger anode potential step.

## S3 Supplementary information for long-term testing

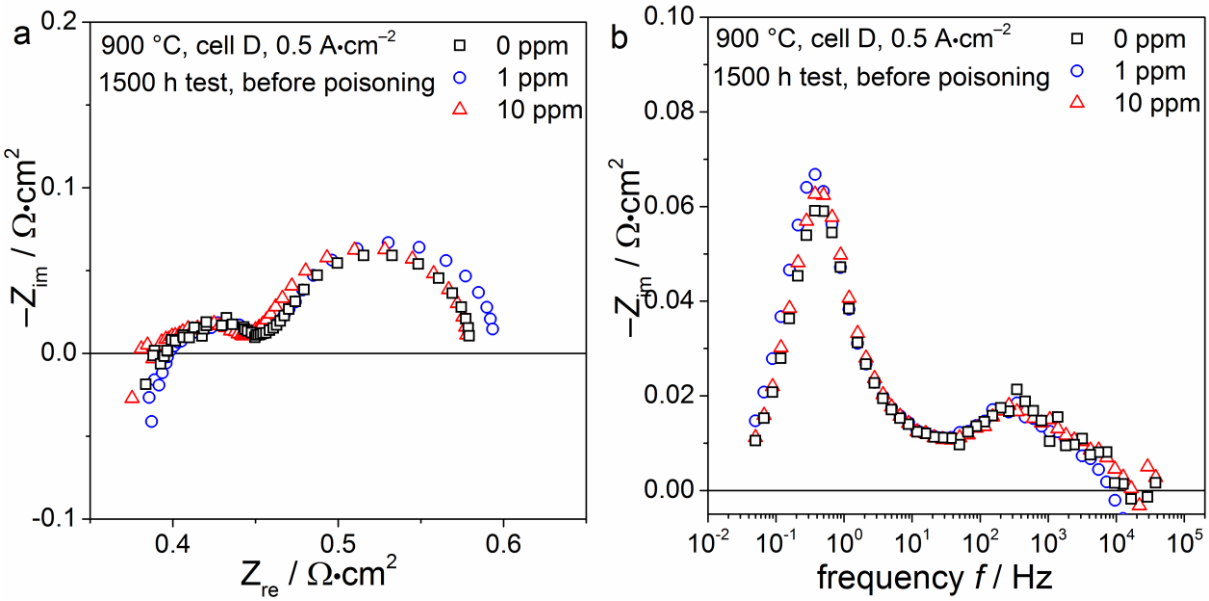


Figure S19. (a) Nyquist and (b) imaginary impedance plots recorded during the initial characterization of the three cells of type D before the start of the 1500 h experiment.

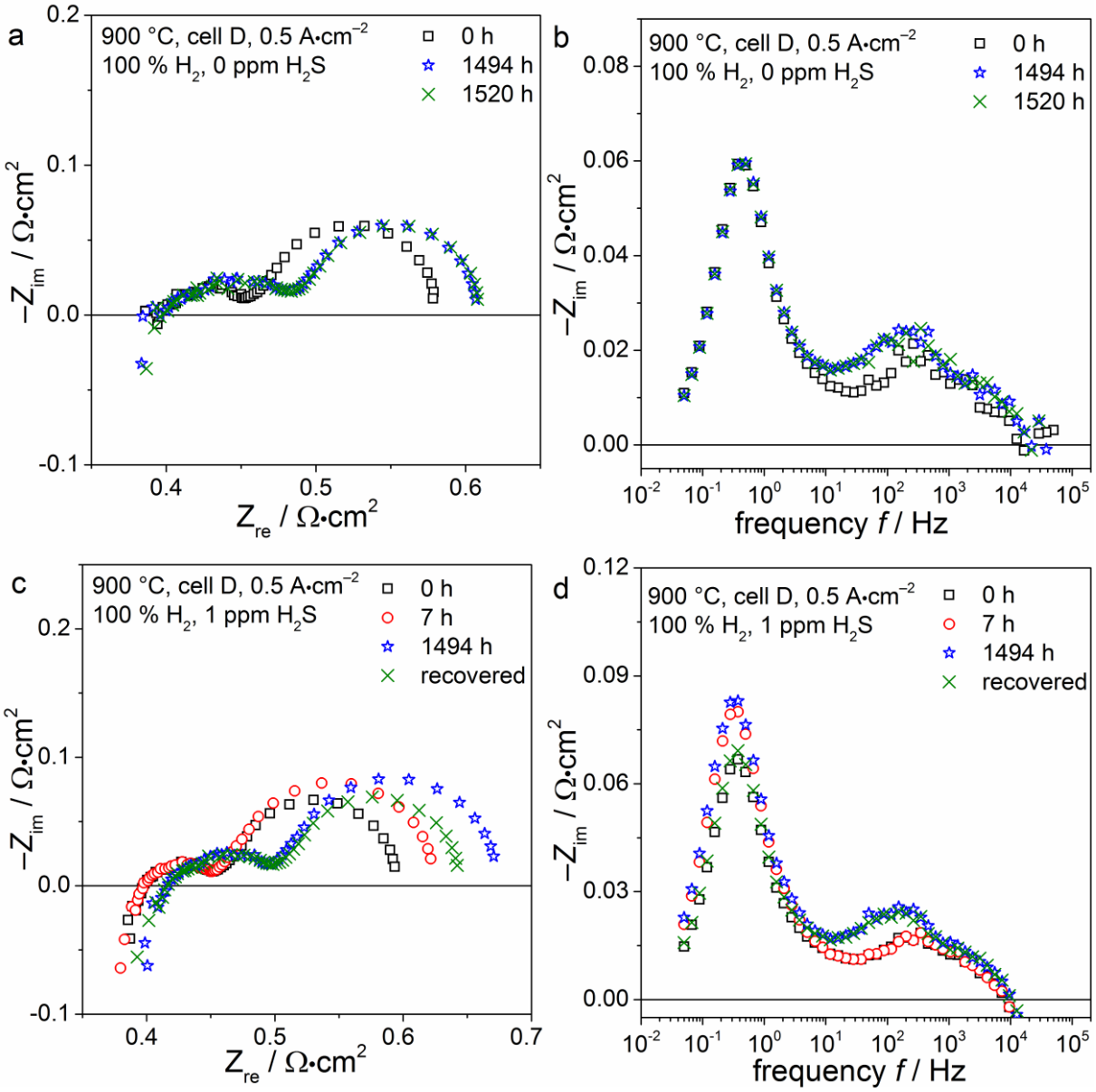


Figure S20. Nyquist and imaginary impedance plots recorded for (a+b) the 1500-0ppm test, (c+d) the 1500h-1ppm test. Impedance spectra are shown at different times $t$ = 0 h (black squares), 7 h (red circles), 1494 h (blue star) and after recovery (dark-green cross).

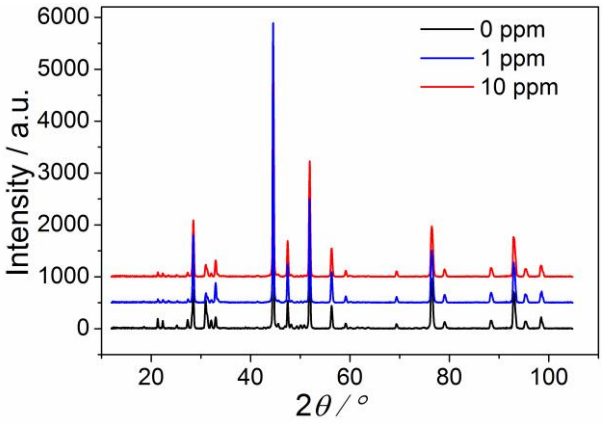


Figure S21. XRD spectra of the samples tested in the 1500 h experiment, exposed to 0, 1 and 10 ppm $H_2S$

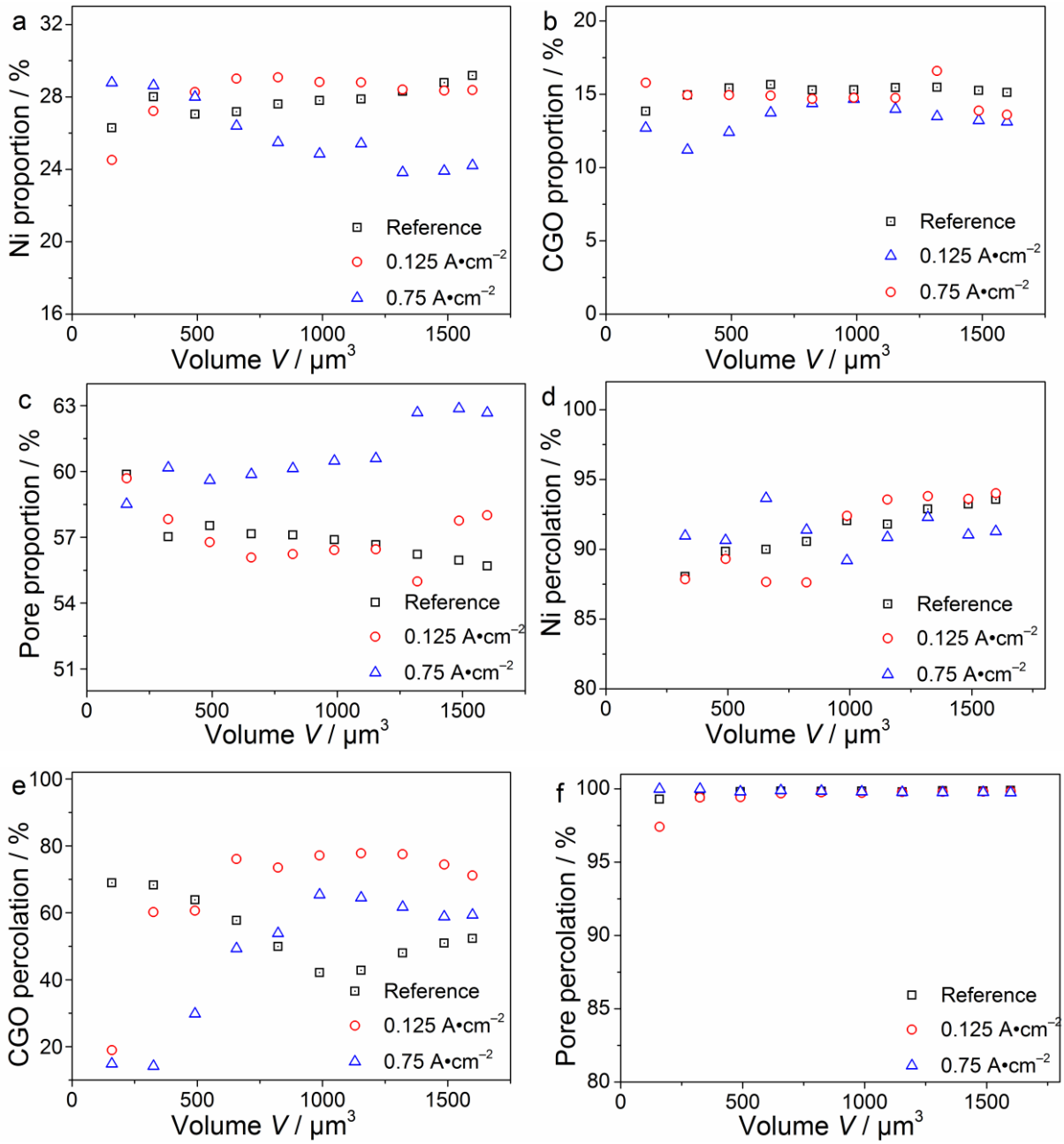


Figure S22. Different microstructural quantities of cells of type D over the reconstructed volume for a reduced reference cell ("reference"), the 200h-2A-10ppm and the 200h-12A-10ppm sample. The data points signify the values at the different subvolumes. (a) Ni proportion, (b) CGO proportion, (c) pore proportion, (d) Ni percolation, (e) CGO percolation and (f) pore percolation.

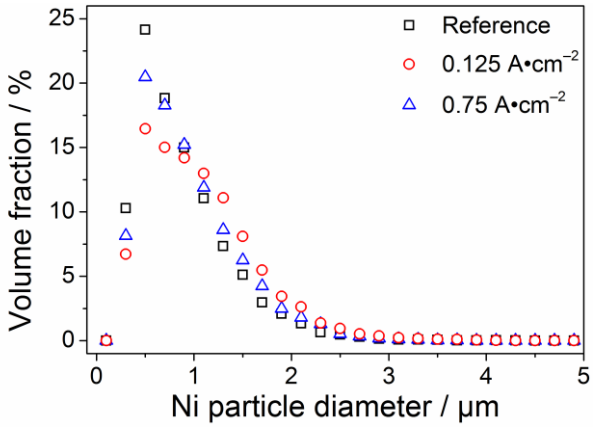


Figure S23. Particle size distribution for the Ni phase of cells of type D. Values are given for a reduced reference cell ("reference"), the 200h-2A-10ppm and the 200h-12A-10ppm sample.

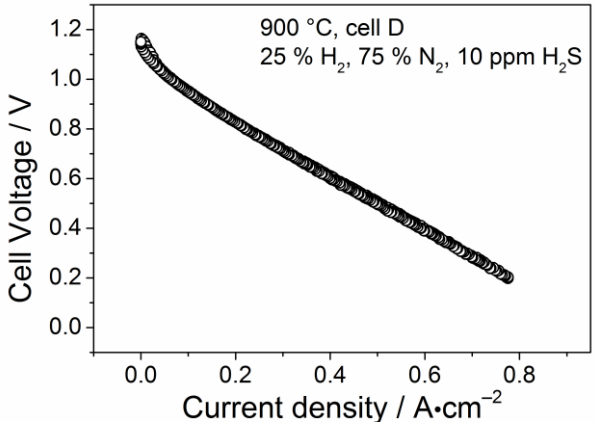


Figure S24. *i-V* curve of the 200h-8A-10ppm test during sulfur exposure, recorded until a cell voltage of 0.2 V.

## References


[1] UNFCCC. Conference of the Parties (COP), *Paris Clim. Chang. Conf. - Novemb. 2015, COP 21* **2015**, *21932*, 1–32.
[2] S. Sorrell, J. Speirs, R. Bentley, A. Brandt, R. Miller, *Energy Policy* **2010**, *38*, 5290–5295.
[3] C. Jorant, *Bull. At. Sci.* **2011**, *67*, 14–17.
[4] R. Kee, H. Zhu, *Combust. Sci. Technol.* **2008**, *180*, 1207–1244.
[5] F. Leucht, W. G. Bessler, J. Kallo, K. A. Friedrich, H. Müller-Steinhagen, *J. Power Sources* **2011**, *196*, 1205–1215.
[6] S. C. Singhal, K. Kendall, *High Temperature Solid Oxide Fuel Cells: Fundamental, Design and Applications*, Elsevier, Oxford, UK, **2003**.
[7] A. Weber, E. Ivers-Tiffée, *J. Power Sources* **2004**, *127*, 273–283.
[8] V. Sauchuk, S. Megel, E. Girdauskaite, N. Trofimenko, M. Kusnezoff, A. Michaelis, *Russ. J. Electrochem.* **2011**, *47*, 522–530.
[9] C. H. Bartholomew, *Appl. Catal., A* **2001**, *212*, 17–60.
[10] R. O'Hayre, S.-W. Cha, W. Colella, *Fuel Cell Fundamentals*, John Wiley & Sons, Hoboken, New Jersey, USA, **2016**.
[11] S. E. Veyo, W. L. Lundberg, S. D. Vora, K. P. Litzinger, in *ASME Pap. No. GT2003-38943*, **2003**, pp. 1–7.
[12] R. A. George, *J. Power Sources* **2000**, *86*, 134–139.
[13] M. C. Tucker, *J. Power Sources* **2010**, *195*, 4570–4582.
[14] C. Sun, U. Stimming, *J. Power Sources* **2007**, *171*, 247–260.
[15] S. P. S. Badwal, *J. Mater. Sci.* **1984**, *19*, 1767–1776.
[16] S. P. S. Badwal, J. Drennan, *J. Mater. Sci.* **1987**, *22*, 3231–3239.
[17] M. J. Verkerk, B. J. Middelhuis, A. J. Burggraaf, *Solid State Ionics* **1982**, *6*, 159–170.
[18] N. Q. Minh, T. Takahashi, *Science and Technology of Ceramic Fuel Cells*, Elsevier, Amsterdam, **1995**.
[19] J. W. Fergus, *J. Power Sources* **2006**, *162*, 30–40.
[20] C. Haering, A. Roosen, H. Schichl, *Solid State Ionics* **2005**, *176*, 253–259.
[21] S. P. S. Badwal, F. T. Ciacchi, D. Milosevic, *Solid State Ionics* **2000**, *136-137*, 91–99.
[22] C. Sun, R. Hui, J. Roller, *J. Solid State Electrochem.* **2010**, *14*, 1125–1144.
[23] J. M. Ralph, A. C. Schoeler, M. Krumpelt, *Electrochem. Technol.* **2001**, *6*, 1161 – 1172.
[24] A. Mai, M. Becker, W. Assenmacher, F. Tietz, D. Hathiramani, E. Ivers-Tiffée, D. Stöver, W. Mader, *Solid State Ionics* **2006**, *177*, 1965–1968.
[25] P. I. Cowin, C. T. G. Petit, R. Lan, J. T. S. Irvine, S. W. Tao, *Adv. Energy Mater.* **2011**, *1*, 314–332.
[26] R. Mukundan, E. L. Brosha, F. H. Garzon, *Electrochem. Solid-State Lett.* **2004**, *7*, A5–A7.
[27] F. Han, R. Semerad, G. Constantin, L. Dessemond, R. Costa, *ECS Trans.* **2015**, *68(1)*, 1889–1896.
[28] H. He, R. J. Gorte, J. M. Vohs, *Electrochem. Solid-State Lett.* **2005**, *8*, A279–A280.
[29] C. Lu, W. L. Worrell, J. M. Vohs, R. J. Gorte, *J. Electrochem. Soc.* **2003**, *150*, A1357–A1359.
[30] J. Marrero-Jerez, A. Murugan, I. S. Metcalfe, P. Núñez, *Ceram. Int.* **2014**, *40*, 15175–15182.
[31] Y. M. Choi, C. Compson, M. C. Lin, M. Liu, *Chem. Phys. Lett.* **2006**, *421*, 179–183.
[32] M. Mogensen, T. Lindegaard, U. R. Hansen, G. Mogensen, *J. Electrochem. Soc.* **1994**, *141*, 2122–2128.
[33] W. G. Bessler, S. Gewies, M. Vogler, *Electrochim. Acta* **2007**, *53*, 1782–1800.

[34] M. Vogler, A. Bieberle-Hütter, L. Gauckler, J. Warnatz, W. G. Bessler, *J. Electrochem. Soc.* **2009**, *156*, B663–B672.
[35] V. Yurkiv, R. Costa, Z. Ilhan, A. Ansar, W. G. Bessler, *J. Electrochem. Soc.* **2014**, *161*, F480–F492.
[36] J. J. Fleig, *Phys. Chem. Chem. Phys.* **2005**, *7*, 2027–2037.
[37] S. Chapman, T. G. Cowling, *Am. J. Phys.* **1961**, *30*, 389–389.
[38] R. B. Bird, E. N. Lightfoot, W. E. Stewart, *Transport Phenomena*, John Wiley & Sons, New York, USA, **1961**.
[39] W. G. Bessler, S. Gewies, *J. Electrochem. Soc.* **2007**, *153*, B548–B559.
[40] Y. Shiratori, T. Ijichi, T. Oshima, K. Sasaki, *Int. J. Hydrogen Energy* **2010**, *35*, 7905–7912.
[41] P. Kowalik, K. Antoniak-Jurak, M. Błesznowski, M. C. Herrera, M. A. Larrubia, L. J. Alemany, I. S. Pieta, *Catal. Today* **2015**, *254*, 129–134.
[42] M. Andersson, H. Paradis, J. Yuan, B. Sundén, *J. Fuel Cell Sci. Technol.* **2011**, *8*, 031013–31021.
[43] W. Sangtongkitcharoen, S. Assabumrungrat, V. Pavarajarn, N. Laosiripojana, P. Praserthdam, *J. Power Sources* **2005**, *142*, 75–80.
[44] W. Wang, C. Su, Y. Wu, R. Ran, Z. Shao, *Chem. Rev.* **2013**, *113*, 8104–8151.
[45] H.-F. Oetjen, V. M. Schmidt, U. Stimming, F. Trila, *J. Electrochem. Soc.* **1996**, *143*, 3838–3842.
[46] V. Yurkiv, A. Utz, A. Weber, E. Ivers-Tiffée, H.-R. R. Volpp, W. G. Bessler, *Electrochim. Acta* **2012**, *59*, 573–580.
[47] V. Yurkiv, D. Starukhin, H.-R. Volpp, W. G. Bessler, *J. Electrochem. Soc.* **2011**, *158*, B5–B15.
[48] Y. Matsuzaki, I. Yasuda, *J. Electrochem. Soc.* **2000**, *147*, 1630–1635.
[49] H. Timmermann, D. Fouquet, A. Weber, E. Ivers-Tiffée, U. Hennings, R. Reimert, *Fuel Cells* **2006**, *6*, 307–313.
[50] H. Timmermann, W. Sawady, D. Campbell, A. Weber, R. Reimert, E. Ivers-Tiffée, *J. Electrochem. Soc.* **2008**, *155*, B356–B359.
[51] E. A. Liese, R. S. Gemmen, *J. Eng. Gas Turbines Power* **2005**, *127*, 86–90.
[52] H. Yokokawa, H. Tu, B. Iwanschitz, A. Mai, *J. Power Sources* **2008**, *182*, 400–412.
[53] R. Knibbe, A. Hauch, J. Hjelm, S. D. Ebbesen, M. Mogensen, *Green* **2011**, *1*, 141–169.
[54] C. Gindorf, L. Singheiser, K. Hilpert, *Steel Res.* **2001**, *72*, 528–533.
[55] K. Hilpert, D. Das, M. Miller, D. H. Peck, R. Weiß, *J. Electrochem. Soc.* **1996**, *143*, 3642–3647.
[56] S. P. Simner, M. D. Anderson, M. H. Engelhard, J. W. Stevenson, *Electrochem. Solid-State Lett.* **2006**, *9*, A478–A481.
[57] V. A. C. Haanappel, J. Mertens, A. Mai, *J. Fuel Cell Sci. Technol.* **2006**, *3*, 263–270.
[58] A. Mai, V. A. C. Haanappel, F. Tietz, D. Stöver, *Solid State Ionics* **2006**, *177*, 2103–2107.
[59] A. Mai, V. A. C. Haanappel, S. Uhlenbruck, F. Tietz, D. Stöver, *Solid State Ionics* **2005**, *176*, 1341–1350.
[60] P. W. Voorhees, *J. Stat. Phys.* **1985**, *38*, 231–252.
[61] H. Galinski, J. Reuteler, J. L. Rupp, A. Bieberle-Hütter, L. J. Gauckler, *ECS Trans.* **2009**, *25*, 2057–2060.
[62] L. Holzer, B. Iwanschitz, T. Hocker, B. Münch, M. Prestat, D. Wiedenmann, U. Vogt, P. Holtappels, J. Sfeir, A. Mai, T. Graule, *J. Power Sources* **2011**, *196*, 1279–1294.
[63] J. S. Cronin, J. R. Wilson, S. A. Barnett, *J. Power Sources* **2011**, *196*, 2640–2643.
[64] A. Hagen, R. Barfod, P. V. Hendriksen, Y.-L. Liu, S. Ramousse, *J. Electrochem. Soc.*

**2006**, *153*, A1165–A1171.
[65] W. Fischer, J. Malzbender, G. Blass, R. W. Steinbrech, *J. Power Sources* **2005**, *150*, 73–77.
[66] J. Neidhardt, M. Henke, W. Bessler, *ECS Trans.* **2011**, *35(1)*, 1621–1629.
[67] K. Haga, S. Adachi, Y. Shiratori, K. Itoh, K. Sasaki, *Solid State Ionics* **2008**, *179*, 1427–1431.
[68] O. A. Marina, C. A. Coyle, E. C. Thomsen, D. J. Edwards, G. W. Coffey, L. R. Pederson, *Solid State Ionics* **2010**, *181*, 430–440.
[69] V. Yurkiv, *Electrochim. Acta* **2014**, *143*, 114–128.
[70] T. Kim, G. Liu, M. Boaro, S. I. Lee, J. M. Vohs, R. J. Gorte, O. H. Al-Madhi, B. O. Dabbousi, *J. Power Sources* **2006**, *155*, 231–238.
[71] C. H. Bartholomew, P. K. Agrawal, J. R. Katzer, *Adv. Catal.* **1982**, *31*, 135–242.
[72] P. Forzatti, L. Lietti, *Catal. Today* **1999**, *52*, 165–181.
[73] European Parliament, European Commission, *Off. J. Eur. Union* **2009**, 63–87.
[74] K. Sasaki, K. Susuki, A. Iyoshi, M. Uchimura, N. Imamura, H. Kusaba, Y. Teraoka, H. Fuchino, K. Tsujimoto, Y. Uchida, N. Jingo, *J. Electrochem. Soc.* **2006**, *153*, A2023–A2030.
[75] S. Zha, Z. Cheng, M. Liu, *J. Electrochem. Soc.* **2007**, *154*, B201–B208.
[76] Z. Cheng, S. Zha, M. Liu, *J. Power Sources* **2007**, *172*, 688–693.
[77] Y. Matsuzaki, *Solid State Ionics* **2000**, *132*, 261–269.
[78] A. Lussier, S. Sofie, J. Dvorak, Y. Idzerda, *Int. J. Hydrogen Energy* **2008**, *33*, 3945–3951.
[79] L. Yang, Z. Cheng, M. Liu, L. Wilson, *Energy Environ. Sci.* **2010**, *3*, 1804–1809.
[80] J. F. B. Rasmussen, A. Hagen, *J. Power Sources* **2009**, *191*, 534–541.
[81] V. Birss, L. Deleebeeck, S. Paulson, T. Smith, *ECS Trans.* **2011**, *35(1)*, 1445.
[82] E. Brightman, D. G. Ivey, D. J. L. Brett, N. P. Brandon, *J. Power Sources* **2011**, *196*, 7182–7187.
[83] A. Ishikura, S. Sakuno, N. Komiyama, *ECS Trans.* **2007**, *7(1)*, 845–850.
[84] T. Yoshizumi, S. Taniguchi, Y. Shiratori, K. Sasaki, *J. Electrochem. Soc.* **2012**, *159*, F693–F701.
[85] S. Kavurucu Schubert, M. Kusnezoff, A. Michaelis, S. I. Bredikhin, *J. Power Sources* **2012**, *217*, 364–372.
[86] J. R. Rostrup-Nielsen, J. B. Hansen, S. Helveg, N. Christiansen, A. K. Jannasch, *Appl. Phys. A: Mater. Sci. Process.* **2006**, *85*, 427–430.
[87] J. B. Hansen, *Electrochem. Solid-State Lett.* **2008**, *11*, B178–B180.
[88] J. B. Hansen, J. Rostrup-Nielsen, *Handb. Fuel Cells* **2010**, *6*, 1–13.
[89] J. P. Trembly, A. I. Marquez, T. R. Ohrn, D. J. Bayless, *J. Power Sources* **2006**, *158*, 263–273.
[90] J. P. Ouweltjes, P. V Aravind, N. Woudstra, G. Rietveld, *J. Fuel Cell Sci. Technol.* **2006**, *3*, 495–498.
[91] P. V. Aravind, J. P. Ouweltjes, N. Woudstra, G. Rietveld, *Electrochem. Solid-State Lett.* **2008**, *11*, B24–B28.
[92] C. Xu, P. Gansor, J. W. Zondlo, K. Sabolsky, E. M. Sabolsky, *J. Electrochem. Soc.* **2011**, *158*, B1405–B1416.
[93] L. Zhang, S. P. Jiang, H. Q. He, X. Chen, J. Ma, X. C. Song, *Int. J. Hydrogen Energy* **2010**, *35*, 12359–12368.
[94] P. Lohsoontorn, D. J. L. Brett, N. P. Brandon, *J. Power Sources* **2008**, *183*, 232–239.
[95] A. Mai, B. Iwanschitz, U. Weissen, R. Denzler, D. Haberstock, V. Nerlich, A. Schuler, *ECS Trans.* **2009**, *25(2)*, 149–158.

[96] M. Kusnezoff, N. Trofimenko, M. Müller, A. Michaelis, *Materials* **2016**, *9*, 906–914.
[97] T. R. Smith, A. Wood, V. I. Birss, *Appl. Catal., A* **2009**, *354*, 1–7.
[98] T. Yoshizumi, C. Uryu, T. Oshima, Y. Shiratori, K. Ito, K. Sasaki, *ECS Trans.* **2011**, *35(1)*, 1717–1725.
[99] J. F. B. Rasmussen, A. Hagen, *Fuel Cells* **2010**, *10*, 1135–1142.
[100] A. Weber, S. Dierickx, A. Kromp, E. Ivers-Tiffée, *Fuel Cells* **2013**, *13*, 487–493.
[101] T. S. Li, M. Xu, C. Gao, B. Wang, X. Liu, B. Li, W. G. Wang, *J. Power Sources* **2014**, *258*, 1–4.
[102] A. Hagen, *J. Electrochem. Soc.* **2012**, *160*, F111–F118.
[103] A. Hagen, G. B. Johnson, P. Hjalmarsson, *J. Power Sources* **2014**, *272*, 776–785.
[104] M. Riegraf, G. Schiller, R. Costa, K. A. Friedrich, A. Latz, V. Yurkiv, *J. Electrochem. Soc.* **2014**, *162*, F65–F75.
[105] Z. Cheng, J.-H. Wang, Y. Choi, L. Yang, M. C. Lin, M. Liu, *Energy Environ. Sci.* **2011**, *4*, 4380–4409.
[106] A. Hagen, J. F. B. Rasmussen, K. Thyden, *J. Power Sources* **2011**, *196*, 7271–7276.
[107] M. Noponen, M. Halinen, J. Kiviaho, J. Saarinen, *J. Fuel Cell Sci. Technol.* **2006**, *3*, 438–444.
[108] J. R. Rostrup-Nielsen, J. Sehested, J. K. Norskov, *Adv. Catal.* **2002**, *47*, 65–139.
[109] H. P. He, A. Wood, D. Steedman, M. Tilleman, *Solid State Ionics* **2008**, *179*, 1478–1482.
[110] A. Kromp, S. Dierickx, A. Leonide, A. Weber, E. Ivers-Tiffée, *J. Electrochem. Soc.* **2012**, *159*, B597–B601.
[111] J. N. Kuhn, N. Lakshminarayanan, U. S. Ozkan, *J. Mol. Catal. A: Chem.* **2008**, *282*, 9–21.
[112] A. Hauch, A. Hagen, J. Hjelm, T. Ramos, *J. Electrochem. Soc.* **2014**, *161*, F734–F743.
[113] P. Lohsoontorn, D. J. L. Brett, N. P. Brandon, *J. Power Sources* **2008**, *175*, 60–67.
[114] H. Kishimoto, T. Horita, K. Yamaji, M. E. Brito, Y.-P. Xiong, H. Yokokawa, *J. Electrochem. Soc.* **2010**, *157*, B802–B813.
[115] D. R. Alfonso, *Surf. Sci.* **2008**, *602*, 2758–2768.
[116] J.-H. H. Wang, M. Liu, *Electrochem. commun.* **2007**, *9*, 2212–2217.
[117] N. M. Galea, E. S. Kadantsev, T. Ziegler, *J. Phys. Chem. C* **2007**, *111*, 14457–14468.
[118] D. S. Monder, K. Karan, *J. Phys. Chem. C* **2010**, 22597–22602.
[119] C. H. Yeh, J. J. Ho, *ChemPhysChem* **2012**, *13*, 3194–3203.
[120] N. N. M. Galea, J. M. H. Lo, T. Ziegler, *J. Catal.* **2009**, *263*, 380.
[121] D. S. Monder, K. Karan, *ECS Trans.* **2013**, *57(1)*, 2449–2458.
[122] I. Alstrup, J. R. J. Rostrup-Nielsen, S. Røen, *Appl. Catal.* **1981**, *1*, 303–314.
[123] B. V. R. S. N. V. R. S. N. Prasad, V. M. Janardhanan, *J. Electrochem. Soc.* **2013**, *161*, 208–213.
[124] D. Monder, K. Karan, *ECS Trans.* **2011**, *35(1)*, 977–985.
[125] V. M. Janardhanan, D. S. Monder, *J. Electrochem. Soc.* **2014**, *161*, F1427–F1436.
[126] S. Appari, V. M. Janardhanan, R. Bauri, S. Jayanti, O. Deutschmann, *Appl. Catal., A* **2014**, *471*, 118–125.
[127] F. N. Cayan, S. R. Pakalapati, I. Celik, C. Xu, J. Zondlo, *Fuel Cells* **2012**, *12*, 464–473.
[128] E. M. Ryan, W. Xu, X. Sun, M. A. Khaleel, *J. Power Sources* **2012**, *210*, 233–242.
[129] T. Nakamura, T. Kobayashi, K. Yashiro, A. Kaimai, T. Otake, K. Sato, J. Mizusaki, T. Kawada, *J. Electrochem. Soc.* **2008**, *155*, B563–B569.
[130] B. Iwanschitz, J. Sfeir, A. Mai, M. Schütze, *J. Electrochem. Soc.* **2010**, *157*, B269–B278.
[131] V. Papaefthimiou, M. Shishkin, D. K. Niakolas, M. Athanasiou, Y. T. Law, R. Arrigo,

D. Teschner, M. Hävecker, A. Knop-Gericke, R. Schlögl, T. Ziegler, S. G. Neophytides, S. Zafeiratos, *Adv. Energy Mater.* **2013**, *3*, 762–769.
[132] W. C. Chueh, Y. Hao, W. Jung, S. M. Haile, *Nat. Mater.* **2011**, *11*, 155–161.
[133] C. Zhang, M. E. Grass, A. H. McDaniel, S. C. DeCaluwe, F. El Gabaly, Z. Liu, K. F. McCarty, R. L. Farrow, M. A. Linne, Z. Hussain, G. S. Jackson, H. Bluhm, B. W. Eichhorn, *Nat. Mater.* **2010**, *9*, 944–949.
[134] W. C. Chueh, S. M. Haile, *Phys. Chem. Chem. Phys.* **2009**, *11*, 8144–8148.
[135] B. Mirfakhraei, S. Paulson, V. Thangadurai, V. Birss, *J. Power Sources* **2013**, *243*, 95–101.
[136] D. R. Mullins, T. S. McDonald, *Surf. Sci.* **2007**, *601*, 4931–4938.
[137] M. Gerstl, A. Nenning, R. Iskandar, V. Rojek-Wöckner, M. Bram, H. Hutter, A. K. Opitz, *Materials* **2016**, *9*, 649–682.
[138] Z. A. Feng, F. El Gabaly, X. Ye, Z.-X. Shen, W. C. Chueh, *Nat. Commun.* **2014**, *5*, 1–9.
[139] S. C. Decaluwe, M. E. Grass, C. Zhang, F. El Gabaly, H. Bluhm, Z. Liu, G. S. Jackson, A. H. McDaniel, K. F. McCarty, R. L. Farrow, M. A. Linne, Z. Hussain, B. W. Eichhorn, *J. Phys. Chem. C* **2010**, *114*, 19853–19861.
[140] A. Glauche, T. Betz, M. Ise, *ECS Trans.* **2011**, *35(1)*, 157–165.
[141] N. Trofimenko, M. Kusnezoff, A. Michaelis, *ECS Trans.* **2011**, *35(1)*, 315–325.
[142] M. Miyake, S. Matsumoto, M. Iwami, S. Nishimoto, Y. Kameshima, *Int. J. Hydrogen Energy* **2016**, *41*, 13625–13631.
[143] V. Sonn, A. Leonide, E. Ivers-Tiffée, *J. Electrochem. Soc.* **2008**, *155*, B675–B679.
[144] J. R. Macdonald, W. B. Johnson, in *Impedance Spectrosc. Theory, Exp. Appl. Second Ed.*, John Wiley & Sons, Inc., **2005**, pp. 1–26.
[145] M. E. Orazem, B. Tribollet, *Electrochemical Impedance Spectroscopy*, **2008**.
[146] B. Boukamp, *Solid State Ionics* **1986**, *20*, 31–44.
[147] S. B. Adler, *Chem. Rev.* **2004**, *104*, 4791–4843.
[148] S. B. Adler, X. Y. Chen, J. R. Wilson, *J. Catal.* **2007**, *245*, 91–109.
[149] J. Nielsen, T. Jacobsen, M. Wandel, *Electrochim. Acta* **2011**, *56*, 7963–7974.
[150] S. Dierickx, T. Mundloch, A. Weber, E. Ivers-Tiffée, *ECS Trans.* **2017**, *78(1)*, 1273–1284.
[151] A. Leonide, V. Sonn, A. Weber, E. Ivers-Tiffée, *J. Electrochem. Soc.* **2008**, *155*, B36–B41.
[152] H. Schichlein, A. Müller, M. Voigts, A. Krügel, E. Ivers-Tiffée, *J. Appl. Electrochem.* **2002**, *32*, 875–882.
[153] S. Risse, N. A. Cañas, N. Wagner, E. Härk, M. Ballauff, K. A. Friedrich, *J. Power Sources* **2016**, *323*, 107–114.
[154] J. P. Neidhardt, D. N. Fronczek, T. Jahnke, T. Danner, B. Horstmann, W. G. Bessler, *J. Electrochem. Soc.* **2012**, *159*, A1528–A1542.
[155] S. B. Adler, W. G. Bessler, in *Handb. Fuel Cells*, John Wiley & Sons, **2009**.
[156] P. Atkins, J. De Paula, *Elements of Physical Chemistry*, Oxford University Press, USA, **2013**.
[157] J. Newman, K. E. Thomas-Alyea, *Electrochemical Systems*, John Wiley & Sons, Hoboken, New Jersey, USA, **2004**.
[158] P. Deuflhard, E. Hairer, J. Zugck, *Numer. Math.* **1987**, *51*, 501–516.
[159] W. G. Bessler, *Solid State Ionics* **2005**, *176*, 997–1011.
[160] A. Zekri, M. Knipper, J. Parisi, T. Plaggenborg, *Phys Chem Chem Phys* **2017**, *19*, 13767–13777.
[161] A. Zekri, B. Schnetger, M. A. Essafi, T. Plaggenborg, J. Parisi, M. Knipper, *J. Electrochem. Soc.* **2017**, *164*, F1385–F1391.

[162] M. Riegraf, V. Yurkiv, G. Schiller, R. Costa, A. Latz, K. A. Friedrich, *J. Electrochem. Soc.* **2015**, *162*, 1324–1332.
[163] W. G. Bessler, M. Vogler, H. Störmer, D. Gerthsen, A. Utz, E. Ivers-Tiffeé, *Phys. Chem. Chem. Phys* **2010**, *12*, 13888–13903.
[164] M.W. Chase, *J. Phys. Chem. Ref. Data Monogr. No. 9* **1998**, 1–1951.
[165] J. G. McCarty, H. Wise, *J. Chem. Phys.* **1980**, *72*, 6332–6337.
[166] N. M. Galea, J. M. H. Lo, T. Ziegler, *J. Catal.* **2009**, *263*, 380–389.
[167] H. Zhu, R. J. Kee, V. M. Janardhanan, O. Deutschmann, D. G. Goodwin, *J. Electrochem. Soc.* **2005**, *152*, A2427–A2440.
[168] J. Warnatz, U. Maas, R. W. Dibble, *Combustion: Physical and Chemical Fundamentals, Modeling and Simulation, Experiments, Pollutant Formation*, Springer, Berlin, **1996**.
[169] E. S. Hecht, G. K. Gupta, H. Zhu, A. M. Dean, R. J. Kee, L. Maier, O. Deutschmann, *Appl. Catal., A* **2005**, *295*, 40–51.
[170] R. B. Getman, W. F. Schneider, *ChemCatChem* **2010**, *2*, 1450–1460.
[171] L. C. Grabow, B. Hvolbæk, J. K. Nørskov, *Top. Catal.* **2010**, *53*, 298–310.
[172] S. D. Miller, J. R. Kitchin, *Surf. Sci.* **2009**, *603*, 794–801.
[173] A. B. Mhadeshwar, J. R. Kitchin, M. A. Barteau, D. G. Vlachos, *Catal. Letters* **2004**, *96*, 13–22.
[174] D. G. Goodwin, H. Zhu, A. M. Colclasure, R. J. Kee, *J. Electrochem. Soc.* **2009**, *156*, B1004–B1021.
[175] C. Bao, X. Zhang, *Electrochim. Acta* **2014**, *130*, 785–790.
[176] H. Zhu, A. Kromp, A. Leonide, E. Ivers-Tiffee, O. Deutschmann, R. J. Kee, *J. Electrochem. Soc.* **2012**, *159*, F255–F266.
[177] E. J. Brightman, R. Maher, D. G. Ivey, G. Offer, N. P. Brandon, *ECS Trans.* **2011**, *35(1)*, 1407–1419.
[178] L. Maier, B. Schädel, K. Herrera Delgado, S. Tischer, O. Deutschmann, *Top. Catal.* **2011**, *54*, 845–858.
[179] R. J. Kee, H. Zhu, D. G. Goodwin, *Proc. Combust. Inst.* **2005**, *30*, 2379–2404.
[180] J. Oudar, *Catal. Rev. Eng.* **1980**, *22*, 171–181.
[181] A. Utz, A. Leonide, A. Weber, E. Ivers-Tiffée, *J. Power Sources* **2011**, *196*, 7217–7224.
[182] A. Kromp, A. Leonide, A. Weber, E. Ivers-Tiffée, *J. Electrochem. Soc.* **2011**, *158*, B980–B989.
[183] A. Glauche, T. Betz, S. Mosch, N. Trofimenko, M. Kusnezoff, *ECS Trans.* **2009**, *25*, 411–419.
[184] M. Riegraf, V. Yurkiv, R. Costa, G. Schiller, K. A. Friedrich, *ChemSusChem* **2017**, *10*, 587–599.
[185] M. Riegraf, M. Hoerlein, R. Costa, G. Schiller, K. A. Friedrich, *ACS Catal.* **2017**, *7*, 7760–7771.
[186] J. Nielsen, J. Hjelm, *Electrochim. Acta* **2014**, *115*, 31–45.
[187] S. Primdahl, M. Mogensen, *Solid State Ionics* **2002**, *152-153*, 597–608.
[188] P. Kim, D. J. L. Brett, N. P. Brandon, *J. Power Sources* **2009**, *189*, 1060–1065.
[189] S. Primdahl, M. B. Mogensen, *J. Electrochem. Soc.* **1999**, *146*, 2827–2833.
[190] W. C. Chueh, S. M. Haile, *Annu. Rev. Chem. Biomol. Eng.* **2012**, *3*, 313–341.
[191] A. Babaei, S. P. Jiang, J. Li, *J. Electrochem. Soc.* **2009**, *156*, B1022–B1029.
[192] M. Chen, B. H. Kim, Q. Xu, B. G. Ahn, D. P. Huang, *Solid State Ionics* **2010**, *181*, 1119–1124.
[193] S. Primdahl, Y. L. Liu, *J. Electrochem. Soc.* **2002**, *149*, A1466–A1472.
[194] M. Mogensen, *Solid State Ionics* **2000**, *129*, 63–94.
[195] S. Gewies, W. G. Bessler, *J. Electrochem. Soc.* **2008**, *155*, B937–B952.

[196] R. Barfod, M. Mogensen, T. Klemenso, A. Hagen, Y.-L. Liu, P. Vang Hendriksen, *J. Electrochem. Soc.* **2007**, *154*, B371–B378.
[197] M. Kornely, A. Neumann, N. H. Menzler, A. Leonide, A. Weber, E. Ivers-Tiffée, *J. Power Sources* **2011**, *196*, 7203–7208.
[198] Y. Tao, S. D. Ebbesen, M. B. Mogensen, *J. Electrochem. Soc.* **2014**, *161*, F337–F343.
[199] L. Jia, X. Wang, B. Hua, W. Li, B. Chi, J. Pu, S. Yuan, L. Jian, *Int. J. Hydrogen Energy* **2012**, *37*, 11941–11945.
[200] W. An, D. Gatewood, B. Dunlap, C. H. Turner, *J. Power Sources* **2011**, *196*, 4724–4728.
[201] H. Yokokawa, T. Horita, N. Sakai, K. Yamaji, M. E. Brito, Y. P. Xiong, H. Kishimoto, *Solid State Ionics* **2004**, *174*, 205–221.
[202] T. Horita, H. Kishimoto, K. Yamaji, Y. Xiong, N. Sakai, M. E. Brito, H. Yokokawa, *Solid State Ionics* **2006**, *177*, 1941–1948.
[203] Z. P. Li, T. Mori, G. J. Auchterlonie, J. Zou, J. Drennan, *Appl. Phys. Lett.* **2011**, *98*, 093104–093106.
[204] J. Fleig, *J. Power Sources* **2002**, *105*, 228–238.
[205] E. Aneggi, J. Llorca, M. Boaro, A. Trovarelli, *J. Catal.* **2005**, *234*, 88–95.
[206] D. Fernández-Torre, J. Carrasco, M. V. Ganduglia-Pirovano, R. Pérez, *J. Chem. Phys.* **2014**, *141*, 014703–041712.
[207] M. Shishkin, T. Ziegler, *J. Phys. Chem. C* **2010**, *114*, 21411–21416.
[208] M. Vogler, W. G. Bessler, *ECS Trans.* **2009**, *25(2)*, 1957–1966.
[209] N. Sakai, K. Yamaji, T. Horita, H. Yokokawa, Y. Hirata, S. Sameshima, Y. Nigara, J. Mizusaki, *Solid State Ionics* **1999**, *125*, 325–331.
[210] H. Kishimoto, K. Yamaji, T. Horita, Y. P. Xiong, M. E. Brito, M. Yoshinaga, H. Yokokawa, *Electrochemistry* **2009**, *77*, 190–194.
[211] D. Goodwin, *Cantera: An Object-Oriented Software Toolkit for Chemical Kinetics, Thermodynamics, and Transport Processes*, Caltech, Pasadena, USA, **2009**.
[212] W. Erley, H. Wagner, *J. Catal.* **1978**, *53*, 287–294.
[213] J. Neidhardt, M. Henke, W. Bessler, *ECS Trans.* **2011**, *35(1)*, 1621–1629.
[214] K. Sasaki, *J. Fuel Cell Sci. Technol.* **2008**, *5*, 031212–031216.
[215] C. Neofytidis, M. Athanasiou, S. G. Neophytides, D. K. Niakolas, *Top. Catal.* **2015**, *58*, 1276–1289.
[216] D. K. Niakolas, *Appl. Catal., A* **2014**, *486*, 123–142.
[217] R. C. Catapan, A. A. M. Oliveira, Y. Chen, D. G. Vlachos, *J. Phys. Chem. C* **2012**, *116*, 20281–20291.
[218] O. A. Marina, M. Mogensen, *Appl. Catal., A* **1999**, *189*, 117–126.
[219] N. Russner, H. Geisler, S. Dierickx, A. Weber, E. Ivers-Tiffée, *ECS Trans.* **2017**, *78(1)*, 2673–2682.
[220] W. C. Chueh, A. H. McDaniel, M. E. Grass, Y. Hao, N. Jabeen, Z. Liu, S. M. Haile, K. F. McCarty, H. Bluhm, F. El Gabaly, *Chem. Mater.* **2012**, *24*, 1876–1882.
[221] Z. A. Feng, M. L. Machala, W. C. Chueh, *Phys. Chem. Chem. Phys.* **2015**, *17*, 12273–12281.
[222] P. Aguiar, C. S. Adjiman, N. P. Brandon, *J. Power Sources* **2004**, *138*, 120–136.
[223] C. Graves, C. Chatzichristodoulou, M. B. Mogensen, *Faraday Discuss.* **2015**, *182*, 75–95.
[224] T. Luo, R. J. Gorte, *Catal. Letters* **2003**, *85*, 139–146.
[225] R. J. Gorte, S. Zhao, *Catal. Today* **2005**, *104*, 18–24.
[226] M. Riegraf, A. Zekri, M. Knipper, R. Costa, G. Schiller, K. A. Friedrich, *J. Power Sources* **2017**, submitted.

[227] A. Hauch, A. Hagen, J. Hjelm, T. Ramos, *ECS Trans.* **2013**, *57*, 615–625.
[228] M. Lang, M. Klein, M. Henke, C. Willich, G. Schiller, F. Hauler, *ECS Trans.* **2013**, *57*, 367–376.
[229] A. Ploner, A. Hagen, A. Hauch, *Fuel Cells* **2017**, *17*, 498–507.
[230] A. Hauch, M. Mogensen, A. Hagen, *Solid State Ionics* **2011**, *192*, 547–551.
[231] A. Zekri, K. Herbrig, M. Knipper, J. Parisi, T. Plaggenborg, *Fuel Cells* **2017**, *17*, 359–366.
[232] M. P. Hoerlein, G. Schiller, F. Tietz, K. A. Friedrich, *ECS Trans.* **2015**, *68(1)*, 3553–3561.
[233] A. Hauch, K. Brodersen, M. Chen, M. B. Mogensen, *Solid State Ionics* **2016**, *293*, 27–36.
[234] M. Chen, Y.-L. Liu, J. J. Bentzen, W. Zhang, X. Sun, A. Hauch, Y. Tao, J. R. Bowen, P. V Hendriksen, *J. Electrochem. Soc.* **2013**, *160*, F883–F891.
[235] M. B. Mogensen, A. Hauch, X. Sun, M. Chen, Y. Tao, S. D. Ebbesen, K. V. Hansen, P. V. Hendriksen, *Fuel Cells* **2017**, *17*, 434–441.
[236] K. Vetter, *Electrochemical Kinetics*, Academic Press, London, **1967**.
[237] M. H. Pihlatie, A. Kaiser, M. Mogensen, M. Chen, *Solid State Ionics* **2011**, *189*, 82–90.
[238] Z. Cheng, M. Liu, *Solid State Ionics* **2007**, *178*, 925–935.
[239] D. G. Ivey, E. Brightman, N. Brandon, *J. Power Sources* **2010**, *195*, 6301–6311.
[240] A. Hauch, S. D. Ebbesen, S. H. Jensen, M. Mogensen, *J. Electrochem. Soc.* **2008**, *155*, B1184–B1193.
[241] Y. Yamada, R. Okubo, M. Kinoshita, E. Niwa, T. Hashimoto, K. Tomomichi, K. Sasaki, *J. Electrochem. Soc.* **2015**, *162*, F1107–F1113.
[242] K. N. Tu, *J. Appl. Phys.* **2003**, *94*, 5451–5473.
[243] D. G. Pierce, P. G. Brusius, *Microelectron. Reliab.* **1997**, *37*, 1053–1072.
[244] S. J. Krumbein, *IEEE Trans. Components, Hybrids, Manuf. Technol.* **1988**, *11*, 5–15.
[245] H. Sezer, I. B. Celik, *Electrochim. Acta* **2015**, *155*, 421–430.
[246] K. Vels Jensen, R. Wallenberg, I. Chorkendorff, M. Mogensen, *Solid State Ionics* **2003**, *160*, 27–37.
[247] M. Zhi, X. Chen, H. Finklea, I. Celik, N. Q. Wu, *J. Power Sources* **2008**, *183*, 485–490.
[248] M. G. Gonzalez, E. N. Ponzi, O. A. Ferretti, C. E. Quincoces, P. Marecot, J. Barbier, *Adsorpt. Sci. Technol.* **2000**, *18*, 541–550.
[249] J. A. Rodriguez, J. Hrbek, *Acc. Chem. Res.* **1999**, *32*, 719–728.
[250] P. Boldrin, E. Ruiz-Trejo, J. Mermelstein, J. M. Bermúdez Menéndez, T. Ramírez Reina, N. P. Brandon, *Chem. Rev.* **2016**, *116*, 13633–13684.
[251] M. C. Verbraeken, T. Ramos, K. Agersted, Q. Ma, C. D. Savaniu, B. R. Sudireddy, J. T. S. Irvine, P. Holtappels, F. Tietz, *RSC Adv.* **2015**, *5*, 1168–1180.
[252] M. C. Verbraeken, B. Iwanschitz, A. Mai, J. T. S. Irvine, *J. Electrochem. Soc.* **2012**, *159*, F757–F762.
[253] R. Barfod, A. Hagen, S. Ramousse, P. V. Hendriksen, M. Mogensen, *Fuel Cells* **2006**, *6*, 141–145.
[254] A. Barbucci, R. Bozzol, G. Cerisola, P. Costamagna, *Electrochim. Acta* **2002**, *47*, 2183–2188.
[255] M. A. Haider, S. McIntosh, *J. Electrochem. Soc.* **2009**, *156*, B1369–B1375.
[256] V. A. C. Haanappel, A. Mai, J. Mertens, *Solid State Ionics* **2006**, *177*, 2033–2037.

## List of peer-reviewed publications

M. Riegraf, A. Zekri, M. Knipper, R. Costa, G. Schiller, K. A. Friedrich. Sulfur Poisoning of Ni/Gadolinium-Doped Ceria Anodes: A Long-Term Study Outlining Stable Solid Oxide Fuel Cell Operation, *J. Power Sources*, 2018, 380, 26–36.

M. Riegraf, M. P. Hoerlein, R. Costa, G. Schiller, K. A. Friedrich. Sulfur Poisoning of Electrochemical Reformate Conversion on Nickel/Gadolinium-Doped Ceria Electrodes. *ACS Catal.*, 2017, 7, 7760–7771.

M. Riegraf, V. Yurkiv, R. Costa, G. Schiller, K. A. Friedrich. Evaluation of the Effect of Sulfur on the Performance of Nickel/Gadolinium-Doped Ceria Based Solid Oxide Fuel Cell Anodes. *ChemSusChem*, 2017, 10, 587–599.

M. Riegraf, G. Schiller, R. Costa, K. A. Friedrich, A. Latz, V. Yurkiv. The Influence of Sulfur Formation on Performance and Reforming Chemistry of SOFC Anodes Operating on Methane Containing Fuel. *J. Electrochem. Soc*., 2015, 162 (1), F1324–1332.

M. Riegraf, G. Schiller, R. Costa, K. A. Friedrich, A. Latz, V. Yurkiv. Elementary Kinetic Numerical Simulation of Ni/YSZ Anode Performance Considering Sulfur Poisoning. *J. Electrochem. Soc.*, 2015, 162 (1), F65–F75.

## List of figures

## List of tables

## Acknowledgments

I thank Prof. Andreas Friedrich and Dr. Günter Schiller for giving me the opportunity to pursue my PhD. I furthermore thank them for the support and advice they gave me whenever needed. I also thank Prof. Anke Hagen for co-supervising my work. In particular, I would like to thank Dr. Vitaliy Yurkiv for being a scientific mentor to me during my first two years at DLR. Furthermore, I want to thank Michael Hörlein for teaching me everything I know about cell measurements and test bench setups and numerous scientific discussions. I also thank Dr. Rémi Costa for his continuous interest in my work and scientific advice. Furthermore, I would like to thank all other members of the high temperature cells and stacks group and the pressurized SOFC systems group for scientific and technical support.

Moreover, I would also like to thank Dr. André Weber, Sebastian Dierickx and Niklas Russner from Karlsruhe Institute of Technology for help with symmetrical cell measurements. Atef Zekri and Dr. Martin Knipper from the University of Oldenburg are acknowledged for collaboration on FIB/SEM, TEM/EDX and XRF analysis.

"The Electrochemical Society" and "Arbeits-Gemeinschaft Elektrochemischer Forschungsinstitutionen" (AGEF) are acknowledged for financial support via travel grants.

## Declaration of authorship

I hereby certify that this dissertation is entirely my own work except where otherwise indicates.

## Erklärung

Hiermit erkläre ich, dass ich die beigefügte Dissertation selbstständig verfasst und keine anderen als die angegebenen Hilfsmittel genutzt habe.

**Matthias Riegraf**

**Stuttgart, 16.01.2018**